Title
A MOLECULAR SURFACE SCIENCE STUDY OF THE STRUCTURE OF ADSORBATES ON SURFACES: IMPORTANCE TO LUBRICATION

Author
Mate, CM.

Publication Date
1986-09-01

Lawrence Berkeley Laboratory
UNIVERSITY OF CALIFORNIA

Materials & Molecular Research Division

A MOLECULAR SURFACE SCIENCE STUDY OF THE STRUCTURE OF ADSORBATES ON SURFACES: IMPORTANCE TO LUBRICATION

C.M. Mate
(Ph.D. Thesis)

September 1986

Prepared for the U.S. Department of Energy under Contract DE-AC03-76SF00098

DISCLAIMER

LBL-21941

A MOLECULAR SURFACE SCIENCE STUDY OF THE STRUCTURE OF ADSORBATES ON SURFACES: IMPORTANCE TO LUBRICATION

Charles Mathew Mate

Lawrence Berkeley Laboratory
University of California
Berkeley, CA 94720

This work was supported by the U.S. Department of Energy under Contract No. DE-AC03-76SF00098.

A MOLECULAR SURFACE SCIENCE STUDY OF THE STRUCTURE OF ADSORBATES ON SURFACES: IMPORTANCE TO LUBRICATION

Charles Mathew Mate

Lawrence Berkeley Laboratory
University of California
Berkeley, CA 94720

ABSTRACT

The interaction and bonding of atoms and molecules on metal surfaces is explored under ultra-high vacuum conditions using a variety of surface science techniques: high resolution electron energy loss spectroscopy (HREELS), low energy electron diffraction (LEED), thermal desorption spectroscopy (TDS), Auger electron spectroscopy (AES), work function measurements, and second harmonic generation (SHG).

Chemisorbed benzene on the Rh(111) crystal surface at 310 K is found to be centered over bridge sites when adsorbed alone on Rh(111) and over hollow sites in the presence of coadsorbed carbon monoxide. For pyridine adsorption on Rh(111), an α-CH bond breaks with pyridine forming an α-pyridyl species on the surface. Below room temperature, a physisorbed pyridine species is observed coadsorbed with the α-pyridyl species.

An important discovery of this thesis is that coadsorbed carbon monoxide can induce long range order in adsorbate overlayers. CO induced ordering is observed for benzene adsorbed on Rh(111) and Pt(111) surfaces and for fluorobenzene, acetylene, ethylidyne, propylidyne, and sodium on the Rh(111) surface. In all these coadsorbed structures,

the adsorbate maintains its molecular integrity in the presence of co-adsorbed CO, though a shift in adsorption site sometimes occurs. Work function measurements indicate that CO induced ordering may be due to the electron accepting character of adsorbed CO and the electron donating character of the coadsorbates.

For hydrogen adsorption on the Rh(111) surface, our HREEL spectra indicate that the vibrational excitations observed by EELS are best thought of as excitations between energy bands for delocalized quantum motion.

Finally, preliminary experiments are described of measurements of the coefficient of friction between a Rh(111) single crystal surface and a rhodium pin, both in air and in ultra-high vacuum.

Acknowledgements

It is hard to sit down and thank all the people who have contributed to making my graduate years at Berkely a rewarding and enjoyable experience. First and foremost, though, I would like to thank Prof. G.A. Somorjai whose enthusiasm was always a source of inspiration and without whose guidance and encouragement to explore new directions many of the projects described in this thesis would never have been attempted.

I would also like to thank Prof. Y.R. Shen for first making me aware of the possibility of doing research in the Somorjai Group, as well as for providing the opportunity of working in his lab on second harmonic generation from surfaces.

One of the great rewards of working in the Somorjai Group has been the opportunity of working with many wonderful people and scientists. In particular, I would like to thank Bruce Koel and John Crowell, who first taught me the fundamentals of surface science and UHV techniques; Brian Bent and Michel Van Hove, who were my collaborators on many of the projects described here, as well as constant sources of encouragement; Harry Tom, X.D. Zhu and Tony Heinz, who were my collaborators on the second harmonic generation experiments and who kept me up to date on the physics department gossip; Chi Tzu Kao, who was my collaborator for the work function measurements; Pete McAnally, who did most of the experiments described in Chapter 8; and Keith Franck, Dan Coulomb and Bob McAllister, who carefully crafted much of the essential apparatus

used in this thesis. I would also like to thank many Somorjai Group members, past and present, for making it a joy to work in the lab: Brian Naasz, Hiroko Ohtani, Dave Kelly, Greg Blackman, Ken Lewis, Mike Hilton, Andy Gellman and Ann Kahn.

Finally, I would like to thank my mother for her constant support and encouragement and my girl friend, Shelli Koszdin, for showing me these past five years that there is more to life than working in the lab.

DEDICATION

To the memory of my father,

who first taught me the joys of science

TABLE OF CONTENTS

CHAPTER 1

INTRODUCTION

Contents

"God made solids, but surfaces were made by the Devil" - Wolfgang Pauli

1.1 Introduction

Great progress has been made in the last fifty years toward developing an understanding of the bulk properties of materials. However, a more challenging problem has been to develop a similar understanding of the surface properties of materials. Experimentally, surfaces are intrinsically more difficult to study than the bulk as there are typically 10^{15} atoms/cm^2 on a surface but 10^{24} atoms/cm^3 in the bulk. Consequently, experimental techniques for studying surfaces must not only be able to detect the relatively small number of atoms on a surface but also must be able to discriminate against the much greater number of atoms in the bulk. Nevertheless, a relatively large number of surface sensitive techniques [1-4] have been developed over the years for studying both atomically clean and adsorbate covered surfaces, some of which are described in this thesis.

One of the major goals of surface science has been to try to provide an atomic scale understanding of important technologies that rely on the surface properties of materials, such as catalysis and lubrication. The ways that surface scientists approach these technological problems can be divided into two categories. The first, and more applied approach, is to use surface science probes to study real systems such as prepared catalysts or lubricated bearings in an attempt to identify the important components and mechanisms. The second, and more fundamental approach, is to study a well defined and characterized

model system, such as adsorption on a single crystal surface, in order to gain a partial understanding of the more complicated systems that occur in the real world. The approach taken in this thesis is the second one, namely to study how atoms and molecules bond and interact with single crystal surfaces with the aim of providing a molecular basis for lubrication.

1.2 Objectives

The primary objective of this thesis is to help develop an understanding of how atoms and molecules bond and interact with metal surfaces. As much work [1] has already been done in investigating the chemical and physical properties of adsorbates on surfaces, this thesis should be regarded as a continuation of those efforts as well as a basis for future research. In this thesis, the focus is mainly on the adsorption of organic molecules on the Rh(111) single crystal surface. The emphasis on organic molecules arises from these molecules being important in both catalysis and lubrication. The choice of a Rh(111) single crystal was made for two reasons: 1) rhodium is an excellent catalyst for a variety of reactions (e.g. hydrogenation of hydrocarbons and the reduction of nitric oxide [1]), and 2) rhodium is located in the center of the periodic table resulting in it being, among transition metals, reactive enough to significantly perturb an adsorbed molecule or to even break some of its bonds, but not so reactive at convenient temperatures (<350 K) to break all the bonds. For a more complete description of the mechanisms for breaking and

forming bonds on the Rh(111) surface, the reader is referred to the thesis of B.E. Bent (UC Berkeley, 1986), where much of the work described was done in conjunction with the work presented here.

As well as organic adsorbates, the adsorption of CO, Na, and hydrogen, both alone and in combination with organic adsorbates, were studied since these combinations of adsorbates are frequently found in real systems.

A secondary objective of this thesis is to develop a way of applying what has been learned about the adsorption of molecules on surfaces towards understanding a technological problem—lubrication. Here the goal is to develop an apparatus capable of measuring the coefficient of friction between a single crystal surface, both clean and covered with adsorbates, and another well characterized surface under ultra-high vacuum conditions. Similar experiments have been done before [5] and dramatic reductions in the coefficients of friction have been observed for even submonolayers of, for example, oxygen or alkanes on single crystal tungsten surfaces [6]; but, in none of these cases, is there a good understanding of the mechanism by which the adsorbate reduces friction. We plan to study how a wide range of adsorbate surface structures effect friction under conditions where the only variable changed is the bonding of the adsorbate to the surface. By concentrating on those adsorbates, such as ones described in this thesis, whose surface structures have been well characterized by other surface science techniques, it is hoped that a deduction of the underlying mechanisms for lubrication by chemisorbed monolayers will be possible.

1.3 Overview

As previously mentioned the primary objective of this thesis is to determine how atoms and molecules bond and interact with the Rh(111) crystal surface. A variety of techniques were used to provide the complimentary information needed to obtain a good understanding of how the adsorbates bond to the surface. Those techniques employed here include the following: high resolution electron energy loss spectroscopy (HREELS) for analysing of surface vibrational and electronic excitations; low energy electron diffraction (LEED) for determining atomic geometry; Auger electron spectroscopy (AES) for determination of surface chemical composition; thermal desorption spectroscopy (TDS) for determining kinetic order, surface concentrations and desorption energies; work function measurements for determining the degree of charge transfer between the adsorbates and the surface; and second-harmonic generation (SHG) for monitoring the electronic properties of the surface. These techniques are described further in Chapters 2 and 3. In this thesis we concentrate on those techniques, HREELS and LEED, that provide information on the atomic structure of the adsorbates.

In Chapter 4, we discuss the adsorption of two of the simplest aromatic molecules, benzene and pyridine, on the Rh(111) crystal surface. Benzene adsorption on Rh(111) has been previously studied by HREELS [7] and LEED [8] and the new results presented here are the more definite determination of the benzene adsorption geometry (i.e. benzene is centered over bridge sites when adsorbed alone at high coverages) and the absence in EELS electronic spectra of $\pi \rightarrow \pi^*$

transitions due to the strong chemisorption bond with the surface. Pyridine adsorption on Rh(111) is found to be similar to pyridine adsorption on Ni(100) [9] and Pt(111) [10] at room temperature in that an α-CH bond breaks with pyridine forming an α-pyridyl species on the surface; at below room temperature, a physisorbed pyridine species is observed coadsorbed with the α-pyridyl species.

One of the important results of this thesis is the discovery that coadsorbed carbon monoxide can induce long-range order in adsorbate overlayers. This result has two important consequences: 1) Once an adsorbate forms an ordered overlayer, its surface structure can be determined by a dynamical LEED analysis, and 2) if two coadsorbates are ordered in an intermixed structure, then it is possible to study the interaction between the coadsorbates in a structure where their relative geometries are known. Chapter 5 presents the results for CO induced ordering of benzene on the Rh(111) and Pt(111) crystal surfaces. Chapter 6 presents the results for CO induced ordering of fluorobenzene, acetylene, ethylidyne, propylidyne, and sodium on the Rh(111) crystal surface.

Chapter 7 presents results for hydrogen adsorption on the Rh(111) crystal surface. The very light mass of hydrogen results in adsorbed hydrogen atoms having a large amplitude of zero point motion; consequently, hydrogen atoms can be very delocalized when adsorbed on surfaces. Our HREEL spectra for hydrogen adsorbed on the Rh(111) surface have several features expected for delocalized surface hydrogen - broad EELS excitations indicating the formation of energy bands for

delocalized motion and EELS excitations that do not show the isotopic shift expected for simple harmonic motion. Consequently, the vibrational excitations observed by EELS for hydrogen adsorbed on close-packed surfaces are best thought of as excitations between energy bands for delocalized motion.

Finally, in Chapter 8, preliminary experiments are discussed of measurements of the coefficient of friction between a rhodium single crystal surface and a rhodium pin, both in air and in ultra-high vacuum.

REFERENCES

1. G.A. Somorjai, Chemistry in Two Dimensions: Surfaces, Cornell University Press, Ithaca, 1981.
2. J.F. O'Hanlon, A User's Guide to Vacuum Technology, Wiley, New York, 1980.
3. G. Ertl and J. Kuppers, Low Energy Electrons and Surface Chemistry, Verlag Chemie, Weinheim 1979.
4. Surface Studies with Lasers, editors: F.R. Aussennegg, A. Leitner, and M.E. Lippitsch, Springer-Verlag, Berlin, 1983.
5. D.H. Buckley, Surface Effects in Adhesion, Friction, Wear and Lubrication, Elsevier, Amsterdam, 1981.
6. Ibid., Chapter 8.
7. B.E. Koel and G.A. Somorjai, J. Electron Spectrosc. 29 (1983) 287; B.E. Koel, J.E. Crowell, C.M. Mate, and G.A. Somorjai, J. Phys. Chem. 88 (1984) 1988.
8. Rongfu Lin, R.J. Koestner, M.A. Van Hove, and G.A. Somorjai, Surface Sci. 134 (1983) 161; M.A. Van Hove, Ronfu Lin, and G.A. Somorjai, Phys. Rev. Lett. 51 (1983) 778.
9. N.J. DiNardo, Ph. Avouris, and J.E. Demuth, J. Chem. Phys. 81 (1984) 2169.
10. V.H. Grassian and E.L. Muetterties, J. Phys. Chem., in press.

CHAPTER 2

EXPERIMENTAL

Contents

Studying atoms and molecules adsorbed on single crystal surfaces under ultra-high vacuum conditions is an excellent way of developing an atomic scale understanding of the bonding of atoms and molecules on metal surfaces. Ultra-high vacuum (i.e. gas pressures less than 10^{-8} torr) ensures that a substantial quantity of gases, other than those of interest, do not adsorb on the metal surface during the course of an experiment. Using atomically clean single crystal surfaces enables one to study the adsorption of atoms and molecules on a well defined metal surface.

This chapter describes the ultra-high vacuum system used during this research for studying the structure and bonding of adsorbates on single crystal surfaces. A variety of experimental techniques were used to provide complimentary information needed to obtain a good understanding of how the adsorbates bonded to the surface. Consequently, a large fraction of this chapter is devoted to describing the techniques used. Since high resolution electron spectroscopy (HREELS) tended to provide the most valuable information about the structure and bonding of adsorbates, the next chapter will be devoted to a more complete description of this technique.

2.1 Vacuum System

A schematic diagram of the ultra-high vacuum system used in this work is shown in Fig. 2.1 and a photograph is shown in Fig. 2.2. The stainless steel chamber is constructed in two levels with the lower

level devoted to the high resolution electron energy loss spectrometer. The spectrometer is enclosed in μ-metal shielding to reduce the background magnetic fields to less than 10 mGauss at the sample position and 20 mGauss inside the sectors of the spectrometer. The μ-metal shielding has holes for viewing the sample, for allowing electrical connections to the spectrometer, and for allowing the sample to be lowered into the spectrometer from the upper level.

The upper level of the vacuum system contains equipment for characterizing and cleaning the sample: a four-grid retarding field energy analyzer (Varian) for low-energy electron diffraction and Auger spectroscopy, a glancing incidence electron gun (Cliftronics) for Auger excitation, a quadruple mass spectrometer (UTI 100 C) for residual gas analysis and thermal desorption spectroscopy, an ion sputtering gun (PHI) for sample cleaning, a nude ionization gauge (Varian) for pressure measurement, two variable leak valves (Varian) for gas exposure, and alkali getter sources (SAES) for controlled alkali dosing. In addition, the upper level also contains a device we call the "friction apparatus" for measuring the coefficients of friction between the surface of a pin and the single crystal surface.

The single crystal sample is transferred from one level to the other by a specially made, extended travel (250 mm) manipulator shown in Fig. 2.3. The sample is mounted either by spot welding thin (0.020 inch dia.) Ta wire to the sides of the sample or, for friction measurements, by using clamps specially made from molybdenum at two ends of the sample. The Ta wires or clamps are mounted on the closed

ends of two stainless steel tubes, through which liquid nitrogen can flow in order to obtain sample temperatures as low as 77 K. The sample is heated to temperatures as high as 1400 K by passing 10 to 20 Amps through the sample with most of the resistive heating occurring at the spot welds or the points of contact of the clamps. Sample temperatures are measured with a digital thermometer (Doric) and a chromel-alumel thermocouple spot welded to the top of the sample.

A 400 l/sec ion pump (Varian) provides the main pumping for the chamber with a titanium sublimation pump and a 2 and 3/4 inch diffusion pump providing auxiliary pumping. Base pressures of ~ 5×10^{-11} torr can be routinely achieved after a 48 hour bake out at 450 K.

2.2 Description of Techniques

2.2.1 High Resolution Electron Energy Loss Spectroscopy (HREELS)

This technique is discussed more completely in chapter 3 and only a brief description is given here.

Figures 2.4 and 2.5 show, respectively, a schematic and a photograph of our HREEL spectrometer. The basic principle behind HREELS is that a monochromator produces a monoenergetic electron beam with a spread in energy between 3 and 10 meV. The electron beam is then accelerated and focussed on the sample surface by a series of electrostatic lenses. During these studies, electron energies between 1 and 30 eV at the sample were used with an electron current typically of

1×10^{-10} Amps at the sample. Most of the electrons are elastically reflected off the surface, but a small fraction can lose energy by exciting either a vibration at the surface or some other surface excitation. The analyzer then determines the energy the electrons lose during the excitation process. By plotting the number of electrons per second versus the energy loss of the electrons, one obtains a vibrational or electronic spectrum for surface excitations.

For our spectrometer, the analyzer is rotatable, allowing the angular distribution of scattered electrons to be measured. As will be explained in Chapter 3, a measurement of the angular distribution of scattered electrons helps distinguish between dipole scattering and impact scattering energy loss processes. In our experiments, the angle of incidence for incoming electrons is set at 65° with respect to the surface normal as measured by an angular scale on the bottom of the analyzer base plate. At this angle of incidence, one can see one's reflection in the sample through the viewpoint, thereby checking the alignment of the sample.

2.2.2 Low Energy Electron Diffraction (LEED)

Figure 2.6 shows a schematic of the LEED experiment. A monochromatic electron beam with energy between 10-500 eV is incident on a single crystal sample. Since the electrons in this energy range have de Broglie wavelengths comparable to the interatomic distances of most solids, they diffract from the periodic arrangement of atoms in the

near surface region. The diffraction pattern is then viewed by accelerating the electrons onto a phosphorescent screen. From the position and symmetry of the diffraction spots, the size and orientation of the 2-D unit cells can be determined.

From LEED it is also possible to determine the precise positions of atoms (to within 0.05 Å) in the near surface region by doing a dynamical analysis of LEED spot intensities as a function of electron energy. Since most of the work presented in this thesis was done in collaboration with researchers involved in the dynamical LEED analysis of the same surface structures, a brief description of the method is presented here. A more complete description of the dynamical LEED analysis method or LEED crystallography, as it is also called, can be found in the thesis of R.J. Koestner (Ph.D U.C. Berkeley 1982) or in that of D.F. Ogletree (Ph.D Berkeley 1986) and in the books by Van Hove and Tong [1] and Clarke [2]. The structures of adsorbed CO on the Rh(111) surface, as determined by Koestner, Van Hove, and Somorjai [3,4], will be used as examples, since they will serve as useful references during the discussion in subsequent chapters of CO coadsorption with other adsorbates on this surface. Figure 2.7 shows the series of LEED patterns observed for CO on Rh(111). At one third of a monolayer of CO (i.e. one CO molecule for every three rhodium surface atoms), a $(\sqrt{3}x\sqrt{3})R30^\circ$ LEED pattern is observed (Fig. 2.7b). With increasing CO coverage, the $(\sqrt{3}x\ \sqrt{3})R30^\circ$ pattern disappears and a split (2x2) pattern appears (Fig. 2.7c). As the CO coverage is further

increased, the split spots coalesce into the half-order beams of a (2x2) pattern (Fig. 2.7d).

Figure 2.8 illustrates the procedure for determining the structure of the ($\sqrt{3}$x $\sqrt{3}$)R30° CO overlayer on Rh(111) by a dynamical LEED analysis. First, the intensity of the LEED spots is measured as a function of electron energy, which can be accomplished by a variety of experimental methods, as discussed in the thesis of R.J. Koestner. These experiments are conducted in a chamber where the angle of incidence of the electron beam can be well defined and the magnetic fields around the sample are shielded to less than 50m Gauss. Then the experimental intensity vs. voltage curves (I-V curves) are compared to those calculated, using the computer programs described in Refs. 1 and 2, for different model geometries of the CO molecules bonded to the surface. The model that provides the best fit to the experimental curve is regarded as an accurate representation of the actual surface structure. Figure 2.8 shows a comparison of one experimental I-V curve for the ($\sqrt{3}$x$\sqrt{3}$)R30° structure of CO on Rh(111) to a series of calculated curves where the C-O bond length was varied. The best agreement between theory and experiment, as determined by an R-factor analysis, was found for CO bonded on top of the metal atoms with C-O bond distance of 1.07 Å. This structure is also illustrated in Fig. 2.8.

Figure 2.9 shows the results of a similar analysis for the (2x2) CO structure on Rh(111). Of the three CO molecules in a unit cell, two are bonded bridging two metal atoms while the third is displaced slightly from the symmetric position on top of the metal atoms and is

close to a position that would result in hexagonal packing of the CO layer. The calculated C-O bond distance of 1.15 ± 0.1 Å compares well with the gas phase value of 1.13 Å.

2.2.3 Thermal Desorption Spectroscopy (TDS)

In TDS, the sample is heated so that the temperature increases linearly with time, and the desorbing species are monitored with a mass spectrometer as a function of temperature or time. Figure 2.10 shows the mass 28 TD spectra for different exposures of CO on Rh(111). By assuming CO desorbs by a 1st order kinetic process, one can determine from the peak temperature, T_p, the activation energy of desorption, E_d, for CO by using

$$E_d/RT_p^2 = (\nu_1 / \beta) \exp(-E_d/RT_p),$$

a formula derived by Redhead [5]. Here, ν_1 is the pre-exponential factor and β is the heating rate. Using a pre-exponential factor of 4×10^{13} sec^{-1} [6], the low coverage activation energy is calculated to be 32.0 kcal/mole. For higher CO coverages, the broadening of the thermal desorption spectra to lower temperatures indicates the activation energy for desorption decreases with increasing coverage.

In addition to determining activation energies, one also gains insight into how molecules react with surfaces by monitoring what species desorb from the surface. For example, for all the hydrocarbons studied in this thesis on Rh(111), the predominant desorption product is H_2

gas, indicating almost complete dissociation of the molecules on the surface at higher temperatures.

If only one desorption product is observed for a particular adsorbate, then TDS provides a convenient way of measuring the surface coverage of that adsorbate, as the area under the TDS curve is proportional to coverage. However, the areas only give the relative coverage and one should calibrate these coverages relative to an overlayer, such as an ordered overlayer with a characteristic LEED pattern, that has a known coverage.

2.2.4 Auger Electron Spectroscopy

The Auger process is a two electron emission process that occurs after excitation. Figures 2.11a and b show schematically the excitation and emission processes, respectively. Excitation is caused by impinging X-rays, ions, or, in our experiments, electrons that have sufficient energy (1000-5000eV) to cause the ejection of electrons from the inner atomic levels. In the Auger process, de-excitation occurs when an outer shell electron drops down in energy to fill the inner level vacancy and, in the process, transfers this energy difference to a second outer shell electron. The energy of this last Auger electron is given by

$$E_{wxy} = E_w - E_x - E_y - e\phi$$

where $E_w - E_x$ is the energy difference between the two levels, ϕ the work function of the surface, and E_y the binding energy of the

ejected electron to the positively charged atom. Since every element will emit Auger electrons at characteristic energies, one can determine the presence of specific elements from Auger electron spectroscopy.

In this work, electrons with energies typically of 2000 eV impinge at an angle of incidence of 80° to the surface normal in order to minimize the penetration depth (5-20 Å). The Auger electrons are detected with a retarding field analyzer shown schematically in Fig. 2.6b. Energy analysis of the elements is achieved by applying a retarding potential to grids G2 and G3 while grids G1 and G4 are grounded so that the LEED optics act as a high pass filter with the florescent screen as the electron collector. The spectra are recorded in the first derivative mode (dN(E)/dE) in order to readily distinguish the Auger electrons from the relatively smooth background of secondary electrons. Differentiation is accomplished electronically by superimposing an AC modulation voltage on the retarding potential and then using a lock-in amplifier to detect the second harmonic of the modulated electron current collected by the screen. An example of an Auger electron spectra for clean Pt(111) is shown in Fig. 2.10c.

2.2.5 Optical Second Harmonic Generation (SHG)

This thesis reports some of the first applications of optical second harmonic generation (SHG) as a technique for studying the adsorption of atoms and molecules on surfaces in ultra-high vacuum. The usefulness of SHG as a surface technique derives from second-order

nonlinear processes being dipole forbidden in media that possess a center of inversion symmetry [7]. Consequently, the SHG signal from the surface layer, which never has an inversion symmetry, can dominate over the contribution from the bulk [8]. However, a detailed understanding of how the SHG signal is generated at the surface is still lacking; even so, a qualitative understanding of the SHG signal can often be achieved by using of an appropriate model such as an electron gas model or by assuming the changes in the SHG signal arise from resonances or near resonances with surface excitations.

Figure 2.12 shows schematically the experimental set up during the SHG experiments. Q-switched Nd:Yag laser pulses at 532 nm or 1.06 μm with a 10 nsec pulse width and 6mJ pulse energy were p-polarized and incident on the rhodium sample at an angle of 67.5° with respect to the surface normal with a beam diameter of 1mm. At this intensity, no laser induced desorption or surface damage could be detected. The SH radiation from the surface was p-polarized and detected after proper filtering by a photomultiplier with a gated integrator system.

2.2.6 Work Function Measurements

The work function of a metal is defined as the energy required to remove an electron from the metal (i.e. to raise an electron from the Fermi level to vacuum level). In this thesis, we are interested in how the work function changes when atoms and molecules are adsorbed on

the surface and what can be inferred from these changes about the surface chemical bond.

Figures 2.13a and b show schematically how we measure work function changes with the available apparatus. The monochromator of the HREEL spectrometer provides a monoenergetic source of electrons, which is focused on the sample. The current to the sample is measured by a floating picoammeter that is connected in series with a bias voltage supplied by a DC ramp. When the negative bias voltage is great enough, the current to the sample drops to zero as the vacuum level of the sample is raised above the energy of incoming electrons (i.e. when the electrons are totally reflected from the sample). Since changes in the work function are also equal to the changes in the position of the energy of the vacuum level relative to the Fermi level, the change in work function is readily determined by measuring the shift in cutoff voltage from a plot of current versus bias voltage (see Fig. 2.13c). Since the spread in energy of the electrons provided by the monochromator is very small (5meV), the main inaccuracy comes from changes in the shape of the current vs. voltage plot. Still, we are able to measure the work function changes to within 0.01 eV by this method.

2.2.7 Friction Measurements

In order to understand how the structure of one monolayer of adsorbate on a surface influences the lubrication between surfaces, an apparatus, similar to that by Buckley and co-workers [9], has been de-

signed and constructed that can measure the coefficient of friction between two surfaces under ultra-high vacuum conditions. Figure 2.1 shows schematically the friction apparatus and how it is mounted in the vacuum system. The friction apparatus consists of 1/4"x1/4"x12" aluminum bar mounted at one end on a manipulator. A pin is mounted near the other end of the bar and can be brought into contact with the sample. Since the bar will bend by an amount proportional to the force exerted on the pin by the sample, strain gauges attached to the bar can be used to measure the load on the sample. A motor drive attached to the manipulator is used to slide the pin across the sample surface. Another set of strain gauges then measures the frictional force on the pin. Dividing the frictional force by the load determines the coefficient of friction between the surface of the pin and the surface of the sample.

Since we are mainly interested how one monolayer of adsorbate affects the coefficient of friction, the apparatus is designed and operated in several ways so as to minimize the other factors on the coefficient of friction: 1) The pin slides across the surface at slow speeds (~ 1mm/min) in order to minimize the temperature rise at the points of contact. 2) Light loads ($\leq$ 100g) are employed to minimize plastic deformation and consequent bulk contributions to the frictional properties of the surface. 3) A single crystal surface is used as the sample so at least one surface can have a monolayer of adsorbate that is well characterized, and 4) a pin of the same material as the sample is used so that both surfaces have similar properties and chemistry.

2.3 Single Crystal Surfaces

Single crystal Rh(111) and Pt(111) samples were used exclusively in this work. A total of five different samples were used--three rhodium crystals and two platinum crystals. Both the platinum and rhodium single crystal rods were purchased from Materials Research Corporation (MRC) and were more than 99.995% pure. The single crystals were cut by spark erosion into thin (~ 1mm) discs to within 1° of the (111) orientation as determined by Laue back reflection X-ray diffraction. The samples were mechanically polished to a mirror finish on both sides using standard methods [10].

2.4 Procedures

2.4.1 Cleaning the Single Crystal Surface

For the Rh(111) samples, the main impurities observed were carbon, boron, sulfur, and phosphorus. Of these, boron is the most prevalent in the bulk as it is used to reduce rhodium oxide to the metal. It was found that the level of bulk impurities could be greatly reduced by heating the sample for several days at 1300 K in an atmosphere of hydrogen before installing it in the vacuum system. In ultra-high vacuum, our standard procedure for cleaning Rh(111) is to heat the sample in $1\text{-}5\times10^{-7}$ torr O_2 at 1000 - 1100 K for 5-10 minutes followed by Ar^+ sputtering (1.0 keV, 5-8 μA, 1×10^{-4} torr Ar) for 20-30

minutes followed by annealing in vacuum for 5 minutes at 1200 K. Surface cleanliness was checked by HREELS, AES, and LEED. Often, HREELS detected trace amounts of boron oxide on the surface after this cleaning procedure, which could be removed by flashing the sample to 1400 K.

The cleaning procedure for the Pt(111) sample is similar, only slightly longer sputtering times (30-40 minutes) are needed to remove the trace amounts of oxides occasionally present.

2.4.2 Gas and Alkali Dosing

Dosing of gases into the vacuum chamber is achieved through variable leak valves either by backfilling the chamber or by introduction through a microchannel array doser. The array doser is mounted ~ 2 cm from the sample and achieves a 20-fold enhancement in pressure at the surface. The unit of gas exposure used in this thesis is the Langmuir (L), which corresponds to a 10^{-6} torr second. The Langmuir is a convenient unit of exposure for surface science studies as it corresponds, for a one Languir exposure, to roughly one atom or molecule striking the surface per available surface site. In this thesis, all the exposures reported are uncorrected for the ion gauge sensitivity.

Dosing of the alkali adatoms is achieved by heating a commercial getter source (SAES) consisting of a zeolite impregnated with the alkali element and enclosed in a tantalum dispenser. The alkali doser are positioned ~ 8 cm from the sample. Currents of 5-8 Amps through the source are needed to achieve dosing rates on the order of one mon-

olayer per minute. The pressure in the chamber during alkali dosing is typically $\leq 1 \times 10^{-9}$ torr. Usually, no impurities are deposited along with the alkali adatoms.

REFERENCES

1. M.A. Van Hove and S.Y. Tong, Surface Crystallography by LEED: Theory, Computation and Structural Results, Springer-Verlag (New York 1979).
2. L.J. Clarke, Surface Crystallography: An Introduction to Low Energy Diffraction, Wiley, (New York, 1985).
3. R.J. Koestner, M.A. Van Hove, and G.A. Somorjai, Surface Sci., 107 (1981) 439.
4. M.A. Van Hove, R.J. Koestner, and G.A. Somarjai, Phys. Rev. Lett. 50 (1983) 903.
5. P.A. Redhead, Vacuum 12 (1962) 203.
6. P.A. Thiel, E.D. Williams, J.T. Yates, Jr., and W.H. Weinberg, Surface Sci. 84 (1979) 54.
7. Y.R. Shen, The Principles of Nonlinear Optics, Wiley (New York 1984).
8. H.W.K. Tom, Ph.D. thesis, University of California, Berkeley, 1984, unpublished.
9. K. Miyoshi and Donald H. Buckley, NASA Technical Memorandum 83067.
10. R.J. Koestner, M.A. Van Hove, and G.A. Somorjai, Surface Sci., 121 (1982) 321.
11. J.E. Crowell and G.A. Somorjai, Appl. Surface Sci. 19 (1984) 73.

FIGURE CAPTIONS

Fig. 2.1 Schematic diagram of vacuum system and friction apparatus. Sample cleaning, surface characterization, and friction measurements occur on the upper level, while vibrational spectroscopy is performed on the lower level.

Fig. 2.2 Photograph of vacuum system shown in Fig 2.1

Fig. 2.3 Schematic of sample manipulator.

Fig. 2.4 Schematic of the HREEL spectrometer used during this work.

Fig. 2.5 Photograph of HREEL spectrometer shown in Fig. 2.4.

Fig. 2.6 (a) Scheme of the low energy electron diffraction experiment from an idealized crystal surface.

(b) Schematic of the LEED/AES analyzer showing the electronics and connections for Auger electron spectroscopy.

Fig. 2.7 Diffraction patterns observed by LEED for CO adsorbed on Rh(111). The photographs are for (a) the clean Rh(111) substrate, (b) the ($\sqrt{3}$x $\sqrt{3}$)R30° structure, (c) the split (2x2) overlayer, and (d) the (2x2) structure observed at saturation.

Fig. 2.8 Schematic illustrating procedure of determining surface structure by LEED crystallography. (Top) ($\sqrt{3}$x $\sqrt{3}$)R30° CO/Rh(111) LEED pattern. (Middle) Comparison of experimental I-V curve (bottom curve) with theoretical curves for different C-O bond lengths with CO bonded on top of the metal atoms (top sites). (Bottom) Real space structure as determined by LEED crystallography.

Fig. 2.9 The real space structure of the (2x2)-3CO layer. The upper figure presents a side view of the surface and the lower figure gives a top view. The large circles represent rhodium atoms (dotted—out of plane, full—in plane); and the small circles are either carbon or oxygen atoms (dotted—hexagonal mesh, full—measured positions). The five structured parameters that were varied in the LEED analysis are illustrated on the left side. (From ref. 4.)

Fig. 2.10 Thermal desorption spectra of CO on Rh(111) for different exposures of CO near 300 K. The heating rate was 15 K/sec. (From Ref. 11.)

Fig. 2.11 (a) Excitation of an atom with a core hole.

(b) De-excitation of the ionized atom via emission of an Auger electron.

(c) An example of a typical Auger electron spectrum of clean Pt(111).

Fig. 2.12 Schematic diagram of the upper level of the vacuum system and laser optics for the SHG experiments.

Fig. 2.13 (a) Schematic diagram of the energy levels of the sample and the monochromator during work function measurements.

(b) Schematic diagram of the experimental set up during work function measurements.

(c) Typical current vs. bias voltage curves for the clean Rh(111) surface and a sodium covered Rh(111) surface. The shift in cutoff voltage gives the work function change.

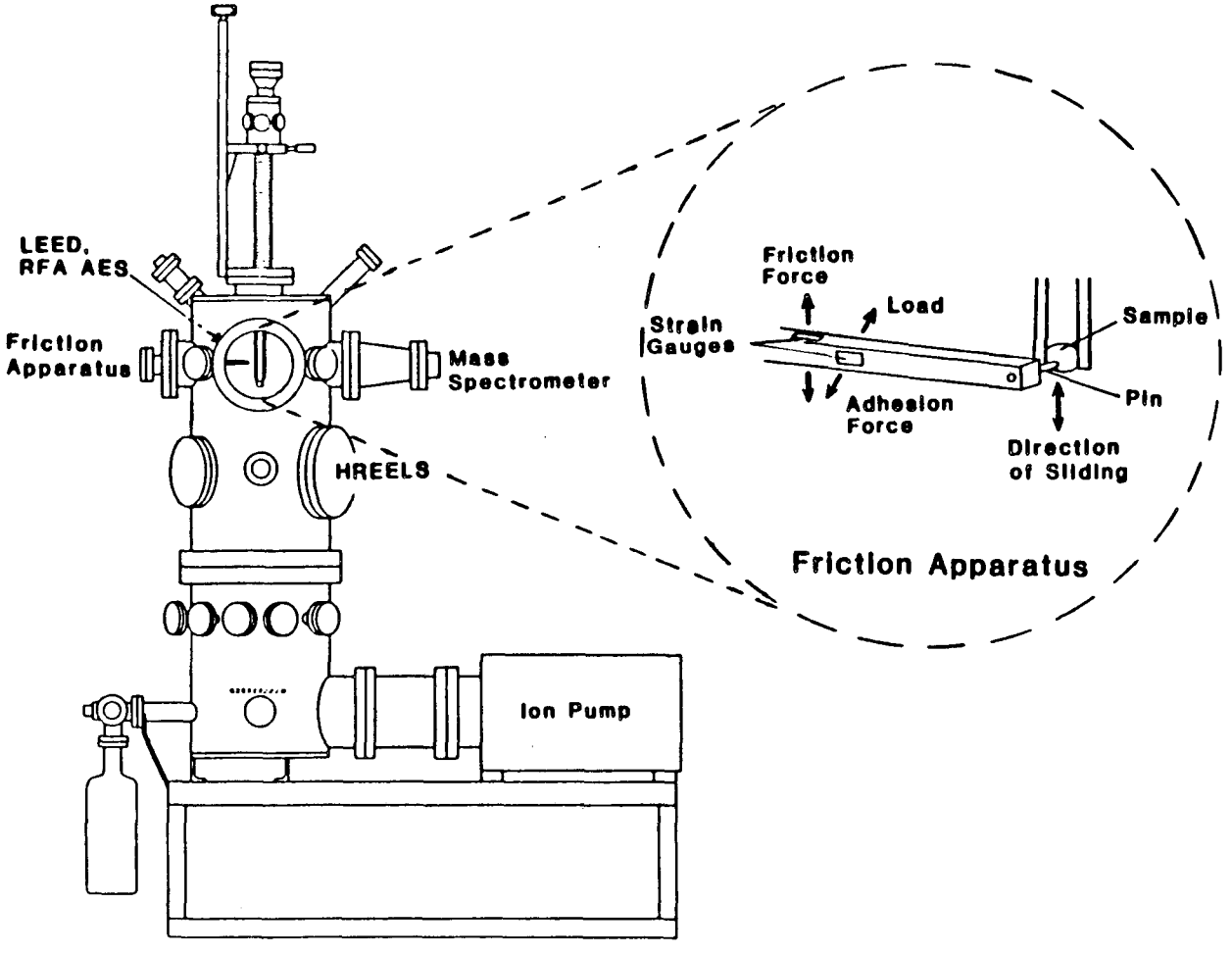

Ultra High-Vacuum System and Friction Apparatus

XBL 862-392

Figure 2.1

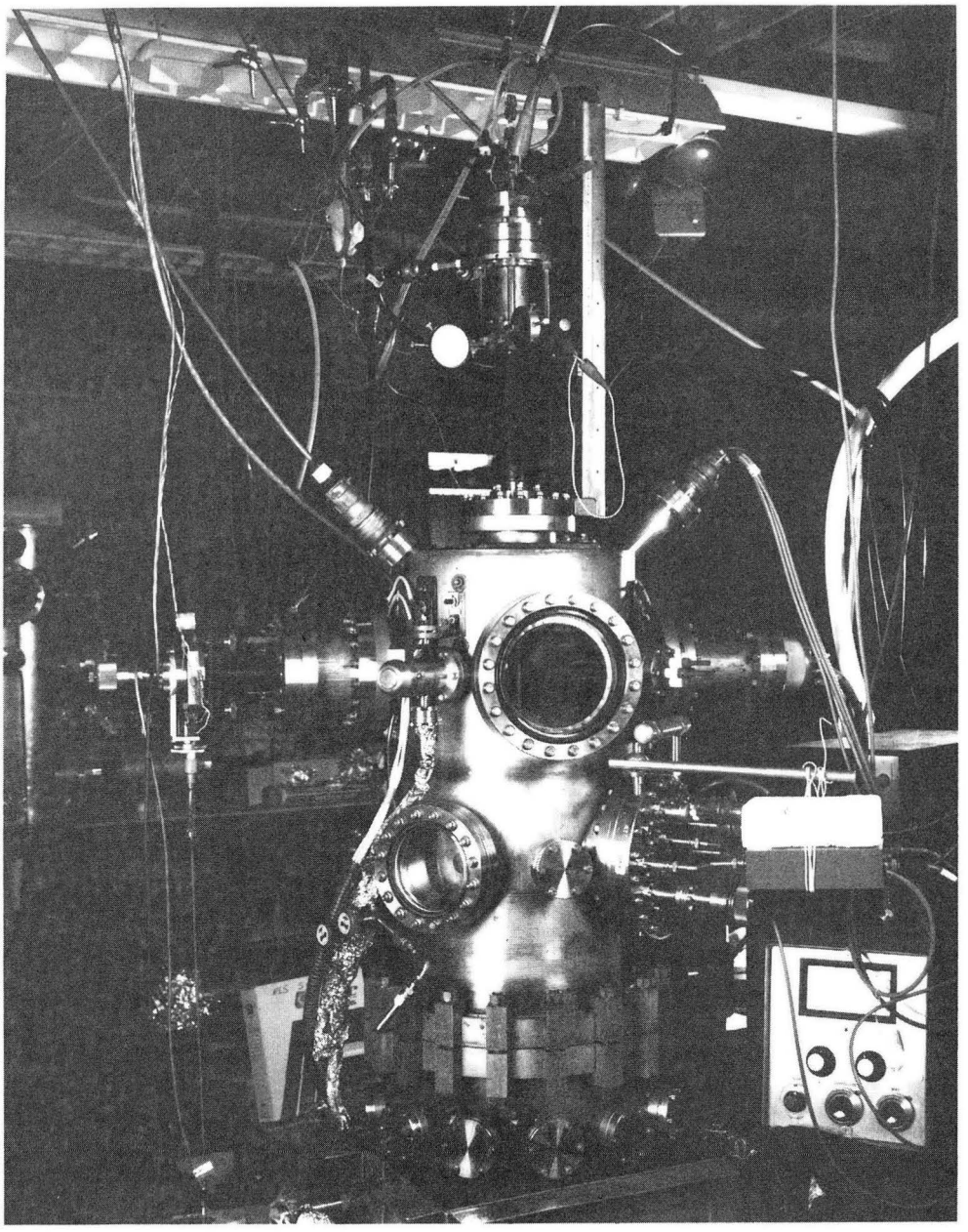

CBB 869-7287

Figure 2.2

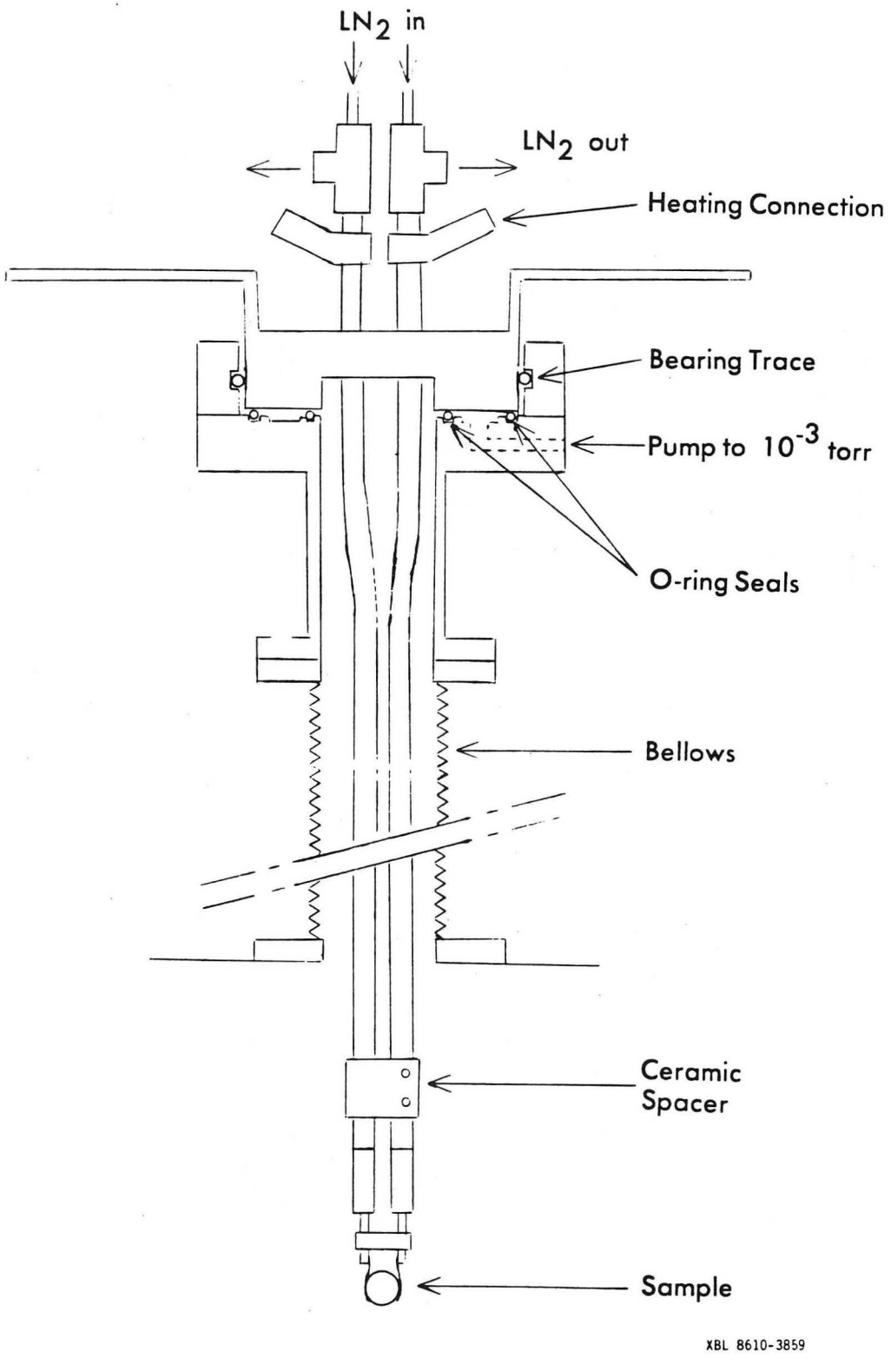
LN2 in
LN2 out
Heating Connection
Bearing Trace
Pump to 10-3 torr
O-ring Seals
Bellows
Ceramic Spacer
Sample
XBL 8610-3859

Figure 2.3

HIGH-RESOLUTION ELECTRON ENERGY LOSS SPECTROMETER

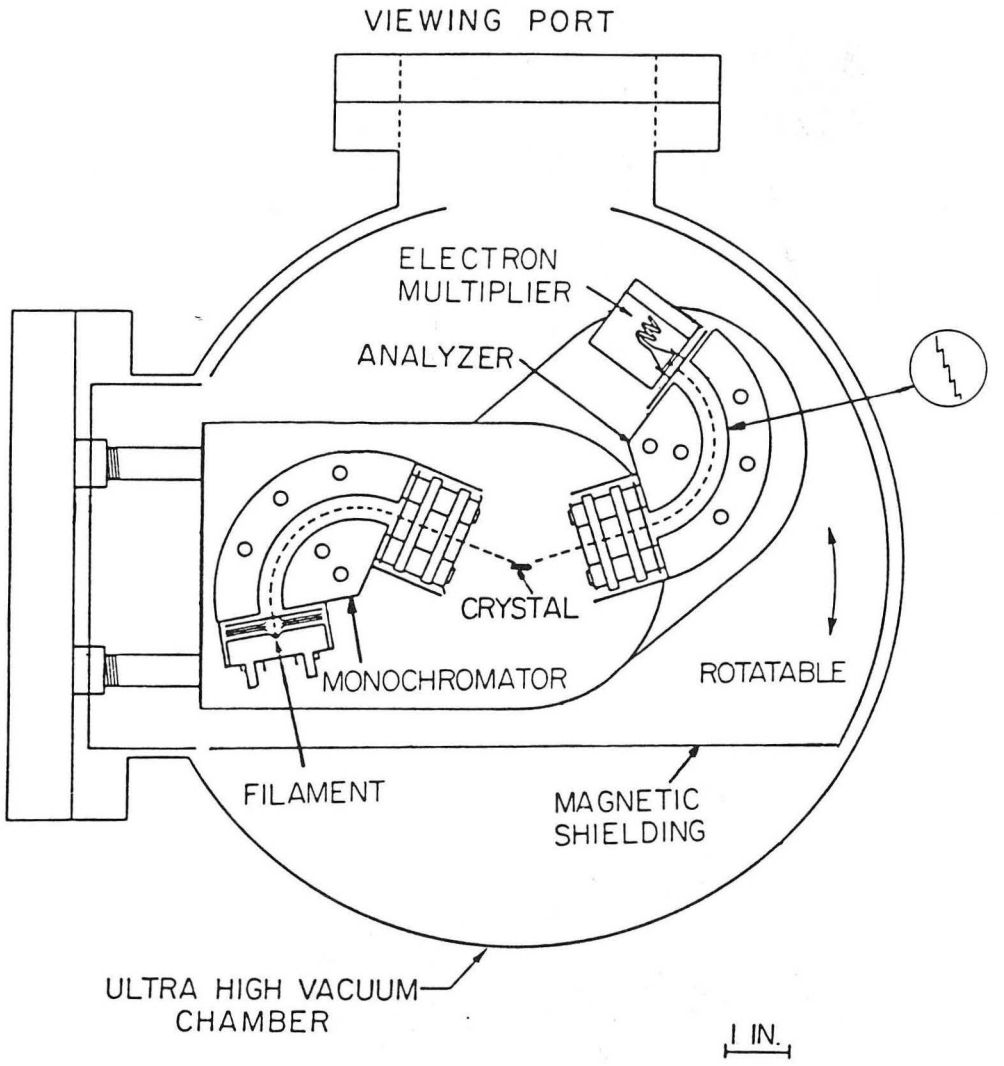

XBL 857-2942

Figure 2.4

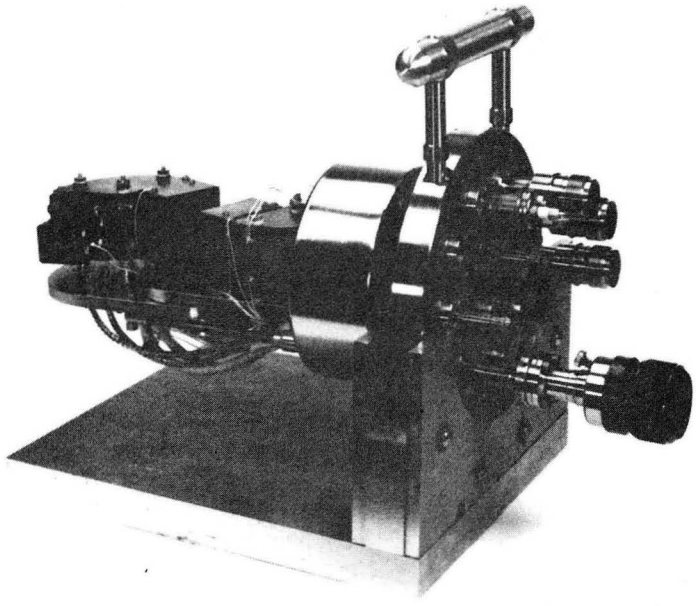

HREEL SPECTROMETER (LEFT VIEW

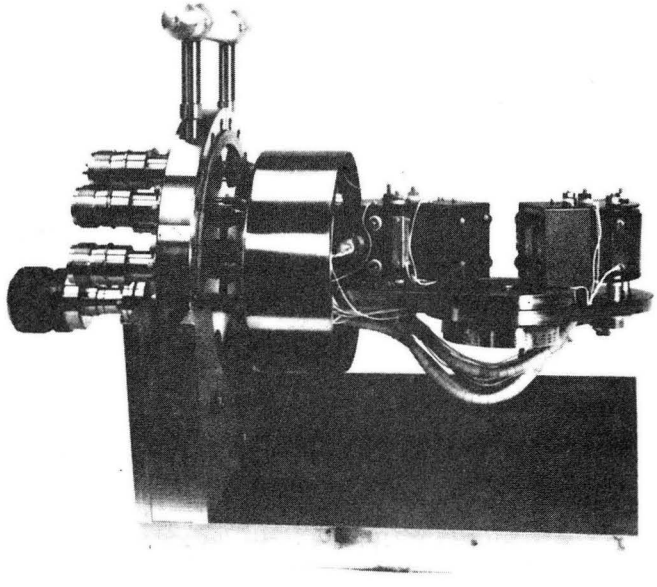

HREEL SPECTROMETER (RIGHT VIEW

XBB 860-8188

Figure 2.5

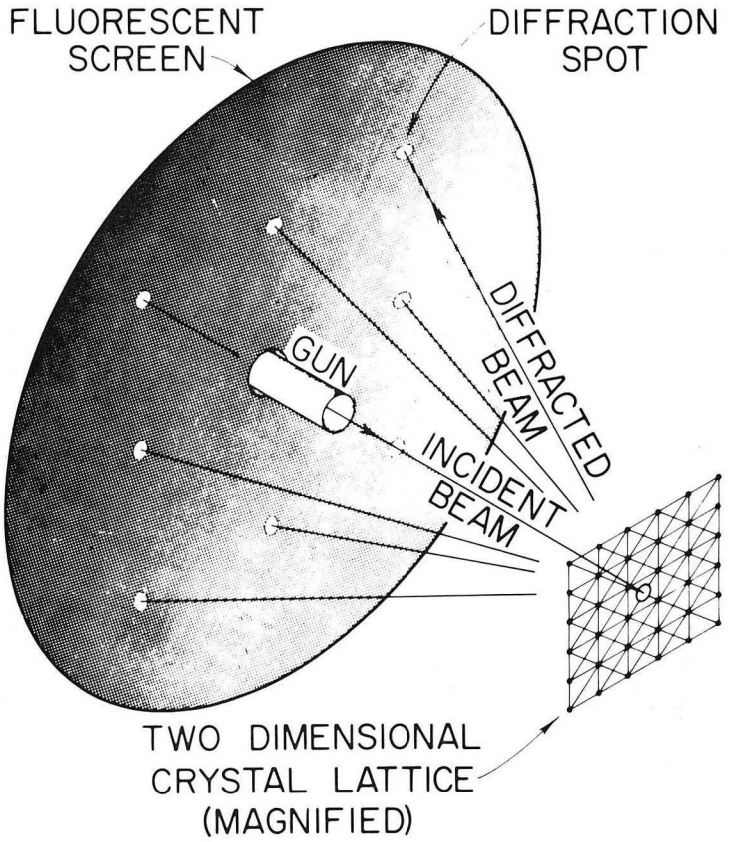

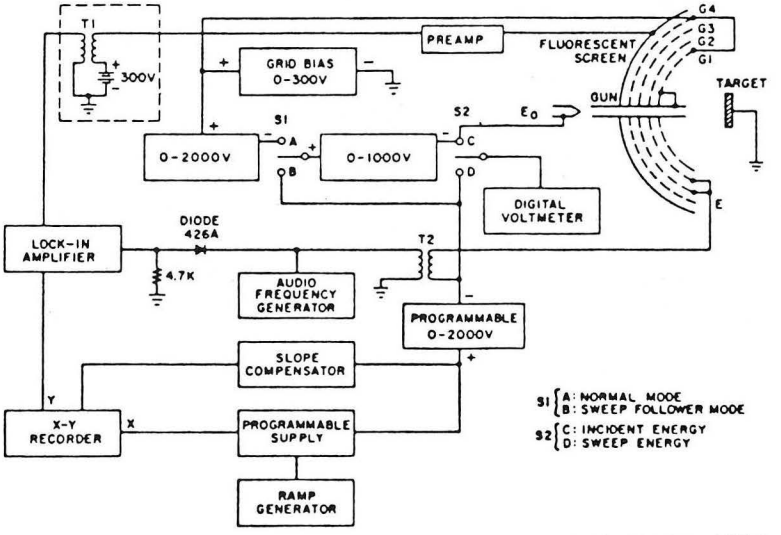

XBL 8312-6874

Figure 2.6

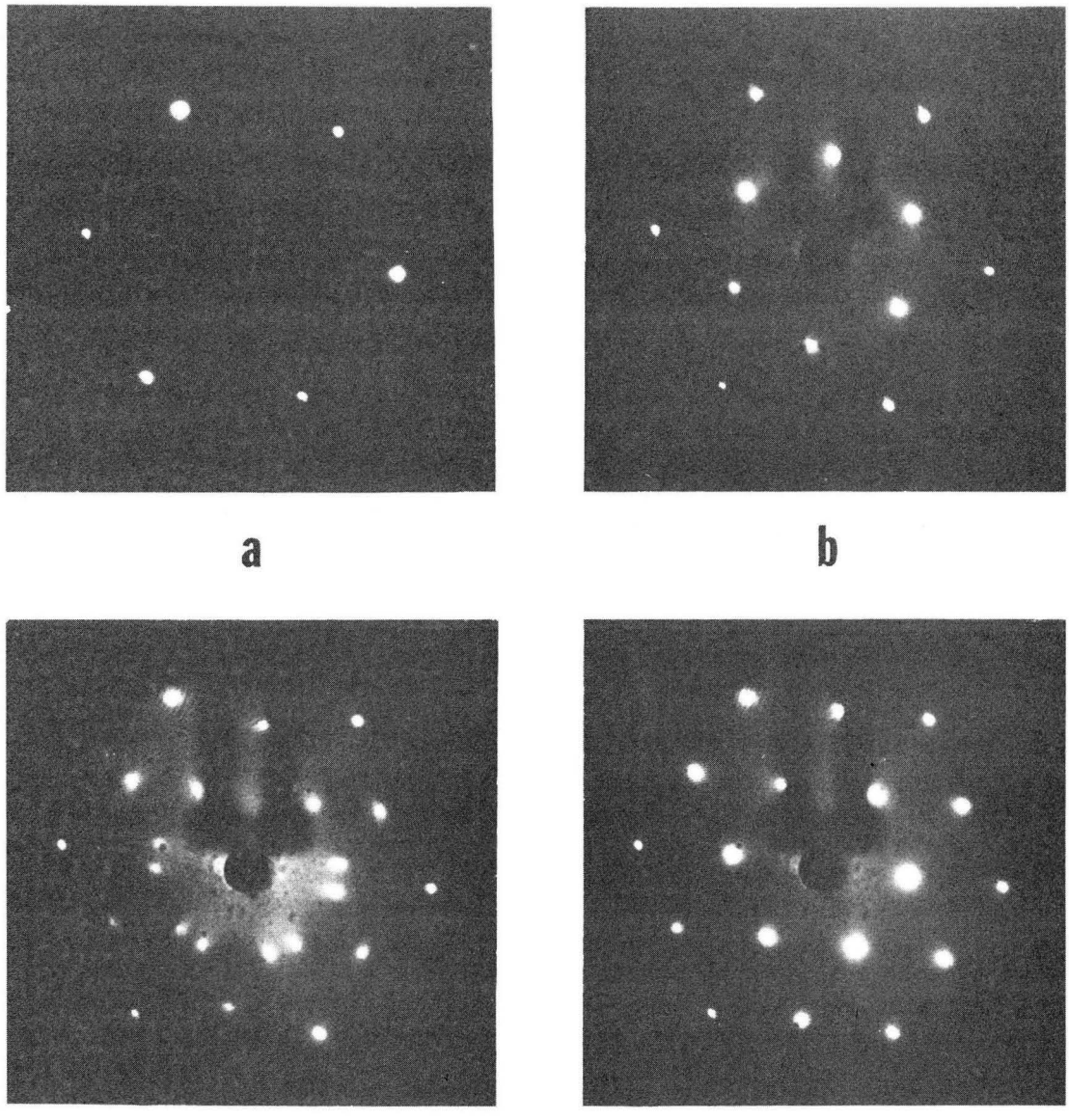

XBB 780-15407

Figure 2.7

Obtain desired LEED pattern

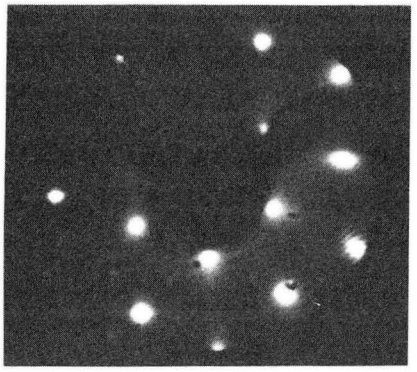

Collect data in the form of Intensity vs Voltage curves

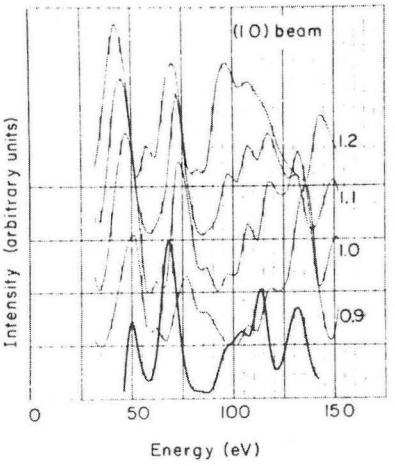

Calculate theoretical curves from model geometries

Compare with experimental curves via R-factors

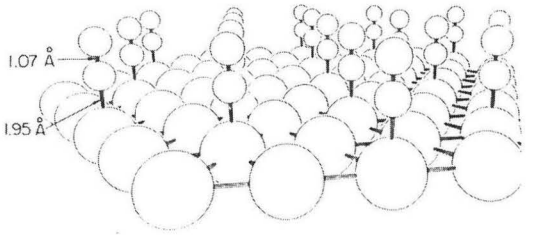

Correct Structure

Rh(111) + $(\sqrt{3}\times\sqrt{3})$R30°CO

XBB 858-6336

Figure 2.8

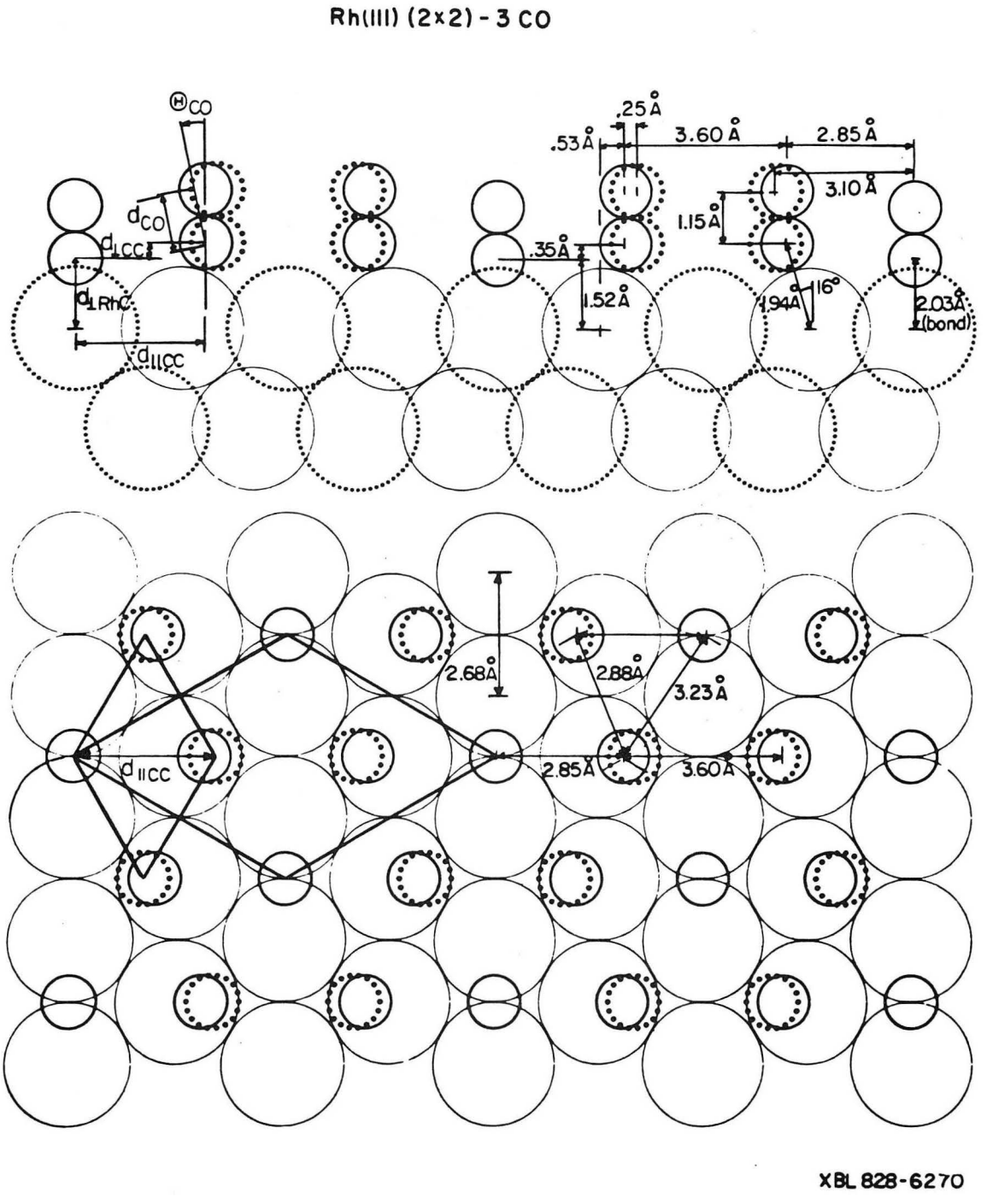
Rh(111) (2×2) - 3 CO
θCO
dCO
dLCC
dLRhC
d||CC
.25 Å
.53 Å
3.60 Å
2.85 Å
3.10 Å
1.15 Å
.35 Å
1.52 Å
1.94 Å
16°
2.03 Å (bond)
2.68 Å
2.88 Å
3.23 Å
2.85 Å
3.60 Å
XBL 828-6270

Figure 2.9

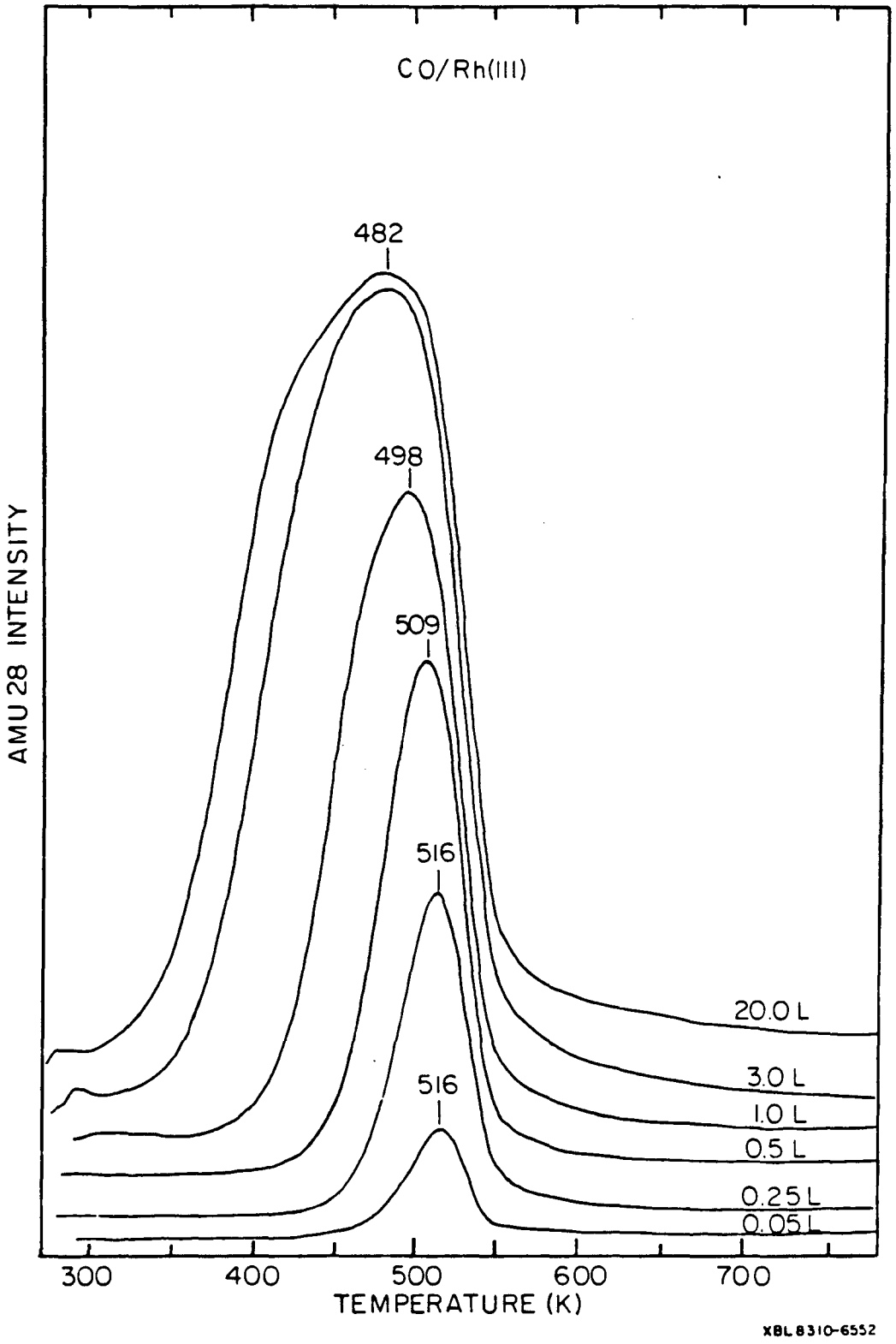
CO/Rh(111)
482
498
509
516
516
20.0 L
3.0 L
1.0 L
0.5 L
0.25 L
0.05 L
AMU 28 INTENSITY
300
400
500
600
700
TEMPERATURE (K)
XBL 8310-6552

Figure 2.10

AUGER ELECTRON EMISSION

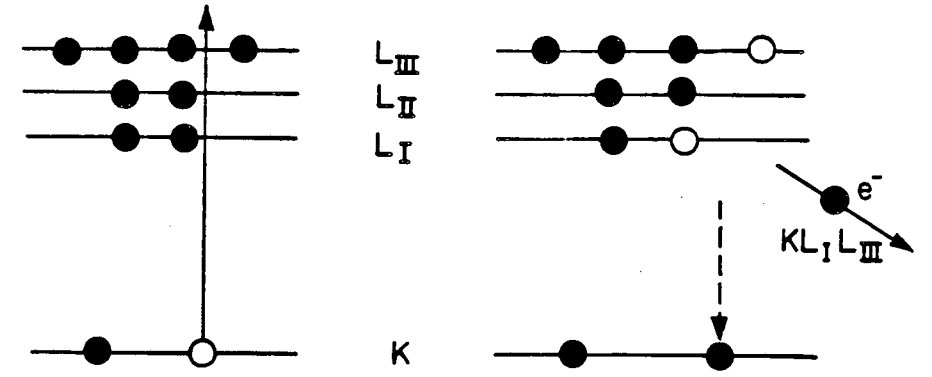

(a) EXCITATION (b) ELECTRON EMISSION

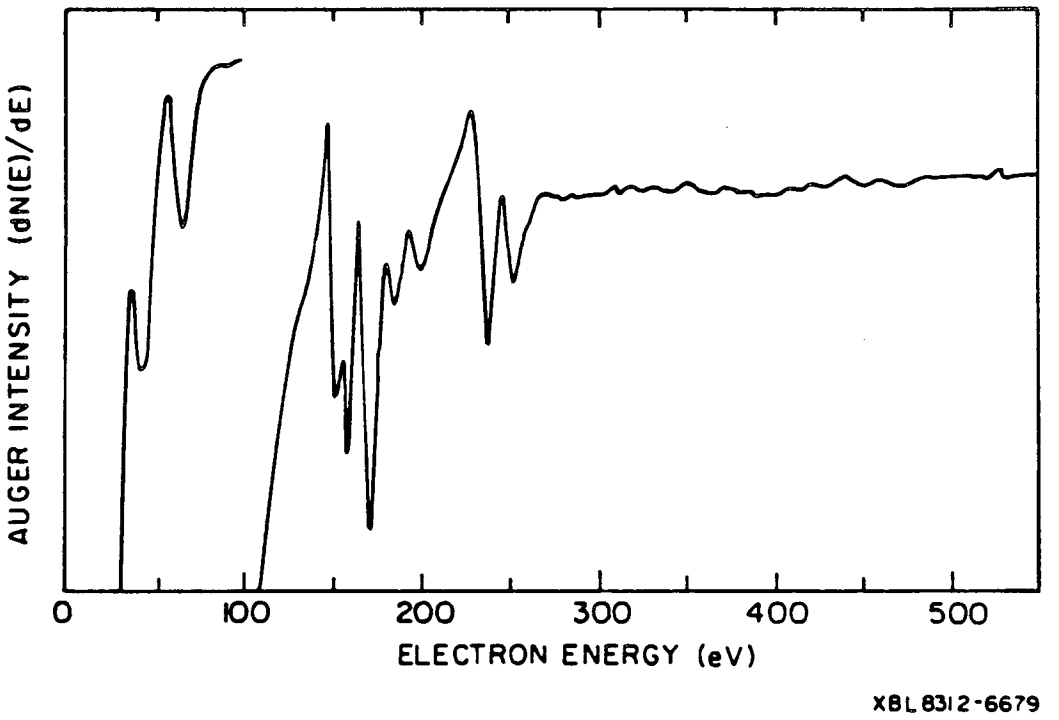

Figure 2.11

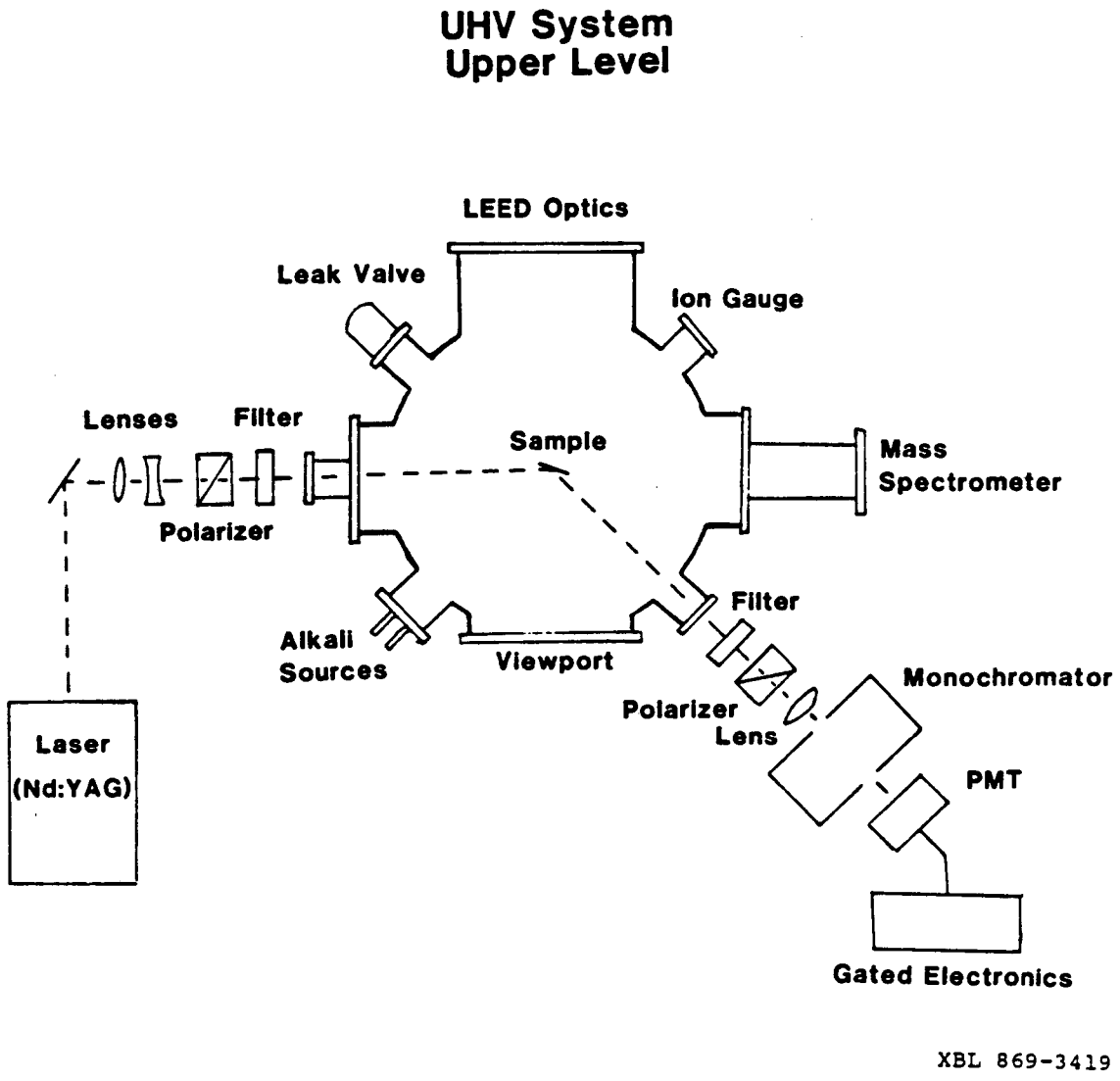
UHV System
Upper Level
LEED Optics
Leak Valve
Ion Gauge
Lenses
Filter
Sample
Mass
Spectrometer
Polarizer
Filter
Alkali
Sources
Viewport
Monochromator
Polarizer
Lens
Laser
(Nd:YAG)
PMT
Gated Electronics
XBL 869-3419

Figure 2.12

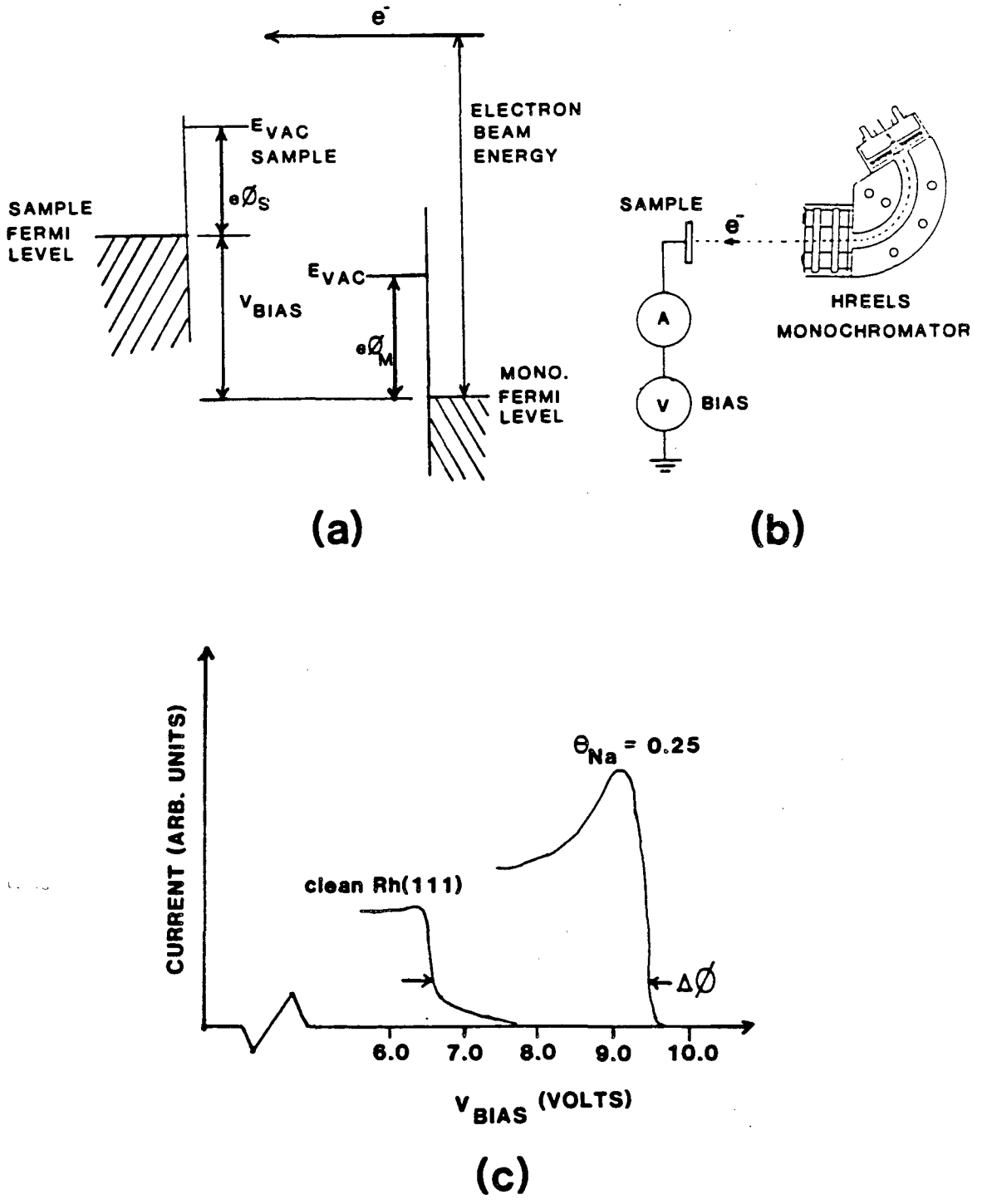

XBL 869-3420

Figure 2.13

CHAPTER 3

HIGH RESOLUTION ELECTRON ENERGY LOSS SPECTROSCOPY

Contents

3.1 Introduction

Vibrational spectroscopy by HREELS is of tremendous value for determining the structure of molecules adsorbed on surfaces; from the frequencies observed, one can usually deduce the identity of adsorbate species and, from the intensities, the orientation of the species. Since determining the structure of adsorbates on surfaces is the main emphasis of this thesis, this entire chapter is devoted to a description of HREELS and how one uses the information it provides.

The number of HREEL spectrometers built to study the vibrations of adsorbates on surfaces has grown rapidly within the last ten years. Even though many other techniques have been developed for surface vibrational spectroscopy, HREELS has become the most popular for studying all types of adsorbates on single crystal surfaces because of its high sensitivity to adsorbates and its ability to obtain spectra over the entire vibrational frequency range (100 - 4000 cm^{-1}) in less than 20 minutes. The major disadvantage of HREELS is a rather poor resolution of 30-100 cm^{-1}, compared to some of the other surface vibrational spectroscopies, like infrared spectroscopy, which have a resolution on the order of 1 cm^{-1}. However, a resolution between 40 to 60 cm^{-1} is usually quite adequate for our research, where we mainly are interested in determining the structure of adsorbates on surfaces. For a more thorough description of the use of HREELS for studying surface vibrations, the reader is referred to several excellent books [1,2] as well as numerous reviews [3-10] that have been written on the subject.

As is shown in this thesis, HREELS has the extra advantage that the same HREEL spectrometer used for vibrational spectroscopy can also be used to study electronic excitations of the surface and of the adsorbed overlayer. While observations of the electronic excitations are not very useful in determining structure, they can provide useful insights, once the surface structure is known, into the nature of the surface chemical bond.

3.2 HREELS Instrumentation

Figure 3.1 shows a schematic diagram of the HREEL spectrometer design by L.H. Dubouis [11], which is similar to that of Froitzheim et. al., [12]; in this figure, all the lens elements, sectors, etc. of the spectrometer are labeled. The spectrometer used during this thesis is based on the design by Dubois but is configured somewhat differently (see Fig. 2.3). The parts for the spectrometer used in this thesis were fabricated by Bob McAllister of McAllister Technical Services, and the spectrometer was assembled and tested by the author. This section is devoted to a discussion of the fundamentals of the design and construction of this spectrometer. For a more general description of HREEL spectrometer design, the reader is referred to the book by Ibach and Mills [1] and the review by Roy and Carette [13].

As illustrated in Fig. 3.1, the hot tungsten filament emits electrons, which are repelled by the repeller and focussed by the A lenses onto the monochromator input slit. The monochromator sector is a 127° cylindrical deflector that disperses the electrons in energy so that

only electrons near the pass energy of the sector exit through the output slit. The B1 and B2 electrostatic lenses then accelerate and focus the electrons onto the sample. The B1 and B2 lenses are split horizontally and vertically, respectively, so that the electron beam can be steered toward the sample. After reflection from the sample, the electrons are deaccelerated and focussed by the B3 and B4 lenses, which are also split vertically and horizontally, respectively, onto the analyzer input slit. The analyzer sector is another 127° cylindrical deflector that disperses the electrons in energy so that only the electrons of a certain energy make it through the exit slit to be counted by the channeltron. The analyzer can scan through the energies of the energy loss spectrum if voltages on the analyzer slits and sector electrodes are ramped linearly.

3.2.1. Sector Design

The monochromator and analyzer sectors are the essential parts of our HREEL spectrometer. These identical 127° cylindrical sectors provide the monochromator electron source that is focussed onto the sample and analyze the electron energies after the electrons are reflected from the sample. Figure 3.2 shows an expanded drawing of one of the sectors.

An electron will travel along the center path of the sector if the centrifugal force equals the force excerted by the cylindrical electric field. For this to happen, we need

$$\frac{mv^2}{R_{mean}} = R\frac{2\,E_o}{R_{mean}} = e\,\xi$$

where m, v, and E_o are, respectively, the mass, velocity, and energy of the electron, R_{mean} is the radius of the center path, and ξ is the radial electric field. If the outer and inner electrodes have radii R_{out} and R_{in}, respectively, then the electric field ξ is given terms of the potential difference ΔV between the electrodes by

$$\xi = \frac{\Delta V}{\ln\,(R_{out}/R_{in})}\,\frac{1}{R_{mean}}$$

and, consequently, the pass energy E_o of the sector is given by

$$E_o = \frac{1}{2}\,e\Delta V/\ln(R_{out}/R_{in})$$

Now, consider an electron with energy equal to the pass energy E_o, but one that enters the sector through the slit with an angle α to the center path. This electron will only make it out of the sector if it is focussed onto the slit at the other end of the sector. For the ideal case of a perfectly cylindrical field inside the sector, focussing in first order of α is achieved when the angle of the arc transverse is $\pi/\sqrt{2} = 127°17'$ [14], which is why the sector is called a <u>127°</u> cylindrical deflector. The spread in energy that makes through the sector can be calculated [14], to second order in α, to be

$$\frac{\Delta E}{E_o} = \frac{S}{R_{mean}} + \frac{2}{3}\,\alpha^2$$

where ΔE is the full width at half maximum (FWHM) of the energy spread and S is the slit width.

As shown in Fig. 3.2, the actual angle of the sector for our spectrometer is 114° and not 127°. There are two reasons for this reduced angle. First, since the slits have equipotential surfaces, fringe fields at ends of the sectors must be taken into account in the design of the sector. According to Herzog [15], the disturbance of fringe field can be minimized by placing the slits a distance d from the sectors with

$$d = 0.265\ (R_{out} - R_{in})$$

and equals 2.6 mm for our spectometer. In this case the angle of the sectors needs to be reduced from the ideal value of $\pi/\sqrt{2}$ to compensate for the extra distance needed to travel to the slit. The reduction in angle, $\Delta\phi$ is given by

$$\Delta\phi = -\ 2\ (d/R_{mean}) + 0\ ((d/R_{mean})^2)$$

and equals 9° for our spectrometer.

The second source for the reduction in angle comes from the asymmetric feeding of the electrons into the sector. Roy and Carette [16] have suggested, based on extensive Monte Carlo calculations of electron trajectories, that preferential injection of electrons to the outside of center path can lead to improved transmission and energy distribution characteristics of the beam. Even though this beneficial effect has been disputed by Ibach and Mills [17], we have designed our sectors so that electrons are injected an average of 3° above the center path with the sector angle further reduced by (4/3) α = 4° to compensate for the extra distance the electrons have to travel.

The maximum beam current that can be produced by a sector is limited by space charge effects. Space charge effects arise from the electrostatic repulsion between electrons, which limits the density of electrons that can be achieved along the path of electrons. A detailed analysis [18] shows that the maximum current, I_m, that the monochromator can achieve is

$$I_m \propto \Delta E^{2.5}$$

where ΔE is the energy spread of the electrons. For ΔE = 5 meV, I_m is about 4×10^{-10} A [18]. Since the intensity of a loss peak in an HREEL spectrum is proportional to both the incident current and the resolution of the analyzer, one has

$$I_{loss} \propto \Delta E^{3.5}$$

Consequently, assuming the monochromator and analyzer are operated at the same resolution, one pays a heavy price in signal intensity for working at very high resolution.

The ultimate resolution that can be achieved by the sectors is limited by stray magnetic fields inside the sectors and the nonuniform work functions of the surfaces of the sectors; both effects tend to deflect electrons from their paths through the sectors.

3.2.2 Spectrometer Construction

The sectors, B lenses, and filament assembly were fabricated from OFHC copper. The A lenses were fabricated from 0.009 in. tantalum. The slits, 0.2 mm x 4 mm, were etched in 0.002 in. molybdenum by Towne Laboratories, Inc. using photolithographic techniques and were then mounted on a 0.040 in. thick tantalum holder. All the conducting parts visible to the electron path were coated with colloidal graphite (Aerodag) to ensure uniform work functions on the spectrometer surfaces. Alumina ceramics were used to hold together the conducting parts. Both the inner and outer electrodes of the sectors were cut with a "sawtooth" profile, as illustrated in Fig. 3.2, to minimize stray electron reflection from the walls of the sector [12]. The analyzer section is mounted on a rotatable base plate so that the angular distribution of scattered electrons in the plane of scattering could be studied. The rotation of the base plate is accomplished by a rotary feedthrough turning a screw with a nut assembly that either pushes or pulls the analyzer base plate. Roulan bushings were used to reduce the friction between the analyzer and monochromator base plates.

3.2.3 Power Supply

Two different power supplies were used during this work. The power supply used during the earlier work was designed and built at Lawrence Berkeley Laboratory and is described in detail elsewhere [19]. Since this power supply can only achieve beam energies up to 10 eV, a second power supply, capable of beam energies up to 150 eV, was purchased

from RHK Technologies. The higher beam energies are needed for electronic spectroscopy while the lower beam energies (< 10 eV) are more suited for vibrational spectroscopy. Both power supplies are very similar in design in that ultrastable, low noise difference amplifiers are used to provide potentials for the 22 elements of the spectometer.

3.3. Vibrational Spectroscopy

As mentioned earlier, from the frequencies observed in a vibrational spectrum, one can usually deduce the identity of an adsorbate species; but it is from the intensities of the observed modes that the orientation and adsorption site symmetry are deduced. Consequently, we next discuss the physical origins of the intensities for the various inelastic scattering processes that occur in HREELS.

3.3.1 Dipole Scattering

Dipole scattering is similar in nature to the vibrational excitation mechanism in infrared (IR) vibrational spectroscopy. The long-range Coulomb field of the incident electrons interacts with the "dynamic dipole" of a vibrating adsorbate just as the electric field of the incident photons in IR spectroscopy interacts with the dynamic dipole of a molecule. This coupling between the electron and the dynamic dipole moment of the adsorbate enables the electron to lose a quantum of energy by exciting an adsorbate vibrational mode.

An important characteristic of dipole scattering arises from the physical nature of the Coulomb field of the incident electron at the metal surface. Electric fields can only have a component perpendicular to a metal surface since parallel components are screened by the metal; therefore, only the component of the dynamic dipole moment perpendicular to the surface can couple with incoming electrons. This results in what is usually called the "surface dipole selection rule" which states that only vibrations which have a net dynamical dipole moment perpendicular to the surface can scatter electrons via the dipole scattering process.

Another characteristic of dipole scattering, which enables one to distinguish between dipole and impact scattering processes, is the angular dependence of the scattering intensity; the dipole scattering intensity falls off rapidly for scattering angles away from the specularly reflected electron beam. The angular halfwidth of the dipole scattering intensity is on the order of $\hbar\omega_0/2E_I$, where ω_0 is the frequency of the vibration and E_I is the incident electron energy. In typical HREELS experiments, the dipole scattered electrons are concentrated within a couple degrees of the specular beam.

The physical basis for the narrow angular distribution of dipole scattered electrons becomes more apparent if one considers the Fourier transform of the potential outside the metal surface from a dipole on the surface and from its image:

$$V(r) = 2P\ Z/r^3 = P \int \frac{d^2Q_p}{\pi} e^{i\vec{Q}_p\vec{r}_p} e^{-Q_pZ}$$

where P is the component of the dipole perpendicular to the surface, $\vec{r}$ is the displacement vector from the dipole to the position of the incident electron and $\vec{r}_p$ and Z are, respectively, the components parallel and perpendicular to the surface. $\vec{Q}_p$ is a two-dimensional wave vector that lies in the plane parallel to the surface.

Conservation of wave vector parallel to the surface requires

$$\vec{Q}_p = (\vec{K}_{incident} - \vec{K}_{scattered})_p$$

where the subscript p denotes the components parallel to the surface. So, if the change in wave vector parallel to the surface of the incident electron is $\vec{Q}_p$, it interacts with the part of the dipole potential that extends a distance $D = Q_p^{-1}$ above the surface. Therefore, scattering that results in small Q_p (i.e. small scattering angles) is much more likely than scattering that results in large Q_p (i.e. large scattering angles). This result is a consequence of the requirement that the electrostatic potential in the vacuum must obey Laplace's equation. Thus, if a contribution to the total potential varies as $\exp(i \vec{Q}_p \cdot \vec{r}_p)$ for a fixed Z, Laplace's equation requires its Z dependance to be $\exp(- Q_p Z)$.

3.3.2 Comparison of Dipole and Quadruple Scattering

Analytical expressions for the scattering cross section for dipole scattering have been derived by several researchers [20-22]. Here, we show how the derivation by Evans and Mills [22] can be extended to inelastic scattering from a surface quadruple moment. To simplify the expressions, we consider only the case of scattering off of a perfect metal surface with an infinite dielectric constant, $\epsilon = -\infty$.

Following Evans and Mills [21], consider an ordered two-dimensional arrangement of n vibrating dipoles on the surface. Then, we can write the part of the potential that scatters an electron such that its wave vector component parallel to the surface changes by Q_p as

$$V_{Qp}(\vec{r}, t) = \Delta(Q_p) e^{-Q_p Z} e^{i\vec{Q}_p \cdot \vec{r}_p} e^{-i\omega t} + c.c.$$

where $\Delta(\vec{Q}_p) = 4\pi n P$.

Now, a charge above a metal surface will have an image charge below the surface as shown in Fig. 3.3a. So, if a dipole is oriented perpendicular to the surface, its image will be oriented in the same direction; whereas, if the dipole is oriented parallel to the surface, the image dipole is oriented so as to cancel the dipole. These cases are illustrated in Figs. 3.3b and c.

Even though the arrangement in Fig. 3.3b does not produce a dipole potential, there is, however, a quadruple potential

$$V(\vec{r}) = 6\ dP\ \frac{xZ}{r^5}$$

where d is the distance of dipole above the image plane, P is the magnitude of the dipole, and the x-z plane contains the dipole and its image. The Fourier transform of this potential is

$$V(\vec{r}) = 6\ dP\ \frac{xZ}{r^5} = dP \int \frac{d^2Q_p}{\pi}\ e^{-i\vec{Q}_p \cdot \vec{x}_p}\ e^{-Q_p Z}\ iQ_x$$

So, for an ordered 2-D arrangement of n dipoles oriented parallel to the surface, the Q_p part of the potential can be written as

$$V_{Qp}(\vec{r},t) = \Delta(\vec{Q}_p)\ e^{-Q_p Z}\ e^{i\vec{Q}_p \cdot \vec{r}_p}\ e^{-i\omega t} + c.\ c.$$

where $\Delta(\vec{Q}_p) = 4\pi\ n\ iQ_x\ Pd$.

Now, Evans and Mills have shown that, quite generally, the inelastic scattering cross section is

$$\frac{dS}{d\Omega} = \frac{4A}{\pi^2}\ m\ E_I\ |\Delta(\vec{Q}_p)|^2\ |R|^2\ \cos\ \theta_I$$

$$\times\ \frac{V^2 Q_p^2}{[V_\perp Q^2 + (\omega - \vec{V}_p \cdot \vec{Q}_p)^2]^2}$$

where A is the surface area, E_I and θ_I are the energy of the incident electron and the angle of its trajectory with respect to the surface normal, $V_\perp$ and V_p are, respectively, the perpendicular and parallel components of the electron's velocity and R is the electron's reflectivity from the surface.

The relative magnitudes then for scattering from dipoles oriented either perpendicular or parallel to surface is simply

$$\frac{\left(\frac{dS}{d\Omega}\right)_{parallel}}{\left(\frac{dS}{d\Omega}\right)_{perpendicular}} = \frac{\left|A(\vec{Q}_p)_{quad.}\right|^2}{\left|A(\vec{Q}_p)_{dipole}\right|^2}$$

$$= \left|Q_x\ d\right|^2$$

A typical order of magnitude for Q_x is 10^6 cm^{-1}, so for d ~ 10^{-8} cm, the ratio parallel vs perpendicular scattering is ~ 10^{-4}. Consequently, dipoles oriented perpendicular to the surface are much more intense scatterers than those oriented parallel to the surface.

However, for real metals, the component of the electric field parallel to the surface is not perfectly screened. For a typical metal, the parallel component of the electric field is on the order 10^{-2} less than the magnitude of the electric field electric field produce by the incident EELS electron over the vibrational frequency range [23]. Consequently, the ratio parallel vs. perpendicular scattering for dipole scattering by a dipole above a real surface is also about ~ 10^{-4}.

Generally, we can interpret the very intense peaks in the HREEL spectra as resulting from vibrations with a large degree of motion perpendicular to the surface, while the very weak peaks correspond to vibrations oriented parallel to the surfaces. Therefore, the intensity of the HREELS peaks can provide information about the orientation of a chemical species on the surfaces. Several examples of this will be presented later in this thesis.

The angular distribution of dipole and quadruple scattered electrons can be seen by introducing the two angles ψ, and ϕ illustrated in Fig. 3.4, into the expressions for the scattering cross section. ψ is the angle between $\vec{K}_{incident}$ and $\vec{K}_{scattered}$, and ϕ is the angle between the plane that contains $\vec{K}_{incident}$ and $\vec{K}_{scattered}$ and the x' - z' plane. Using these labels, the dipole scattering cross section becomes [22]

$$\left(\frac{dS}{d\Omega}\right)_{\text{dipole}} = \frac{16An^2 me^2 P^2 |R|^2}{E_I \cos\theta_I} \frac{[\psi\cos\phi \cos\theta_I - \psi_E \sin\theta]^2 + \psi^2\sin^2\theta}{[\psi^2 + \psi_E^2]^2}$$

and the quadruple scattering cross section beams

$$\left(\frac{dS}{d\Omega}\right)_{\text{quad}} = \frac{16An^2 me^2 P^2 d^2 |R|^2 K_I^2}{E_I \cos\theta_I} \frac{[\psi\cos\phi \cos\theta_I - \psi_E\sin\theta]^2 + \psi^2 \sin^2\phi}{[\psi + \psi_E^2]}$$
$$\times [\cos\theta' (\psi_E\sin\theta_I - \psi\cos\theta_I \cos\phi) - \sin\theta'\psi \sin\phi]^2$$

where $\psi_E = \hbar\omega/2E_I$ and θ' is the angle between $\vec{K}_{Ip}$ and the direction of the dipole parallel to the surface. The factor $(\psi^2 + \psi_E^2)^{-2}$ in these expressions of the scattering cross sections results in the angular distribution being concentrated mainly to angles $0 \leq \psi < \hbar\omega/2E_I$ around the specular direction.

3.3.3 Impact Scattering

Another scattering mechanism responsible for inelastic scattering of electrons from surfaces is impact scattering. During the impact scattering process, the incident electrons lose energy by interacting

directly with the atomic potentials while the electrons are within a few Angstroms of the surface. During this very short-range interaction, the electrons essentially become "impacted" in the surface atoms for a short period of time, allowing vibrational modes, oriented both parallel and perpendicular to surface, to be excited by the electrons.

The short-range, impact scattering mechanism is physically a much more complicated process than the long-range, dipole scattering process. Since most of the scattering occurs within a few Angstroms of the surface, the $A(\vec{Q}_p)$ for impact scattering must be very large for large Q_p. Consequently, inelastically scattered electrons that are impact scattered tend to have a broad angular distribution, unlike the narrow angular distribution for dipole or quadruple scattering. Precise calculations for the scattering cross section for impact scattering are difficult due to the complicated nature of the short-range electron-surface interactions, though some progress has been made by several researchers [24-26].

Quite large scattering cross sections can be observed for impact scattering when the energy of the incident electron is resonant with an unoccupied state localized near the surface. This "resonant" impact scattering is analogous to resonant electron scattering from gas phase atoms and molecules where the incident electron is temporarily captured to form a short-lived negative ion [27]. An example of "resonant" impact scattering will be discussed in Chapter 7 for hydrogen adsorbed in Rh(111).

3.3.4 Selection Rules

We previously mentioned the "surface dipole selection rule" that only vibrations which produced a net change of the dipole moment perpendicular to the surface are observable by dipole scattering. In other words, only vibrations belonging to totally symmetric representations (A_1, A', A) are observed by dipole scattering [28].

For quadruple scattering, a very different selection rule occurs as can be seen from the expression for its scattering cross section. According to this rule, the inelastic scattering intensity vanishes for a vibration that is odd with respect to a mirror plane if trajectories of both the incident and scattered electrons lie in this symmetry plane.

For impact scattering, several selection rules have been derived based on time reversal symmetry [29]: 1) The inelastic scattering intensity vanishes for a vibration that is odd with respect to a mirror plane symmetry if trajectories of both the incident and scattered electrons lie in this symmetry plane. (Note, this is the same selection rule as for quadruple scattering). 2) The inelastic scattering intensity vanishes in the specular direction for a vibration that is odd with respect to a mirror plane symmetry if the plane containing the trajectories of the incident and scattered electrons is perpendicular to the mirror plane and the surface. 3) The inelastic scattering intensity vanishes in the specular direction for a vibration that is odd with respect to a two-fold rotation symmetry.

To fully exploit the selection rules for impact and quadruple scattering, one needs to rotate the sample in the azimuthal direction, which is not possible with our apparatus. Instead, we are only able to look at the scattering distribution in one, fixed direction parallel to the surface. However, by determining whether the scattered intensity is peaked along the direction of specular scattering, we can distinguish dipole and quadruple scattering from impact scattering. Then, by identifying the more intense modes as dipole scattered, we can sometimes determine the adsorption site symmetry by identifying these modes as the totally symmetric modes of the surface species.

3.4 Electronic Spectroscopy

The previous analysis can, of course, also be applied to transitions between electronic states. All that one needs to do is replace the matrix element between vibrational states with the appropriate one between electronic states. However, it is enlightening to consider an alternate approach. The dielectric constant, $\epsilon(q,\omega) = \epsilon_1(q,\omega)+i\epsilon_2(q,\omega)$, is a useful entity for describing the response of a medium to the perturbation by a moving electron, since it includes contributions from collective electron oscillations on an equal footing with single electron excitations.

Now, the energy of an electron field is reduce at a rate proportional to the imaginary part of the dielectric constant, ϵ_2. For an electron traveling through the bulk, its electric field is reduced by a factor $1/\epsilon$ and the intensity by $1/|\epsilon|^2$. So, the scattering ampli-

tude for energy loss of an electron traveling through the bulk is proportional to

$$d^2S_b \alpha \frac{\epsilon_2}{|\epsilon|^2} = - \text{Im} \left(\frac{1}{\epsilon}\right) = \frac{\epsilon_2}{\epsilon_1^2 + \epsilon_2^2} .$$

For electrons outside the medium, as in the case of an electron reflecting off the surface, the electric field is screened by a factor $1/\epsilon + 1$; as a result, the scattering amplitude becomes

$$d^2S_s \alpha \frac{\epsilon_2}{|\epsilon + 1|^2} = - \text{Im} \left(\frac{1}{\epsilon + 1}\right) = \frac{\epsilon_2}{(\epsilon_1 + 1)^2 + \epsilon_2^2}$$

Consequently, $-\text{Im}\ (1/\epsilon)$ and $-\text{Im}\ (1/\epsilon+1)$ are called the volume loss function and surface loss function, respectively. Transitions between electronic states appear in the loss functions through the maxima of ϵ_2, while collective electron excitations appear through the poles of $1/\epsilon+1$ if they are localized near the surface or through the poles of $1/\epsilon$ if they are bulk excitations.

REFERENCES

1. H. Ibach and D.L. Mills, Electron Energy Loss Spectroscopy and Surfaces Vibrations, Academic, New York, 1982.
2. R.F. Willis Ed., Vibrational Spectroscopy of Adsorbates, Springer-Verlag, Berlin-Heidelberg-New York, 1980.
3. H. Froitzheim, Electron Energy Loss Spectroscopy, Published in Electron Spectroscopy for Surface Analysis, Topics in Current Physics 4, H. Ibach Ed., Springer-Verlag, Berlin-Heidelberg-New York, 1977, 205-250.
4. H. Ibach, H. Hopster, and B. Sexton, Appl. Surface Sci. 1 (1977) 1.
5. B.E. Koel and G.A. Somorjai, Surface Structural Chemistry, Published in Catalysis: Science and Technology Vol. 38, J.R. Anderson, M. Boudart Eds., Springer-Verlag, Berlin-Heidelberg-New York, in press.
6. B.A. Sexton, Appl. Phys. A26 (1981) 1.
7. Ph. Avouris and J.E. Demuth, Ann. Rev. Phys. Chem. 35 (1984) 49.
8. N. Sheppard and J. Erkelens, Applied Spectroscopy, 38 (1984) 471.
9. P.A. Thiry, J. Electron Spectrosc. Related Ph., 30 (1983) 261-273.
10. P.A. Thiry, J. Electron Spectrosc. Related Ph., 39 (1986) 273-288.
11. L. H. Dubois, Ph.D. Thesis, University of California, Berkeley, 1980, unpublished.
12. H. Froitzheim, H. Ibach and S. Lehwald, Rev. Sci. Instrum. 46(1975) 1325.

13. D. Roy and J.D. Carette, Design of Electron Spectrometers for Surface Analysis, Published in Electron Spectroscopy for Surface Analysis, Topics in Current Physics 4, H. Ibach Ed., Springer-Verlag, Berlin-Heidelberg-New York, 1977, 13-58.

14. Ref. 1, pp. 23-24.

15. R. Herzog, Z. Physik 97 (1935)556; 41 (1940) 18.

16. D. Roy and J.D. Carette, Appl. Phys. Lett. 16 (1970) 413; Canad. J. Phys. 49(1971) 2138.

17. Ref. 1, p.32.

18. Ibid, pp. 49-56.

19. J.E. Katz, P.W. Davies, J.E. Crowell, and G.A. Somorjai, Rev. Sci. Instrum. 53(1982) 785.

20. A.A. Lucas and M. Sunjic, Phy. Rev. Lett. 26(1971) 229.

21. D.M. Newns, Theory of Dipole Electron Scattering from Adsorbates, in Ref. 2, pp. 7-22.

22. E. Evans and D.L. Mills, Phys. Rev. B5 (1972) 4126.

23. Ref. 1, p. 132.

24. J.W. Davenport, W. Ho, and J.R. Schreiffer, Phys. Rev. B17, (1978) 3115.

25. S.Y. Tong, C.H. Li, and D.L. Mills, Phys. Rev. Lett. 44(1980) 407; C.H. Li, S.Y. Tong, and D.L. Mills, Phys. Rev. B21, (1980) 3057; S.Y. Tong, C.H. Li,and D.L. Mills, ibid. 24(1981) 806.

26. Ref. 1 pp. 102-123.

27. G.J. Schulz, Rev. Mod. Phys. 45(1973) 378.

28. Ref. 1, p. 171.

29. Ibid, pp. 116-120.

FIGURE CAPTIONS

Fig. 3.1. Schematic diagram of the HREEL Spectrometer used by Dubois.

Fig. 3.2 Expanded view of one of the spectrometer sectors for our spectometer. The insert shows the details of the "sawtooth" profiling.

Fig. 3.3 (a) A charge and its image charge.

(b) A dipole oriented parallel to surface and its image below the surface.

(c) A dipole oriented perpendicular to a surface and its image below the surface.

Fig. 3.4 Angles ψ and ϕ used to define the direction of the scattered beam.

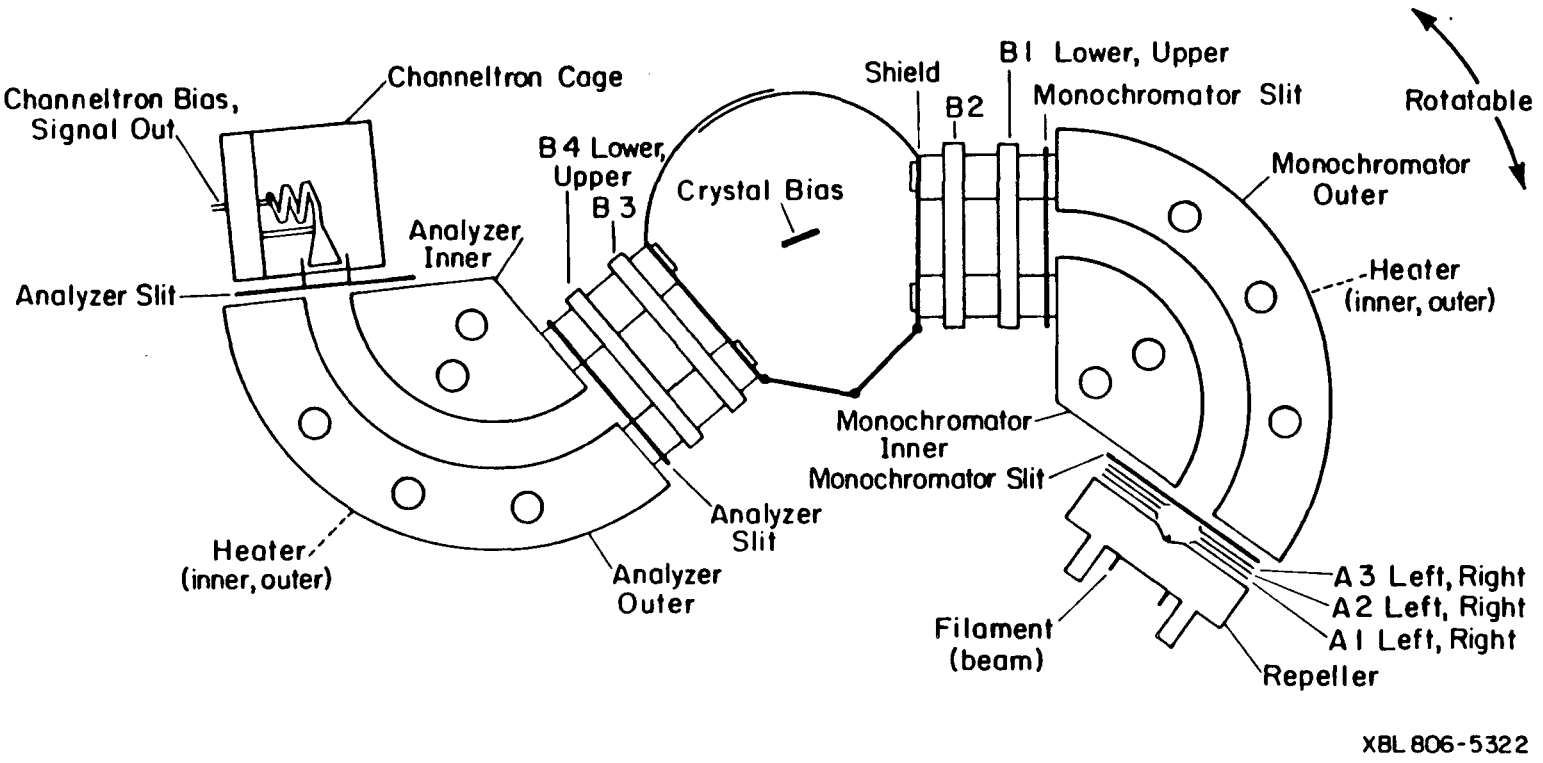
Channeltron Bias,
Signal Out
Channeltron Cage
Shield
B1 Lower, Upper
Monochromator Slit
B2
Rotatable
B4 Lower,
Upper
B3
Crystal Bias
Monochromator
Outer
Analyzer
Inner
Heater
(inner, outer)
Analyzer Slit
Monochromator
Inner
Monochromator Slit
Analyzer
Slit
Heater
(inner, outer)
Analyzer
Outer
A3 Left, Right
A2 Left, Right
A1 Left, Right
Filament
(beam)
Repeller
XBL 806-5322

Figure 3.1

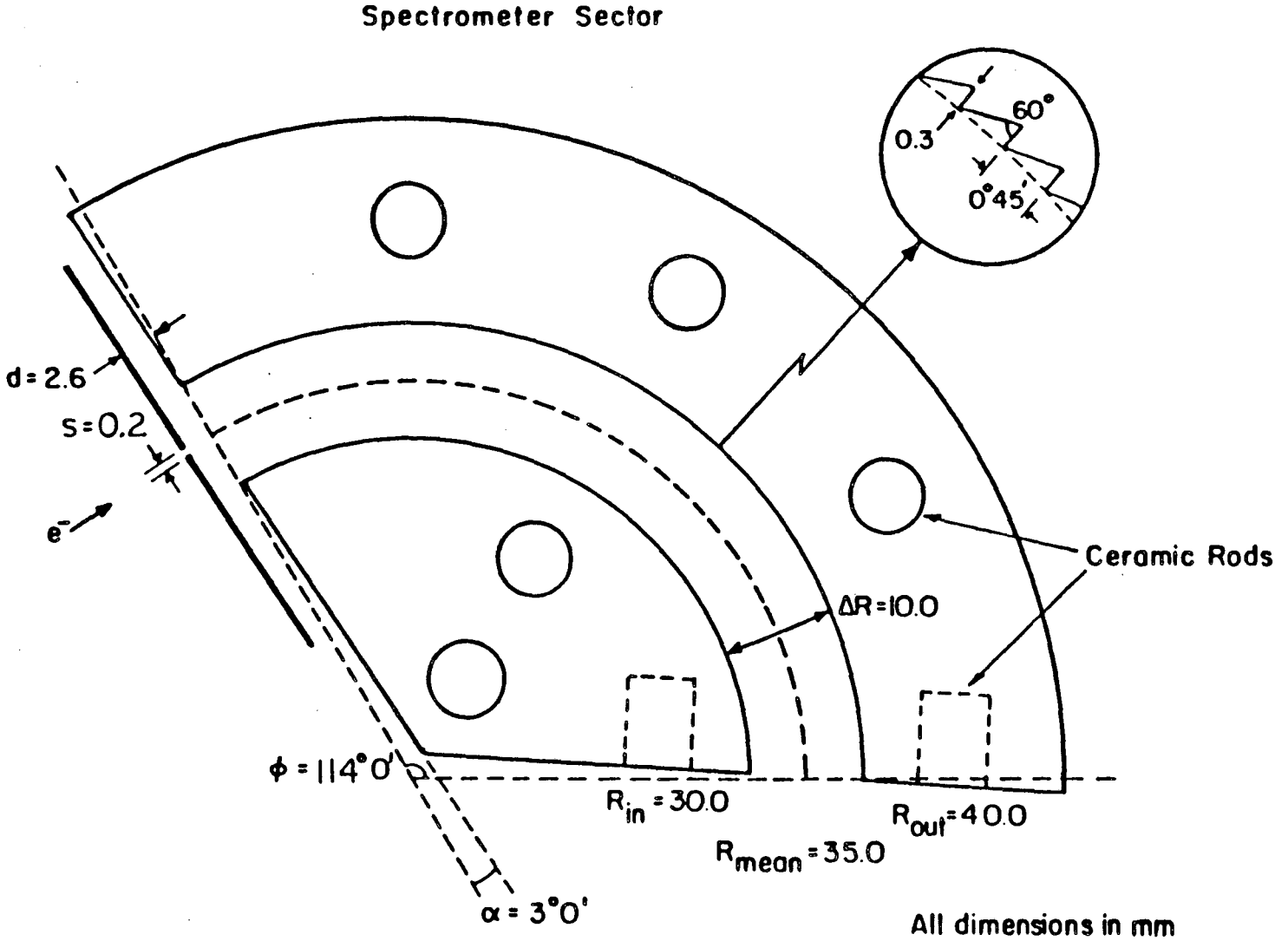
Spectrometer Sector
60°
0.3
0°45'
d=2.6
s=0.2
e⁻
Ceramic Rods
ΔR=10.0
φ=114°0'
R_in=30.0
R_out=40.0
R_mean=35.0
α=3°0'
All dimensions in mm
XBL 806-5321

Figure 3.2

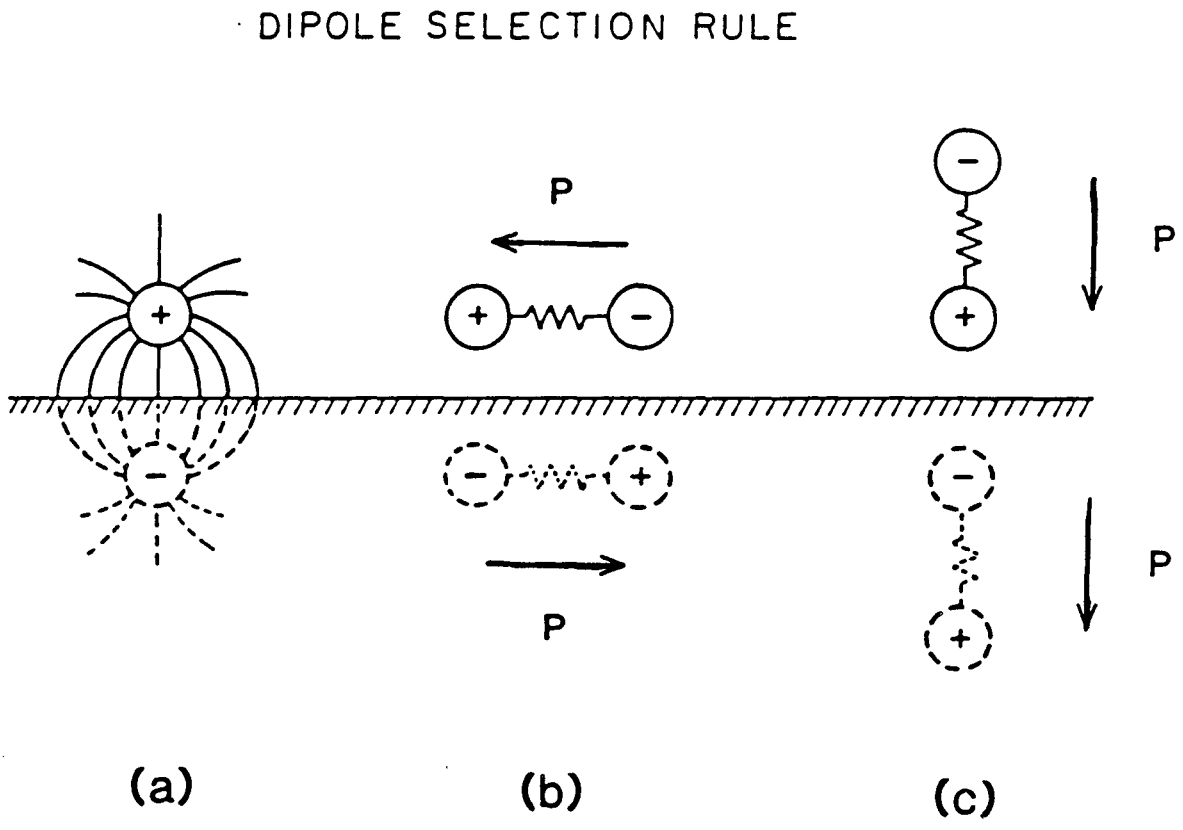

Figure 3.3

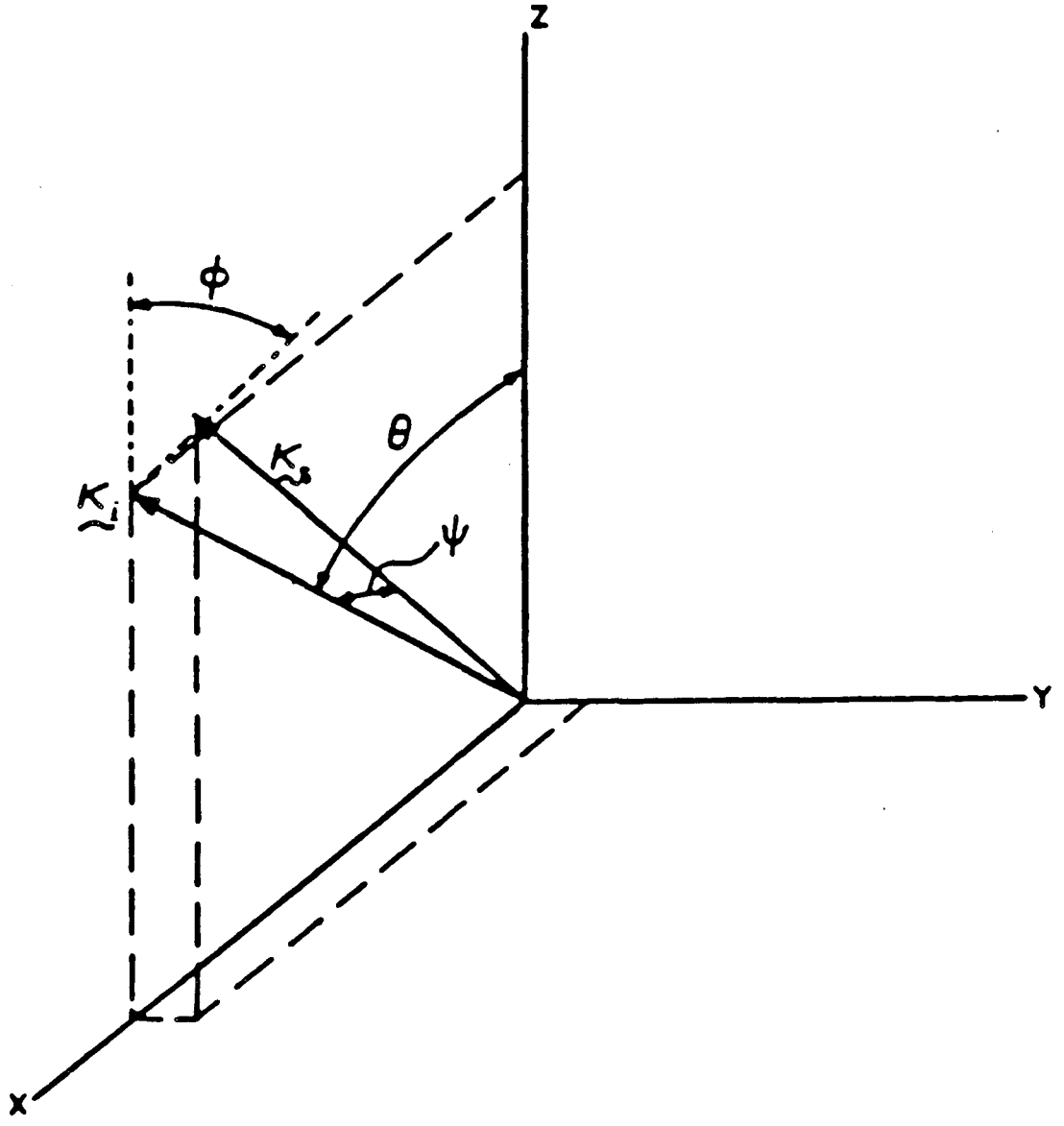

XBL 869-3429

Figure 3.4

CHAPTER 4

Benzene and Pyridine Adsorption on Rh(111)

Contents

4.1 Introduction

The bonding of benzene and pyridine, two of the simplest aromatic molecules, to metal surfaces has recently been the subject of considerable interest [1-19]. Most studies have concentrated on the molecular adsorption of benzene and pyridine, with particular emphasis being placed on determining the orientation, adsorption site, bond lengths, and electronic structure of the adsorbed molecules. Generally, benzene has been found to bond with its molecular ring oriented parallel to the surface and to form the adsorption bond through its π-orbitals. Generally, pyridine has been found to be tilted on the surface, due to competition between the π-orbitals and the nitrogen lone pair orbitals for bonding to the surface. Also, the tilt angle of adsorbed pyridine is found to be dependent on the temperature and pyridine coverage.

Aromatic compounds are also important in both catalysis and lubrication. For example, aromatic compounds are desirable catalytic products in the refining of crude oil into high octane fuels [20]. In lubrication, aromatic compounds are frequently used as functional groups in extreme pressure additives [21], even though their role is not understood. Therefore, a molecular scale understanding of how aromatic molecules interact with metal surfaces should lead to an eventual understanding of the role aromatic compounds play in catalysis and lubrication.

In this chapter, we discuss the adsorption of benzene and pyridine alone on the Rh(111) surface. In the following chapter, CO-induced ordering of adsorbed benzene is discussed.

4.2 Benzene Adsorption on Rh(111)

The adsorption of benzene on the Rh(111) surface has been studied extensively both by workers in our laboratory [1-6] and by researchers in other laboratories [7-9] and has become one of the best characterized aromatic adsorption systems. In this section, we discuss what has been learned in our laboratory by HREELS and LEED about the absorption of benzene alone in Rh(111).

At saturation coverage, benzene orders in a $(2\sqrt{3}x3)$rect lattice [a $(\sqrt{7}x\ \sqrt{7})R\ 19.1^{\circ}$ structure has also been reported [4] but cannot be formed reproducibly]. For the $(2\sqrt{3}x3)$ LEED pattern, we observe the extinction of certain spots revealing the presence of a glide plane symmetry for this structure. This symmetry means that the ordered structure can be transformed back into itself by a reflection through the glide plane followed by a translation of half a lattice spacing along the direction of the plane. In order to satisfy this symmetry requirement, there needs to be an even number of benzene molecules per unit cell. Consequently, there should be two benzenes per unit cell, since the $(2\sqrt{3}x3)$rect unit cell is too small to accommodate more than two flat lying benzene molecules. (Flat lying benzene molecules are indicated by the vibrational spectra, as discussed below.)

The glide plane symmetry also helps us to deduce the bonding site of benzene within the ($2\sqrt{3}$x3) structure. Benzene adsorption at top or three-fold hollow sites is highly unlikely since adsorption at these sites in an arrangement that also satisfies the glide plane symmetry would result in substantial overlap of the flat lying benzene molecules. Consequently, we conclude that benzene adsorbs at bridge sites since these sites enable the benzene molecules to lie flat and to satisfy the glide plane symmetry without significant overlap between neighboring molecules. Figure 4.1 shows how two benzene molecules can be arranged in a ($2\sqrt{3}$x3)rect unit cell to satisfy the glide plane symmetry. Rotation of the benzene molecules is also possible but this would result in a slight overlap of neighboring molecules.

Figure 4.2 shows the HREEL spectra obtained in the specular direction at 310 K for the ($2\sqrt{3}$x3)rect structure of benzene on the Rh(111) surface. Given in Table 4.1 is our assignment of the observed vibrational frequencies to the corresponding frequencies of gas phase benzene, along with the mode number and symmetry representation of the gas phase vibrational modes. This assignment was aided by the calculated frequencies of the normal modes for benzene chemisorbed on Raney Nickel [24]. Not all the vibrational modes of gas phase benzene are observed for chemisorbed benzene since some modes overlap with other modes and/or have intensities too low to be observed.

However, the assignment in Table 4.1 differs from our previously published assignments [4,5] for $C_6H_6(C_6D_6)$ adsorbed on Rh(111) in that the 775, 804 cm^{-1} (560, 645 cm^{-1}) doublet is now assigned

to different CH out-of-plane bending ($^{\gamma}$CH) modes of benzene bonded at bridge sites rather than to the same $^{\gamma}$CH mode of benzene bonded at two different types of sites, as was done in earlier work. The new assignment of the $^{\gamma}$CH doublet is consistent with the work of Waddill and Kesmodel [25], who have pointed out that the ν_{11} vibrational mode can become dipole active when benzene bonds at a bridge site with C_s symmetry. We prefer the new assignment since the isotopic shifts - 1.34 and 1.25, respectively, for the 775 cm^{-1} (580 cm^{-1}) and 850 cm^{-1} (640 cm^{-1}) modes of C_6H_6 (C_6D_6) - are more in line with the gas phase shifts of 1.35 for ν_4 and 1.28 for ν_{11}. Further, we believe that the large intensity of the 805 cm^{-1} vibration in the C_6H_6/Rh(111) spectrum is probably due to coupling with the symmetric ring stretch (ν_2), which is visible at 845 cm^{-1} in the C_6D_6/Rh(111) spectrum and has the correct symmetry to couple to the ν_{11} mode for chemisorbed benzene with C_s symmetry. We should note, however, that the alternate explanation for the γ_{CH} doublet of two different types of benzene adsorption sites can not be completely ruled out.

That the observed vibrational frequencies for chemisorbed benzene can be assigned to those of gas phase benzene provides strong evidence that, at 310 K, benzene adsorbs on the Rh(111) surface molecularly intact. Further experimental evidence that benzene adsorbs molecularly at 310 K comes from TDS [4], where a small fraction of the benzene is observed to desorb molecularly, and from UPS [7], where the occupied orbitals of adsorbed molecular benzene are observed.

The intensities of the peaks in Fig. 4.2 provide information on the orientation of the benzene molecule chemisorbed on Rh(111). The intensities of the in-plane modes of chemisorbed benzene are very weak compared to the intensities of the out-of-plane modes. Since the metal effectively screens the dipole contribution to the HREEL spectrum for modes oriented parallel to the surface, the weak intensities of the in-plane modes indicate that the ring of the benzene molecule is oriented parallel to the surface.

The vibrational frequencies for chemisorbed benzene also provide insight into the nature of the chemisorption bond. The upward shift of the symmetric ν_{CH} mode, (ν_4) and the downward shift of the ring stretching modes (ν_2 and ν_{13}) and the CH stretching modes indicate that the bonds within the benzene molecule rehybridize away from sp^2 hybridization and toward sp^3 hybridization [26] when it bonds to the rhodium surface. The direction of these shifts appears to be characteristic of benzene bonded to metal surfaces [4] or in organometalic clusters [27]. The large magnitudes of the shifts of some of the chemisorbed benzene frequencies relative the gas phase frequencies indicates that a strong chemisorption bond occurs between the adsorbed benzene molecule and the Rh(111) surface.

4.3 Pyridine Adsorption on Rh(111)

Besides benzene, pyridine is one of the simplest aromatic molecules. The nitrogen atom of pyridine, however, can participate in some interesting chemistry when pyridine adsorbs on a metal surface.

First, there can be competition between the electrons in the nitrogen lone-pair and the π-orbitals as to which will be dominately responsible for the pyridine-metal bond. Such competition has been observed for pyridine adsorbed on the Ag(111) surface, where the molecule converts from a relatively flat lying, π-bonded species to a tilted, nitrogen-bonded species with increasing coverage. Second, pyridine has also been observed on several metal surfaces (Pt(111) [12a], Ni(100) [11]) to lose one of the α-hydrogens above a particular temperature and to form an α-pyridyl species, which bonds to the surface through the nitrogen atom and one of the α-carbon atoms.

As discussed below, our studies indicate that two pyridine surface species occur for pyridine adsorbed on Rh(111). At 310 K, a chemisorbed pyridine species, probably an α-pyridyl species, is present and orders into a $(2\sqrt{3}x3)$rect overlayer at high coverages. Electronic spectroscopy indicates that this α-pyridyl species also has contribution from π-bonding to the surface as well as bonding through the nitrogen and α-carbon atoms. At lower temperatures, a second pyridine species appears to be coadsorbed with the chemisorbed pyridine species. This second species is thought to be a more weakly bound, physisorbed pyridine molecule, with an undetermined orientation.

4.3.1 TDS - Pyridine/Rh(111)

The upper part of Fig. 4.3 shows the thermal desorption spectrum for molecular desorption of NC_5H_5 following ~50 L exposure at 80 K, an amount sufficient to form multilayers of pyridine on the Rh(111)

surface. The intense peak at 165 K results from the desorption of the pyridine multilayers, while the smaller peak at 295 K results from molecular pyridine desorbing from the pyridine monolayer in contact with the surface.

The lower part of Fig. 4.3 shows the thermal desorption spectrum for D_2 desorption following the same exposure of NC_5D_5 at 80 K as used for the molecular TDS. The first D_2 desorption peak occurs at a temperature (330 K) that is characteristic of hydrogen and deuterium desorption from the bare Rh(111) surface [28], suggesting that pyridine decomposition starts at temperatures below the onset of 330 K desorption peak (250 K). The area of the first D_2 desorption peak is approximately 7% of the total D_2 desorption area. This first peak would then correspond to one third of the pyridine decomposing by losing one hydrogen or a smaller fraction losing more hydrogen.

While the exact nature of the other desorption peaks is not understood, they are fairly similar to those observed for benzene decomposition on Rh(111) [29], except the higher temperature peaks at 525 and 680 K are more pronounced. Benzene is proposed to decompose on Rh(111) at 400 K into a mixture of C_xH fragments, which polymerize with increasing temperature. As discussed below, our HREELS results indicate that similar decomposition may occur for pyridine.

4.3.2 HREELS of Pyridine/Rh(111) - Temperature Dependence

Figure 4.4a shows the the HREEL spectrum obtained in the specular direction at 77 K for multilayers of pyridine on the Rh(111) surface. The pyridine exposure was the same as used for the thermal desorption spectra in Fig. 4.3. For the multilayer spectrum, the elastic peak is weak (1200 cps) and substantially broader (105 cm^{-1}) than the instrumental resolution of 60 cm^{-1}. The HREEL spectrum taken at ten degrees off specular has virtually the same peak intensities as the specular spectrum indicating that the predominant scattering mechanism is impact scattering.

Our assignment of the observed HREELS frequencies for the pyridine multilayer spectrum to the corresponding vibrational frequencies of liquid pyridine is given in Table 4.2, along with the mode number and symmetry representation of the liquid phase vibrational modes. Generally, the observed HREELS frequencies have been assigned to more than one pyridine vibrational mode, since the poor resolution makes it impossible to separate out vibrations close in frequency. The HREELS frequencies for the pyridine multilayer do not differ substantially from those of liquid pyridine, leading us to conclude the pyridine in the multilayers should be fairly similar to that in the liquid phase, as would be expected.

Figure 4.4b shows the HREEL spectrum obtained in the specular direction at 77 K after the pyridine multilayer has been heated to 185 K. Heating to 185 K removes the pyridine multilayer but does not remove the second pyridine molecular desorption peak. For this spectrum, the

elastic peak narrows to the instrumental resolution of 60 cm^{-1} and increases in intensity to 2.7 x 10^4 cps. For spectra taken off specular, the 360, 465, 650, and 840 cm^{-1} features decrease in intensity indicating that dipole scattering predominates for these features. Since the 360, 465, 650, and 840 cm^{-1} features have the same frequencies and scattering mechanism as the vibrations of the chemisorbed pyridine species observed at 310 K (this species is discussed in detail in the following section), we assign these features to the same chemisorbed pyridine species occurring at 185 K.

The remaining HREELS features in Fig. 4.4b have similar intensities off specular as on specular, indicating that impact scattering dominates for these features. Since features have similar frequencies and absolute intensities, as well as the same scattering mechanism, as those observed for the pyridine multilayer spectrum, we assign these features to a more weakly bound, physisorbed pyridine species that is coadsorbed with the chemisorbed species at 185 K. Since impact scattering dominates for the features of the physisorbed species we are unable to use the dipole selection rule to determine the orientation of this species.

Figure 4.4c shows the HREEL spectrum at 77 K after momentarily heating to 230 K. This spectrum is similar to the 185 K spectrum except for the reduction in intensity of the features from the physisorbed pyridine species, indicating that some of this species has desorbed.

Figure 4.4d shows the HREEL spectrum at 77 K after momentarily heating to 320 K. Except for the 730 cm^{-1} peak, the spectrum is identical to that obtained for pyridine adsorbed at 310 K in the $(2\sqrt{3}x3)$rect structure, discussed in the following section, indicating that the same surface species is present. (The pyridine overlayers for the Fig. 4.4d spectrum, was disordered.) We attribute the 730 cm^{-1} peak to a small amount of the physisorbed pyridine species that has readsorbed during cooling from the residual background pressure of pyridine.

Since the intensities of the HREELS peaks of the chemisorbed species for the 320 K spectrum are similar to those in the 185 and 230 K spectra, we conclude that the physisorbed pyridine species desorbs molecularly during the 295 K molecular desorption peak rather than converting to the chemisorbed pyridine species.

Figure 4.4e shows the HREEL spectrum after momentarily heating to 445 K. Many of the features that are characteristic of pyridine vibrations have disappeared, indicating that chemisorbed pyridine has completely decomposed by this temperature. The 445 cm^{-1} and 820 cm^{-1} peaks and the broad feature centered around 1350 cm^{-1} are similar to those observed for benzene decomposition on Rh(111), where a mixture of C_xH fragments has been proposed to occur [29]. In addition, the 445 K spectrum has peaks at 330, 1435, and 1575 cm^{-1}, indicating the presence of other types of fragments, possibly containing the nitrogen atom from the pyridine molecule.

4.3.3 HREELS of Pyridine/Rh(111) - 310 K

For intermediate pyridine exposures (4 to 30 L) with the Rh(111) sample temperature at 310 K, we observed a $(2\sqrt{3}x3)$rect LEED pattern; the same LEED pattern observed for benzene adsorbed in Rh(111) except for the absence of the glide plane symmetries. High pyridine exposures caused this pattern to disorder. No other LEED patterns were observed for pyridine adsorbed on Rh(111), even when coadsorbed with CO.

Figure 4.5 shows the HREEL spectra obtained in the specular direction for the $(2\sqrt{3}x3)$rect structure of pyridine on the Rh(111) surface. All the features in these spectra decrease in intensity for scattering angles off specular, indicating dipole scattering as the scattering mechanism for these features. Also shown is the HREEL spectrum of a low coverage (10% of the $(2\sqrt{3}x3)$rect coverage) of pyridine on Rh(111). For the $(2\sqrt{3}x3)$rect structure, Table 4.2 gives our assignment of the observed HREELS frequencies to the corresponding vibrational frequencies of liquid pyridine. The HREELS frequencies have been assigned to vibrational modes of liquid pyridine that are closest in frequency. Many of the HREELS frequencies are assigned to more than one pyridine vibrational mode, since the relatively poor resolution of HREELS makes it difficult to separate vibrations close in frequency.

The good correspondence between the HREELS frequencies and the vibrational frequencies of liquid pyridine is strong evidence that the pyridine ring is still intact for chemisorbed pyridine. However, a recent study by Grassian and Muetterties [12a] of two Osmium cluster

compounds - $Os_3(CO)_{11}(NC_5H_5)$, a pyridine complex, and $HOs_3(CO)_{10}(NC_5H_4)$, an α-pyridyl complex - has demonstrated that the pyridine species and the α-pyridyl species have very similar vibrational frequencies when measured with the relatively poor resolution of HREELS. Consequently, we cannot tell unambiguously from the vibrational frequencies alone whether pyridine chemisorbed on Rh(111) at 310 K is a completely intact pyridine species (NC_5H_5) or an α-pyridyl species (NC_5H_4).

As the thermal desorption spectra for pyridine adsorbed on Rh(111) indicates some pyridine decomposition has occurred by 310 K, we prefer to interpret the HREEL spectra in Fig. 4.5 as those of an α-pyridyl species on the Rh(111) surface, since this would be consistent with partial pyridine decomposition. As mentioned previously, the 330 K D_2 TDS peak, which is completely absent for pyridine adsorption at 310 K, contains 7% of the total D_2 desorption yield. Therefore, either only a fraction of the adsorbed pyridine has formed an α-pyridyl species or all the adsorbed pyridine has formed an α-pyridyl species but a fraction of the detached α-hydrogens remains on the surface to higher temperatures. We prefer the second interpretation that all the pyridine forms α-pyridyl for two reasons: 1) The HREELS peaks are fairly narrow, as would be the case for only one species on the surface rather than being broad or being doublet, as would be expected if two surface species were present; and 2) the $(2\sqrt{3}x3)$rect LEED pattern is sharp with the low background, which is expected if there is only one ordered surface species rather than one ordered and one disordered

surface species. Another possible interpretation of the 330 K D_2 TDS peak, which cannot be completely ruled out, is that a small fraction pyridine loses more than one deuterium or hydrogen atom, while the remaining pyridine molecules are completely intact. We think this is unlikely, however, since several features of the decomposed pyridine spectrum (Fig. 4.4e) - the 330 cm^{-1} peak, the broad feature centered at 1350 cm^{-1}, and the large, sloping background - are absent from the $(2\sqrt{3}x3)$rect pyridine spectrum (Fig. 4.5b). Also, the HREELS peaks for decomposed pyridine are fairly broad rather than the sharp peaks present in Fig. 4.5b. For the rest of our discussion of pyridine adsorption on Rh(111), we will assume that only one species is present on the surface for adsorption at 310 K and that this species is an α-pyridyl species, i.e. pyridine that lost one α-hydrogen and is bonded to the surface through the nitrogen atom and an α-carbon atom.

Since the metal effectively screens dipole moments oriented parallel to the surface, some information about the orientation of the molecular ring of the α-pyridyl species can be gained by comparing the relative intensities of the HREELS peaks in Fig. 4.5. By comparing the relative intensities of the α-pyridyl vibrational modes oriented parallel to molecular ring (i.e. those corresponding to modes of A_1 or B_1 symmetry in liquid pyridine) to the α-pyridyl modes oriented perpendicular to the molecular ring (i.e., those corresponding to modes of B_2 symmetry in liquid pyridine), we see that the modes oriented perpendicular to the ring are more intense than those oriented parallel to the ring, suggesting that the plane of the molecular ring is oriented

more parallel to the surface than perpendicular to the surface. However, several of the in-plane modes (such as the 635 and 1420 cm^{-1} modes in Fig. 4.5b) are fairly intense indicating that the α-pyridyl is tilted somewhat away from the surface.

At this point, it is useful to compare pyridine adsorption on Rh(111) at 310 K to pyridine adsorption on Ag(111) and Pt(111), where the orientation of the surface species has been determined by NEXAFS [18,19]. For pyridine adsorption on Ag(111) at 100 K, the tilt angle (i.e. the angle between the ring plane and the surface plane) is 45° ± 5° for low pyridine coverages and 70° ± 5° for high pyridine coverages. For pyridine adsorption on Pt(111), the angle between the ring plane and the surface plane, at 90 K, is 52° ± 6° after annealing to 240 K and is 85° ± 10° after annealing to 320 K. HREEL spectra have also been obtained for pyridine adsorption on Ag(111) and Pt(111). For conditions similar to when NEXAFS finds a large tilt angle (i.e. 70° or 85°) for pyridine adsorption, the vibrational modes oriented parallel to the molecular ring are very intense in the corresponding HREEL spectra. However, for conditions where NEXAFS finds a smaller tilt angle (i.e., 45° or 52°) for pyridine adsorption, the vibrational modes oriented perpendicular to molecular ring are more intense in the HREEL spectra than those oriented parallel to the ring.
The intensities of our HREEL spectra for the $(2\sqrt{3}x3)$rect pyridine Rh(111) structure are more similar to those for pyridine with the smaller tilt angle on Ag(111) and Pt(111) than those with the larger

tilt angles. Consequently, we think that an angle between 40° and 55° is a reasonable tilt angle for the α-pyridyl species on Rh(111) at 310 K.

Next, we note that the main difference between the low coverage α-pyridyl spectrum (Fig. 5a) and the high coverage $(2\sqrt{3}x3)$rect α-pyridyl spectrum (Fig. 5b) is that the in-plane modes are more intense for the high coverage spectrum. This suggests that the tilt angle between the molecular ring and the surface plane increases as the pyridine coverage increases, which might be expected to occur with increased crowding at higher coverages.

Finally, as was the case for benzene adsorbed on Rh(111), we can gain some insight in the nature of the surface chemical bond of the α-pyridyl species on Rh(111) from the shifts of observed HREELS frequencies as compared to those of liquid pyridine and those reported for the $HOs_3(CO)_{10}(NC_5H_4)$, α-pyridyl complex [12a]. First, the 750 and 840 cm^{-1} modes the α-pyridyl/Rh(111) species, which correspond to ν_{25} and ν_{26} of liquid pyridine, are strongly shifted upward from the liquid pyridine frequencies of 700 and 744 cm^{-1} and $HOs_3(CO)_{10}(NC_5H_4)$ frequencies of 758, 745, and 740 cm^{-1}. Second, the CH stretching frequencies (~3010 cm^{-1}) is strongly shifted downward from those of liquid pyridine (~3060 cm^{-1}). As discussed earlier, similar shifts in frequency are observed for similar modes of benzene adsorbed on Rh(111), suggesting that the α-pyridyl species is rehybridized more toward sp^3 than sp^2. Such a rehybridization would be possible if

there is an interaction of the π-orbitals of the α-pyridyl species with the surface. Evidence for such an interaction from electronic spectroscopy is discussed in the following section.

4.4. Electronic Excitations

4.4.1 Benzene/Rh(111)

Figure 4.6 shows the electronic energy loss spectra for multilayers of benzene and for the ordered benzene and benzene plus CO monolayers on the Rh(111) surface. The incident beam energy for these spectra was near 20 eV and the resolution was 15 meV, which is about equal to the width of the figure border. At this beam energy and resolution, the elastic peak intensity was generally too intense to measure accurately due to saturation of our counting electronics. Consequently, we have plotted the absolute intensity of the energy loss features, rather than relative intensities scaled to the intensity of the elastic peak as was done for the vibrational spectra.

The bottom part of Fig. 4.6 shows the electronic EEL spectrum for several multilayers of benzene on the Rh(111) surface at 77 K. For the free benzene molecule, the low energy excitations result from the promotion of an electron from the highest occupied π (e_{1g}) orbital to the lowest unoccupied π* (e_{2u}) orbital. The four-fold degeneracy of this transition is split by electron-electron repulsion to give the $^{1,3}B_{1u}$, $^{1,3}B_{2u}$, and $^{1,3}E_{1u}$ excited states. For gas phase benzene [31], the $^{3}B_{1u} \leftarrow {}^{1}A_{1g}$, $^{1}B_{2u} \leftarrow {}^{1}A_{1g}$, $^{3}E_{1u} \leftarrow {}^{1}A_{1g}$, $^{1}B_{1u} \leftarrow {}^{1}A_{1g}$, and $^{1}E_{1u} \leftarrow$

$^1A_{1g}$ transitions are observed, respectively, at 3.9, 4.92, 4.85, 6.2, and 6.95 eV. As shown in Table 4.3, the electronic transitions centered at 4.0, 4.8, 6.2, and 6.8 eV in benzene multilayer spectrum agree well with those of gas phase benzene.

The upper part of Fig. 4.6 shows the electronic EEL spectra for the three ordered structures of benzene and benzene plus CO on the Rh(111) surface at 310 K. The striking feature of these spectra is the absence of the π to π^* transitions that are readily observable for the multilayer spectrum. The absence of π to π^* transitions in electronic spectra has been reported for aromatics chemisorbed on other metal surfaces: Pd(111) [16], Pt(111) [32], Ir(111) [13], Ni(111) [15], and Ni(100) [11]. While this absence has been proposed to be due to screening effects [13,32], Avouris and Demuth [33] have pointed out, however, that the ability of these metal surfaces to screen electronic transitions is comparable to that of Ag(111) where the electronic transitions are clearly observed for physisorbed benzene [14]. Instead, Avouris and Demuth have proposed that the absence is directly related to the nature of the strong chemisorption bond that benzene forms with metal surfaces. Since benzene bonds to metal surfaces through its π-orbitals [7], the π levels can become very broad in energy due to mixing with the surface states. Consequently, $\pi \gg \pi^*$ excitations will not be observed if the levels are sufficiently broadened.

The spectra for chemisorbed benzene and benzene plus CO in Fig. 4.6 are shown in comparison to that of the clean Rh(111) surface. For the bare surface, there is a relatively strong excitation centered at 0.7 eV, which we attribute to transitions to rhodium surface states, since it is very sensitive to the presence of adsorbates. Also, a weak, broad excitation is centered at 5.6 eV, which we assign to interband transitions of bulk rhodium [34]. When benzene or benzene plus CO is adsorbed on Rh(111), the 0.7 eV excitation is slightly reduced and shifted in energy and there is now extra intensity in the region from 2 eV to 6 eV. Since the extra intensity in the 2 eV to 6 eV region does not occur for CO adsorbed alone on Rh(111), we assign it to excitations related to chemisorbed benzene. Similar low energy (1 eV to 5 eV) electronic excitations have been observed for aromatics adsorbed on Ag(111) [14], Ni(100) [11], Pt(111) [16] and Ir(111) [13] and have generally been ascribed to a metal → molecule charge-transfer excitation [33], (i.e., an electron is excited from a metal state to a benzene molecular state). Interestingly, all the ordered structures of benzene on Rh(111) appear to have the same charge-transfer excitation, even though the shape of the excitation is somewhat different in the different structures.

4.4.2 Pyridine/Rh(111)

For pyridine adsorption on the Rh(111) surface, electronic EELS was only done for the $(2\sqrt{3}x3)$rect structure. The resulting spectrum is shown in Fig. 4.7 and is compared to that of the clean Rh(111)

surface. The spectrum is similar to that observed for chemisorbed benzene on Rh(111) in that the $\pi \rightarrow \pi^*$ excitations are absent and there is extra intensity in the region from 2 eV to 5 eV. We interpret the absence of $\pi \rightarrow \pi^*$ excitations as indicating that the π-orbitals are involved in the bonding of the α-pyridyl species to the Rh(111) surface and the extra intensity as corresponding to charge-transfer excitations.

4.5 Optical Second-Harmonic Generation (SHG) from Benzene and Pyridine on Rh(111)

We have also monitored benzene and pyridine adsorption on the Rh(111) surface using optical second-harmonic generation. The experimental setup for these experiments is described in detail in Chapter 2. It should be noted, however, that the SHG experiments were actually performed before the other experiments described in this chapter and a different manipulator was used which was unable to translate the sample into the HREEL spectrometer. Two incident wavelengths were used, 1.06μm and 532 nm, corresponding to photon energies of 1.17 and 2.34 eV, respectively. So the second-harmonic generated photons have energies of 2.34 eV for the 1.06μm incident wavelength and 4.68 eV for the 532 nm incident wavelength.

In Fig. 4.8, we show how the SH signal for the Rh(111) surface varied as the surface was continuously exposed to benzene. For the 532 nm excitation wavelength, the SH signal is constant for the first 0.68 Langmuirs, then drops from the normalized bare metal value of 1

to the saturation value of 0.44 at about 4.0 Langmuirs of benzene. A $(2\sqrt{3}x3)$rect LEED pattern was often observed for exposures greater than 4.0 Langmuirs. For the 1.06μm excitation, the SH signal dips slightly to 0.84 of original bare metal value before returning to the bare metal value.

To interpret the SHG results, it is convenient to express the surface nonlinear susceptibility in the form [35]

$$\chi^{(2)}_{surface} \propto \sum_{gmm'} \left\{ \frac{\langle g|r_i|n\rangle\langle n|r_j|n'\rangle\langle n'|r_K|g\rangle}{(2\omega-\omega_{ng}+i\Gamma_{ng})(\omega-\omega_{n'g}+i\Gamma_{n'g})} + \text{seven other similar terms} \right\}$$

where the $\langle g|r_i|n\rangle$ terms are the dipole matrix elements for the electronic transitions (i.e., transitions from one metal state to another metal state, from one molecular state to another molecular state, or from a metal (molecular) state to a molecular (metal) state. From this expression, it is apparent that $\chi^{(2)}_{surface}$ and, hence, the SH signal will be resonantly enhanced when $\hbar\omega$ and/or $\hbar(2\omega)$ are in resonance with electronic transitions of the surface.

So, as can be seen from the electronic ELS spectrum for the $(2\sqrt{3}x3)$rect benzene structure (Fig. 4.5), the second harmonic for λ_{ex} = 532 nm, 4.68 eV, is in resonance with the center of the band of charge-transfer excitations, while the fundamental, 2.34 eV, is slightly off resonance and lies in the low energy tail of this band. Consequently, the contribution to the SH signal generated by transitions between metal states and molecular states (charge-transfer excitations) will be resonantly enhanced for λ_{ex} = 532 nm and, if

opposite in phase, will tend to cancel the contribution to the SH signal from the bare metal surface, resulting in the observed reduction in the SH signal.

For λ_{ex} = 1.06 μm, the fundamental, 1.17 eV, lies in the high energy tail of the surface excitation centered at 0.7 eV, while the second harmonic, 2.34 eV, lies in low energy tail of the band of charge-transfer excitations for adsorbed benzene. The slight dip in the SH signal for λ_{ex} = 1.06 μm during the benzene exposure may be due to changes that occur in the 0.7 eV electronic peak as well as the growth in the charge-transfer excitations as the benzene coverage increases. It is possible, that the contribution from the changes in the 0.7 eV electronic peak may tend to cancel that from the charge-transfer excitations at higher benzene coverages, resulting in the return to the bare metal value observed at saturation coverage.

The initial plateau of the SH signal for λ_{ex} = 532 nm can be explained with the help of the results of Koel et al., [4] who have studied benzene adsorption on Rh(111) as a function of coverage using REELS, LEED, and TDS. Based on subtle changes that occur in the HREEL spectra with increasing benzene coverage, Koel et al. concluded that, at low coverages, benzene bonds at one type of adsorption site while, at higher coverages, a second adsorption site becomes occupied. If the charge-transfer excitations for benzene bonded at the low coverage adsorption site are off resonance with the SH signal, then the SH signal will be relatively constant until the second adsorption site starts to become occupied at higher coverages.

Figure 4.9 shows the SHG results for pyridine adsorption on the Rh(111) surface. For λ_{ex} = 532 nm, the sample temperature was 275 K. We attribute the steady drop in the SH signal for λ_{ex} = 532 nm to the fundamental and second harmonic being resonant with the band of charge-transfer excitations, which we observed by electronic EELS between 1.5 eV and 5 eV for the α-pyridyl species (Fig. 4.7). Therefore, the decrease in the λ_{ex} = 532 nm SH signal for pyridine adsorption has a similar physical origin as the decrease in the λ_{ex} = 532 nm SH signal observed for benzene adsorption.

For λ_{ex} = 1.06 μm, the sample temperature ranged from 275 K at the start of the pyridine exposure to 235 K at the end of the pyridine exposure. Since at 235 K HREELS indicates both a physisorbed and a chemisorbed pyridine species are present, the SH signal cannot be interpreted unambiguously. We note, however, that the changes in the λ_{ex} = 1.06 μm SH signal are smaller than those for λ_{ex} = 532 nm, similar to what was observed for benzene adsorption on Rh(111).

4.6 Conclusions

In this study of benzene and pyridine adsorbed on Rh(111), HREELS has been used for both vibrational and electronic spectroscopy. From the vibrational spectra, benzene is determined to bond molecularly intact at room temperature (310 K) with ring parallel to the surface. At this temperature, pyridine bonds with its ring intact and somewhat tilted with respect to the surface. TDS indicates, however, that some decomposition of pyridine occurs at 310 K; consequently, we propose that pyridine forms an

α-pyridyl species when adsorbed on Rh(111) at 310 K. In the 185 to 230 K temperature range, HREELS and TDS indicate that a physisorbed pyridine species is coadsorbed with the α-pyridyl species.

In the electronic spectra, only excitations due to a charge-transfer band are observed for benzene and pyridine adsorbed at 310 K. The absence of observed $\pi \rightarrow \pi^*$ transitions implies that the π-orbitals are strongly involved in the chemisorption bond for these adsorbates. Optical second-harmonic generation has been used to monitor benzene and pyridine adsorption on Rh(111); the resulting second harmonic signal is interpreted with the aid of the electronic spectra.

A $(2\sqrt{3}x3)$rect LEED pattern is observed for both benzene and pyridine adsorption on Rh(111) at 310 K. The presence of a glide plane symmetry for the benzene structure allows a model for this structure to be proposed with benzene centered over bridge sites. No ordered structures are observed for CO coadsorbed with pyridine on Rh(111). CO-induced ordering of benzene on Rh(111) as well as on Pt(111) is discussed in the next chapter.

REFERENCES

1. R.F. Lin, R.J. Koestner, M.A. Van Hove, and G.A. Somorjai, Surface Sci. 134 (1983) 161.
2. M.A. Van Hove, R.F. Lin, and G.A. Somorjai, Phys. Rev. Lett. 51 (1983) 778.
3. B.E. Koel and G.A. Somorjai, J. Electron Spectrosc. 29 (1983) 287.
4. B.E. Koel, J.E. Crowell, C.M. Mate, and G.A. Somorjai, J. Phys. Chem. 88 (1984) 1988; this paper contains a review of vibrational spectroscopy of benzene on metal surfaces.
5. C.M. Mate and G.A. Somorjai, Surface Sci. 160 (1985) 542.
6. M.A. Van Hove, R.F. Lin, and G.A. Somorjai, J. Am. Chem. Soc. 108 (1986) 2532; and to be published.
7. M. Neumann, J.U. Mack, E. Bertel, and F.P. Netzer, Surface Sci. 155 (1985) 629.
8. E. Bertel, G. Rosina, and F.P. Netzer, Surface Sci. 172 (1986) L515.
9. E.L. Garfunkel, C. Minot, A. Gavezzotti, and M. Simonetta, Surface Sci. 167 (1986) 177.
10. J.E. Demuth, K. Christmann, and P.N. Sanda, Chem. Phys. Lett. 76 (1980) 201.
11. N.J. DiNardo, Ph. Avouris, and J.E. Demuth, J. Chem. Phys. 81 (1984) 2169.
12. a. V.H. Grassian and E.L. Muetterties, J. Phys. Chem., in press;
    b. V.H. Grassian and E.L. Muetterties, submitted.

13. F.P. Netzer, E. Bertel and J.A.D. Mathew, Surface Sci. 92 (1980) 43.

14. Ph. Avouris and J.E. Demuth, J. Chem. Phys. 75 (1981) 4783.

15. H.J. Robota, P.M. Whitmore and C.B. Harris, J. Chem. Phys. 76 (1982) 1692.

16. F.P. Netzer and J.U. Mack, J. Chem. Phys. 79 (1983) 1017.

17. Ph. Avouris, N.J. DiNardo, and J.E. Demuth, J. Chem. Phys. 80 (1984) 491.

18. A.L. Johnson, E.L. Muetterties, J. Stohr, and F. Sette, J. Phys. Chem. 89 (1985) 4071.

19. M. Bader, J. Hasse, K.-H. Frank, A. Puschmann, and A. Otto, Phys. Rev. Lett. 56 (1981) 1921.

20. F.G. Ciapetta and D.N. Wallace, Catal. Rev. 5 (1972) 67.

21. Buckley Book

22. T. Shimanouchi, Tables of Molecular Vibrational Frequencies, Consolidated Vol. I, NSRDS-NBS39; Vol. II, J. Chem. Ref. Data 6 (1977) 993.

23. G. Herzberg, Molecular Spectra and Molecular Structure II, Infrared and Raman Spectra of Polyatomic Molecules, Van Nostrand, Princeton, NJ, 1945.

24. H. Jobic, J. Tomkinson, J.P. Candy, P. Fouilloux, and A.J. Renouprez, Surface Sci. 95 (1980) 496.

25. G.D. Waddill and L.L. Kesmodel, Phys. Rev. B31 (1985) 4940.

26. H. Ibach and D.L. Mills, Electron Energy Loss Spectroscopy and Surface Vibrations, Academic Press, New York, 1982, pp. 195-7.

27. H.F. Efner, D.E. Tevault, W.B. Fox, and R.R. Smardzewski, J. Organomet. Chem. 146 (1978) 45.

28. J.T. Yates, Jr., P.A. Thiel, and W.H. Weinberg, Surface Sci. 84 (1979) 427.

29. B.E. Koel, J.E. Crowell, B.E. Bent, C.M. Mate, and G.A. Somorjai, J. Phys. Chem. 90 (1986) 2949.

30. K.B. Wiberg, V.A. Walters, K.N. Wong, and S.D. Colson, J. Phys. Chem. 88 (1984) 6067.

31. J.P. Doering, J. Chem. Phys. 67 (1977) 4065.

32. F.P. Netzer and J.A.D. Mathew, Solid State Commun. 29 (1979) 209.

33. Ph. Avouris and J.E. Demuth, Surface Sci. 158 (1985) 21.

34. J.H. Weaver, C.G. Olson, and D.W. Lynch, Phys. Rev. B15 (1977) 4115.

35. Y.R. Shen, The Principles of Nonlinear Optics, Wiley, New York, 1984, pp. 17.

Table 4.1. Assignment of observed vibrational frequencies (cm^{-1}) for benzene chemisorbed on Rh(111) in the $(2\sqrt{3}x3)$rect structure.

Gas Phase Frequencies [22] C_6H_6 (C_6D_6)	Chemisorbed Frequencies C_6H_6 (C_6D_6)	Mode Type	Gas Phase Mode No. (Symm. Representation) [23]
out-of-plane modes			
—	345 (340)	RhC stretch (ν_{Rh-C})	—
—	545 (not obs.)	RhC stretch (ν_{Rh-C})	—
673 (497)	775 (580)	CH bend (γ_{CH})	4 (A_{2u})
849 (662)	805 (645)	CH bend (γ_{CH})	11 (E_{1g})
in-plane-modes			
992 (943)	not obs. (845)	ring stretch (ν_{CC})	2 (A_{1g})
1150 (824)	1115 (845)	CH bend (δ_{CH})	10 (B_{2u})
1310 (1286)	1330 (1210)	ring stretch (ν_{CC})	9 (B_{2u})
1486 (1335)	1430 (1365)	ring str. and deform (δ_{CC})	13 (E_{1u})
3062 (2293)	2970 (2260)	CH stretch (ν_{CH})	1 (A_{1g})

Table 4.2. Assignment of observed vibrational frequencies (cm^{-1}) for pyridine adsorbed on Rh(111).

$(2\sqrt{3}x3)$rect Pyridine/Rh(111) $NC_5H_5(NC_5D_5)$	Multilayer Pyridine/Rh(111)	Liquid Phase Frequencies [30] $NC_5H_5(NC_5D_5)$	Liquid Phase Mode No. (Symm. Representation) [30]
345 (345)		—	pyridine-Rh
465 (425)	410	403 (367)	27 (B_2)
635 (635)		601 (579)	10 (A_1)
		652 (625)	19 (B_1)
750 (565)		700 (526)	26 (B_2)
	730		
840 (725)		744 (631)	25 (B_2)
		936 (765)	24 (B_2)
		991 (963)	9 (A_1)
1025 (825)	1000	1007 (828)	23 (B_2)
(990)		1032 (1014)	8 (A_1)
		1072 (823)	7 (A_1)
		1079 (835)	18 (B_1)
1130 (825)		1143 (856)	17 (B_1)
1240 (825)	1220	1218 (882)	6 (A_1)
(1240)		1227 (1226)	16 (B_1)
		1362 (1046)	15 (B_1)
1420 (1325)	1450	1442 (1303)	14 (B_1)
		1483 (1340)	5 (A_1)
1550 (1485)	1590	1581 (1546)	13 (B_1)
		1583 (1554)	4 (A_1)
		3030 (2268)	3 (A_1)
3010 (2240)	3060	3042 (2256)	12 (B_1)
		3087 (2289)	11 (B_1)
		3094 (2302)	1 (A_1)

Table 4.3. Electronic excitation energies (in eV) for gas phase benzene and multilayers of benzene on Rh(111).

Transitions	Gas phase [31]	Benzene multilayers on Rh(111)
$^3B_{1u} \leftarrow {}^1A_{1g}$	3.9	4.0
$^1B_{2u} \leftarrow {}^1A_{1g}$	4.92	4.8
$^3E_{1u} \leftarrow {}^1A_{1g}$	4.85	4.8
$^1B_{1u} \leftarrow {}^1A_{1g}$	6.2	6.2
$^1E_{1u} \leftarrow {}^1A_{1g}$	6.95	6.8

FIGURE CAPTIONS

Fig. 4.1 Proposed arrangement of benzene in the $(2\sqrt{3}x3)$rect unit cell in Rh(111). Gas phase Van der Waals dimensions are shown. The dashed lines indicate the location of the glide planes.

Fig. 4.2 Vibrational spectra obtained by HREELS in the specular direction for benzene chemisorbed in Rh(111) in an ordered $(2\sqrt{3}x3)$rect structure: a) C_6H_6 b) C_6D_6. The lines indicate how the CH vibrational modes shift with deuteration. The C-O stretching modes are from $\leq$ 1/1000 of a monolayer of coadsorbed CO.

Fig. 4.3 Thermal desorption spectra of NC_5H_5 (Amu 79) and D_2 (Amu 4) following a large exposure to NC_5H_5 or NC_5D_5 on Rh(111) at 80 K.

Fig. 4.4 Vibrational spectra obtained by HREELS in the specular direction for multilayers of pyridine on Rh(111) and after momentarily heating to the indicated temperatures. The spectra were taken with a sample temperature of 77 K for spectra a, b, c, and d, and of 310 K for spectra e.

Fig. 4.5 Vibrational spectra for pyridine adsorbed on Rh(111) at 310 K.

Fig. 4.6 Electronic energy loss spectra for benzene and benzene plus CO on Rh(111). The dashed curves show the spectrum of the clean Rh(111) surface for comparison. The resolution is 15 meV.

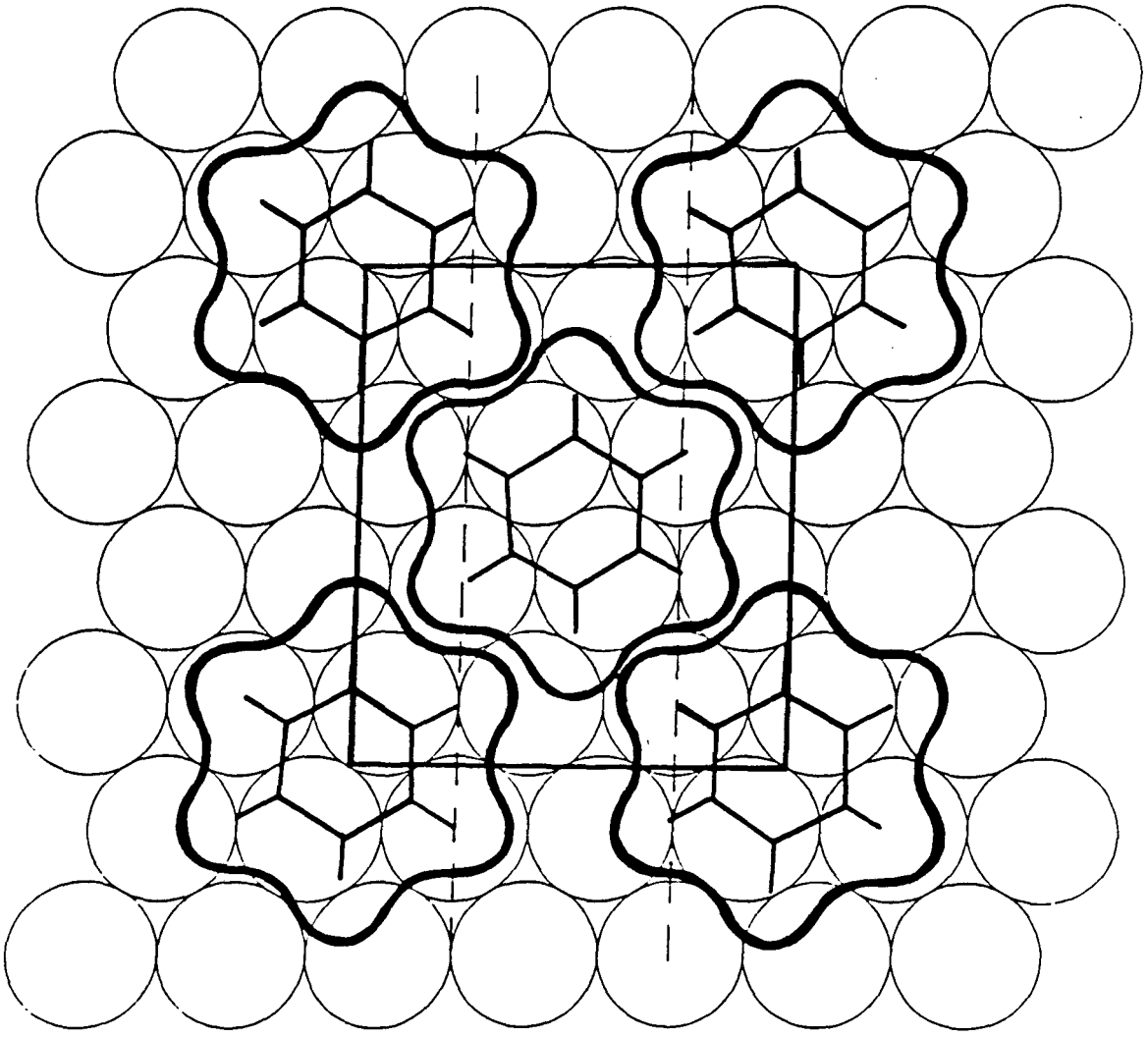

Rh(111)+(2√3x3)rect C_6H_6

XBL 852-1410

Figure 4.1

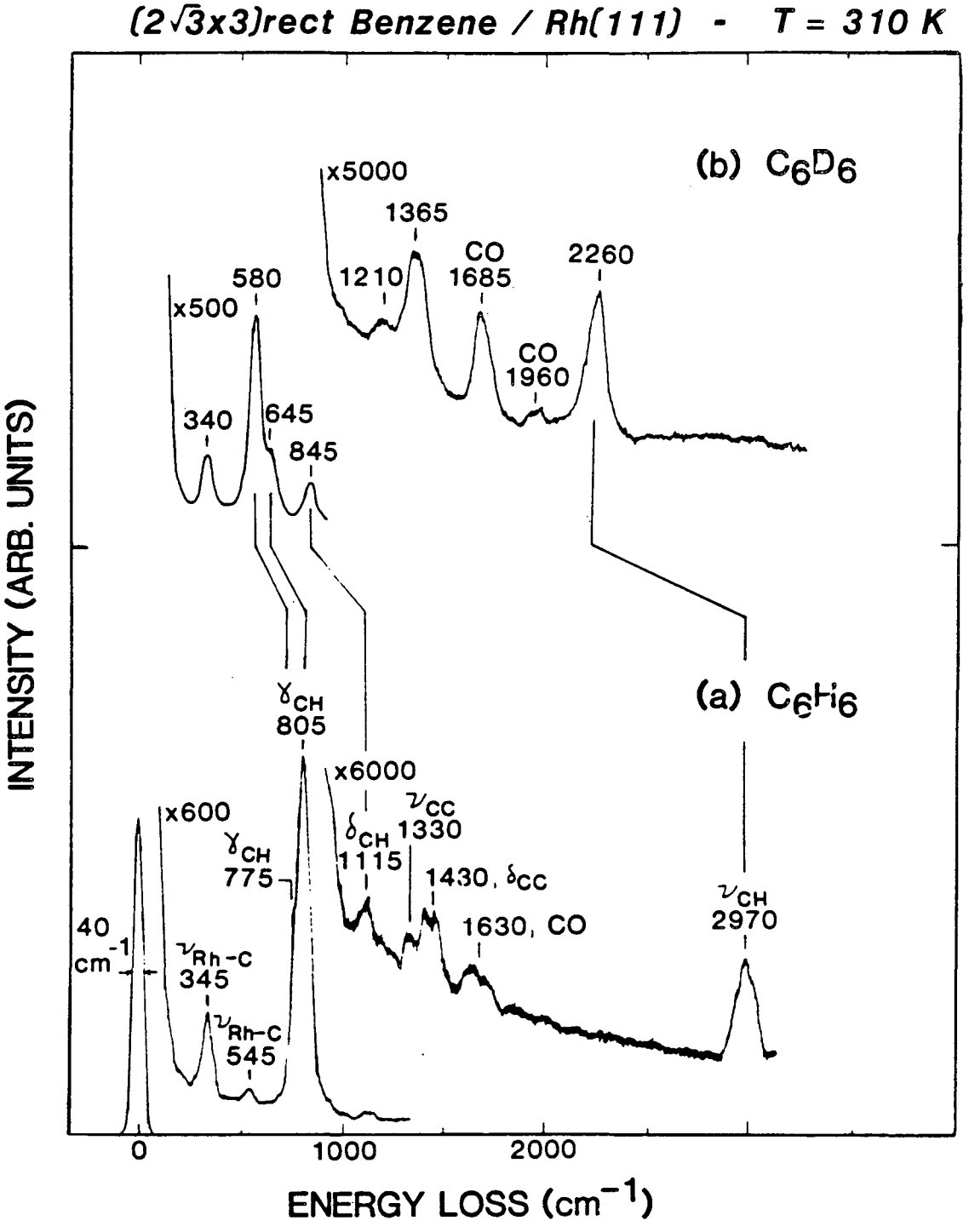

XBL 869-3434

Figure 4.2

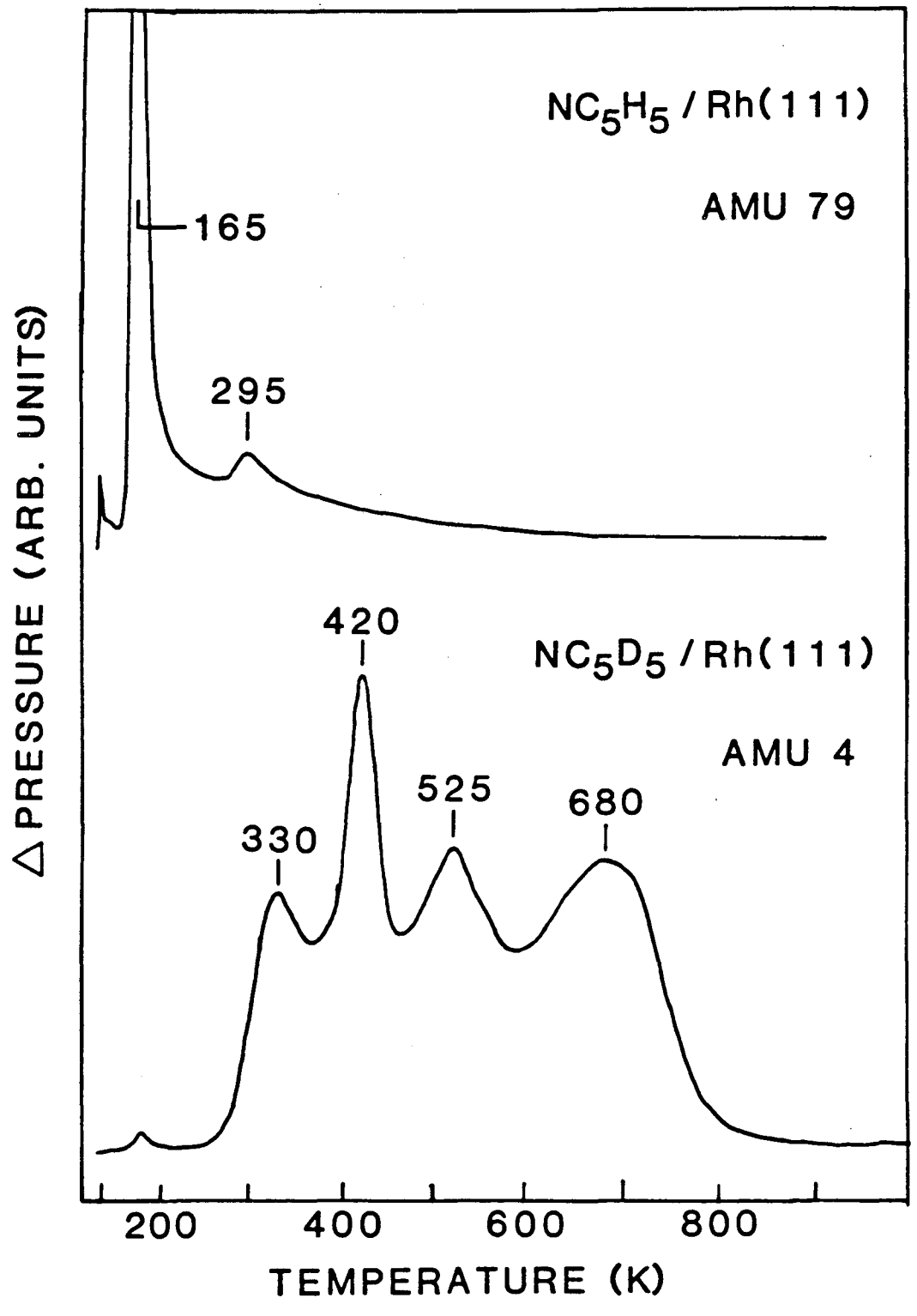

XBL 869-3421

Figure 4.3

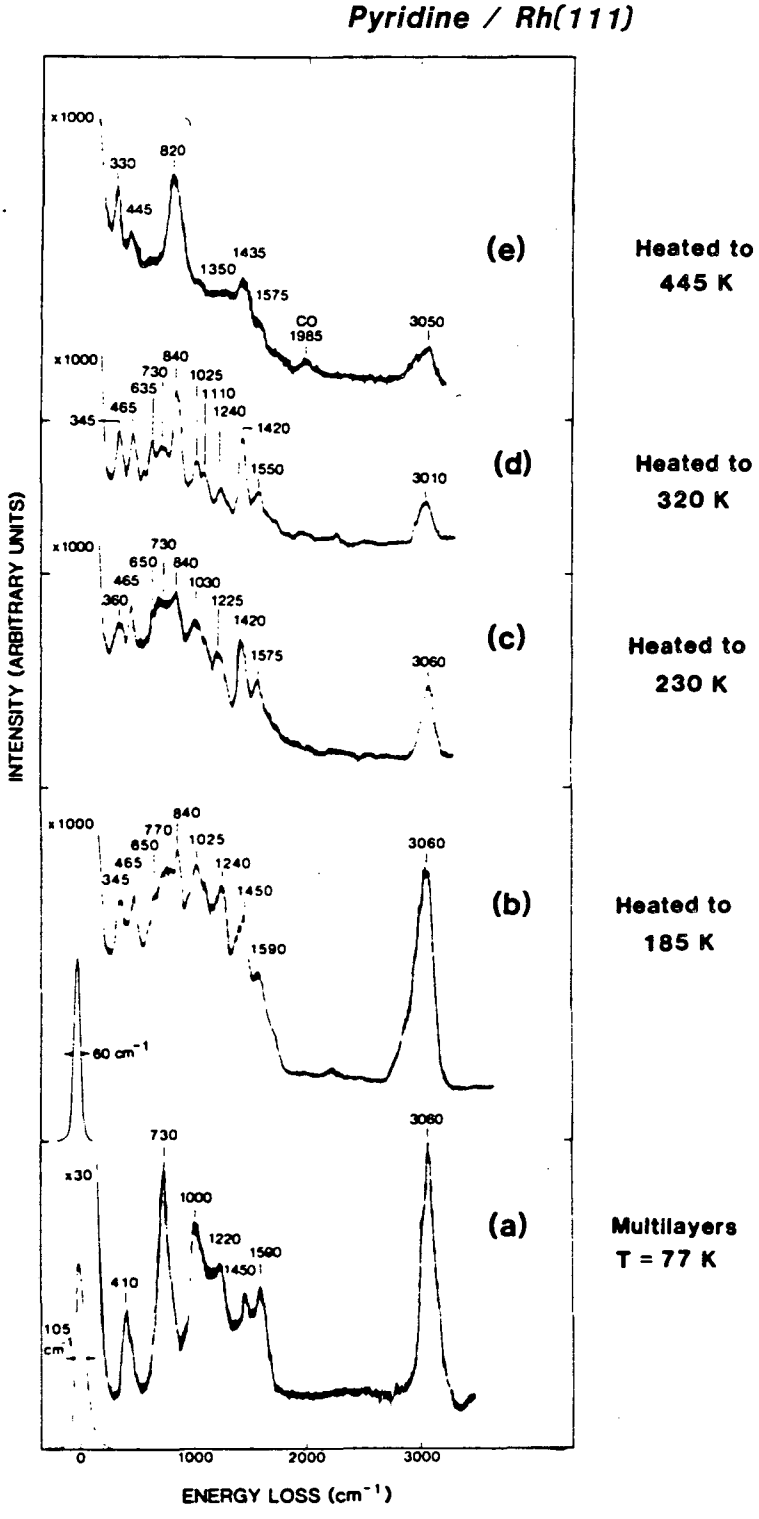

XBL 869-3436

Figure 4.4

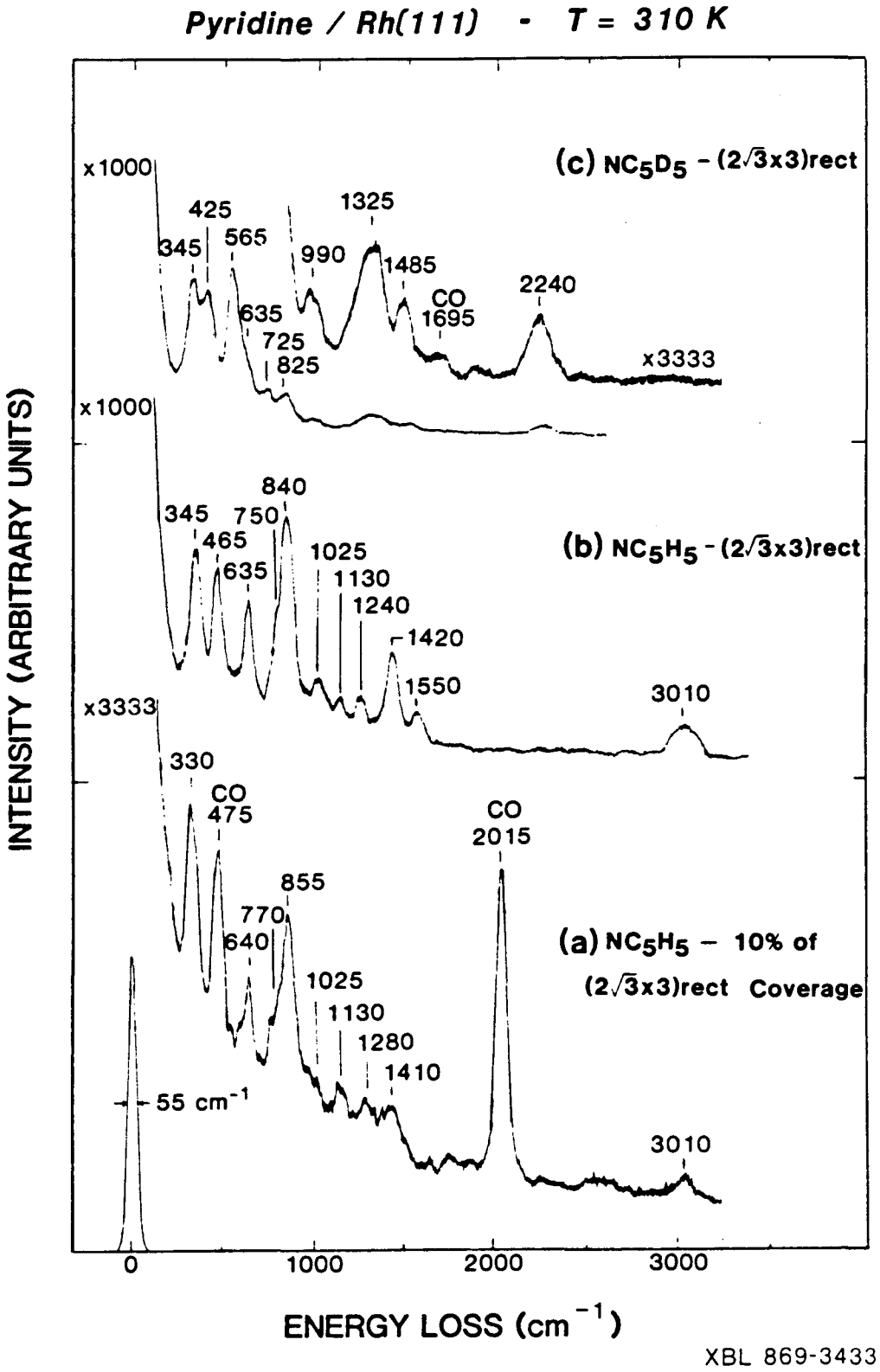
Pyridine / Rh(111) - T = 310 K
(c) NC5D5 - (2√3x3)rect
x1000
425
345
565
1325
990
1485
CO
1695
2240
635
725
825
x3333
x1000
840
345
750
465
635
1025
1130
1240
1420
1550
3010
(b) NC5H5 - (2√3x3)rect
x3333
330
CO
475
CO
2015
855
770
640
1025
1130
1280
1410
55 cm-1
3010
(a) NC5H5 - 10% of
(2√3x3)rect Coverage
INTENSITY (ARBITRARY UNITS)
0
1000
2000
3000
ENERGY LOSS (cm-1)
XBL 869-3433

Figure 4.5

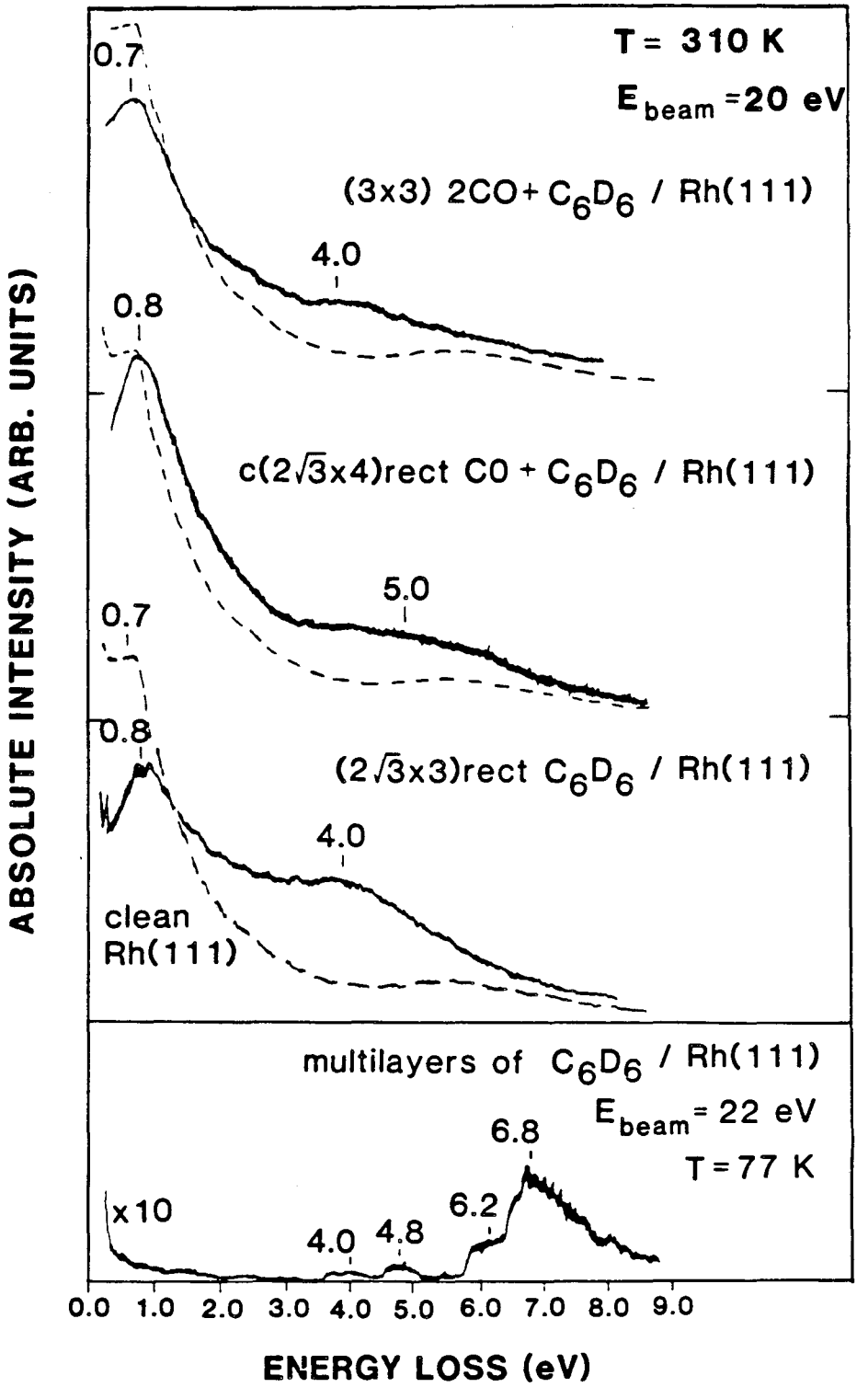

XBL 869-3423

Figure 4.6

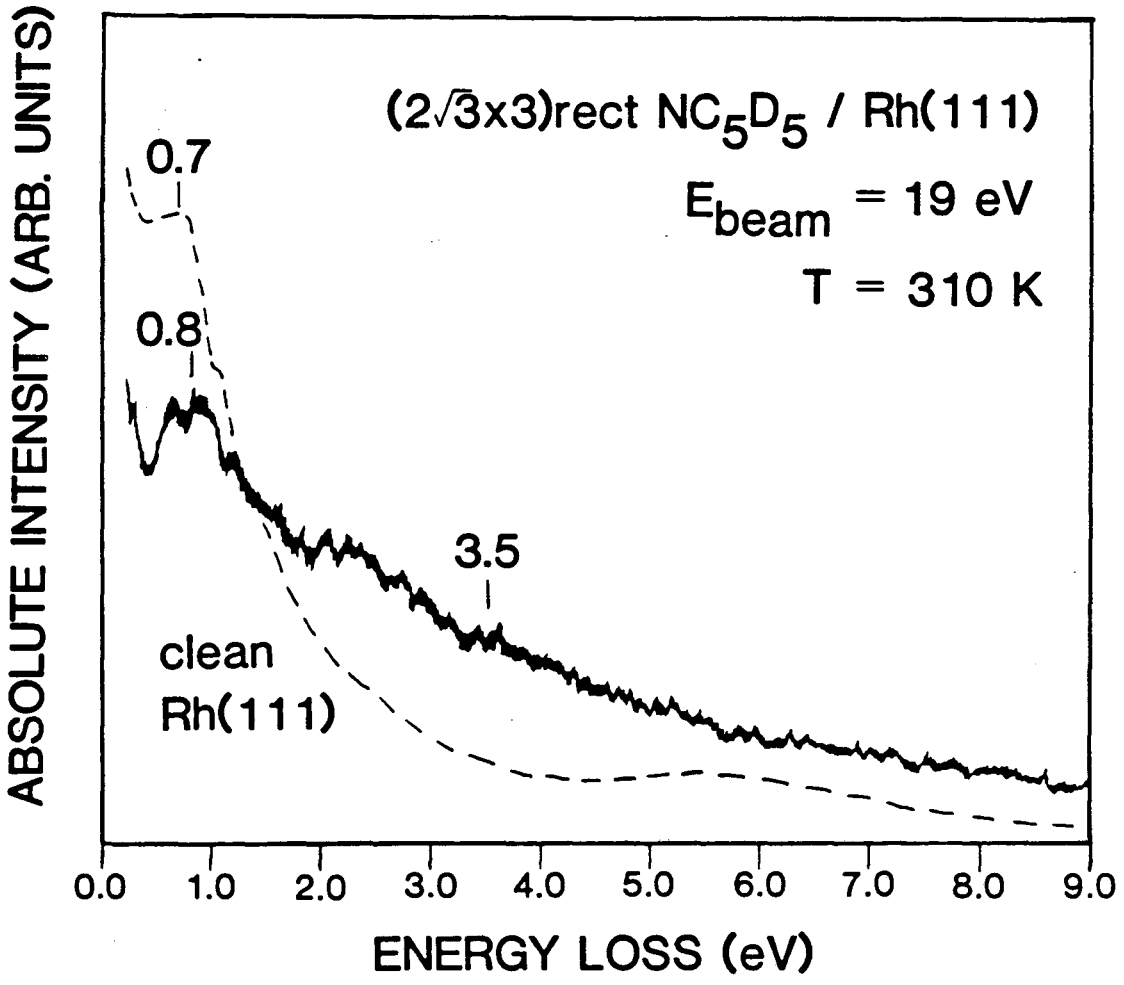

XBL 869-3422

Figure 4.7

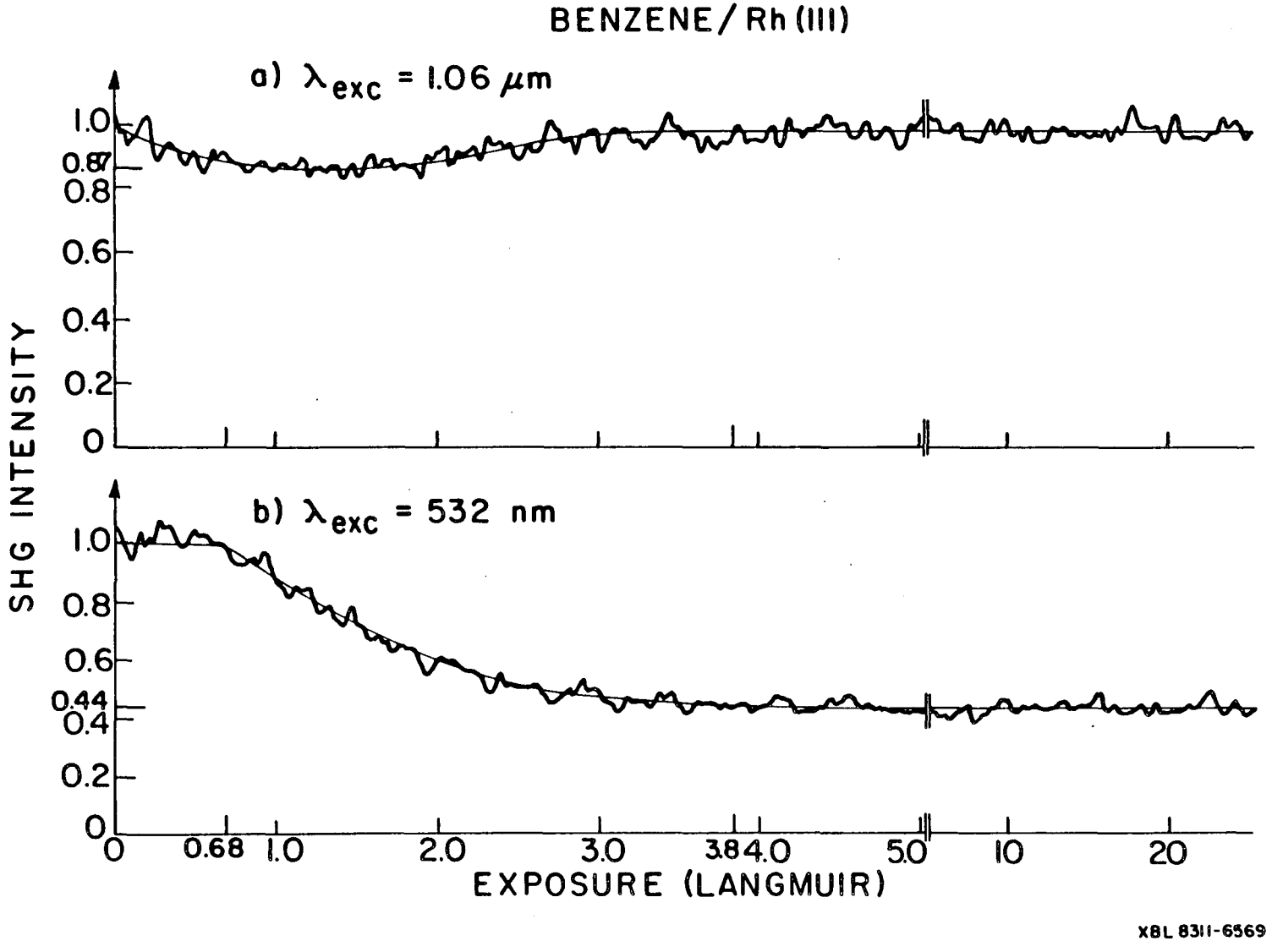
BENZENE / Rh (III)
a) λ_{exc} = 1.06 μm
b) λ_{exc} = 532 nm
SHG INTENSITY
1.0
0.87
0.8
0.6
0.4
0.2
0
0.44
0.68
1.0
2.0
3.0
3.8
4.0
5.0
10
20
EXPOSURE (LANGMUIR)
X8L 8311-6569

Figure 4.8

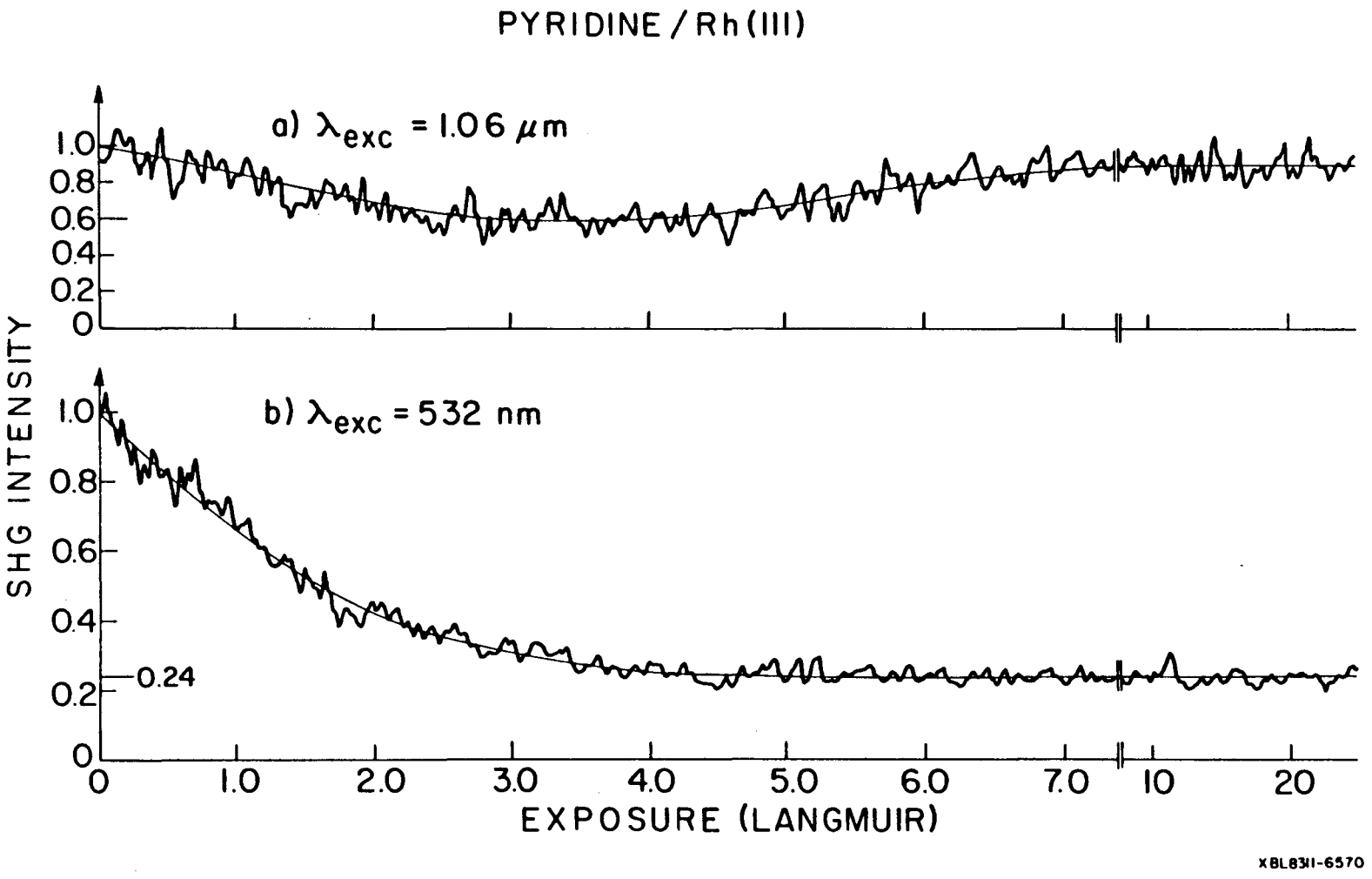
PYRIDINE / Rh(III)
a) λexc = 1.06 μm
b) λexc = 532 nm
SHG INTENSITY
1.0
0.8
0.6
0.4
0.2
0
0.24
0
1.0
2.0
3.0
4.0
5.0
6.0
7.0
10
20
EXPOSURE (LANGMUIR)
XBL8311-6570

Figure 4.9

CHAPTER 5

Carbon Monoxide Induced Ordering of Adsorbates: I. Benzene on Pt(111) and Rh(111)

Contents

5.1. Introduction

In recent years, crystallography by low-energy electron diffraction (LEED) has been a very successful technique for determining the surface structure of ordered monolayers of small molecular adsorbates on single crystal surfaces [1], However, surface structure determination of larger organic molecules by LEED has been limited since these organic adsorbates frequently do not form ordered overlayers readily on surfaces. Although a new method has recently been demonstrated [2] for using LEED to determine the structure of disordered overlayers, LEED crystallography of ordered overlayers will probably remain the more practical way of determining the structure of adsorbates on surfaces.

This chapter reports how a particular organic adsorbate, benzene, can be induced into several ordered lattices by the coadsorption with CO on the Pt(111) and Rh(111) crystal surfaces. The following chapter discusses CO-induced ordering of a variety of adsorbates on the Rh(111) surface. On Pt(111), ordering in the adsorbed benzene layer does not occur in the absence of coadsorbed CO. Therefore, CO induced ordering enables us to determine the surface structure of benzene on Pt(111) by a dynamical LEED analysis. On Rh(111), benzene orders at saturation coverage into a $(2\sqrt{3} \times 3)$rect structure without coadsorbed CO, but orders differently with coadsorbed CO. The formation of CO-induced ordered structures on both Pt(111) and Rh(111) illustrates that this effect is not restricted to one metal surface. CO-induced ordering of

benzene on these surfaces can be explained by the interactions between adsorbed CO molecules in the presence of coadsorbed benzene. Therefore, by coadsorbing an ordering agent such as carbon monoxide with organic adsorbates, it should become possible to determine the structure of the resulting ordered overlayers by a LEED analysis.

The ordered structures of CO and benzene on Pt(111) and Rh(111) were studied using low-energy electron diffraction (LEED), high-resolution electron energy loss spectroscopy (HREELS), and thermal desorption spectroscopy (TDS). From the LEED patterns, the periodicity and symmetry of the ordered structures are deduced. The integrity and orientation of the CO and benzene within the ordered structures are determined from HREEL spectra. The relative coverages of CO and benzene within the various unit cells are determined by TDS. Using the information obtained from these three techniques, we propose geometries for the ordered structures of benzene plus CO on Pt(111) and Rh(111), which, in most details, agree with the structures determined by a subsequent dynamical LEED analyses.

Within these structures, we find that CO molecules prefer to adsorb at bridge and hollow sites rather than at top sites as on clean Pt(111) and Rh(111) surfaces. This shift in CO sites can result from both blocking of top sites by benzene molecules and charge transfer via the substrate to the $2\pi^*_{CO}$ orbital. We also find that benzene adsorbed on Rh(111) shifts from bridge to hollow sites when coadsorbed with CO.

5.2. Results

5.2.1 $CO/C_6H_6/Pt(111)$

The adsorption of benzene on Pt(111) has been studied previously by several researchers [3,4,5]. Gland and Somorjai reported in 1973 the observation of two LEED patterns [4], which can be labeled $(2\sqrt{3}x4)$rect and $(2\sqrt{3}x5)$rect, after exposing a Pt(111) surface to large doses of benzene ($\geq$50L). The notation $(2\sqrt{3}x4)$rect means that the overlayer orders in a rectangular superlattice and the lattice spacing is $2\sqrt{3}$ by 4 times the substrate nearest neighbor distance. We were able to reproduce the two LEED structures reported by Gland and Somorjai by similar large exposures of benzene. However, HREEL spectra indicated a significant amount of CO had coadsorbed on the surface from the vacuum background gases during the large exposures to benzene. We were also able to form these LEED structures by simply adding CO to a Pt(111) surface precovered with a disordered saturation coverage of benzene. CO exposures between 0.1L and 0.5L induced a well ordered $(2\sqrt{3}x4)$rect pattern. Between 0.5L and 1.0L of CO, the LEED pattern transformed from a $(2\sqrt{3}x4)$rect pattern to a $(2\sqrt{3}x5)$rect pattern by a continual splitting of the LEED spots. Continued exposure of the $(2\sqrt{3}x5)$rect structure to CO gas eventually caused it to disorder after 5L CO and completely displaced benzene from the Pt(111) surface after 20L. During our experiments, no LEED patterns of benzene on Pt(111) were observed without coadsorbed CO except for a dis-

ordered ring pattern at saturation coverage similar to that observed by other workers [3,5].

Figure 5.1 shows vibrational spectra obtained by HREELS in the specular direction for a disordered monolayer of pure benzene on Pt(111) and for the two different ordered monolayers of CO coadsorbed with a saturation coverage of benzene. In these experiments, the Pt(111) sample was maintained at 300 K during the adsorption of benzene and carbon monoxide and then cooled to 77 K during the HREELS measurements. HREEL spectra taken at 300 K are the same as those at 77 K in Fig. 1 except in the C-O stretching region. At 300 K, the loss at ~2030 cm^{-1} does not occur for CO exposures less than 1.5L, and the two losses at ~1700 cm^{-1} and ~1800 cm^{-1} appear as one broad loss. The LEED patterns do not change when the sample is cooled from 300 K to 77 K except for a reduction in background intensity.

The assignment of the vibrational frequencies for benzene chemisorbed on Pt(111) is given in Table 5.1. This assignment differs slightly from that of Lehwald et al [4] where the loss at ~1420 cm^{-1} was assigned to the ν_9 of benzene and the shoulder at 930 cm^{-1} was assigned to a ν_4 vibration of benzene at a different adsorption site. Our assignment of the 930 cm^{-1} mode is consistent with that of Waddill and Kesmodel [8b], who have recently suggested that the two losses in the region 750 - 950 cm^{-1} can be interpreted as the ν_4 and ν_{11} modes of benzene bonded to bridge sites rather than to the ν_4 mode of benzene bonded at two different types of sites. While we prefer this interpretation since it is consistent with LEED results that ben-

zene bonds at bridge sites in the ordered structures on Pt(111), it does not rule out the alternate interpretation of two benzene adsorption sites. Our assignment of the 1420 cm^{-1} mode is consistent with more recent studies of benzene on other metal surfaces [8,9,10]. The differences in assignment do not change the conclusion that benzene bonds to Pt(111) with its ring oriented parallel to the surface as indicated by the intense out-of-plane C-H bending mode (γ_{CH}) and the weak in-plane modes in the vibrational spectra.

When CO is coadsorbed with benzene on the Pt(111) surface, the vibrational spectra in Fig. 5.1 clearly show the following. 1) The orientation and bonding of the benzene molecules on the surface do not change significantly when coadsorbed with CO. 2) CO is adsorbed in three different types of sites. The CO mode at ~2030 cm^{-1} is probably due to a small amount of CO adsorbing from the CO background pressure during cooling of the sample onto bare top sites outside the ordered lattice since this mode was not observed in the HREEL spectra of the ordered structures taken at 300 K. At this point, it is unclear whether or not the other two CO modes are both due to CO adsorbed within the ordered lattice.

We have observed in agreement with other researchers [11] the extinction of certain spots within the LEED patterns revealing the presence of glide plane symmetries. This symmetry means the ordered structures can be transformed back into themselves by a reflection through the glide plane followed by a translation of half a lattice spacing along the direction of the plane. In order to satisfy this symmetry

requirement, the number of molecules per unit cell adsorbed at a particular type of site must be even. Consequently, there should be two benzene molecules per unit cell since the unit cells are not large enough to accommodate more than two flat lying benzene molecules. Also, there should be a minimum of four CO molecules per unit cell since the HREEL spectra indicate that CO is adsorbed at two different types of sites within a unit cell. By comparison of the thermal desorption yield of CO when coadsorbed with benzene to that of the c(4x2) structure of CO on Pt(111) [12,13], we determined that there are four CO molecules per $(2\sqrt{3}x4)$rect unit cell and six CO molecules per $(2\sqrt{3}x5)$rect unit cell.

The glide plane symmetries also help us to deduce the bonding sites of benzene and CO within the ordered structures. Benzene adsorption at top sites or at threefold hollow sites is highly unlikely since adsorption at these sites in an arrangement that also satisfies the glide plane symmetries would result in substantial overlap of the flat lying benzene molecules. Consequently, we conclude that benzene adsorbs at bridge sites, since these sites enable the benzene molecules to lie flat and to satisfy the glide plane symmetries without significant overlap between neighboring molecules.

Recently, Ogletree et al. [14] have reported a dynamical LEED analysis of the $(2\sqrt{3}x4)$rect benzene - CO structure. Figure 5.2 shows the structural model favored by the analysis. Benzene is confirmed to bond at bridge sites and some distortion of the benzene ring is indicated by the analysis. The bonding geometry of the CO molecules is

less definite from the analysis; the most probable geometry is shown. As mentioned previously, up to three C-O stretching frequencies were observed for this benzene + CO structure, but it is not clear, at this point, which of the frequencies correlate to the CO within the ordered structure.

5.2.2 $CO/C_6H_6/Rh(111)$

Like benzene adsorbed on Pt(111), different LEED patterns were observed for benzene on Rh(111) at 300 K depending on the coverage of coadsorbed CO. On a Rh(111) surface with no CO adsorbed, benzene orders in a $(2\sqrt{3}x3)$rect lattice at saturation coverage. When benzene and CO are coadsorbed, we observed, depending on CO coverage, two new and different ordered structures, which can be labeled $c(2\sqrt{3}x4)$rect and (3x3). These LEED structures have been reported previously [8,11,15], but the authors did not realize at the time how important CO impurities from the background pressure ($\sim 5x10^{-10}$ torr) were in ordering the structures.

We were able to observe the CO-benzene LEED patterns most readily when the rhodium surface, at 300 K, was first precovered with CO and then exposed to 5L of benzene, an amount sufficient to saturate the surface. In Fig. 5.3, the closed circles give the benzene and CO coverages when the surface was exposed to CO and benzene in this manner. The open circles in Fig. 5.3 represent experiments where the surface, predosed with CO, was exposed to the minimum amount of benzene for

which LEED patterns were observed. The similarity of the results for a minimum benzene exposure to that of a saturation exposure indicates that ordering of coadsorbed CO and benzene occurs when the surface coverage is close to saturation.

For Fig. 5.3, the coverages of CO and benzene were determined by comparison of the CO and D_2 thermal desorption yields to those of LEED structures that occur over a narrow range of coverages. Benzene-d_6 (C_6D_6) was used in these experiments to minimize the effect of the hydrogen background pressure on the results. The CO desorption yields were compared to that of the $(\sqrt{3}x\sqrt{3})R30^\circ$ structure of pure adsorbed CO on Rh(111) [15,16]. Benzene-d_6 coverages were determined by comparing the D_2 desorption yield to that of the $(2\sqrt{3}x3)$rect benzene-d_6 structure. For the benzene coverages, we assume that there are two benzene molecules per $(2\sqrt{3}x3)$rect unit cell and that the D_2 desorption yield is proportional to the benzene-d_6 coverage since less than two percent of a monolayer of benzene desorbs molecularly from Rh(111) [8]. CO and benzene coverages are defined as the ratio of adsorbed molecules to rhodium surface atoms.

Figures 5.4A and B show thermal desorption spectra for CO and D_2 when 5L of benzene-d_6 is coadsorbed with CO on Rh(111) along with the thermal desorption spectra for CO and benzene-d_6 adsorbed alone on Rh(111). The thermal desorption spectra show that benzene decomposition and CO desorption both occur at ~490 K on Rh(111). These processes continue to occur near this temperature when CO and benzene are coadsorbed.

As shown in Fig. 5.3, the LEED patterns are observed over a range of coverages, indicating the formation of ordered domains. If there is one CO molecule per c(2 $\sqrt{3}$x4)rect unit cell, then domains of this structure should completely cover the surface at a CO coverage of one-eighth of a monolayer (0.125 monolayer coverage). Since the c(2$\sqrt{3}$x4)rect LEED pattern was sharpest and most intense at ~0.12 of a monolayer of CO, we conclude that there is only one CO molecule per c(2$\sqrt{3}$x4)rect unit cell. Similarly, we conclude that there are two CO molecules per (3x3) unit cell since the (3x3) LEED pattern was sharpest and most intense at ~0.22 of a monolayer of CO.

Figure 5.5 shows HREEL vibrational spectra for the three ordered structures on Rh(111) at 300 K. The assignment of the vibrational frequencies for benzene chemisorbed on Rh(111) is given in Table 5.1. This assignment is discussed in Chapter 4. When coadsorbed with CO, the spectrum of benzene is essentially unchanged except for small changes in the region of the out-of-plane bending (γ_{CH}) modes. Figure 5.6 shows this region with an expanded scale to illustrate these changes.

For the (2$\sqrt{3}$x3)rect structure, two losses are observed at 775 cm^{-1} and 805 cm^{-1}, which are discussed in Chapter 4 as resulting from two CH bending modes that are dipole active for benzene bonded at bridge sites with C_s symmetry. For the c(2$\sqrt{3}$x4)rect or (3x3) structures, only one CH bending mode is observed in this frequency region, indicating a high adsorption site symmetry, such as C_{2v} or C_{3v} for benzene in these two surface structures. Also, the spectra in Fig. 5.5 indicate

that CO is bonded at only one site within the ordered CO-benzene structures on Rh(111). This site is most likely a threefold hollow site since the low C-O stretching frequency (1655 cm^{-1} to 1700 cm^{-1}) is characteristic of that observed for CO bonded to three metal atoms in metal-carbonyl clusters [18]. This leads us to propose that both CO and benzene are bonded at threefold hollow sites within the c($2\sqrt{3}$x4)rect and (3x3) structures.

Recently, Van Hove and coworkers have reported dynamical LEED analyses of the c($2\sqrt{3}$x4)rect [19] and (3x3) [20] CO-benzene structures. Figures 5.7 and 5.8 show the structural models for the two structures favored by the dynamical analyses. The analyses confirm that both benzene and CO are centered over hcp hollow sites. Also, a significant amount of distortion of the benzene ring is indicated by the analyses.

5.3 Discussion

5.3.1 Ordering of Coadsorbed CO and Benzene

The coadsorption of CO with benzene strongly promotes ordering of the organic molecule into a two-dimensional structure. This somewhat unexpected finding indicates that there are interactions between the coadsorbed molecules on the transition metal surface. These interactions must be weak when compared to the adsorbate-metal interaction since the vibrational and thermal desorption spectra of benzene do not change significantly when coadsorbed with CO.

Theoretical calculations of the interaction between chemisorbed atoms or molecules have shown that adsorbate-adsorbate interactions are generally at least an order of magnitude smaller than the adsorbate-substrate interaction [21]. When the chemisorbed atoms and molecules are separated so that the overlap of adsorbate orbitals is negligible, these calculations have also found that the interaction between adsorbates are primarily indirect (i.e., via substrate wavefunctions), oscillate in sign as a function of separation distance, and decrease in magnitude with increasing separation distance. When, these interactions are found to be attractive at certain separation distances, ordered domains can form [21,22].

In our discussion of the interactions responsible for the CO induced ordering of adsorbed benzene, we will mainly consider coadsorbed CO and benzene on Rh(111). In connection with this discussion, we find it useful to refer to the work by Ruckenstein and Halachev [23] who have used quantum-chemical calculations to study the interaction between CO molecules adsorbed on the Rh(111) surface. These authors considered only interactions occurring through the metal substrate. For two adsorbed CO molecules, these calculations indicate the interaction energy is positive (repulsive) when the CO molecules occupy first nearest neighbor sites and is negative (attractive) when they occupy second and third nearest neighbor sites. In other words, two CO molecules are repelled from sites separated by small distances but are attracted to sites separated by intermediate distances. The observed ordering of the quarter monolayer p(2x2) CO structure and the

$(\sqrt{3}x\sqrt{3})R30^\circ$ CO structure [16,17] where CO occupy respectively third and second nearest neighbor sites can then be explained in terms of favorable interaction energies.

Since this kind of interaction between adsorbates has been found in various studies to result in the formation of ordered domains, it is reasonable to propose that the trend in interaction energies (i. e., positive for CO molecules separated by small distances and negative for CO molecules separated by intermediate distances) does not change when CO is coadsorbed with benzene. This trend can also explain the observed dependence of the LEED patterns on the CO and benzene coverages.

As shown in Fig. 5.3, the c($2\sqrt{3}$x4)rect LEED pattern is observed for CO coverages ranging from 0.05 of a monolayer to 0.12 of a monolayer. Benzene coverages are always close to saturation. If one assumes there is only one CO molecule per unit cell, then at 0.05 monolayer of CO coverage, the observation of a c(2 $\sqrt{3}$x4)rect pattern implies that about half of the surface is covered with domains of the c($2\sqrt{3}$x4)rect structure. The adsorption of CO within domains at this low coverage is possible if the interaction energy between CO molecules within a c(2 $\sqrt{3}$x4)rect lattice is more negative than when spread uniformly over the surface.

Figure 5.3 shows that the (3x3) pattern is observed for CO coverages ranging from 0.22 of a monolayer to 0.44 of a monolayer. If one assumes one benzene molecule and two CO molecules per unit cell, then the observation of a (3x3) pattern over this wide range of CO coverages indicates the formation of domains. Assuming all the benzene is adsorbed

within the (3x3) domains, we estimate the CO concentration in regions outside the (3x3) domains to be close to the saturation concentration of CO that occurs at 0.75 of a monolayer. If CO is arranged within the (3x3) unit cell as shown in Fig. 5.8, the CO molecules would form a $(\sqrt{3}x\sqrt{3})R30^\circ$ lattice with one third of the sites occupied by benzene molecules forming the (3x3) superlattice. Therefore, the interaction between CO molecules should be attractive in this structure. Outside of the domains, the CO molecules should have a repulsive interaction because the high concentration of CO in this region results in the molecules occupying nearest neighbor sites. The CO molecules can then lower their energy by occupying sites within the (3x3) domains rather than sites outside of the domains. For the same reason, the adsorption of the benzene molecules within the domains helps to minimize the CO-CO interaction energy. Essentially, the (3x3) CO-benzene structure enables the maximum number of CO molecules to have the same CO-CO separation distance as in the $(\sqrt{3}x\sqrt{3})R30^\circ$ CO structure on Rh(111).

The preceding arguments show that the interactions that exist between adsorbed CO on clean Rh(111) are sufficient to explain the observed LEED structures for coadsorbed CO and benzene. This does not rule out the possibility that the CO-CO interaction may be modified somewhat in the presence of coadsorbed benzene; some change is to be expected due to the different CO adsorption site in the coadsorbed structure. We argue, however, that the trend in interaction energies, repulsive for CO molecules separated by small distances and attractive for CO molecules separated by intermediate distances, does not change

substantially in the presence of benzene. Also, other interactions such as those between benzene-benzene and CO-benzene are not ruled out and may further stabilize the ordered CO-benzene structures. Figures 5.2, 5.7, and 5.8 show that, while CO and benzene are closely packed within the ordered structures, they are still separated by approximately their Van der Waals dimensions, indicating that the main interactions between them will be either Van der Waals interactions or indirect interactions through the substrate. The benzene-benzene interactions are probably weaker than the CO-CO interactions since, in the absence of CO, only a tightly packed $(2\sqrt{3}x3)$rect structure is detected and no loosely packed, ordered benzene structures are observed. An attractive CO-benzene interaction would stabilize ordered structures with CO and benzene intermixed in the unit cell, whereas a repulsive interaction would favor segregation. The following chapter further explores the nature of the CO-benzene interaction. However, the important point is that coadsorbed CO and benzene are likely to form an ordered overlayer since CO readily orders on Rh(111) due to favorable interaction energies. The ordered structures of CO and benzene on the Pt(111) surface are other possible examples of this effect. Without any coadsorbate, benzene does not order on Pt(111). Adsorbed CO, however, readily orders on this surface into a variety of structures [12,13]. Coadsorbing CO with benzene results in either the $(2\sqrt{3}x4)$rect or the $(2\sqrt{3}x5)$rect ordered structures.

5.3.2 Adsorption Sites of Coadsorbed CO and benzene

As mentioned earlier, the CO and benzene adsorption sites change when benzene is coadsorbed with CO. CO adsorbs preferentially at hollow sites on benzene-covered Rh(111). On initially clean Rh(111) surfaces, CO chemisorbs first at sites atop of metal atoms [17]. Our results suggest two possible causes for the change in CO adsorption site. 1) When adsorbed at hollow sites, benzene blocks CO from adsorbing at nearby top sites. 2) Since benzene donates electrons to the metal surface as detected by work function measurements described in Chapter 6, adsorbed benzene could cause CO adsorption at hollow sites to become energetically more favorable.

Shifts of CO to more highly coordinated adsorption sites have also been observed for CO coadsorbed with alkali atoms, which are also charge donors to the metal surface [24,25,26]. When CO is adsorbed at bridge and hollow sites, the $2\pi^*$ orbital of CO has greater overlap with substrate orbitals of the correct symmetry for bonding than when CO is adsorbed at top sites. Consequently, the $2\pi^*$ CO orbital is able to accept more of the charge donated to the surface by benzene molecules or alkali atoms when CO is bonded at bridge or hollow sites than when bonded at top sites. Discussed in the next chapter is evidence from detailed work function measurements that coadsorbed CO accepts electrons donated to the surface by adsorbed benzene.

There is also a shift in adsorption site for benzene on Rh(111) when it is coadsorbed with CO. As discussed in Chapter 4, in the absence of CO, benzene adsorbs at saturation coverage predominantly at

bridge sites. When benzene is coadsorbed with CO in an ordered structure on Rh(111), it adsorbs entirely at threefold hollow sites. As with the shift in CO sites, our results suggest two possible causes for the shift in benzene adsorption site, 1) CO adsorption in hollow sites, which could be caused by charge donation from the benzene to the substrate, blocks benzene adsorption at nearby bridge sites. 2) The electron accepting properties of CO adsorbed at hollow sites may cause benzene adsorption at hollow sites to become energetically more favorable than at bridge sites.

Several previous studies of benzene on Pt(111) and Rh(111) surfaces [4,8] have tried to determine the adsorption site symmetry of benzene using HREELS. These studies concluded that the symmetry of adsorbed benzene was $C_{3v}(\sigma_d)$ since only a small number of benzene modes are observed in the HREEL spectra and those modes that are observed are consistent with a local symmetry of $C_{3v}(\sigma_d)$. It was thought that more modes would become dipole active if benzene was bonded to a site of lower symmetry and that these modes would then be observed in the HREEL spectra. The spectra in Fig. 5.5 illustrate the difficulty, however, in determining the adsorption site of benzene on metal surfaces using only HREELS. There are only small differences in the vibrational spectra of benzene for the $(2\sqrt{3}x3)$rect and $c(2\sqrt{3}x4)$rect structures even though LEED results indicate that benzene bonds at bridge sites, which have C_s symmetry, in the $(2\sqrt{3}x3)$rect structure and at hollow sites, which have $C_{3v}(\sigma_d)$, in the $c(2\sqrt{3}x4)$rect structure. This indicates that the metal surface does not significantly

distort the benzene molecule from C_{3v} symmetry or that any distortions do not result in any new dynamic dipole moments perpendicular to the surface.

5.4 Conclusions.

Benzene coadsorbed with CO forms a variety of ordered overlayer structures on Pt(111) and Rh(111). In the case of Pt(111), CO-induced ordering of benzene enables the structure determination of benzene chemisorbed on this surface by a dynamical LEED analysis that would be difficult without the presence of CO since benzene does not order on Pt(111) without CO.

In principle, it should be possible to order any adsorbate by coadsorbing an appropriate ordering agent which has interactions strong enough to induce ordering. The surface structure of such a molecule, which might not otherwise order, could be determined by LEED crystallography.

The next chapter describes how CO induces many other adsorbates besides benzene to order on the Rh(111) surface. Here also, the role of the CO - adsorbate interaction is explicitly studied.

Table 5.1. Assignment of observed vibrational frequencies (cm^{-1}) for benzene chemisorbed on Pt(111) and Rh(111).

Gas phase frequencies [6]	Frequencies of chemisorbed C_6H_6 on Pt(111)	on Rh(111) $(2\sqrt{3}x3)$rect	Mode type	Mode number [9] and symm. representation
3062	3000	2970	CH stretch(ν_{CH})	ν_1 A_{1g}
673	830	775	CH bend(γ_{CH})	ν_4 A_{2u}
849	920	805	CH bend (γ_{CH})	ν_{11} E_{1g}
1310	1330	1330	ring stretch(ν_{CC})	ν_9 B_{2u}
1150	1130	1115	CH bend(γ_{CH})	ν_{10} B_2u
1486	1420	1430	ring str. (δ_{CC}) and deform	ν_{13} E_{1u}
--	360	345	M-C stretch(ν_{M-C})	
--	--	545	M-C stretch(ν_{M-C})	

REFERENCES

1. For a recent review see, B. E. Koel and G. A. Somorjai, "Surface Structural Chemistry," in Catalysis: Science and Technology, Vol. 38, J. R. Anderson and M. Boudart, Eds., (Springer-Verlag, New York, 1983).
2. D. K. Saldin, J.B. Pendry, M. A. Van Hove, and G. A. Somorjai, Phys. Rev. B 31, (1985) 1216; K. Heinz, D. K. Saldin, and J. B. Pendry, Phys. Rev. Lett. 55 (1985) 2312.
3. J. L. Gland and G. A. Somorjai, Surface Sci. 38, (1973) 157.
4. S. Lehwald, H. Ibach and J. E. Demuth, Surface Sci. 78, (1978) 577.
5. P. C. Stair and G. A. Somorjai, J. Chem. Phys. 67 (10), (1977) 4361.
6. T. Shimanouchi, Tables of Molecular Vibrational Frequencies, Consolidated Volume I, NSRDS-NBS39; Vol. 2, J. Chem. Ref. Data 6, (1977) 993.
7. G. Herzberg, Molecular Spectra and Molecular Structure II, Infrared and Raman Spectra of Polyatomic Molecules, (Van Nostrand, Princeton, N. J., 1945).
8. L. L. Kesmodel, Phys. Rev. Lett, 53, (1984) 1001; G. D. Waddill and L. L. Kesmodel, Phys. Rev. B31 (1985) 4940.
9. B. E. Koel, J. E. Crowell, C. M. Mate, and G. A. Somorjai, J. Phys. Chem. 88, (1984) 1988.

10. H. Jobic, J. Tomkinson, J. P. Candy, P. Fouilloux and A. J. Renouprez, Surface Sci. 95, (1980) 496.

11. R. F. Lin, R.J. Koestner, M. A. Van Hove and G. A. Somorjai, Surface Sci. 134, (1983) 161.

12. G. Ertl, M. Neumann and K. M. Streit, Surface Sci. 64, (1977) 393.

13. B. E. Hayden and A. M. Bradshaw, Surface Sci. 125, (1983) 787.

14. E. F. Ogletree, M. A. Van Hove and G. A. Somorjai, submitted to Surface Science.

15. M. A. Van Hove, Rongfu Lin, and G. A. Somorjai, Phys. Rev. Lett. 51, (1983) 778.

16. P. A. Thiel, E. D. Williams, J. T. Yates, Jr. and W. H. Weinberg, Surface Sci. 84, (1979) 427.

17. R. J. Koestner, M. A. Van Hove, and G. A. Somorjai, Surface Sci. 107, (1981) 439.

18. R. Eischens and W. A. Pliskin, Advan. Catalysis 10, (1958) 1.

19. M. A. Van Hove, R. F. Lin and G. A. Somorjai, J. Am. Chem. Soc. 108 (1986) 2532.

20. M. A. Van Hove, R. F. Lin, G. S. Blackman, and G. A. Somorjai, submitted.

21. T. L. Einstein, CRC Critical Rev. Solid State Mater. Sci. 7, (1978) 261, and references therein.

22. T. L. Einstein, Surface Sci. 83, (1979) 141.

23. E. Ruckenstein and T. Halachev, Surface Sci. 122, (1982) 422.

24. J. E. Crowell and G. A. Somorjai, Appl. Surface Sci. 19, (1985) 73.

25. J. E. Crowell, E. L. Garfunkel and G. A. Somorjai, Surface Sci. 121, (1982) 303.

26. R. A. de Paola, J. Hrbek, and F. M. Hoffmann, J. Chem. Phys. 82, (1985) 1.

FIGURE CAPTIONS

Fig. 5.1. Vibrational spectra and LEED patterns for benzene and benzene plus CO adsorbed at 300 K on Pt(111) and then cooled to 77 K.

Fig. 5.2. Structure of Pt(111) - $(2\sqrt{3}x4)$rect - 2 C_6H_6 + 4 CO, in side view and top view, including Van der Waals contours with radii 1.8 Å for C in benzene, 1.6 Å for C and O in CO, and 1.2 Å for H (the H positions are assumed, including possible CH bending away from the surface). The CO molecules are shown hatched. A $(2\sqrt{3}x4)$rect unit cell is shown with solid lines and the dash lines show the location of the glide planes. Bond lengths parallel to the surface are accurate to within ± 0.15 Å, while those perpendicular to the surface are accurate to within ± 0.05 Å.

Fig. 5.3. Benzene coverage versus CO coverage when benzene is coadsorbed with CO. For the open circles, the surface was precovered with a given CO coverage then exposed to 5.0L of benzene-d_6. For the closed circles, the surface was predosed with a certain CO coverage then exposed to the minimum benzene dose needed to observe a LEED pattern.

Fig. 5.4 Thermal-desorption spectra of A) CO and B) D_2 after coadsorbing CO and benzene-d_6 at 300 K on Rh(111).

Fig. 5.5. Vibrational spectra for benzene and benzene plus CO adsorbed at 300 K on Rh(111).

Fig. 5.6. The CH out-of-plane bending mode of benzene is shown with an expanded energy scale for two of the ordered structures on Rh(111).

Fig. 5.7 The structure of Rh(111) - c(2$\sqrt{3}$x4)rect — C_6H_6 + CO in side view and top view, including Van der Waals contours. The accuracy of the bond lengths as well as Van der Waals radii are the same as in Fig. 5.2. A $\begin{pmatrix} 3 & 1 \\ 1 & 3 \end{pmatrix}$ = c(2$\sqrt{3}$x4)rect unit cell is outlined. Dots between surface metal atoms denote second-layer metal atoms.

Fig. 5.8 The structure of Rh(111) - (3x3) - C_6H_6 + 2 CO in side view and top view, including van der Waals contours. The accuracy of the bond lengths as well as Van der Waals radii are the same as in Fig. 5.2. A (3x3) unit cell is outlined. Dots between surface metal atoms denote second-layer metal atoms.

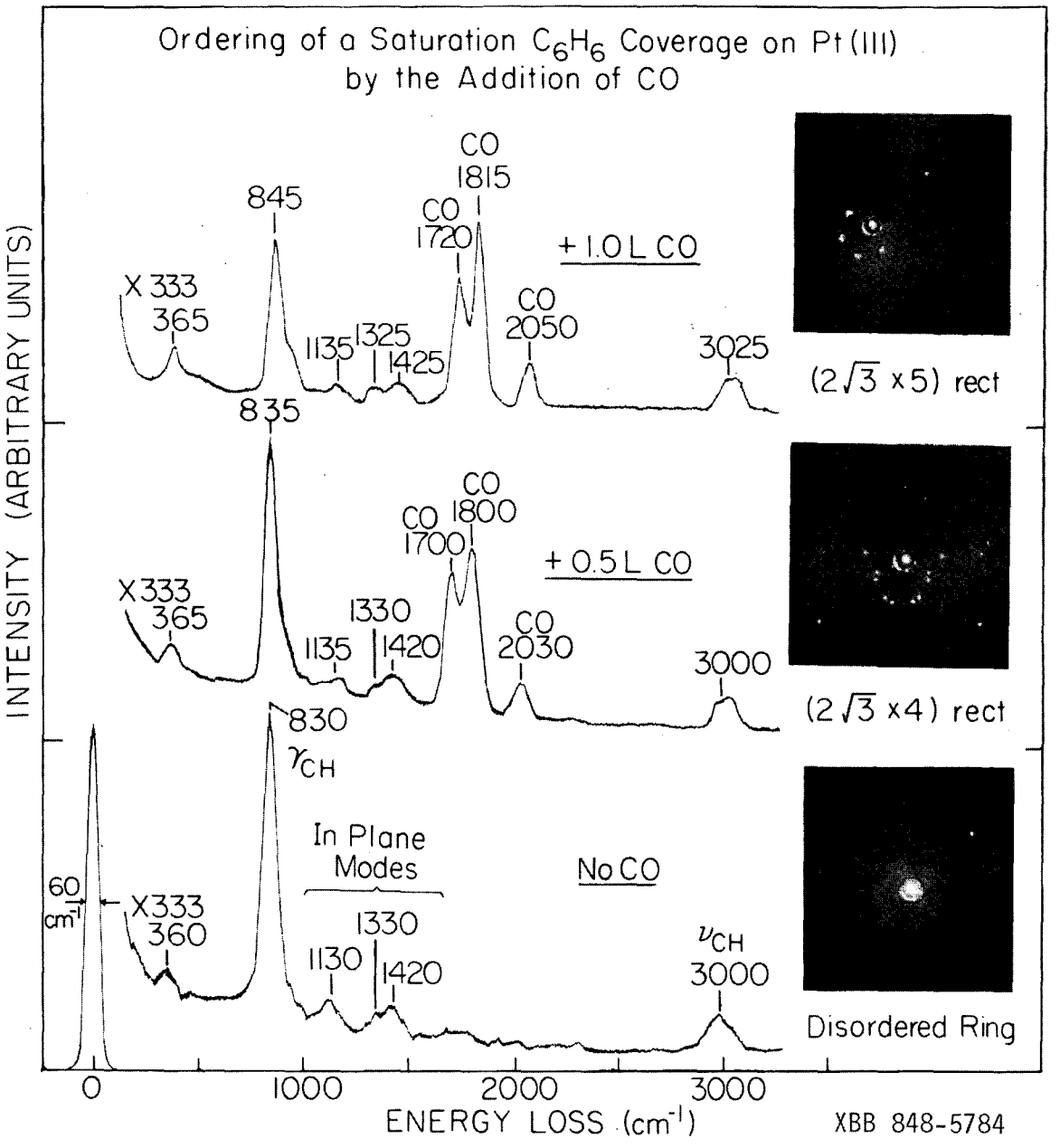
Ordering of a Saturation C_6H_6 Coverage on Pt(111)
by the Addition of CO
INTENSITY (ARBITRARY UNITS)
CO
1815
845
CO
1720
+1.0 L CO
X 333
365
1135
1325
1425
CO
2050
3025
835
(2√3 x5) rect
CO
1800
CO
1700
+0.5 L CO
X333
365
1330
1135
1420
CO
2030
3000
(2√3 x4) rect
830
γ_{CH}
In Plane
Modes
No CO
60
cm⁻¹
X333
360
1330
1130
1420
ν_{CH}
3000
Disordered Ring
0
1000
2000
3000
ENERGY LOSS (cm⁻¹)
XBB 848-5784

Figure 5.1

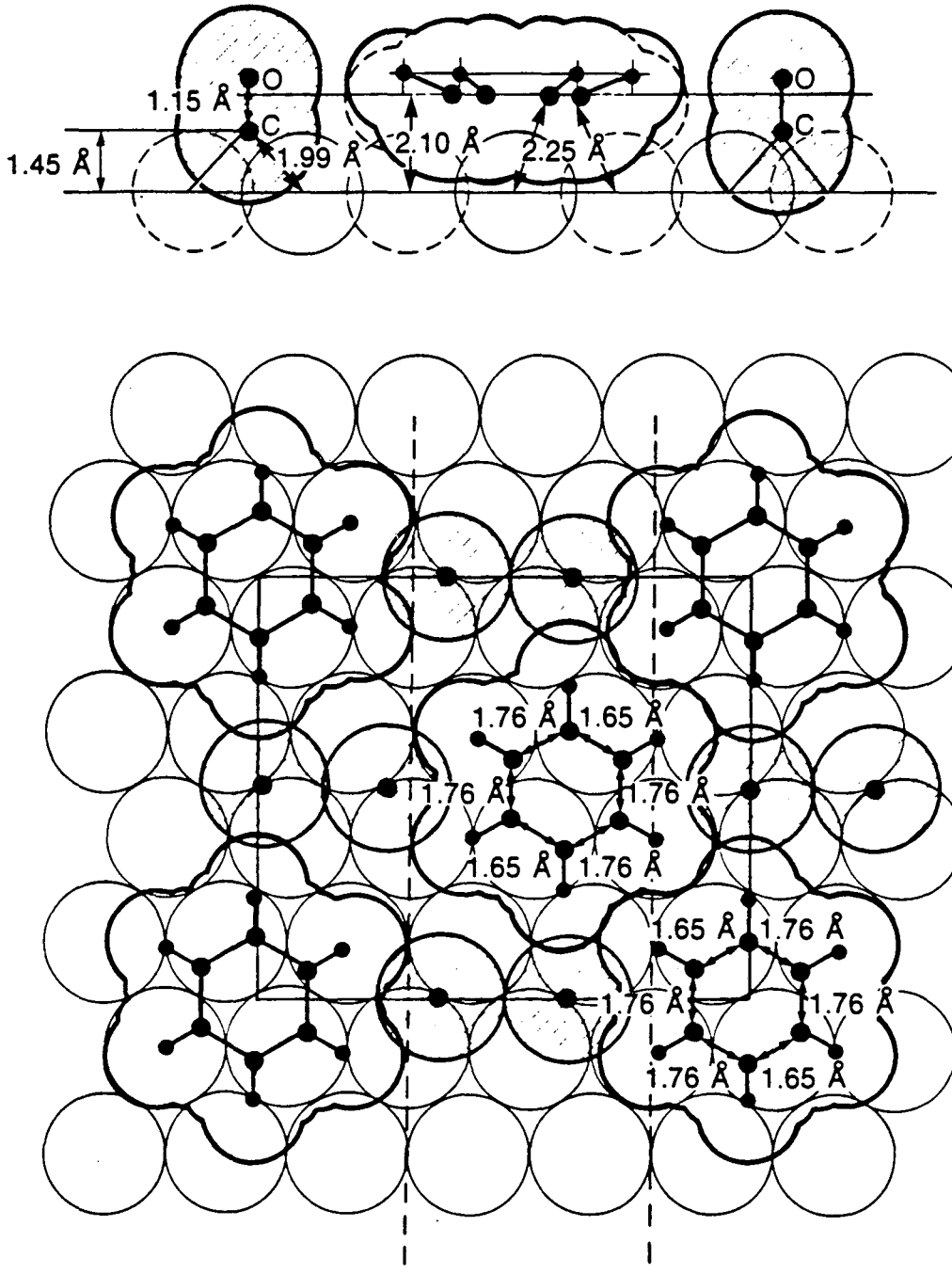

$Pt(111) - (2\sqrt{3}\times 4)rect - 2C_6H_6 + 4CO$

XBL 867-2543

Figure 5.2

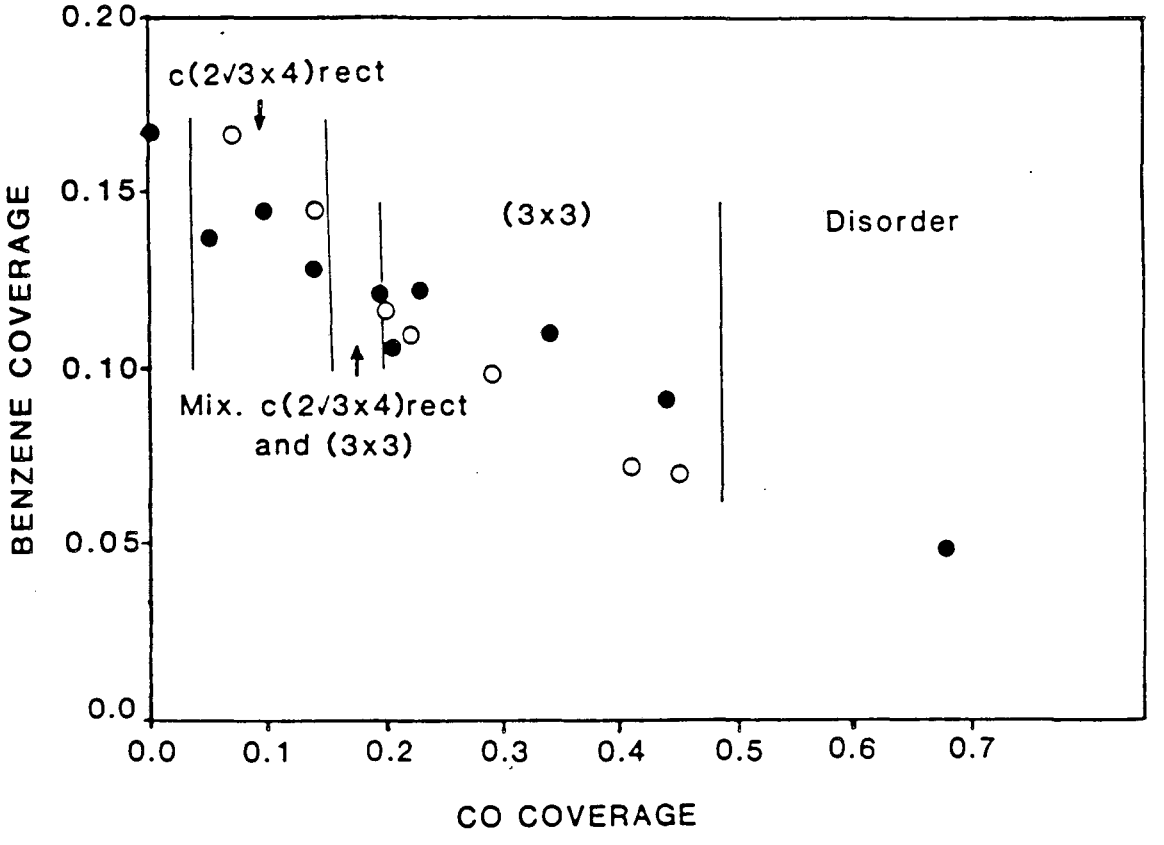

XBL 852-1411

Figure 5.3

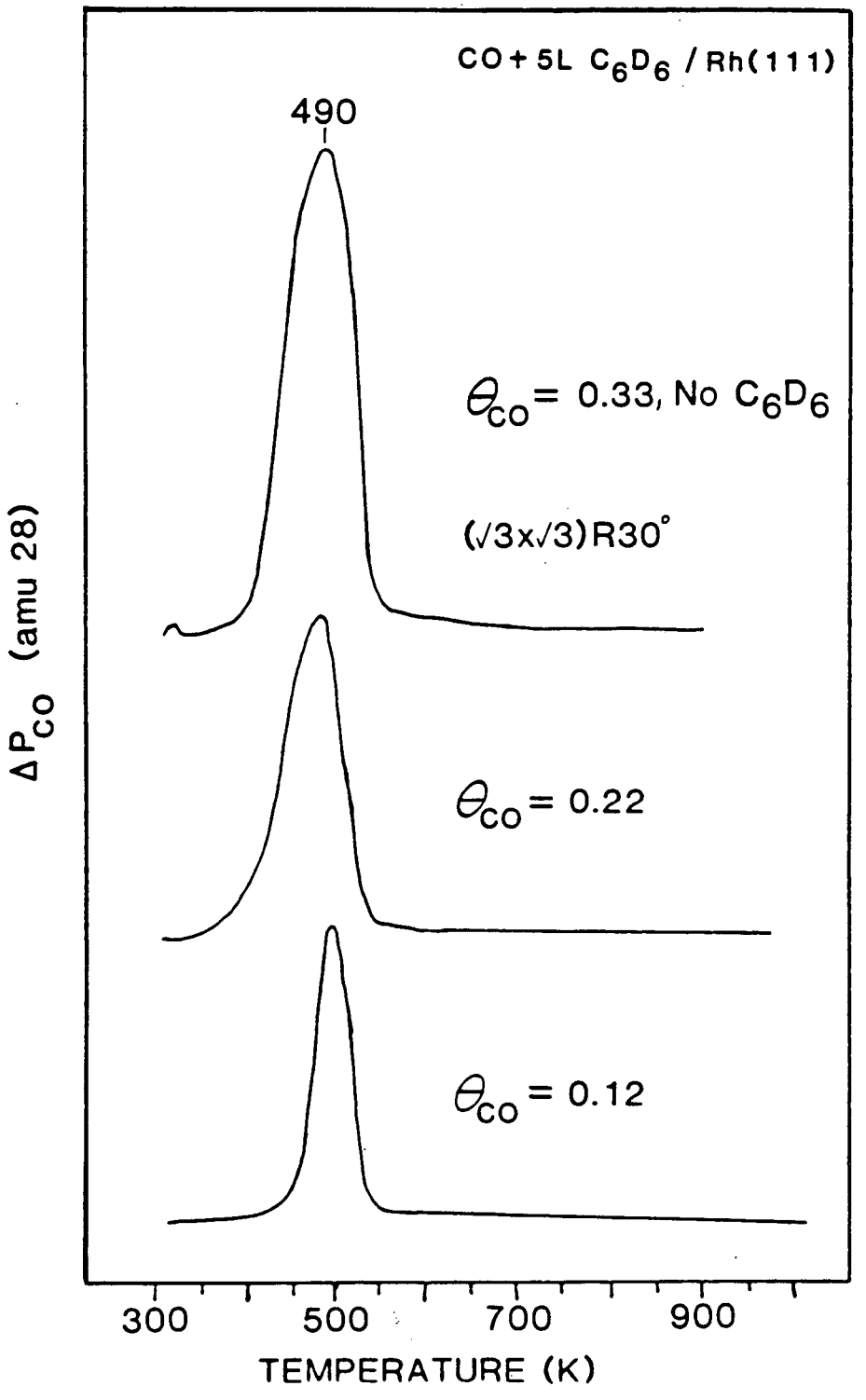

XBL 852-1409

Figure 5.4A

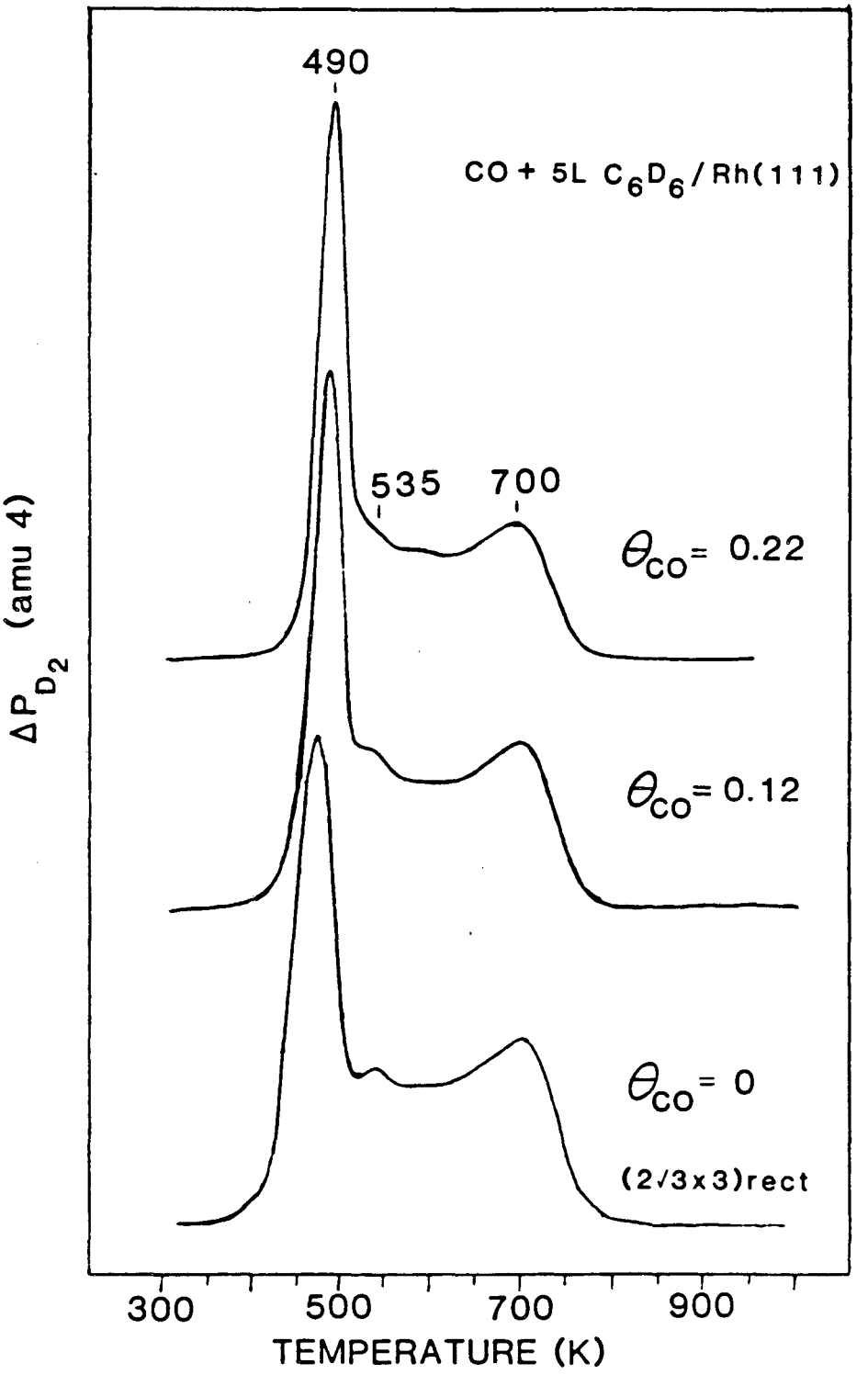

XBL 852-1408

Figure 5.4B

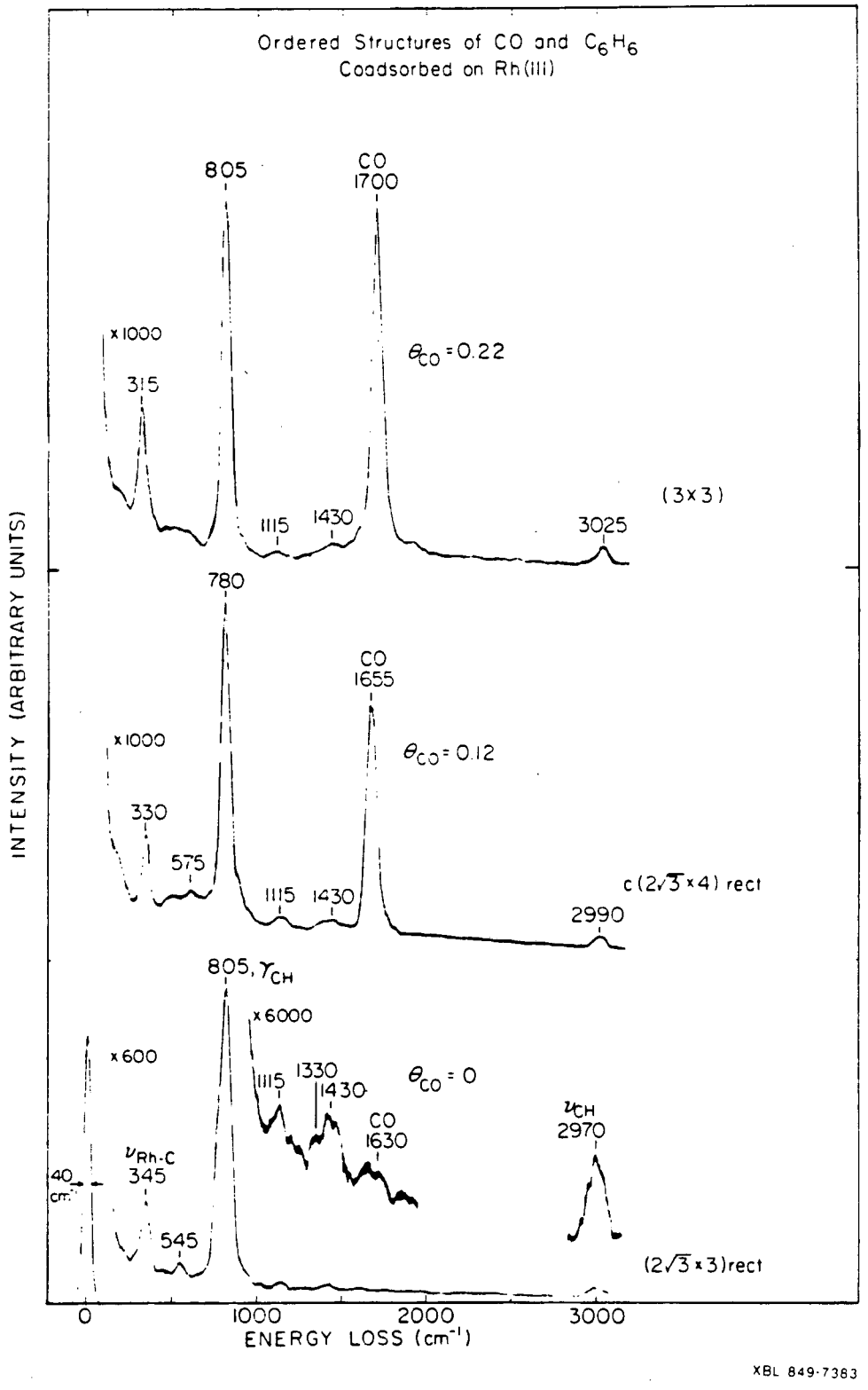
Ordered Structures of CO and C_6H_6
Coadsorbed on Rh(111)
805
CO
1700
x1000
315
θ_{CO} = 0.22
(3x3)
1115
1430
3025
780
CO
1655
x1000
330
575
θ_{CO} = 0.12
c(2√3x4) rect
1115
1430
2990
805, γ_{CH}
x6000
x600
1115
1330
1430
θ_{CO} = 0
CO
1630
ν_{CH}
2970
ν_{Rh-C}
345
40
cm⁻¹
545
(2√3x3)rect
INTENSITY (ARBITRARY UNITS)
0
1000
2000
3000
ENERGY LOSS (cm⁻¹)
XBL 849-7383

Figure 5.5

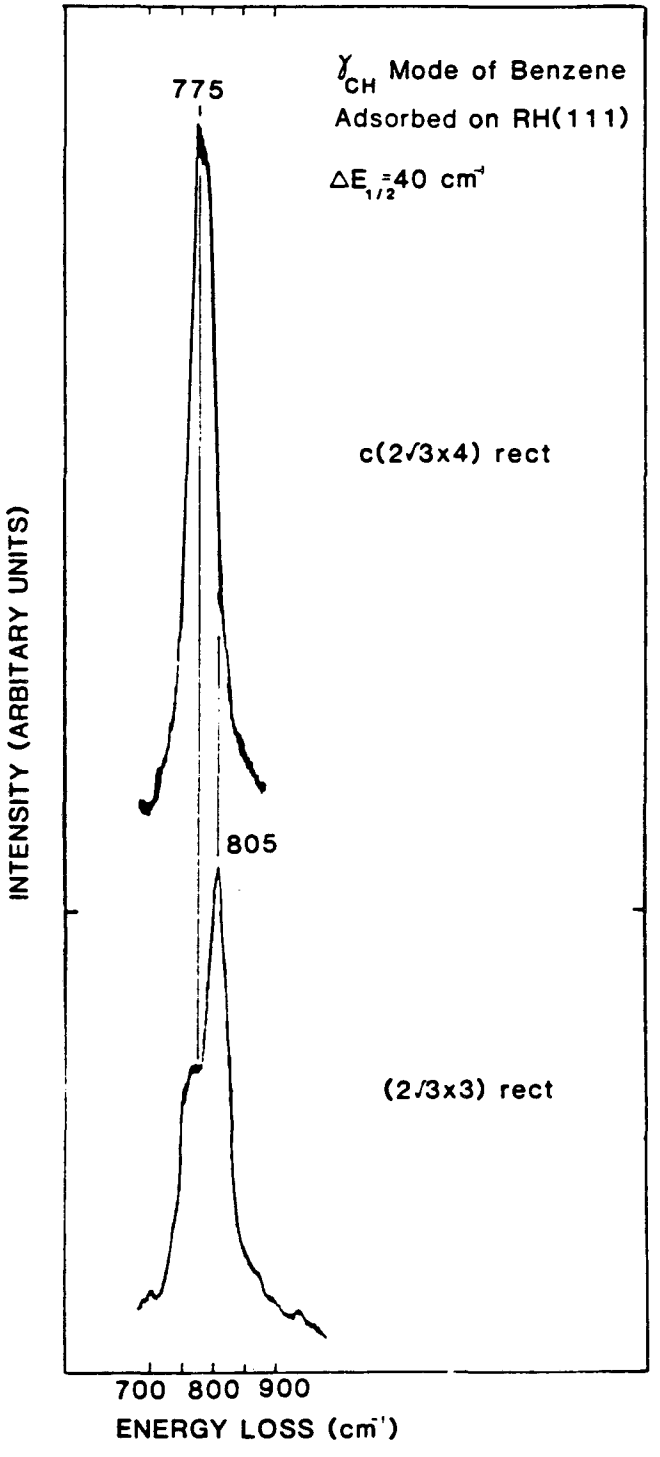
γ_{CH} Mode of Benzene
Adsorbed on RH(111)
$\Delta E_{1/2}$=40 cm^{-1}
775
805
c(2√3x4) rect
(2√3x3) rect
INTENSITY (ARBITARY UNITS)
700 800 900
ENERGY LOSS (cm^{-1})
XBL 851-1000

Figure 5.6

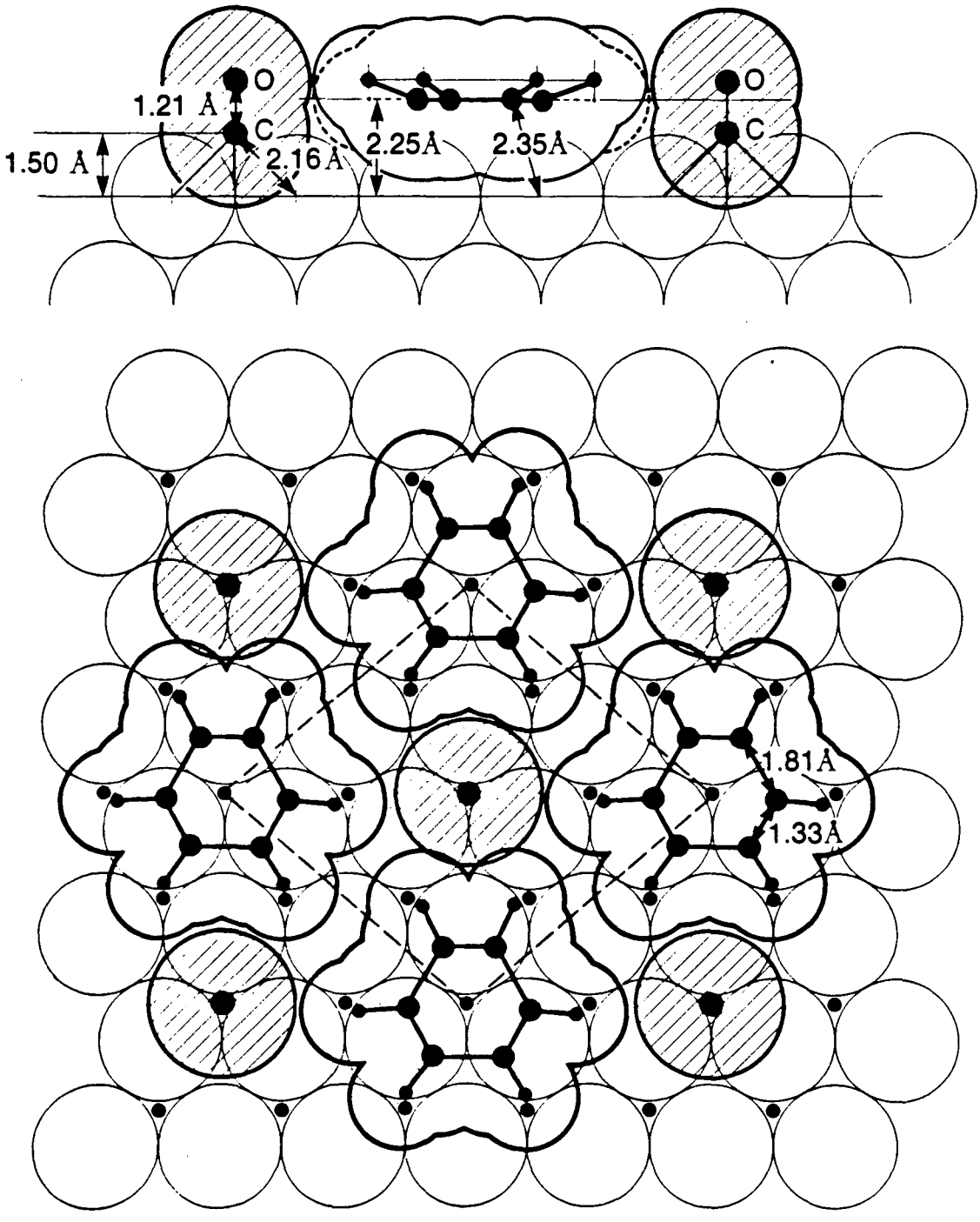

$Rh(111)-\binom{31}{13}-C_6H_6 + CO$

XBL 851-9917 A

Figure 5.7

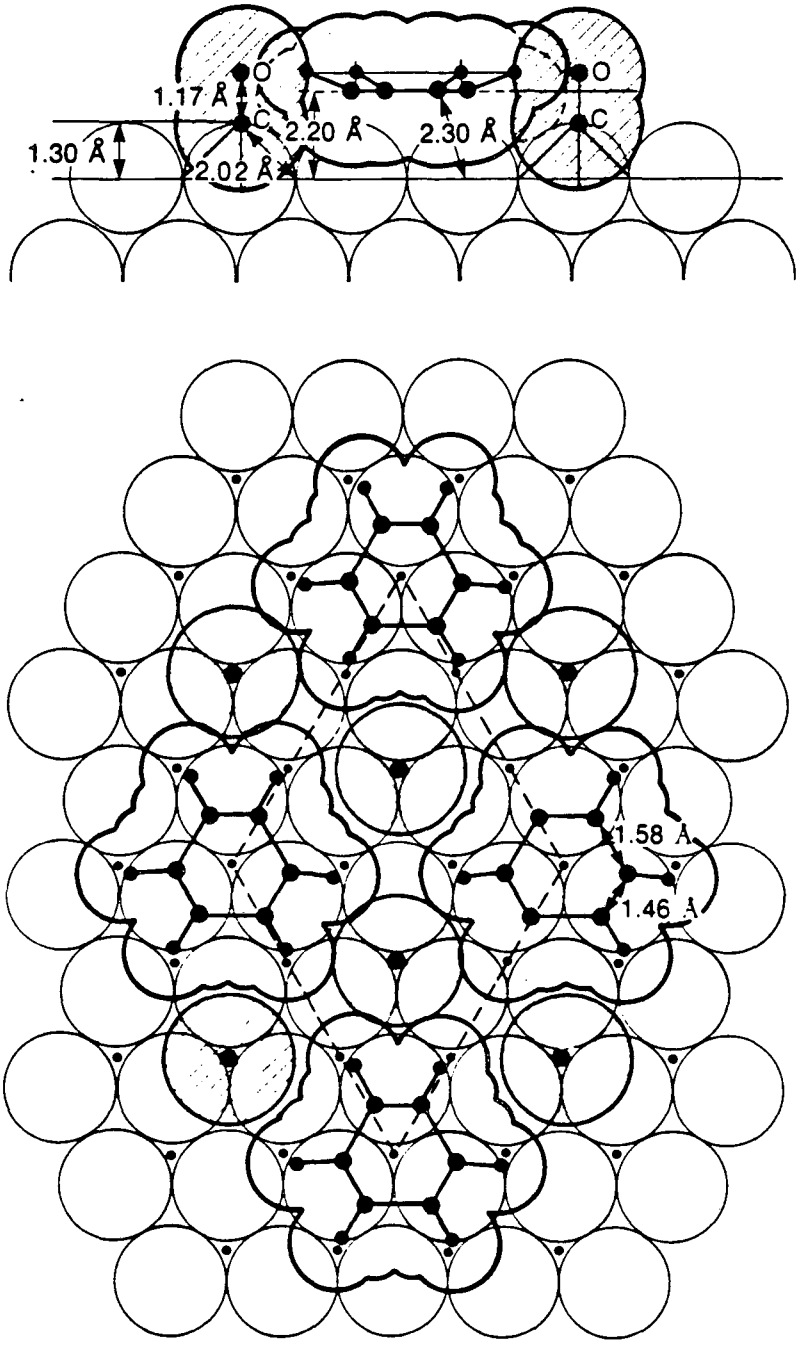

Rh(111) – (3×3) – C_6H_6 + 2CO

XBL 863-10701

Figure 5.8

CHAPTER 6

Carbon Monoxide Induced Ordering of Absorbates

II. Absorbates on Rh(111)

Contents

6.1 Introduction

In the previous chapter, we discussed how CO induces benzene to order on Rh(111) and Pt(111) surfaces. In this chapter, we continue our discussion of CO induced ordering of adsorbates on the Rh(111) surface. First, we discuss the adsorption of CO, fluorobenzene, acetylene, ethylidyne, propylidyne, and sodium alone on the Rh(111) surface as well as in the presence of coadsorbed CO. We find that all the adsorbates that form ordered structures when coadsorbed with CO on Rh(111) can be classified as net donors of electrons to the metal surface. This is supported by work function measurements that show that these adsorbates decrease the work function of the surface when adsorbed. Finally, we present a simplified theoretical discussion of the various effects that may be responsible for CO induced ordering of adsorbates. In particular, we suggest CO induced ordering is promoted by the combination of the electronegative character of adsorbed CO and the electropositive character of the other adsorbates.

6.2 CO Adsorbed Alone on Rh(111)

The adsorption of CO alone on the Rh(111) surface has been studied extensively by several researchers [1-3]. Here, we briefly summarize their results in order to compare with our results for coadsorbed CO. In this chapter, adsorbate coverages are defined to be the ratio of adsorbate molecules to rhodium surface atoms.

Figure 6.1 shows the HREEL spectra and LEED patterns for CO adsorbed alone on the Rh(111) surface at room temperature. For CO coverages less than or equal to a third of a monolayer (i.e., CO exposures less than 1.0L), CO adsorbs atop of the rhodium surface atoms, as indicated by a C-O stretching frequency of ~2020 cm^{-1}, which is characteristic of terminally bonded CO in metal clusters [4] and on metal surfaces [5]. At one third of a monolayer coverage, CO orders into a $(\sqrt{3} \times \sqrt{3})R30^{\circ}$ LEED structure. As discussed in Chapter 2, a dynamical LEED analysis [2] of this structure confirms that CO bonds atop of the rhodium surface atoms. Since the $(\sqrt{3} \times \sqrt{3})R30^{\circ}$ LEED pattern forms over a narrow range of CO coverages, we use the thermal desorption yield from this structure to calibrate the thermal desorption yields for other CO coverages.

For CO coverages greater than one third of a monolayer, some CO bonds to the surface bridging two rhodium atoms, as indicated in the HREEL spectrum by the C-O stretching mode at ~1850 cm^{-1}, which is characteristic of bridge bonded CO in metal clusters [4] and on metal surfaces [5]. The CO coverage saturates on Rh(111) at three quarters of a monolayer and, at this coverage, forms a (2x2) LEED structure. The dynamical LEED analysis [3] of the (2x2) LEED structure (discussed in Chapter 2) determined that, per unit cell, one CO molecule bonds in a bridge site and two CO molecules bond at sites displaced slightly from top sites.

6.3 Fluorobezene (C_6H_5F)/Rh(111)

As fluorobenzene is chemically very similar to benzene, the surface structure of fluorobenzene on Rh(111) at 310 K turns out to be similar to that of benzene. In particular, we observe the same CO—induced ordered structures on Rh(111) for fluorobenzene as for benzene. However, the substituted fluorine atom results in some structural differences between chemisorbed fluorobenzene and benzene at high coverages, possibly due to an interaction of the fluorine atom with neighboring molecules.

Figure 6.2 shows the HREEL spectra for a low coverage (~ 1/3 of saturation coverage) of fluorobenzene chemisorbed on the Rh(111) surface at 310K. Table 6.1 gives our assignment of the observed frequencies to the corresponding vibrational modes of the free fluorobenzene molecule. For the C_6H_5F/Rh(111) spectrum, the 340, 520, and 785 cm^{-1} peaks decreased in intensity in the off specular spectra, indicating that these peaks are from dipole scattering [7]. However, the 1115, 1315 and 1410 cm^{-1} peaks have similar intensity off specular, indicating that these peaks are from impact scattering [8]. Since there is little or no dipole scattering from those modes assigned to vibrations oriented parallel to molecular ring of fluorobenzene (i.e., those with A_1 or B_1 symmetry in the free molecule), we conclude that, at low coverages, fluorobenzene bonds to the Rh(111) surface with its molecular ring oriented parallel to the surface, in the same manner that we concluded in Chapter 4 the orientation of benzene bonded to the Rh(111) surface.

At saturation coverage, fluorobenzene orders [on Rh(111) at 310K] into a $(\sqrt{19} \times \sqrt{19})R23.4^\circ$ superlattice. Figure 6.3 shows the HREEL spectra for C_6H_5F and C_6D_5F adsorbed in the $(\sqrt{19} \times \sqrt{19})R23.4^\circ$ structure. Off specular measurements indicate that all the vibrational peaks observed for the $(\sqrt{19} \times \sqrt{19})R23.4^\circ$ structure are due to dipole scattering. Table 6.1 gives our assignment of the vibrational frequencies observed for the $(\sqrt{19} \times \sqrt{19})R23.4^\circ$ structure to the corresponding vibrations of the free fluorobenzene molecule.

For the $(\sqrt{19} \times \sqrt{19})R23.4^\circ$ structure, the observation of more vibrational modes than observed at low coverages probably results from a slight tilting of the fluorobenzene molecules within the $(\sqrt{19} \times \sqrt{19})R23.4^\circ$ structure. A slight tilting of the molecules would cause more modes to have a net dynamic dipole moment perpendicular to the surface and, hence, these modes would be observable in the HREEL spectra by dipole scattering. The $(\sqrt{19} \times \sqrt{19})R23.4^\circ$ unit cell is large enough to accommodate three fluorobenzenes per unit cell with only a slight overlap of neighboring molecules; a slight overlap could account for the tilting of the molecules. Therefore, the $(\sqrt{19} \times \sqrt{19})R23.4^\circ$ fluorobenzene/Rh(111) structure differs substantially from the $(2\sqrt{3} \times \sqrt{3})$rect benzene/Rh(111) structure in that, at saturation benzene coverages, only flat lying benzene molecules are observed. Consequently, we suggest that the tilting of adsorbed fluorobenzene at saturation coverage is due to the interaction of the substituted fluorine atom with neighboring molecules.

Like benzene coadsorbed with CO on Rh(111), fluorobenzene on Rh(111) forms a c($2\sqrt{3}$ x 4)rect LEED structure when the surface is precovered with one eighth of a monolayer of CO and a (3x3) LEED structure when the surface is precovered with two ninths of a monolayer of CO. Unlike benzene coadsorbed with CO on Rh(111), however, we were unable to observe a well ordered c($2\sqrt{3}$ x 4)rect LEED pattern, but instead only observed a "streaky" c($2\sqrt{3}$ x 4)rect LEED pattern, indicating some disorder for this overlayer.

Figures 6.4 and 6.5 show the HREEL spectra for the CO plus fluorobenzene structures. While the observed vibrational frequencies for the coadsorbed structures are similar to those of the ($\sqrt{19}$ x $\sqrt{19}$)R23.4° structure, there are differences in intensities, which we are unable to explain at this point. We believe, however, that the structure of fluorobenzene within the coadsorbed unit cell is likely to be similar to that found for benzene in the same unit cells (see Chapter 5), with possibly a slight tilting of the fluorobenzene molecule.

6.4 Acetylene/Rh(111)

Below 270K, acetylene chemisorbs on Rh(111) molecularly. For acetylene coverages near 0.25 of a monolayer, a (2x2) LEED pattern is observed for temperatures as low as 60K. Figure 6.6 shows the HREEL spectra for acetylene adsorbed in a (2x2) monolayer at 77K. Figure 6.7 shows how we assign the chemisorbed acetylene vibrational frequencies to those of the gas phase molecule. Off specular measurements indicate that, for the chemisorbed C_2H_2 spectrum, the 1120

and 1260 cm^{-1} peaks are predominantly due to impact scattering, while the remaining peaks are due to dipole scattering. This, coupled with our assignment of the chemisorbed frequencies, indicates that chemisorbed acetylene on Rh(111) has C_s symmetry with the mirror plane perpendicular to the C-C bond. Further, the shifts in frequencies and the intensities of the vibrational modes are characteristic of those found for acetylene "di - σ + π" bonded in metal clusters or on other metal surfaces [10]. Consequently, we propose the structural model shown in Fig. 6.8 for the (2x2) acetylene overlayer.

When CO is coadsorbed with acetylene on Rh(111), it is possible to form a c(4x2) LEED structure; however, we found this LEED structure to be more difficult to form than other coadsorbed structures. Figure 6.9 shows the HREEL spectra for C_2H_2 and CO + C_2H_2 on Rh(111). For these spectra, the surface, at 77K, was exposed first to CO then to C_2H_2. To form the c(4x2) structure, it was necessary to anneal the sample above 200K. The HREEL spectra for coadsorbed acetylene and CO still exhibit the vibrational peaks of chemisorbed acetylene, indicating that acetylene maintains its molecular integrity when coadsorbed with CO. However, the vibrational frequencies for coadsorbed acetylene are shifted slightly from those observed for the (2x2) acetylene structure, indicating that some interaction occurs between coadsorbed acetylene and CO.

Two C-O stretching modes at ~1780 and ~2025 cm^{-1} are observed in the spectra for the c(4x2) structure in Fig. 6.9c. However, we were also able to form the c(4x2) CO + C_2H_2 structure by first forming the (2x2) C_2H_2 structure, then exposing the surface, at 240K, to CO. In this case, only one C-O stretching mode is observed at 1725 cm^{-1}. Consequently, we believe that CO occupies only one type of site within the c(4x2) unit cell, rather than two sites as one would deduce from Fig. 6.9c. The CO adsorption site within the c(4x2) unit cell is probably a hollow site, since the C-O stretching frequency (1725 cm^{-1}) is fairly low. The C-O stretching mode at ~2025 cm^{-1} in Fig. 6.9c is probably from some disordered CO adsorbed outside the c(4x2) CO + C_2H_2 structure.

6.5 CO-induced Ordering of Ethylidyne and Propylidyne/Rh(111)

For sample temperatures between 220 and 400K, ethylene decomposes on the Rh(111) surface to form an ethylidyne ($\equiv CCH_3$) species [11]. For temperatures below 270K, ethylidyne orders into a (2x2) superlattice [11,12]. It has been previously reported [11,12] that the (2x2) ethylidyne LEED structure transforms to a c(4x2) structure when warmed slowly to room temperature. In our experiments, we observed only disordering for temperatures above 270K. However, we did observe that the (2x2) to c(4x2) transformation could be induced by coadsorption of CO. Up to 0.25 monolayers of CO can be coadsorbed with a (2x2) coverage of ethylidyne to produce a c(4x2) LEED structure. Best ordering is achieved by preadsorbing the quarter monolayer of CO followed by exposure to 10 L of

ethylene. Although preadsorption of CO does not change the temperature at which ethylidyne forms, the c(4x2) structure can be produced preferentially over the (2x2) structure, even at 220K, by CO preadsorption. Also, CO coadsorption does not change the decomposition temperature of ethylidyne (400 K).

Figure 6.10 shows three representative HREEL spectra and LEED photos for ethylidyne and ethylidyne plus CO on the Rh(111) surface at 310K. The LEED photo for ethylidyne plus 0.03 monolayers of CO is characteristic of ethylidyne adsorption at 310K. Adding CO causes the blotches in the $\sqrt{3}$ x$\sqrt{3}$ R30° positions of the LEED pattern to spread apart until the c(4x2) pattern shown in Fig. 6.10 is reached for 0.25 of a monolayer of added CO. While preadsorption of CO was necessary to form a sharp c(4x2) pattern, we find that adsorption of NO, a ligand similar to CO, readily produced a sharp c(4x2) pattern, when adsorbed after forming a disordered ethylidyne monolayer.

Several features of the ethylidyne + CO vibrational spectra in Fig. 6.10 are noteworthy. First, the ethylidyne frequencies are unchanged when CO is added, suggesting that ethylidyne bonding at 3-fold hollow sites [12] is unchanged. Second, the predominant C-O stretching frequency at 1790 cm^{-1} is again characteristic of CO bonded at 3-fold hollow sites on this surface. These observations and use of Van der Waals radii to determine the most probable packing of adsorbates lead to an obvious structural model for the c(4x2) CCH_3 + CO monolayer. Figure 6.11 shows a top view of the c(4x2) structure, which is consistent with the experimental observations,

along with the (2x2) and disordered ethylidyne overlayer structures. Also shown are the temperature ranges for which each structure is stable.

Recently, the c(4x2) structure has been solved by a dynamical LEED analysis [13]. This analysis, consistent with our proposed structure, has determined that ethylidyne bonds at hcp 3-fold hollow sites with the same bond lengths as the CO-free (2x2) structure [12] (i.e., a C-C bond length of 1.45 Å and a Rh-C bond length of 2.03 Å). Further the coadsorbed CO is determined to bond at fcc 3-fold hollow sites.

Propylene adsorption on Rh(111) is similar to ethylene adsorption in that, between 220-270K, propylene decomposes to form a (2x2) propylidyne ($\equiv CCH_2CH_3$) overlayer, a structure similar to the (2x2) ethylidyne ($\equiv CCH_3$) overlayer [14]. In the (2x2) propylidyne overlayer, the bottom two carbon atoms of the propylidyne species are thought to be ordered in a (2x2) lattice while the methyl groups are disordered [14].

We find that, by postadsorbing CO to the (2x2) propylidyne overlayer, the propylidyne methyl groups can be induced to order into a $(2\sqrt{3} \times 2\sqrt{3})R30^\circ$ superlattice. The C-O stretching frequency of the CO within the $(2\sqrt{3} \times 2\sqrt{3})R30^\circ$ structure is 1750 cm^{-1}, again characteristic of CO adsorption at a 3-fold hollow site. In Fig. 6.12, we show our proposed model for the $(2\sqrt{3} \times 2\sqrt{3})R30^\circ$ propylidyne + CO structure, which is the same as that proposed by Koestner et al. [14] except for the addition of coadsorbed CO.

6.6 Sodium + CO/Rh(111)

We have also studied the CO-induced ordering of sodium on Rh(111). Figure 6.13 shows the HREEL spectra and several LEED patterns for a quarter of a monolayer of sodium on Rh(111) at 310K following various exposures of CO. For low CO exposures, a c(4x2) LEED pattern is observed and an exceptionally low C-O stretching frequency of 1410 cm^{-1} appears in the corresponding HREEL spectrum. With increasing CO exposure, the c(4x2) LEED pattern disorders into a streaky, intermediate LEED pattern before reforming another c(4x2) LEED pattern. Between the formation of the low CO coverage c(4x2) LEED pattern and the high CO coverage c(4x2) LEED pattern, the CO to Na ratio increases from less one CO per Na to two CO's per Na, as determined from the CO thermal desorption yield. With further increase in CO exposure, a series of complicated LEED patterns occurs until, finally, a ($\sqrt{3}$ x 7)rect LEED pattern is observed for a saturation CO exposure on the quarter monolayer sodium covered Rh(111) surface.

With increasing CO exposure, the C-O stretching increases continuously from 1410 to 1695 cm^{-1} when coadsorbed with a quarter monolayer of sodium on Rh(111). While for low CO exposures only one, narrow C-O stretching mode is observed, indicating only one type of CO adsorption site, for higher CO exposures, the C-O stretch is somewhat broader and has a low frequency shoulder, indicating possibly more than one type of CO adsorption site is occupied at higher CO coverages. For all CO exposures, however, the C-O stretching frequency is substantially lower than either that of gas phase CO (2145 cm^{-1}) or of CO adsorbed alone

on the Rh(111) surface. We attribute the low C-O stretching frequency to charge transfer from the sodium adatoms through the substrate and into the $2\pi^*$ orbital of CO. This model has been proposed previously to explain reduced C-O stretching frequencies for CO coadsorbed with alkali adatoms on numerous metal surfaces [1,15-17] and has been substantiated by other experimental techniques [18]. This model will be elaborated on in the following sections.

It is interesting that sodium, along with acetylene and ethylidyne, orders into a (2x2) lattice on Rh(111) without coadsorbed CO and a c(4x2) lattice with coadsorbed CO. In the hexagonal (2x2) lattice, the adsorbates have the maximum number of nearest neighbors, which helps to reduce total energy of the ordered overlayer. However, a CO molecule cannot fit into a (2x2) unit cell that already has one Na, acetylene, or ethylidyne, so the adsorbates must reorder into a c(4x2) lattice, where the unit cell has the same area as the (2x2) unit cell, but now has room for a CO molecule to adsorb in the center due to the rectangular shape of the c(4x2) unit cell.

6.7 Work Function Measurements

Table 6.2 lists the various combinations of adsorbates that we have coadsorbed on the Rh(111) surface. From Table 6.2, one sees that all the ordered, coadsorbed structures contain CO or a CO like ligand, NO. In part, the prevalence of CO in the coadsorbed structures comes from CO being so successful at inducing order in our initial studies that we tended to prefer it in subsequent studies. Another, but less obvious

common characteristic of the ordered, coadsorbed structures is that each pair of coadsorbates can be classified as a donor-acceptor pair. [By donor, we mean that an adsorbate is a net donor of electrons to the surface and, by acceptor, that an adsorbate (e.g., CO or NO) is a net acceptor of electrons from the surface.] We believe that the combination of donor-acceptor pairs plays an important role in the ordering of intermixed surface structures. This becomes more apparent when one considers the combinations of coadsorbates on Rh(111) that form disordered or segregated overlayers; these combinations can be classified as acceptor-acceptor or donor-donor pairs.

To further investigate the donating or accepting character of the coadsorbates on Rh(111), we have measured the work function changes that occur during the adsorption of those adsorbates that form ordered, coadsorbed structures on Rh(111) at room temperature. The experimental set up used for measuring work function changes is described in Section 2.2.6. In the following sections, we present the results of our work function measurements, first for the various adsorbates alone on Rh(111) and then for them coadsorbed in ordered structures. Finally, we present a simplified theoretical discussion for how CO can induce order in an adsorbed overlayer and the role donor-acceptor pairs play in this ordering.

6.7.1 Work Function Measurements: Adsorption Alone

When an atom or molecule is adsorbed on a surface, the work function can change due to a transfer of electronic charge between the adsorbate and the surface. Figure 6.14 illustrates a simplified model of the physical basis for this effect. Basically, the charge transfer creates a surface dipole layer that results in an increase or decrease in the energy needed to remove an electron from the bulk, depending on the direction of charge transfer. Generally, an adsorbate that accepts electrons from the surface increases the work function; whereas, an adsorbate that donates electrons to the surface decreases the work function.

Figure 6.15 shows the work function change as a function of CO coverages on Rh(111). The positive increase in the work function indicates that adsorbed CO is a net acceptor of electrons from the Rh(111) surface. For CO coverages less than 0.33, where CO adsorbs only at top sites, the work function change may be fit with a simplified model for mobile adsorption. If we consider an isolated adsorbed species with surface density N, an effective dipole moment μ, and polarizability α, then the work function change ($\Delta\phi$) is given (in SI units) by [19,20]

$$\Delta\phi = \frac{-eN\mu}{\epsilon_0[1 + (9/4\ \pi)\ \alpha N^{3/2}]} \qquad (1)$$

where ϵ_0 is the vacuum permittivity. A good fit for $\theta_{CO} \leq 0.33$ (shown by the dashed curve in Fig. 6.15) can be obtained with $\mu_{CO} = -0.67 \times 10^{-30}$ C.m and $\alpha_{CO} = 0.34 \times 10^{-28}$ m^3.

For $\theta_{CO} > 0.33$, $\Delta\phi$ increases dramatically until reaching a value of 1.05 eV at a saturation CO coverage ($\theta_{CO} = 0.75$). To achieve the (2x2) LEED structure that occurs at saturation, we found it necessary to cool the sample to -100°C, while the other CO coverages could be done at room temperature. We attribute the dramatic increase in $\Delta\phi$ for $\theta_{CO} > 0.33$ to bridge bonded CO molecules on the Rh(111) having a much larger effective dipole moment than top bonded CO. For $\theta_{CO} > 0.33$, CO bonds at both bridge and top sites; but, since we are unable to determine the relative coverages of bridge and top bonded CO for CO coverages between 0.33 and 0.75, we are unable to model this system in order to determine the effective dipole moment or polarizability for bridge bonded CO on this surface.

Figure 6.16 shows the work function of the Rh(111) surface as a function sodium coverage. The value of 5.4 eV for the work function for the clean Rh(111) surface is from Ref. 21. Sodium coverages were determined from the sodium thermal desorption yield and calibrated against the $(\sqrt{3} \times \sqrt{3})R30°$ and close-packed LEED structures [22]. The dashed line shows that the work function change is linear at low sodium coverages; from this line, we deduce an effective dipole moment, μ_{Na}, of 16×10^{-30} C.m. Consequently, we see that sodium adatoms are strong electron donors to the surface. Also by assuming a polarizability, α_{Na}, of 3.0×10^{-28} m^3, we can achieve a good fit for the work function changes, for $\theta_{Na} < 0.2$, using the same model as for adsorbed CO.

Figure 6.17 shows the work function of the Rh(111) surface as a function benzene and fluorobenzene exposure. The decrease in work function upon benzene and fluorobenzene adsorption indicates that both molecules donate electrons to the surface. For benzene adsorbed on Rh(111), we determined from the H_2 desorption yield that the benzene coverage is linear as a function of exposure up to saturation coverage. (Only a small fraction of benzene desorbs molecularly.) If we assume that the fluorobenzene coverage is also linear as a function of exposure, then we can deduce, for benzene and fluorobenzene, effective dynamic dipole moments, $\mu_{ben} = 6.7 \times 10^{-30}$ cm and $\mu_{fb} = 6.5 \times 10^{28}$ C.m, and polarizabilities, $\alpha_{ben} = 1.3 \times 10^{-30}$ m^3 and $\alpha_{fb} = 1.5 \times 10^{-28}$ m^3, respectively. (It should be noted that the benzene-fluorobenzene values are within experimental error of each other.)

Figure 6.18 shows the work function of the Rh(111) surface at 310K as a function of ethylene exposure. At this temperature ethylene decomposes to form ethylidyne, which saturates at a coverage of 0.30 of a monolayer [23]. If we assume that the ethylidyne coverage is linear with ethylene exposure up to saturation coverage, then we find that $\mu_{eth} = 3.1 \times 10^{-30}$ C.m and $\alpha_{eth} = 0.62 \times 10^{-28}$ m^3. If the ethylene sticking probability actually decreases with increasing coverage, as often occurs for adsorption processes, then μ_{eth} and α_{eth} would be smaller than determined here.

Table 6.3 summarizes the results of our work function measurements for adsorption alone on the Rh(111) surface at room temperature. As already mentioned, the sign of the effective dipole moment indicates

the direction of charge transfer to the surface, with adsorbed CO being a net acceptor of electrons and the other adsorbates being net donors of electrons.

6.7.2 Work Function Measurements: Coadsorption with CO

When CO is adsorbed on metal surfaces, the C-O stretching frequency is generally observed to be reduced from the value of 2145 cm^{-1} of gas phase CO. Also, a further reduction in the C-O stretching frequency has been observed when CO is coadsorbed with alkali atoms [1,15-17]. In both cases, the reduction in the C-O stretching frequency has been explained in terms of charge transfer into the antibonding, $2\pi^*$ orbital of the adsorbed CO molecule [1,15-18, 25]. Consequently, it is interesting to see if the reduction in stretching frequency of coadsorbed CO correlates to the amount of charge donated to the surface by the coadsorbate. To study this idea, we will assume the magnitude of the effective dipole moment of an adsorbate alone on Rh(111) to be a measure of how much charge the adsorbate donates to the surface in a coadsorbed structure. In Fig. 6.19, we plot, for the coadsorbed, ordered structures where there is one CO molecule per coadsorbate, the C-O stretching frequency of coadsorbed CO versus the effective dipole moment of the coadsorbate. While more data points are needed to confirm the trend, it appears that the more the coadsorbate donates electrons to the surface, the greater the reduction in the C-O stretching frequency.

Our measurements of the work function of the CO coadsorbed structures also indicates that CO accepts electrons from the surface within these surface structures. Table 6.4 lists the changes in work function, relative to the clean Rh(111) surface, that we observed for CO coadsorbed with organic adsorbates on Rh(111). As can be seen from Table 6.4, the absolute value of the work function increases (i.e., the work function change from the clean surface decreases) as the ratio of CO's to coadsorbates increases, indicating that CO acts as a net acceptor of electrons from the surface within these coadsorbed, ordered structures.

Figure 6.20 shows the work function of Rh(111) surface as a function of exposure to CO when the surface has been precovered with 0.15 and 0.25 of a monolayer of sodium. For both sodium coverages, the work function increases toward the clean metal value with increasing CO exposure, indicating the CO acts as an electron acceptor when coadsorbed with sodium. For $\theta_{Na} = 0.25$, the initial dip in work function can be explained using a model developed by Albano [25]. This model shows that a dip in the work function can occur, due to cross depolarization effects, when a surface precovered with an electropositive adsorbate (i.e., an electron donor) is exposed to an electronegative adsorbate (i.e., an electron acceptor). The dip occurs if the electropositive adsorbate (i.e., Na) has a much larger polarizability than the electronegative adsorbate (i.e., CO). In this case, the dipole moment of adsorbed CO induces a much larger increase in the dipole

moment of adsorbed Na than Na induces in CO, leading to the initial decrease in work function with the addition of CO.

It is interesting to note that the same series of LEED patterns were observed for CO exposure to a $\theta_{Na} = 0.15$ covered surface as for $\theta_{Na} = 0.25$, including the two c(4x2) patterns. The observation of a c(4x2) pattern, which implies a sodium coverage of 0.25 within the ordered domains for CO coadsorbed with $\theta_{Na} = 0.15$, indicates that an interaction exists that draws the coadsorbed CO's and Na's together to form domains of the coadsorbed, ordered structures. In the next section, we discuss how the interaction between coadsorbates may be related to the donor and acceptor properties of coadsorbed Na and CO.

6.8 Theoretical Basis for CO-induced Ordering

A necessary condition for the formation of intermixed, ordered structures when CO is coadsorbed with other adsorbates is that the Helmholtz free energy is less for the ordered structure compared to that of a disordered overlayer:

$$F_{ordered} - F_{disordered} = (U_{ordered} - U_{disordered}) - T(S_{ordered} - S_{disordered}) < 0$$

The difference in free energy, $\Delta F = F_{ordered} F_{disordered}$, between an ordered and disordered overlayer is composed of two terms—an entropy term, $T\Delta S = T(S_{ordered} - S_{disordered})$ that drives the system toward disorder and a interaction energy term, $\Delta U = U_{ordered} - U_{disordered}$ that drives the system toward order.

Since adsorbed a CO molecule blocks several neighboring adsorption sites as well as its own adsorption site, coadsorbed CO will reduce the entropy of a disordered overlayer reducing the number of adsorption sites accessible to the coadsorbate. Consequently, CO site blocking reduces the difference in entropy between a disordered and ordered coadsorbed overlayer, thereby making an ordered overlayer more likely. This reduction in entropy, therefore, helps the 0.25 monolayers of sodium and ethylidyne, which are disordered at room temperature, to order at this temperature in a c(4x2) structure when coadsorbed with CO.

Coadsorbed systems can be further promoted to form ordered structures by the interaction energies between adsorbates. As mentioned in Section 5.3.2, calculations of the interaction energy between CO's adsorbed on Rh(111) by Ruckenstein and Halachev [26] indicate that the interaction energy is positive (repulsive) for small separation distances and negative (attractive) for intermediate distances. Within the coadsorbed, ordered structures the CO molecules are separated by intermediate distanced (4 to 8 Å), so the CO-CO interaction should help to stabilize these ordered structures. Likewise, the coadsorbate coadsorbate interactions may also help to stabilize the ordered structures; but these interactions have not yet been extensively investigated, either theoretically or experimentally, for adsorbates on Rh(111), so we are unable to comment further on the role of these interactions in the ordering of the coadsorbed overlayer.

Another interaction, which we believe plays an important role in the formation of ordered, coadsorbed structures, is the CO-coadsorbate interaction. As mentioned earlier, the combinations that form ordered, coadsorbed structures can be classified as donor-acceptor pairs, while those combinations that do not form ordered, coadsorbed structures can be classified as donor-donor or acceptor-acceptor pairs. This correlation suggests that the interactions between unlike adsorbates may be related to their donor-acceptor character.

The interactions between coadsorbed donor and acceptor adsorbates have been investigated theoretically by Norskov et al. [27]. The interaction energy between two coadsorbates can be divided into two terms. The first term describes the direct interaction due to an overlap between the molecule and coadsorbate orbitals as well as the indirect interaction mediated through the surface electrons. The second term describes the interaction energy between one adsorbate and the electrostatic potential induced by the other adsorbate. Norskov et al. [27] consider only the contribution of the second term to the interaction energy. They find an electropositive (electronegative) adsorbate induces an electrostatic potential that makes it energetically favorable for an electronegative (electropositive) adsorbate to occupy a nearest neighbor adsorption site. They also find that the metal quickly screens the induced electrostatic potential for distances much further away from the adsorbate than the nearest neighbor sites, so the interaction is only strong between coadsorbates sitting next to each other. For K and CO coadsorbed on Fe(110), Norskov et al.

calculate an interaction energy in the range between 0.1 and 0.3 eV. We can use this result to obtain an order of magnitude feel for the electrostatic interaction energy between CO and the coadsorbates on Rh(111). We can do this by assuming that adsorbed sodium behaves similarly to adsorbed potassium and that the interaction energy scales with effective dipole moment of the coadsorbate. In this case, the interaction energy should range from a few tenths of an eV for CO coadsorbed Na to a few hundredths of an eV for CO coadsorbed with CCH_3. If one compares these values with the values of a few hundredths of an eV calculated by Ruckenstein and Halachev [26] for the CO-CO interaction energy, one can see that the CO-coadsorbate interaction energy is at least the same order of magnitude and usually greater than the CO-CO interaction energy. Consequently, the CO-coadsorbate interaction can strongly stabilize an intermixed, ordered structure if the coadsorbate is a net donor of electrons to the surface.

6.9 Conclusions

CO induced ordering on the Rh(111) surface has been observed for numerous adsorbates: benzene, fluorobenzene, acetylene, ethylidyne, propylidyne, and sodium. Work function measurements indicate that a common characteristic of these coadsorbates with CO is that they donate electrons to the surface. Work function measurements also indicate that the C-O stretching frequency of coadsorbed CO is correlated to amount of the electron charge donated to the surface by the coadsorbate. Since CO is a net acceptor of electrons from the surface as

indicated by work function measurements, we suggest that the ability of coadsorbed CO to induce order in the adsorbed overlayer is related to the formation of donor-acceptor pairs.

Two important questions still remain to be fully answered. The first question is whether CO can promote ordering on other crystal surfaces besides Rh(111) and Pt(111). Here, we note that Hiroko Ohtani of our group has recently observed CO induced ordering of benzene on the Pd(111) surface and that Brian Bent, Chi-Tzu Kao, and Al Slavin, also of our group, have recently observed CO induced ordering of benzene and ethylidyne on the Rh(100) surface. The second question is whether or not the ordering of donor-acceptor pairs is a general phenomenon on surfaces. So far there have been only a few reports [17,28] of coadsorbed species forming long range ordered structures; largely we believe because coadsorption of adsorbates has not been extensively studied by LEED. Consequently, more LEED studies are necessary, particularly with a wider variety of electropositive and electronegative adsorbates, to determine if ordering of donor-acceptor pairs is a general phenomenon.

Table 6.1. Assignment of observed vibrational frequencies for fluorobenzene adsorbed on Rh(111) at 310K.

Low Coverage $C_6H_5F(D_6D_5F)$	$(\sqrt{19} \times \sqrt{19})R23.4^\circ$ $C_6H_5F(C_6D_5F)$	Liquid C_6H_5F[6]	Mode Type	Liquid Phase Symmetry Representation
	225 (215)	—	ν_{Rh-FB}	—
340 (330)	345 (355)	—	ν_{Rh-FB}	—
520 (not obs.)	510 (510)	501	γ_{CF}	B_2
785 (575)	760 (580)	752	γ_{CH}	B_2
not obs.	not obs. (700)	685	ϕ_{CC}	B_2
not obs.	1015 (990) (1050)	1009	ring	A_1
1115 (835)	1105 (765)	1156	β_{CH}	B_1
not obs.	not obs. (1220)	1220	ν_{CF}	A_1
1315 (1300)	1345 (not obs.)	1326	ν_{CC}	B_1
1410 (1375)	1405 (1365)	1460	ν_{CC}	B_1
3015 (2225)	3015 (2220)	3067	ν_{CH}	A_1
		3053		A_1
		3040		A_1
		3100		B_1

FB = flourobenzene

Table 6.2. Combinations of adsorbates coadsorbed on the Rh(111) surface.

Intermixed, Ordered Coadsorbates	LEED Pattern(s) Observed
CO + C_6H_6	c($2\sqrt{3}$ x 4)rect, (3x3)
CO + C_6H_5F	streaky c($2\sqrt{3}$ x 4)rect, (3x3)
CO + C_2H_2	c(4x2)
CO + $\equiv CCH_3$	c(4x2)
NO + $\equiv CCH_3$	c(4x2)
CO + Na	c(4x2), ($\sqrt{3}$ x 7)rect, plus several others
CO + $\equiv CCH_2CH_3$	($2\sqrt{3}$ x $2\sqrt{3}$)R30°

Nonintermixed or Disordered Coadsorbates	LEED Patterns Observed
CO + NO	Disorder
Na + C_2H_2	Disorder
Na + $\equiv CCH_3$	Disorder
Na + C_6H_6	($\sqrt{3}$ x $\sqrt{3}$)R30° + ($2\sqrt{3}$ x 3)rect*

*Since the ($\sqrt{3}$ x $\sqrt{3}$)R30° and ($2\sqrt{3}$ x 3)rect are observed for Na and benzene, respectively, adsorbed alone on Rh(111), the observation of a mixture of these two LEED structures implies that these two coadsorbates segregate on the surface.

Table 6.3. Effective dipole moments, μ, and polarizability, α, for adsorbates alone on Rh(111).

Adsorbate	μ (10^{-30} C.m)	α (10^{-28} m^3)
CO (top site)	- 0.67	0.34
Na	+ 16	3.0
C_6D_6	+ 6.7	1.3
C_6D_5F	+ 6.5	1.5
$\equiv CCH_3$	+ 3.1	0.62

Table 6.4. Work function changes (in eV) relative to the clean Rh(111) surface for various ordered structures, with and without coadsorbed CO

Coadsorbate	Number of CO's per Coadsorbate		
	0	1	2
C_6D_6	$(2\sqrt{3} \times 3)$rect	$c(2\sqrt{3} \times 4)$rect	(3x3)
	-1.36	-0.64	-0.26
C_6D_5F	$(\sqrt{19} \times \sqrt{19})R23.4^\circ$	$c(2\sqrt{3} \times 4)$rect	(3x3)
	-1.24	-0.61	-0.24
$\equiv CCH_3$	disorder	c(4x2)	—
	-1.23	-0.32	—

REFERENCES

1. J.E. Crowell and G.A. Somorjai, Appl. Surface Sci. 19 (1984) 73.
2. R.J. Koestner, M.A. Van Hove, and G.A. Somorjai, Surface Sci. 107 (1981) 439.
3. M.A. Van Hove, R.J. Koestner, and G.A. Somorjai, Phys. Rev. Lett. 50 (1983) 903.
4. R. Eischens and W.A. Pliskin, Advan. Catalysis 10 (1958) 1.
5. H. Ibach and D.L. Mills, Electron Energy Loss Spectroscopy and Surface Vibrations, Academic, New York, 1982, pp. 284-293.
6. D.H. Whiffen, J. Chem. Soc. (1956) 1350.
7. See Section 3.3.2.
8. See Section 3.3.3.
9. G. Herzberg, Infrared and Raman Spectra of Polyatomic Molecules, Van Nostrand, New York, 1945.
10. N. Sheppard, J. Electron Spectrosc. Related Ph. 38 (1986) 175.
11. L.H. Dubois, D.G. Castner, and G.A. Somorjai, J. Chem. Phys. 72 (1980) 5234; B.E. Bent, C.M. Mate, and G.A. Somorjai, in preparation.
12. R.J. Koestner, M.A. Van Hove, and G.A. Somorjai, Surface Sci. 121 (1982) 321.
13. C.M. Mate, B.E. Bent, M.A. Van Hove, R.J. Koestner, G.S. Blackman, C.-T. Kao, and G.A. Somorjai, in preparation.
14. R.J. Koestner, M.A. Van Hove, and G.A. Somorjai, J. Phys. Chem. 87 (1983) 203.

15. J.E. Crowell, E.L. Garfunkel, and G.A. Somorjai, Surface Sci. 121 (1982) 303.

16. L. Wallden, Surface Sci. 134 (1983) L513.

17. R.A. de Paola, J. Hrbek, and F.M. Hoffmann, J. Chem. Phys. 82 (1985) 1; and references therein.

18. J. Lee, C.P. Hanrahan, J. Arias, R.M. Martin, and H. Metiu, Phys. Rev. Lett. 51 (1983) 1803.

19. J.R. MacDonald and C.A. Barlow, Jr., J. Chem. Phys. 39 (1963) 412.

20. J.R. MacDonald and C.A. Barlow, Jr., J. Chem. Phys. 44 (1966) 202.

21. E. Bertel, G. Rosina, and F.P. Netzer, Surface Sci. 172 (1986) L515.

22. H.W.K. Tom, C.M. Mate, X.D. Zhu, J.E. Crowell, Y.R. Shen, and G.A. Somorjai, Surface Sci., 172 (1986) 466.

23. B.E. Bent, unpublished results.

24. G. Blyholder, J. Phys. Chem. 68 (1964) 2772.

25. E.V. Albano, Appl. Surface Sci. 14 (1982) 183.

26. E. Ruckenstein and T. Halachev, Surface Sci. 122 (1982) 422.

27. J.K. Norskov, S. Holloway, and N.D. Lang, J. Vac. Sci. Technol. A3 (1985) 1668; N.D. Lang, S. Holloway, and J.K. Norskov, Surface Sci. 150 (1985) 24.

28. E.L. Garfunkel and G.A. Somorjai, Surface Sci. 115 (1982) 441.

FIGURE CAPTIONS

Fig. 6.1 The left hand side shows vibrational spectra obtained using HREELS for CO chemisorbed on Rh(111) at 300K as a function of CO exposure (from ref. 1). The right hand side shows the LEED patterns observed for the clean Rh(111) surface and the two ordered structures of CO on Rh(111).

Fig. 6.2 Vibrational spectra obtained by HREELS in the specular direction for a ~1/3 of a saturation coverage of fluorobenzene chemisorbed on Rh(111) at 310K: (A) C_6H_5F; (B) C_6D_5F.

Fig. 6.3 Vibrational spectra obtained by HREELS in the specular direction for the saturation coverage, $(\sqrt{19} \times \sqrt{19})R23.4^\circ$ structure of fluorobenzene chemisorbed on Rh(111) at 310K: (A) C_6H_5F; (B) C_6D_5F.

Fig. 6.4 Vibrational spectra for C_6H_5F coadsorbed with CO on Rh(111) at 310K: (A) the surface was precovered with a 1/8 monolayer CO then exposed to 30 L of C_6H_5F to form a streaky $c(2\sqrt{3} \times 4)$rect LEED pattern; (B) the surface was first exposed to 2.0 L of C_6H_5F then to 1.0 L of CO to form a (3x3) LEED pattern.

Fig. 6.5 Vibrational spectra for C_6D_5F coadsorbed with CO on Rh(111) at 310K. For both spectra, the surface was first precovered with CO then exposed to enough C_6D_5F to saturate the surface: (A) θ_{CO} = 0.12, streaky ($2\sqrt{3}$ x 4)rect LEED pattern; (B) θ_{CO} = 0.22, (3x3) LEED pattern.

Fig. 6.6 Vibrational spectra obtained by HREELS in the specular direction the (2x2) structure of C_2H_2 and C_2D_2 on Rh(111) at 77K.

Fig. 6.7 Assignment of the observed frequencies of chemisorbed C_2H_2 on Rh(111) to the corresponding vibrations of gas phase C_2H_2 [9].

Fig. 6.8 Proposed structure for the (2x2) structure of acetylene on Rh(111). Large, open circles represent the rhodium surface atoms, smaller, open circles represent carbon atoms, and the small, black circles represent hydrogen atoms.

Fig. 6.9 Vibrational spectra of C_2H_2 and C_2H_2 plus CO on Rh(111). (A) is the same spectra in Fig. 6.8. For (B) and (C) the surface, at 77K, was first exposed to CO, then exposed to C_2H_2, and annealed to 220K. All the spectra were taken at a sample temperature of 77K.

Fig. 6.10 HREEL spectra and LEED patterns obtained for ethylidyne and ethylidyne plus CO adsorbed on Rh(111) at 310K.

Fig. 6.11 Top view of the proposed models for the (2x2), c(4x2), and disordered ethylidyne overlayers on Rh(111). Also indicated are the temperature ranges that the structures are stable and how the structures transform from one to the other.

Fig. 6.12 Proposed models for the $(2\sqrt{3} \times 2\sqrt{3})R30^{\circ}$ propylidyne ($\equiv CCH_2CH_3$) plus CO structure. The open circles represent rhodium surface atoms, and the black circles represent the CO molecule viewed end on. In the upper part of the figure, the hatch circles represent the Van der Waals dimensions of the propylidyne hydrogen atoms, while, on the lower part of the figure, the hydrogen atoms are represented by black dots in order to make the rhodium surface atoms and the propylidyne carbon skelton more visible.

Fig. 6.13 Vibrational spectra of CO coadsorbed with a quarter monolayer of sodium on Rh(111) at 310K.

Fig. 6.14 Formation of a dipole layer for a (A) donor adsorbate and an (B) acceptor adsorbate.

Fig. 6.15 Work function change of the Rh(111) surface as a function of CO coverage. The dashed curve shows the fit with the model discussed in the text.

Fig. 6.16 The work function of the Rh(111) surface as a function of sodium coverage. The clean Rh(111) work function is from Ref. 21.

Fig. 6.17 Work function of the Rh(111) surface at 310K as a function of benzene and fluorobenzene exposure. The clean Rh(111) work function is from Ref. 21.

Fig. 6.18 Work function of the Rh(111) surface at 310K as a function of ethylene exposure. The clean Rh(111) work function is from Ref. 21.

Fig. 6.19 The C-O stretching frequency of CO coadsorbed in structures that have one CO per coadsorbate is plotted against the effective dipole moment of the coadsorbate alone on Rh(111).

Fig. 6.20 The work function of the Rh(111) surface at 310K as a function of CO exposure when the surface was first precovered with θ_{Na} = 0.0, 0.15, and 0.25.

CO / Rh(111)

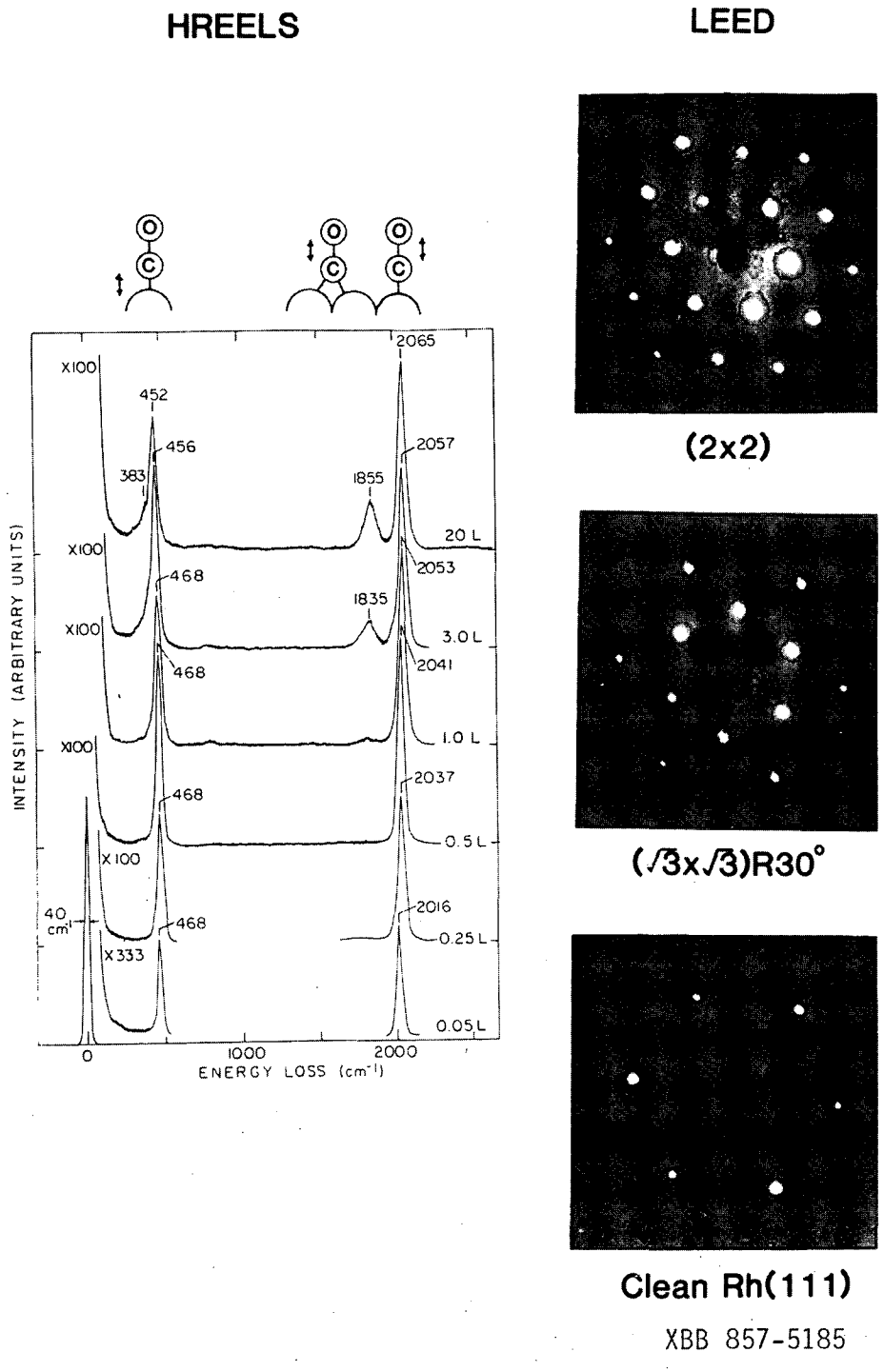

Figure 6.1

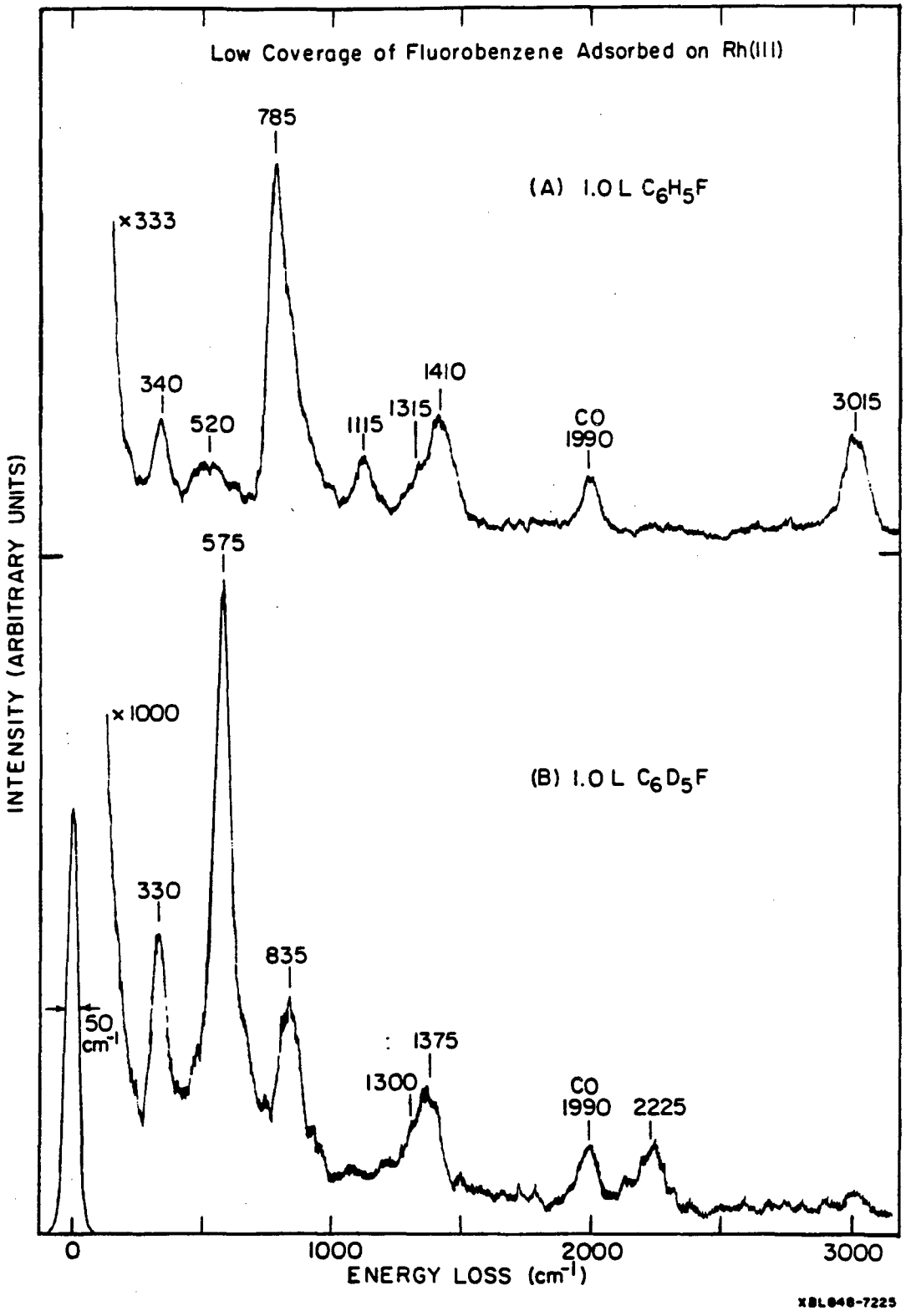
Low Coverage of Fluorobenzene Adsorbed on Rh(111)
785
(A) 1.0 L C_6H_5F
×333
340
520
1115
1315
1410
CO
1990
3015
575
×1000
(B) 1.0 L C_6D_5F
330
835
50
cm⁻¹
1375
1300
CO
1990
2225
INTENSITY (ARBITRARY UNITS)
0
1000
2000
3000
ENERGY LOSS (cm⁻¹)
XBL848-7225

Figure 6.2

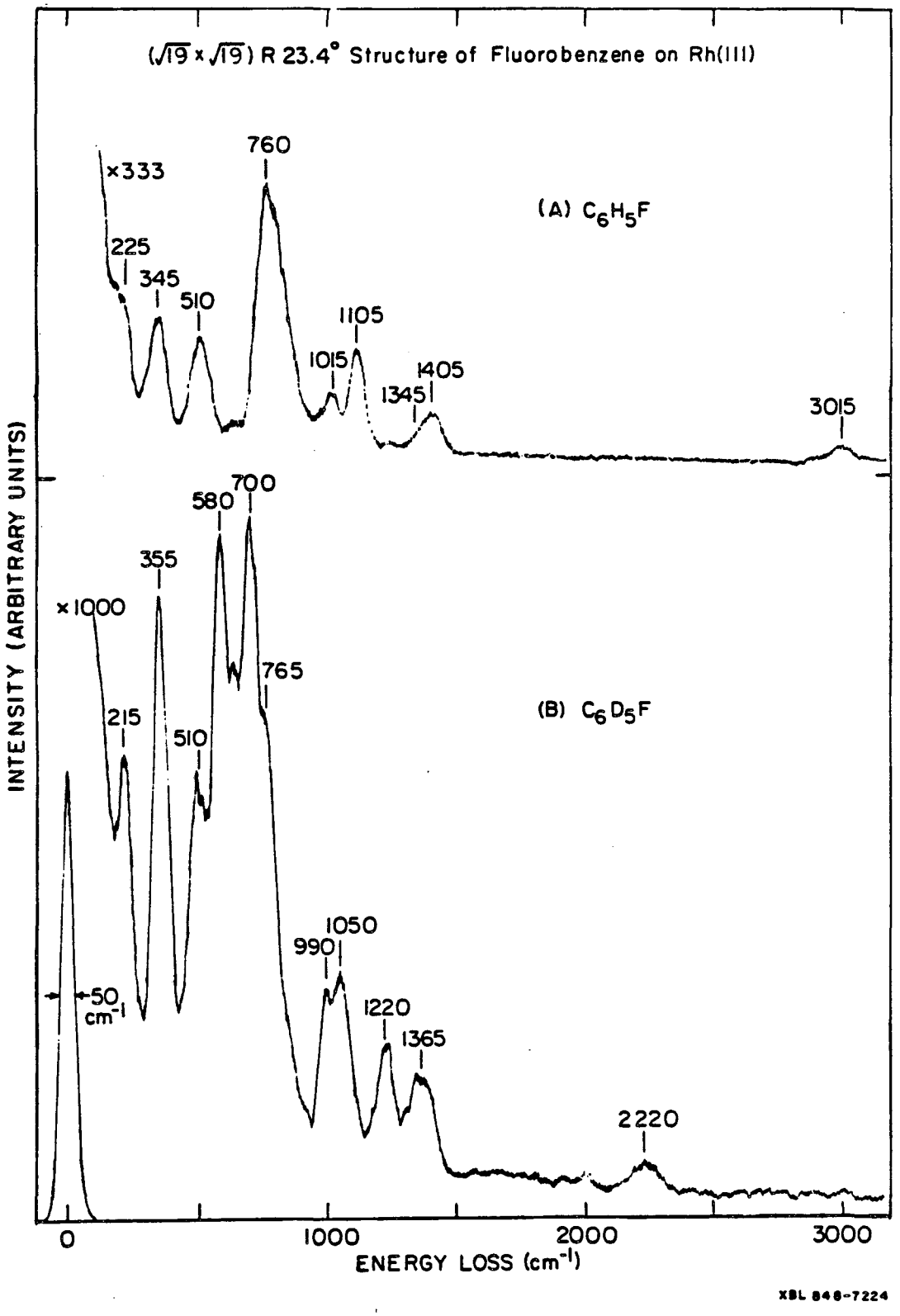
(√19 x √19) R 23.4° Structure of Fluorobenzene on Rh(111)
×333
760
225
345
510
1105
1015
1405
1345
3015
(A) C6H5F
INTENSITY (ARBITRARY UNITS)
580
700
355
×1000
765
215
510
(B) C6D5F
1050
990
50 cm-1
1220
1365
2220
0
1000
2000
3000
ENERGY LOSS (cm-1)
XBL 848-7224

Figure 6.3

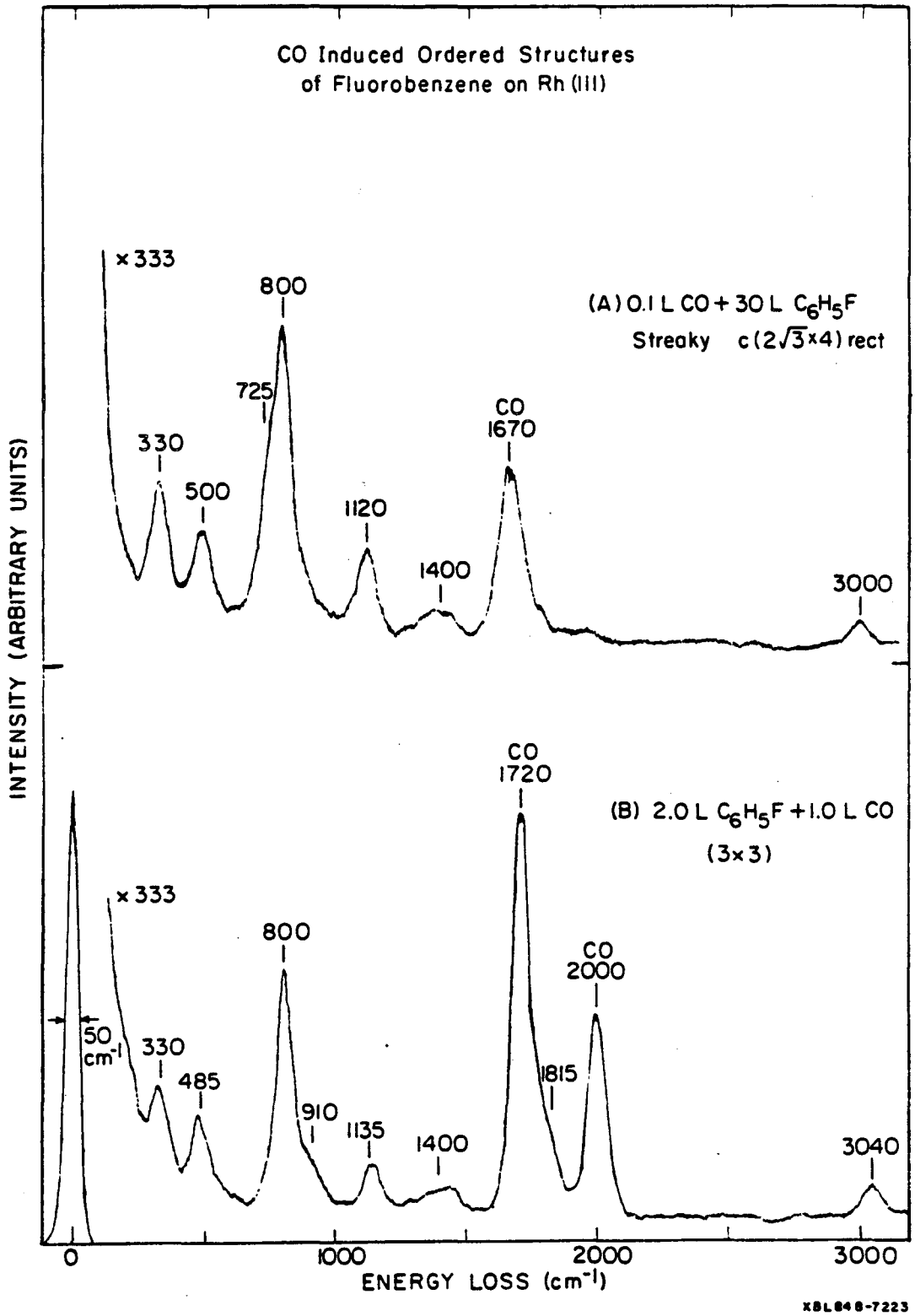
CO Induced Ordered Structures
of Fluorobenzene on Rh (111)
INTENSITY (ARBITRARY UNITS)
×333
800
725
330
500
1120
1400
CO
1670
3000
(A) 0.1 L CO + 30 L C6H5F
Streaky c(2√3×4) rect
CO
1720
(B) 2.0 L C6H5F + 1.0 L CO
(3×3)
×333
800
CO
2000
50
cm-1
330
485
910
1135
1400
1815
3040
0
1000
2000
3000
ENERGY LOSS (cm-1)
XBL848-7223

Figure 6.4

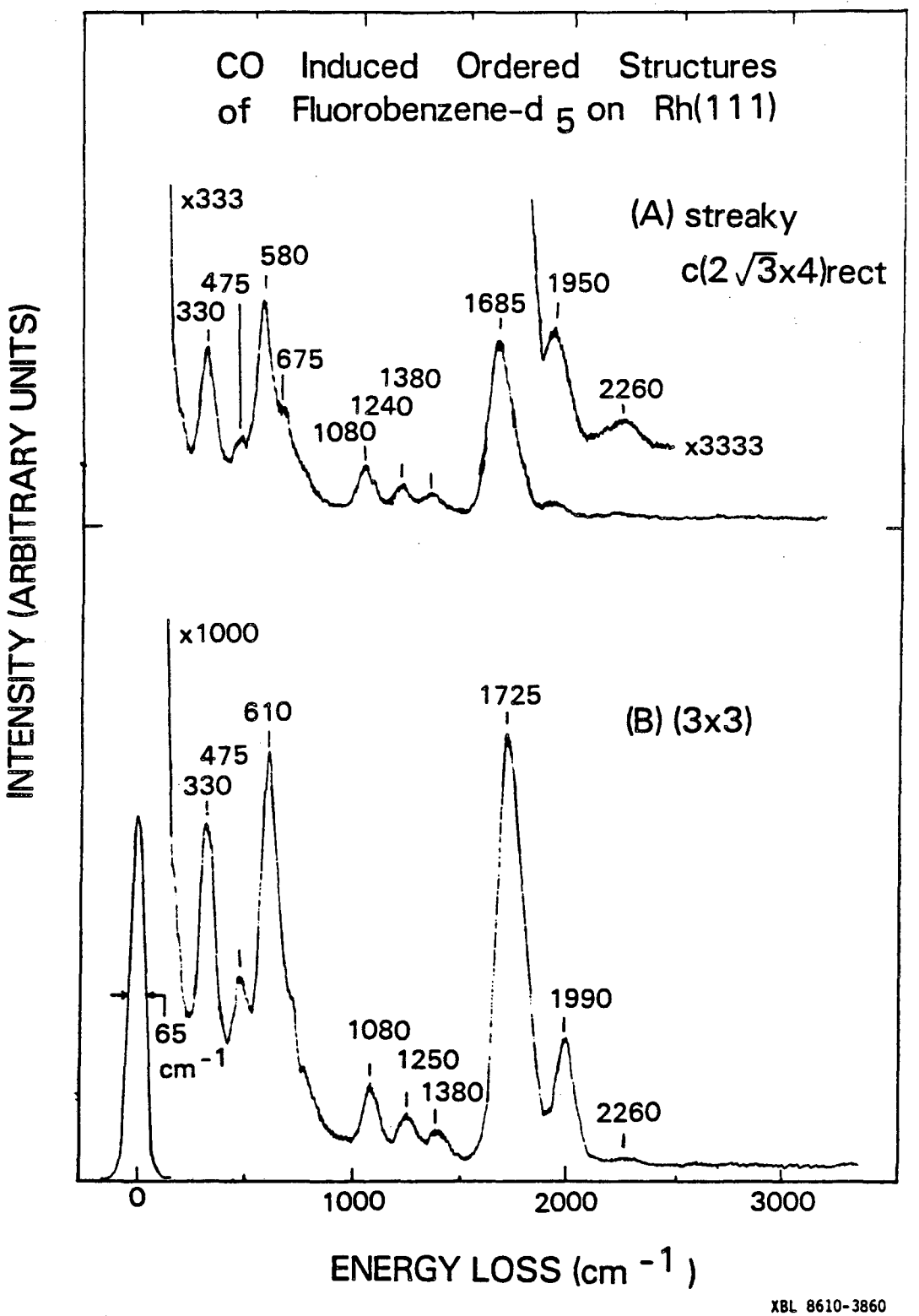
CO Induced Ordered Structures
of Fluorobenzene-d 5 on Rh(111)
x333
(A) streaky
c(2√3x4)rect
580
475
330
675
1685
1950
1380
1240
1080
2260
x3333
x1000
1725
610
(B) (3x3)
475
330
1990
65
cm -1
1080
1250
1380
2260
INTENSITY (ARBITRARY UNITS)
0
1000
2000
3000
ENERGY LOSS (cm -1)
XBL 8610-3860

Figure 6.5

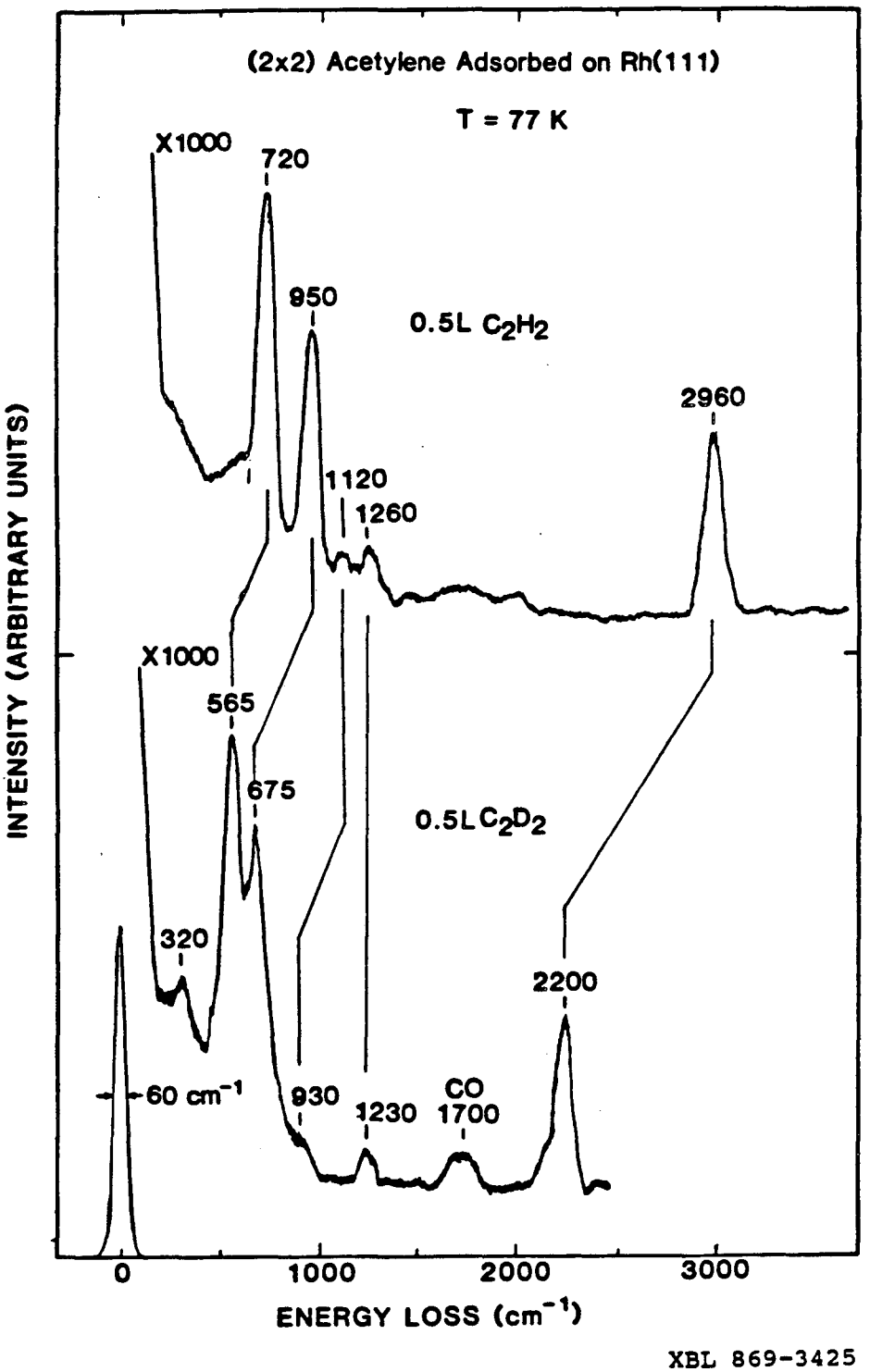
(2x2) Acetylene Adsorbed on Rh(111)
T = 77 K
X1000
720
950
0.5L C_2H_2
2960
1120
1260
X1000
565
675
0.5L C_2D_2
320
2200
60 cm^{-1}
930
1230
CO
1700
INTENSITY (ARBITRARY UNITS)
0
1000
2000
3000
ENERGY LOSS (cm^{-1})
XBL 869-3425

Figure 6.6

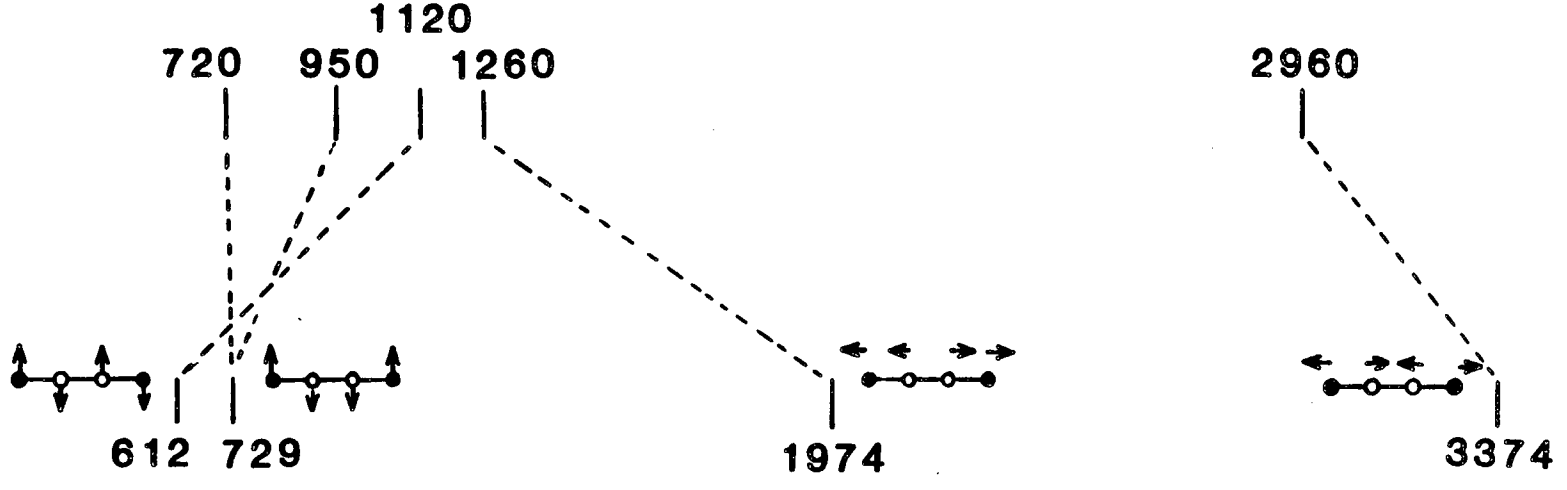

XBL 869-3432

Figure 6.7

Proposed Structure:

(2x2)-C2H2 on Rh(111)

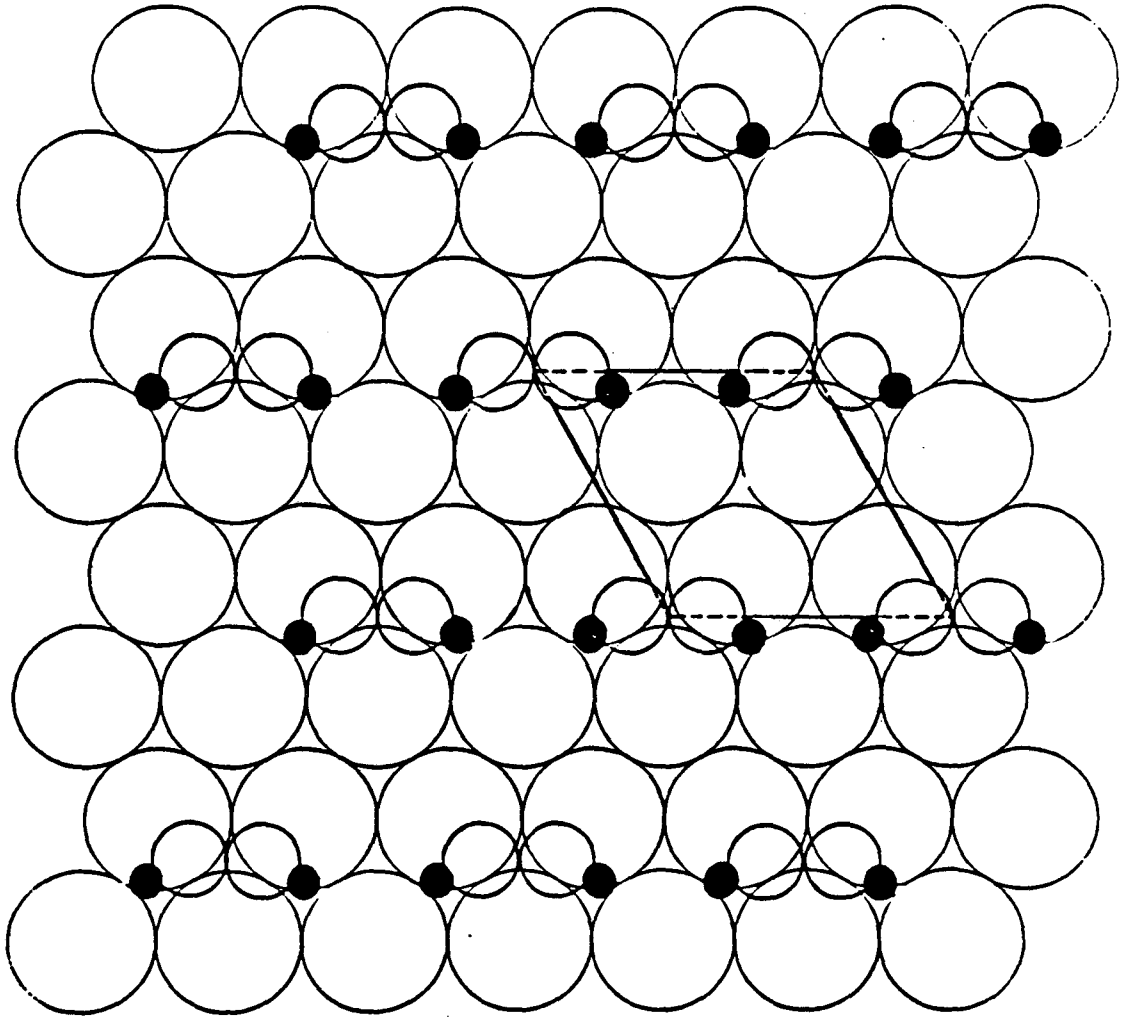

XBL 869-3424

Figure 6.8

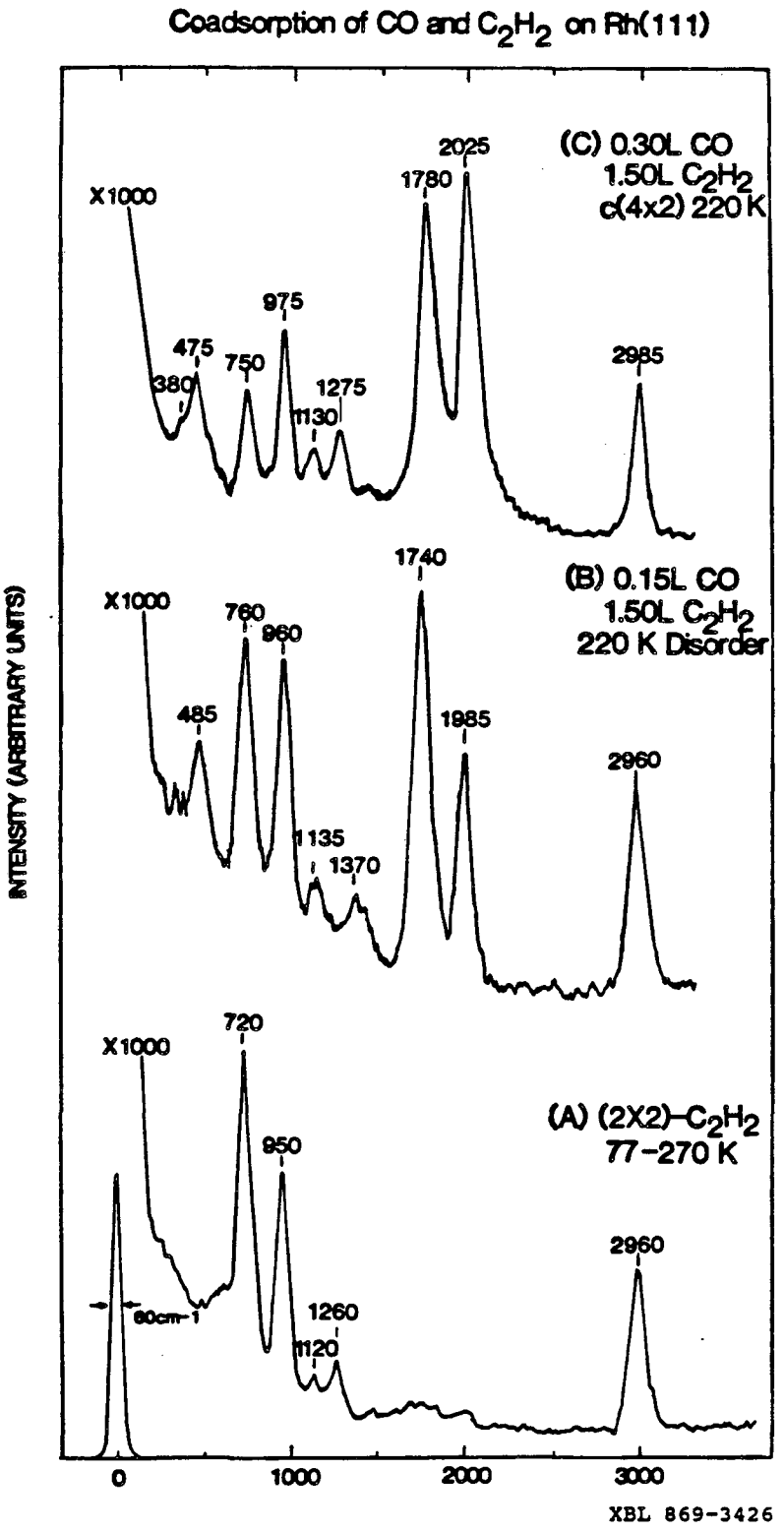
Coadsorption of CO and C_2H_2 on Rh(111)
(C) 0.30L CO
1.50L C_2H_2
c(4x2) 220 K
X1000
2025
1780
975
475
750
380
1275
1130
2985
(B) 0.15L CO
1.50L C_2H_2
220 K Disorder
1740
X1000
760
960
485
1985
2960
1135
1370
(A) (2X2)-C_2H_2
77-270 K
720
X1000
950
2960
60cm-1
1260
1120
INTENSITY (ARBITRARY UNITS)
0
1000
2000
3000
XBL 869-3426

Figure 6.9

Coadsorption of CO and Saturation Coverage of Ethylidyne

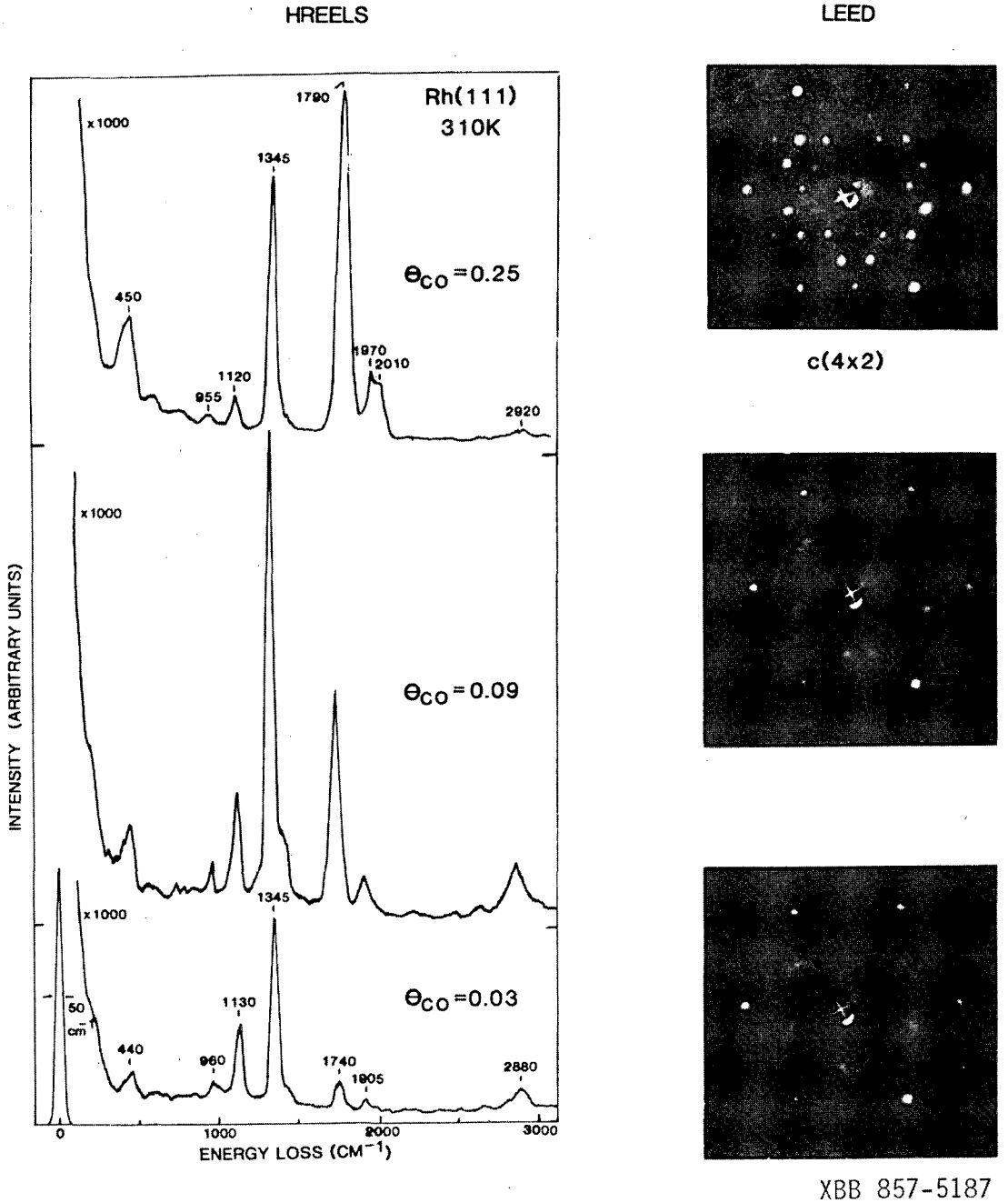

Figure 6.10

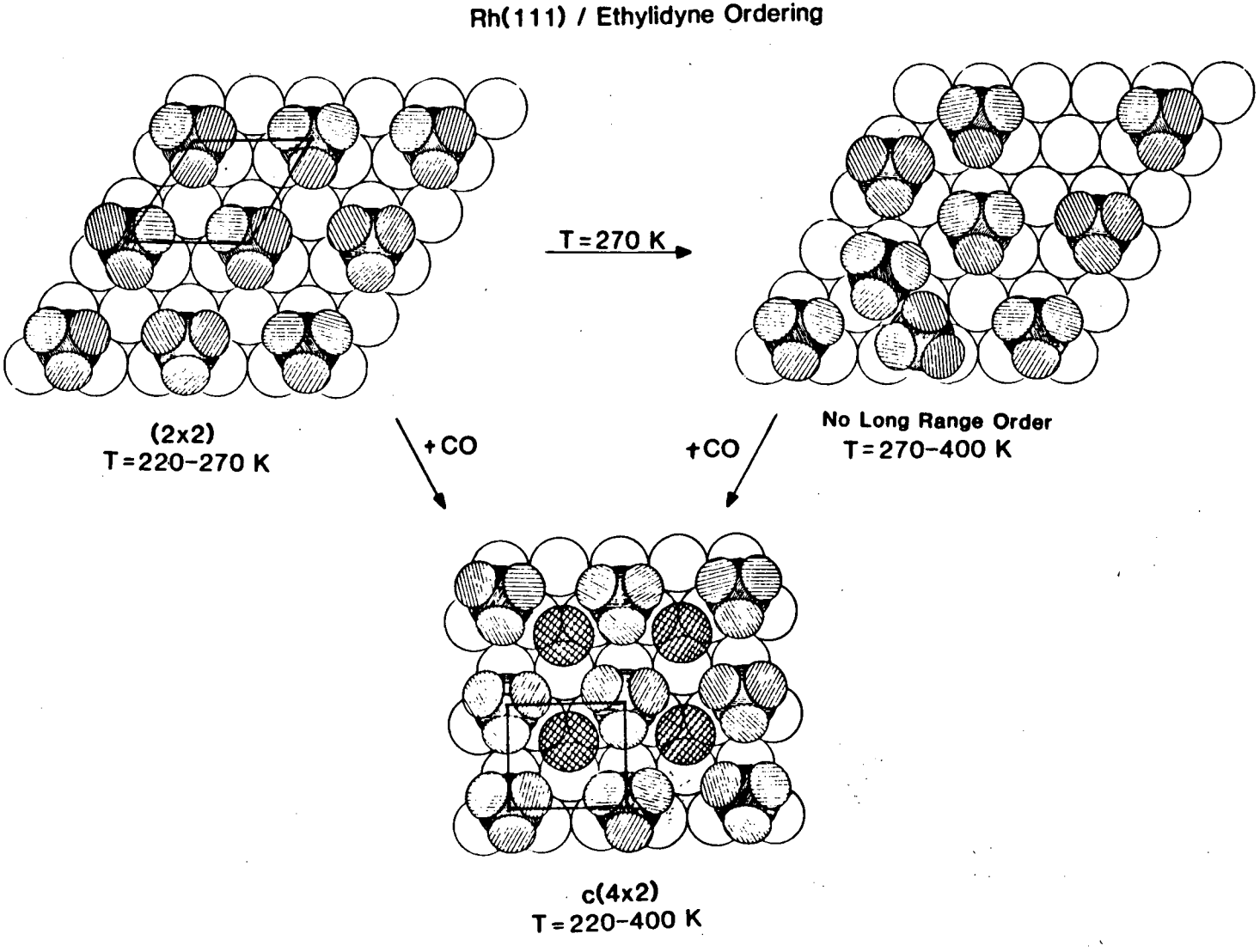
Rh(111) / Ethylidyne Ordering
T=270 K
(2x2)
T=220-270 K
+CO
+CO
No Long Range Order
T=270-400 K
c(4x2)
T=220-400 K
XBL 866-2421

Figure 6.11

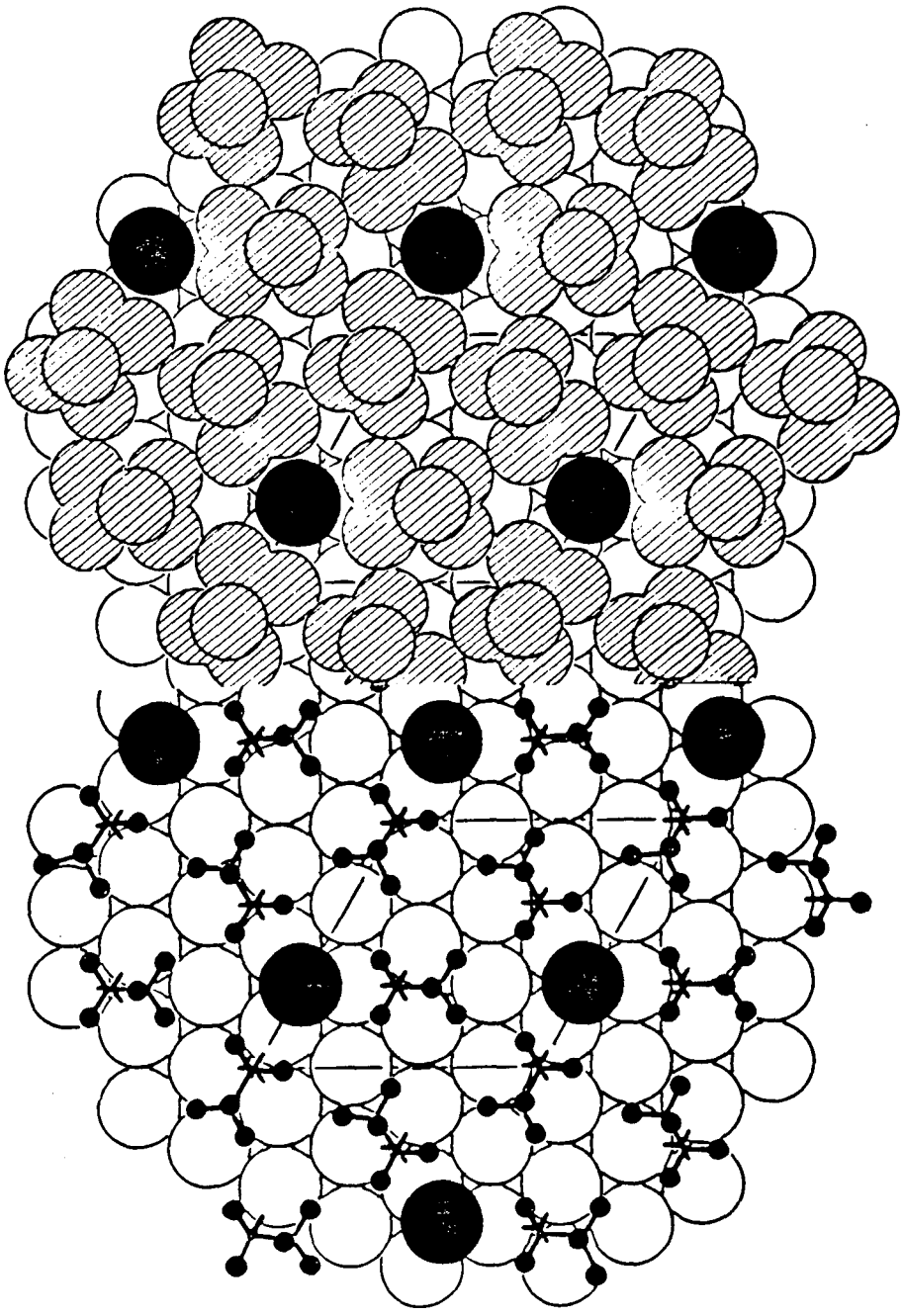

$Rh(111) + (2\sqrt{3} \times 2\sqrt{3})R30^\circ \; C_3H_5$ (propylidyne) + CO

XBL 813-5410

Figure 6.12

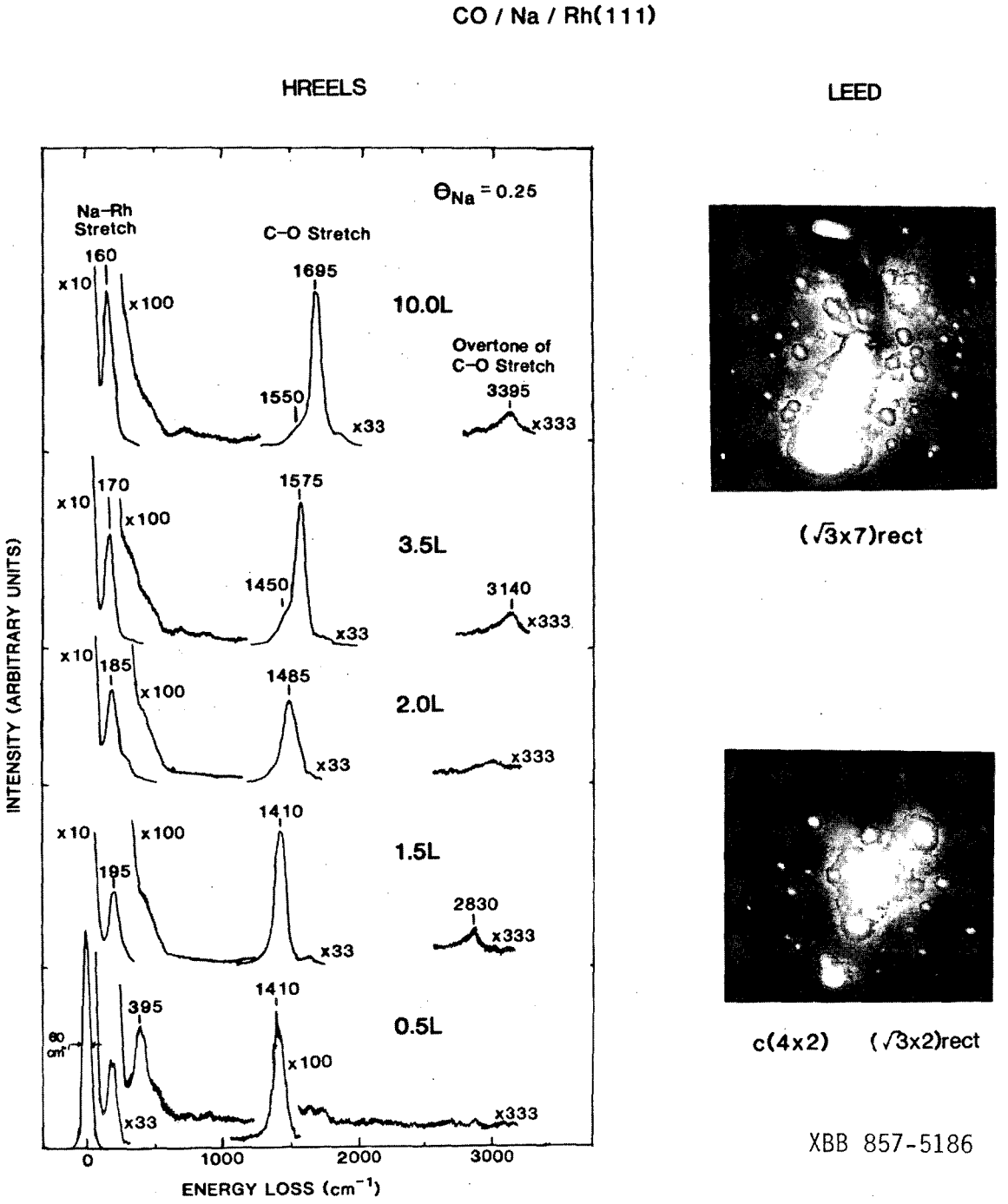
CO / Na / Rh(111)
HREELS
LEED
Θ_{Na} = 0.25
Na–Rh Stretch
C–O Stretch
160
1695
x10
x100
10.0L
Overtone of C–O Stretch
1550
3395
x33
x333
170
1575
3.5L
1450
3140
185
1485
2.0L
1410
1.5L
195
2830
395
1410
0.5L
60 cm⁻¹
INTENSITY (ARBITRARY UNITS)
0
1000
2000
3000
ENERGY LOSS (cm⁻¹)
(√3x7)rect
c(4x2)
(√3x2)rect
XBB 857-5186

Figure 6.13

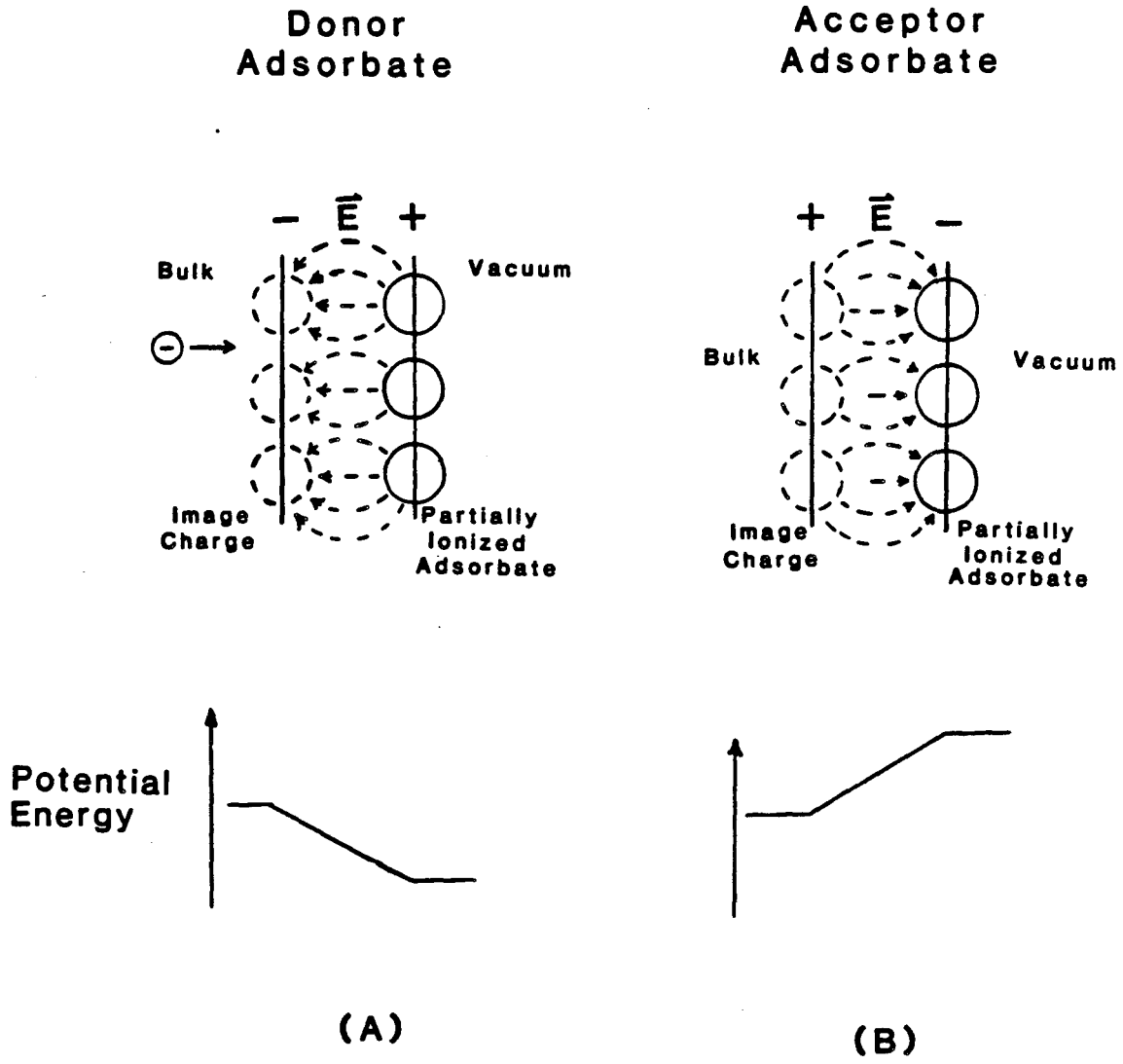
Donor
Adsorbate
Acceptor
Adsorbate
− Ē +
+ Ē −
Bulk
Vacuum
Image
Charge
Partially
Ionized
Adsorbate
Potential
Energy
(A)
(B)
XBL 869-3582

Figure 6.14

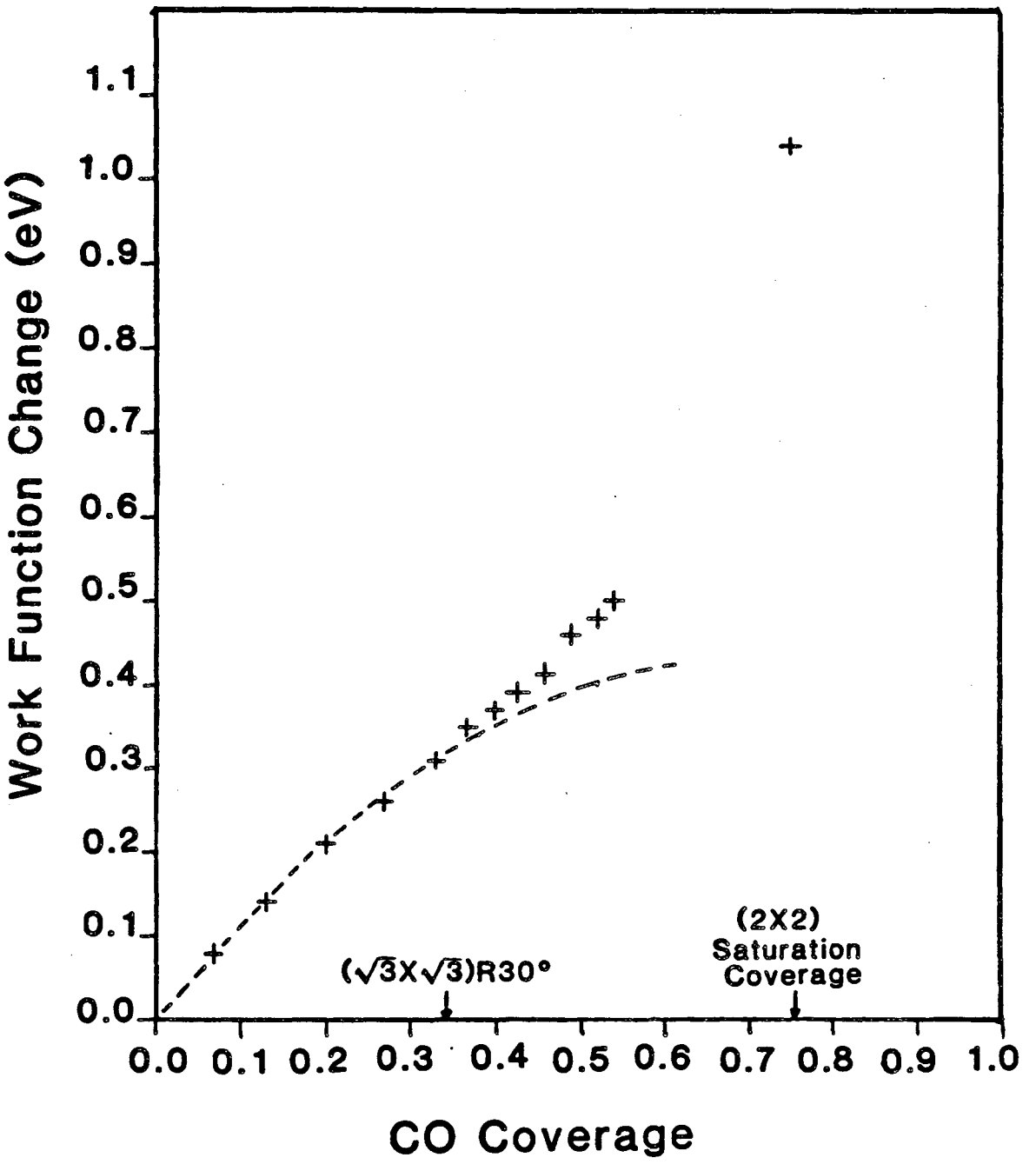
Work Function Change (eV)
1.1
1.0
0.9
0.8
0.7
0.6
0.5
0.4
0.3
0.2
0.1
0.0
0.0 0.1 0.2 0.3 0.4 0.5 0.6 0.7 0.8 0.9 1.0
CO Coverage
(√3X√3)R30°
(2X2)
Saturation
Coverage
XBL 8610-3585

Figure 6.15

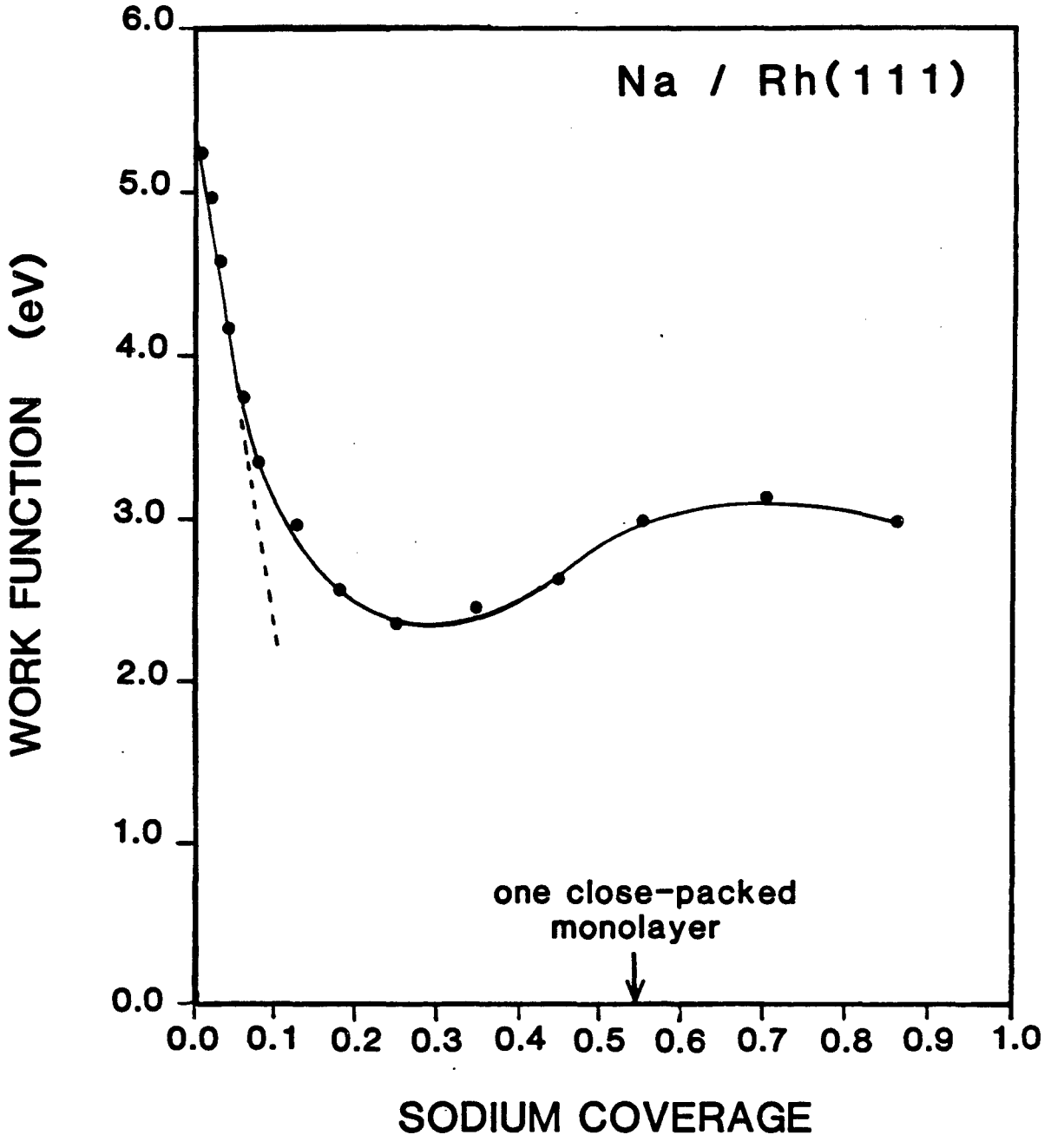

XBL 8610-3583

Figure 6.16

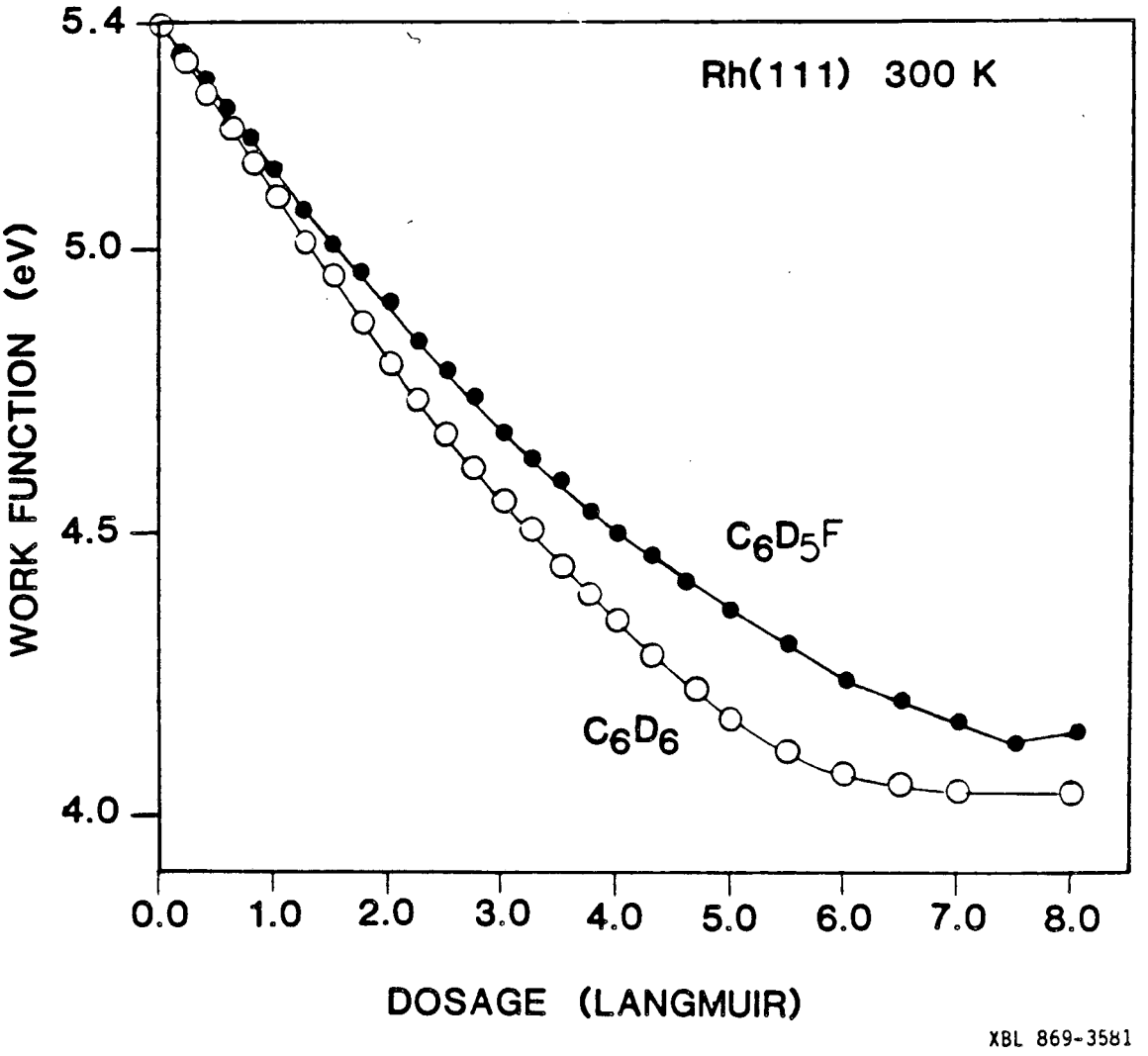
Rh(111) 300 K
C_6D_5F
C_6D_6
WORK FUNCTION (eV)
5.4
5.0
4.5
4.0
0.0
1.0
2.0
3.0
4.0
5.0
6.0
7.0
8.0
DOSAGE (LANGMUIR)
XBL 869-3581

Figure 6.17

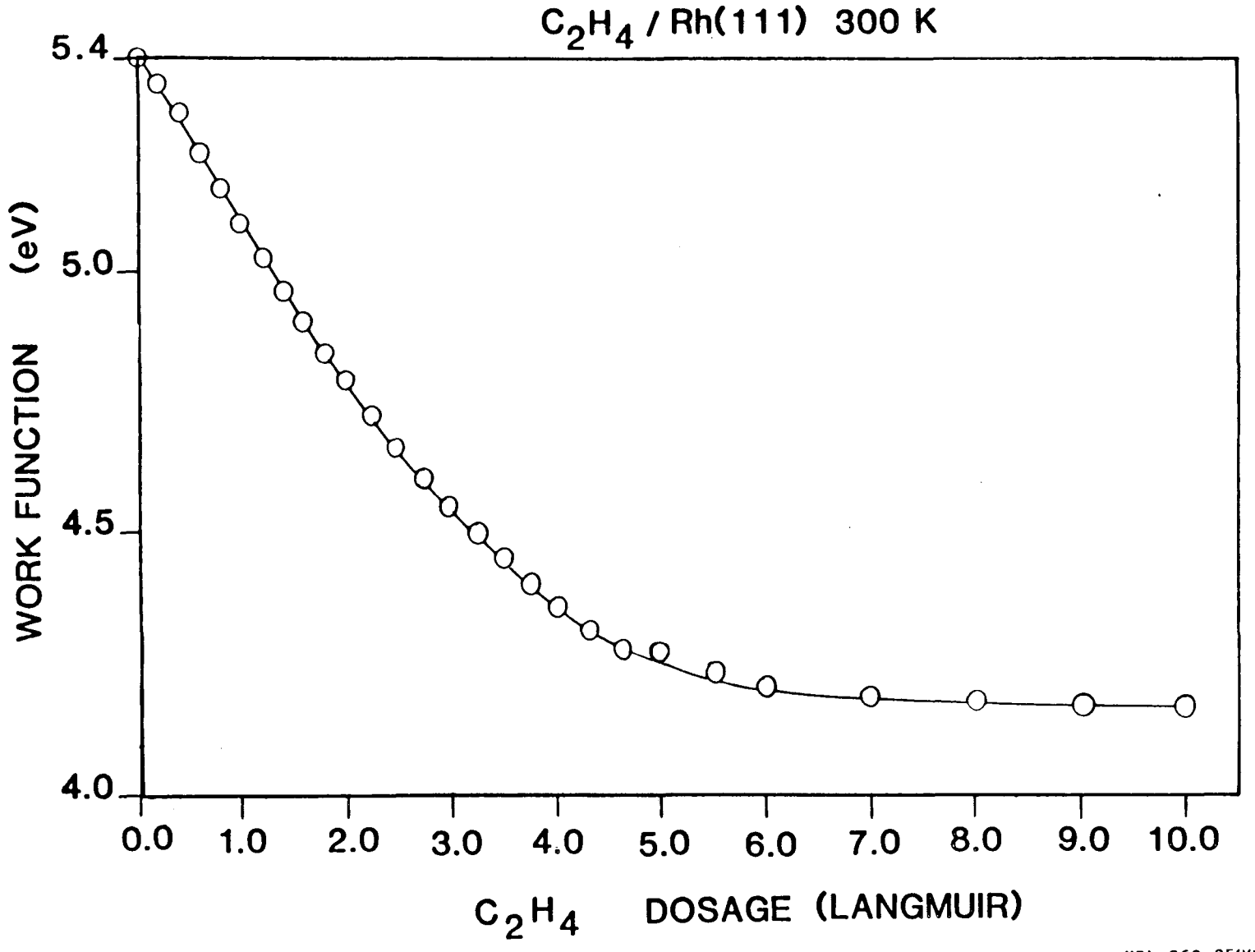

XBL 869-3580

Figure 6.18

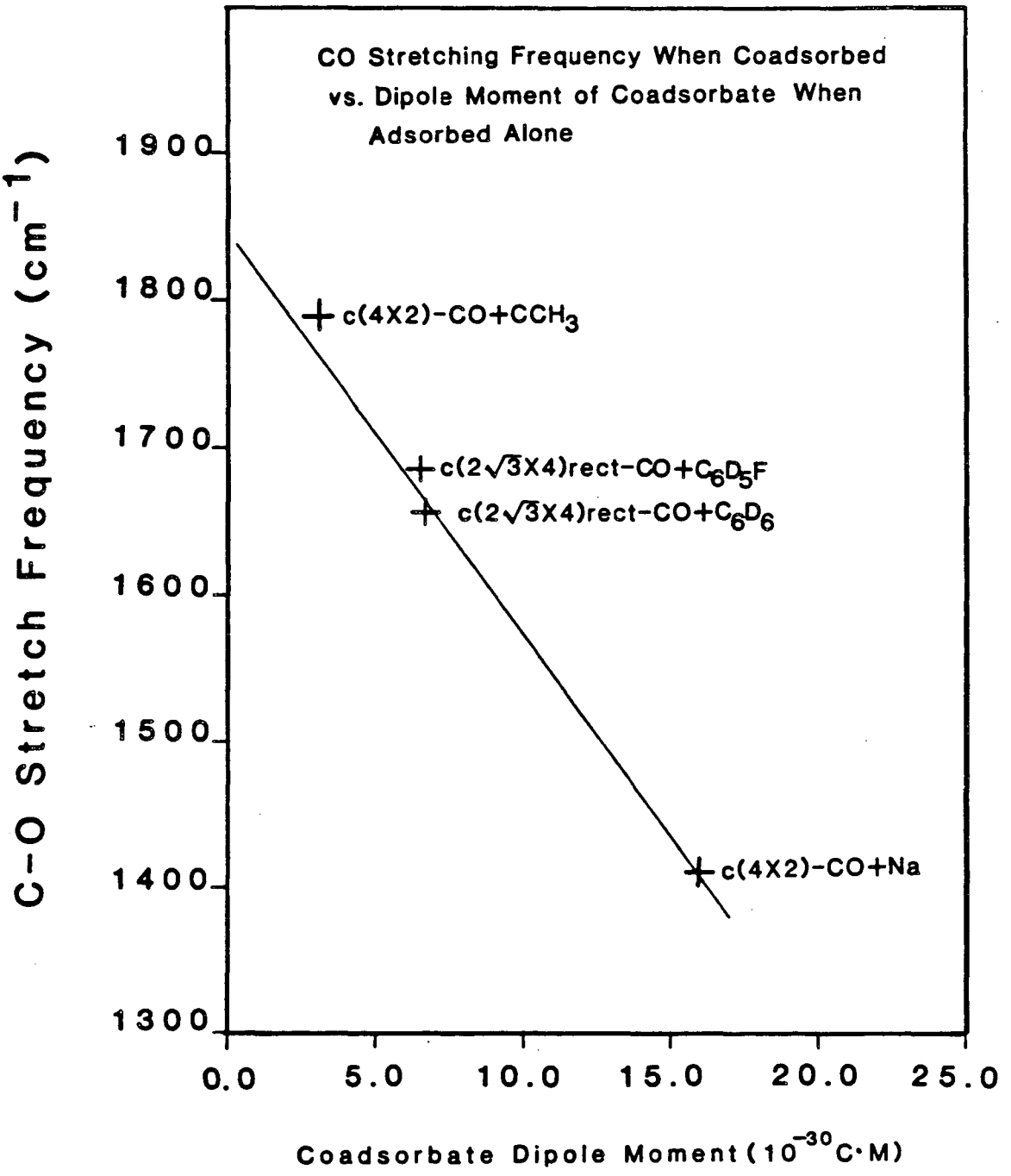
CO Stretching Frequency When Coadsorbed
vs. Dipole Moment of Coadsorbate When
Adsorbed Alone
C-O Stretch Frequency (cm^{-1})
1900
1800
1700
1600
1500
1400
1300
c(4X2)-CO+CCH_3
c(2√3X4)rect-CO+C_6D_5F
c(2√3X4)rect-CO+C_6D_6
c(4X2)-CO+Na
0.0
5.0
10.0
15.0
20.0
25.0
Coadsorbate Dipole Moment (10^{-30} C·M)
XBL 8610-3584

Figure 6.19

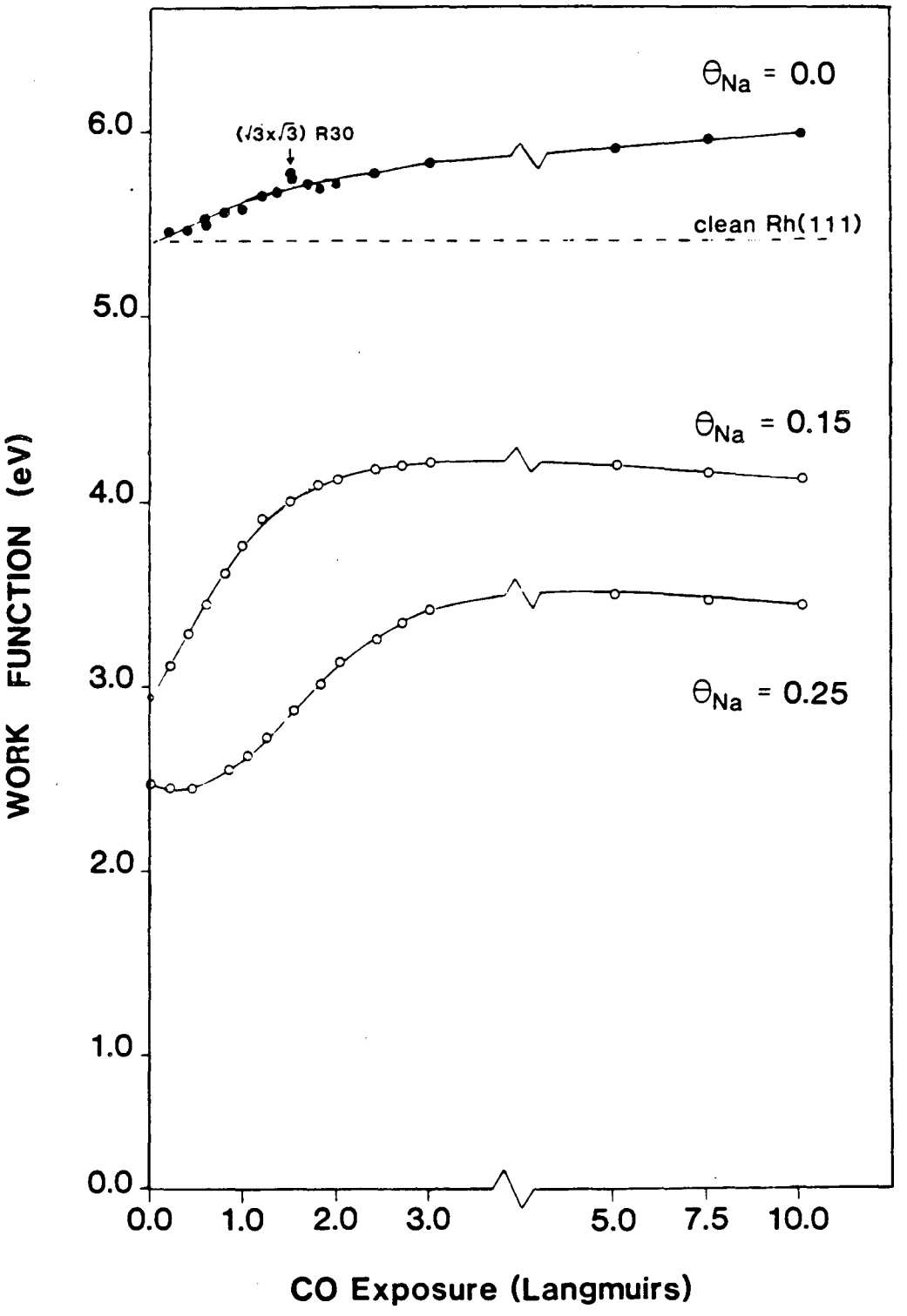

XBL 869-3435

Figure 6.20

CHAPTER 7

Hydrogen Adsorption on Rh(111)

Contents

7.1 Introduction

Vibrational spectra for hydrogen adsorption on metal surfaces have usually been interpreted as resulting from the harmonic motion of the hydrogen atoms at well localized adsorption sites [1]. In this chapter we present evidence, obtained by high resolution electron energy loss spectroscopy (HREELS), indicating that hydrogen atoms, adsorbed on the Rh(111) crystal surface, exhibit delocalized quantum behavior in their motion. This behavior can be described as the existence of a two-dimensional band structure for motion parallel to the surface. Evidence for this quantum motion of adsorbed hydrogen atoms includes: 1) The absence of a deuterium isotope shift for the lowest energy loss excitation [this excitation is associated with quantum motion of hydrogen atoms parallel to the Rh(111) surface]. 2) Broadened energy loss peaks as a result of the delocalized nature of hydrogen adsorption. And 3) good agreement with theoretical predictions for hydrogen adsorption on the Ni(111) surface by Puska, et al. [2], whose calculations indicate that quantum behavior needs to be taken into consideration in the appropriate description for the motion of hydrogen atoms on metal surfaces.

The possibility of quantum motion of atoms on surfaces was originally proposed by Christmann et al. [3] in connection with hydrogen chemisorption. They pointed out that, if diffusion barriers are ignored, the de Broglie wavelength resulting from the thermal energy of hydrogen atoms moving parallel to a surface is on the order of 1 Å. Consequently, these authors proposed that the motion of hydrogen atoms

parallel to a surface should be described in terms of a band structure with band gaps arising from the diffraction of hydrogen atoms from the two-dimensional periodic potential. In the limit of small diffusion barriers, the band gaps would be approximately equal to twice the appropriate Fourier component of the periodic potential.

More recently, Puska et al. [2] have reported the results of detailed calculations for the quantum motion of hydrogen adsorbed on nickel surfaces. As well as supporting the delocalized quantum nature of adsorbed hydrogen, these calculations also indicate that the motion of hydrogen perpendicular to the surface couples strongly to the motion parallel to the surface because of the anharmonicity of the combined perpendicular and parallel potentials and the delocalized nature of hydrogen adsorption. The coupling between the perpendicular and parallel motions results in both these motions having bandlike properties.

The delocalized quantum model of hydrogen adsorption is in many ways analogous to the nearly-free electron gas model, which is commonly used to describe the formation of electronic bands in simple metals. Since hydrogen is bound in a deep potential well perpendicular to the surface, it might form a "hydrogen fog" along the surface, a term we use to describe the delocalized quantum behavior of hydrogen adsorption on a metal surface in the same way as an "electron gas" is used to describe conduction electrons in a metal.

7.2 Results and Interpretation

7.2.1 HREEL Spectra for E_{beam} = 2.0 eV

Figure 7.1a shows the electron energy loss spectra obtained in the specular direction for several coverages of hydrogen and deuterium on the Rh(111) surface at 80 K, as well as for the clean Rh(111) surface. Coverages were determined by comparing the hydrogen thermal desorption yield with that of a (2x2) ethylidyne overlayer [6]. A coverage of θ_H = 1.0 corresponds to one adsorbed hydrogen atom per surface rhodium atom. For these spectra, the incident electron beam energy was 2.0 eV. At this beam energy, the Rh(111) surface has an exceptionally high electron reflectivity making it impossible to measure accurately the intensity of the elastic electrons due to saturation of our counting electronics. However, only at beam energies near 2.0 eV was the lowest energy excitation at 450 cm^{-1} clearly visible. No vibrational modes were observed above 1450 cm^{-1} that could be attributed to the H-H vibration of molecularly adsorbed hydrogen, indicating the hydrogen adsorbs dissociatively at 80 K on Rh(111).

First, we discuss the θ = 0.4 hydrogen spectrum, which is characteristic of the spectra for low hydrogen coverages. The most prominent feature of this spectrum is the loss peak at 450 cm^{-1}. Great care was taken to ensure that this excitation was not due to an impurity on the surface. We assign the 450 cm^{-1} loss to transitions from the ground-state band to the first excited-state band for the motion

of hydrogen on the Rh(111) surface. For hydrogen on Ni(111), a surface with the same structure as Rh(111), the calculations of Puska et al. [2] indicate that the first excited-state band has E symmetry, corresponds mainly to quantum motion parallel to the surface and is centered 320 cm^{-1} above the ground-state band, close to the frequency of 450 cm^{-1} we observe on Rh(111).

If the 450 cm^{-1} excitation does indeed correspond to transitions to an E symmetry band, then this excitation should have little or no contribution from dipole scattering [7]. This was checked by monitoring the angular dependence of the 450 cm^{-1} loss intensity, as shown in Fig. 7.1b. The intensity decreases at angles away from the specular scattering directions, but in a manner uncharacteristic of dipole scattering (exemplified by a Rh-CO stretch in Fig. 7.1b), indicating that impact scattering dominates for this loss.

A surprising characteristic of the 450 cm^{-1} loss peak is that no corresponding loss peak exists in the deuterium spectrum at a frequency reduced by a factor $\sqrt{2}$, which would be expected if hydrogen and deuterium were bound in a totally harmonic potential; instead, the 450 cm^{-1} loss appears to shift only slightly in the corresponding deuterium spectrum (Fig. 7.1a). The calculations by Puska et al., [2] predict that all bands, for hydrogen adsorbed on Ni(111), should shift in energy by about a factor of $\sqrt{2}$. However a suitably anharmonic potential for hydrogen adsorption on Rh(111) could provide a possible explanation for the lack of an observed shift in the 450 cm^{-1} loss. If the potential is suitably anharmonic in the direction perpendicular

to the surface, the hydrogen position wavefunctions can extend further above the surface than the deuterium wavefunctions due to the larger zero point motion of hydrogen. Consequently, hydrogen atoms can see a substantially smaller barrier to delocalized motion parallel to the surface than deuterium atoms; this effect tends to cancel the expected isotopic shift. A similar effect has been reported for the motion of the different isotopes of helium on graphite surfaces [8]. Recent calculations by Tomanek et al. [9] for hydrogen adsorbed on Pd(100) indicate that the large interatomic spacing between palladium atoms contributes to the anharmonicity of the hydrogen potential on Pd(100). Therefore, the larger lattice spacing of rhodium compared to nickel should result in a more anharmonic potential for hydrogen adsorption on Rh(111) compared to Ni(111). However, more detailed calculations for both the potential and the motion of hydrogen and deuterium adsorbed on Rh(111) are needed to confirm this interpretation.

Next, we discuss the higher energy loss peaks that appear in the spectra for adsorbed hydrogen and deuterium. In the $\theta = 0.4$ spectra, these excitations are broad and weak. For coverages greater than 0.4, these become narrower and more intense as well as shifting slightly to higher energies. The reduction in bandwidth at higher coverages can be explained within the delocalized model of hydrogen adsorption as resulting from a reduction in hydrogen mobility due to blocking by neighboring hydrogen atoms [2]. The shifts in energies of the excitations may be due to hydrogen-hydrogen interactions, which become

apparent at higher coverages. No ordered overlayers were observed by low energy electron diffraction (LEED) for hydrogen and deuterium on Rh(111) down to T = 80 K.

Within the "hydrogen fog" model, we interpret these higher energy excitations centered at 750, 1100, and 1450 cm^{-1} as corresponding to transitions from the ground-state band to excited-state bands, which result from the combination of motion both perpendicular and parallel to the surface. Evidence that the 750 and 1100 cm^{-1} excitations correspond to a significant amount of motion perpendicular to the surface comes from off-specular measurements of the loss intensities shown in Fig. 7.1c. These two losses decreased in intensity at angles away from the specular scattering direction in a manner characteristic of dipole scattering. Dipole scattering is expected if these excitations are associated with motion perpendicular to the surface and with transitions between the ground-state band and A_1 symmetry states [7]. Consequently, we assign the 750 and 1100 cm^{-1} losses to transitions from the ground-state band to the A_1^1 and A_1^2 bands, respectively, which are predicted to occur at 590 and to the 1100 cm^{-1} for hydrogen adsorption on Ni(111) [2]. Because of the low intensity of the 1450 cm^{-1} loss, it was not possible to determine the scattering mechanism of this loss. We assign this loss to transitions to the E^2 band, even though there may be overlapping contributions from transitions to the A_2^1 bands. E^2 and A_2^1 bands are predicted to occur at 1090 and 1040 cm^{-1}, respectively, for hydrogen adsorbed on Ni(111) [2]. If these excitations do indeed correspond to a large

degree of motion perpendicular to the surface, then their observed deuterium shift of about $\sqrt{2}$ is not surprising, since the potential perpendicular to the surface, even though anharmonic, approximates that of a harmonic oscillator.

The higher excited-state bands, as well as the 450 cm^{-1} band, involve a significant amount of quantum motion parallel to the surface, as indicated by the broadness of the loss peaks in the HREEL spectra. The excited-state bands are expected to be fairly broad within the "hydrogen fog" model, since the delocalized quantum nature of hydrogen adsorption results in extensive overlap of hydrogen position wavefunctions for excited states centered over neighboring adsorption sites [2]. Further, the calculations by Puska et al., indicate that, for hydrogen on a close-packed surface (like Ni(111) or Rh(111)), the ground-state energy band is fairly narrow, ~4 meV. Consequently, at the temperature for which the spectra in Fig. 7.1a were taken (80 K), all the states of the ground-state band should be thermally populated, and vertical transitions ($\Delta k = 0$) between the ground-state band and the excited-state bands should be observable at any point in the Brillouin zone. Therefore, the observed excitations in the HREELS spectra should have a width dominated by that of the excited-state band. For the $\theta_H = 1.0$ spectra in Fig. 7.1a, the FWHM widths of the 450, 750, 1100, and 1450 cm^{-1} excitations are, respectively, 110, 110, 95, and 160 cm^{-1} after deconvolution of the instrumental resolution of 65 cm^{-1}. These experimental values give approximate values of 220, 220, 190, and 320 cm^{-1} for the energy bandwidths of

hydrogen on Rh(111), which agree reasonably well with the values of 350, 320, 210, and 470 cm^{-1} predicted for similar energy bands for hydrogen on Ni(111) [2]. The discrepancies may be due to the difference in metals, to finite coverage effects, or to the dependence of the measured widths on the incident beam energy, as is discussed below.

Other mechanisms, besides delocalization, that can broaden vibrational lines of adsorbates have been considered quite generally by Gadzuk and Luntz [10] and are often found to have a characteristic temperature and/or isotope dependence. Where it was possible to measure the bandwidths for hydrogen (deuterium) on Rh(111) under similar conditions, the 750 cm^{-1} (560 cm^{-1}) and 1100 cm^{-1} (830 cm^{-1}) bandwidths showed, within experimental error, no isotope or temperature dependence over the 80 - 200 K temperature range. This isotope and temperature dependence points away from mechanisms such as inhomogenous broadening from defects or exchange-coupling dephasing, which are expected to have a strong isotope or temperature dependence [10]; other broadening mechanisms, however, cannot be completely ruled out. The observed isotope dependence is consistent though with the irregular changes in band shapes predicted by Froyen et al. [11] for the quantum motion of hydrogen and deuterium on Ni(100).

7.2.2 Energy Dependence of HREEL Spectra

For hydrogen adsorbed on Rh(111), we have also observed a remarkable dependence of the intensity and widths of the HREELS losses on the beam energy at which the HREEL spectra are taken. First, the 450 cm^{-1} loss is only clearly visible at beam energies near 2 eV. Second, the dipole active 750 and 1100 cm^{-1} losses go through a strong resonance near a beam energy of 4.7 eV as is shown in Fig. 7.2. This figure shows the loss intensities as a function of beam energy, along with the elastically reflected electron intensity and the measured widths of the transitions. Off specular measurements indicate that the impact scattering is the predominant scattering mechanism for beam energies > 3 eV. Similar resonances in inelastic scattering intensities have been observed for adsorbed molecules on other metal surfaces [12], where the resonances are thought to be due to the incident electrons, at particular beam energies, being trapped for a short period of time in surface or molecular electron states. Further, a dramatic decrease in band widths of the dipole active 750 and 1100 cm^{-1} excitations is observed as the beam energy goes from energies (< 3 eV) where the principal scattering mechanism is dipole scattering to energies (> 3 eV) where the principal scattering mechanism is impact scattering. As far as we can ascertain, this is the first report of an energy dependent linewidth for an excitation in an electron energy loss spectrum and as yet is not understood.

7.3 Comparison to Other Metals

Finally, we examine whether results previously reported for hydrogen adsorbed on other close packed surfaces can also be interpreted within the delocalized, "hydrogen fog" model. Gomer and coworkers [13] have observed, using field emission microscopy, temperature independent diffusion of the three hydrogen isotopes adsorbed on the W(110) surface for temperatures in the range 27-120 K. These experiments imply that tunneling is the dominant mechanism for hydrogen diffusion on W(110) for temperatures less than 120 K. However, tunneling is some physical mechanism as "quantum motion", but in the tunneling diffusion process only quantum motion within the ground state band is important. The tunneling rate is directly related to the ground state bandwidth [14], but calculations by Whaley et al. [14] indicate that a very narrow ground state band width ($\sim 10^{-9}$ meV), much narrower than those calculated by Puska et al. [2], can explain the diffusion results for hydrogen on W(110).

Further evidence for delocalized hydrogen on other closed packed surfaces with the same surface structure as Rh(111) can be found in previously reported HREELS results. Table 7.1 lists the experimentally observed excitation energies, which are assigned by us to transitions between the energy bands expected for delocalized hydrogen. Also listed in Table 7.1 are the calculated transition energies and widths for hydrogen on Ni(111). In Table 7.1, the notation A_1^0, E^1, etc. refers to the symmetry of the bands, with the superscript referring to the order of the bands relative to

other bands of the same symmetry. The 750 and 1100 cm^{-1} excitations of hydrogen on Rh(111), the 820 and 1140 cm^{-1} of hydrogen on Ru(001) and the 550 cm^{-1} excitation on Pt(111) are assigned to $A_1^0 \rightarrow A_1^n$ transitions since off-specular measurements indicate they are dipole active. The remaining observed excitations listed in Table 7.1 occur predominantly by impact scattering. Since there could be a small dipole scattering contribution to these losses, it is not clear whether they should be assigned to non-dipole active $A_1^0 \rightarrow E^n$ transitions or to dipole active $A_1^0 \rightarrow A_1^n$ transitions. Consequently, these frequencies have been assigned by us simply to transitions that are closest to those predicted theoretically for hydrogen on Ni(111). Since many of the excitations observed are very broad, they could also be due to transitions to several overlapping bands rather than to single band as assigned in Table 7.1.

Table 7.1 shows that previously reported experimental results for hydrogen adsorbed on closed packed surfaces can be interpreted in a consistent manner within a delocalized, quantum description of hydrogen adsorption. Further, where bandwidths have been reported, they are fairly large, which also supports a delocalized, quantum description for hydrogen adsorption on these surfaces. That not all the predicted transitions have been observed for hydrogen adsorbed on these various surfaces may be due to the very low HREELS excitation probabilities for hydrogen. We have only been able to observe a relatively large number of transitions by HREELS by choosing an appropriate incident beam energy (2.0 eV). Consequently, we feel that hydrogen adsorption

on these surfaces, as well as on other metal surfaces, should be re-examined more carefully by vibrational spectroscopy for features characteristic of delocalized, quantum behavior.

7.4 Conclusions

We have made HREELS observations that strongly favor a delocalized, quantum description of adsorbed hydrogen ("hydrogen fog") over the classical harmonic-oscillator model. Specifically, we have been able to observe excitations between the ground-state band and the broad, low energy bands expected for quantum motion of hydrogen on a close packed surface. We also observe that the lowest energy excitation in the hydrogen spectra appears not to shift in energy in the corresponding deuterium spectra; this excitation is interpreted to result from quantum motion parallel to the surface.

Table 7.1. Transition energies (and band widths) in cm^{-1} for hydrogen adsorbed on hexagonally closed-packed surfaces.

	$A_1^0 \rightarrow A_1^1$	$A_1^0 \rightarrow A_1^2$	$A_1^0 \rightarrow E^1$	$A_1^0 \rightarrow E^2$
Calculated				
Ni(111) [2]	590(350)	1100(320)	320(210)	1090(770)
Experimental				
Rh(111)	750(220)	1100(190)	450(220)	1450(320)
Ni(111) [15]	710	1120	—	—
Ru(001) [16]	820	1140	—	1550
Pt(111) [17]	550	1230	—	--

REFERENCES

1. H. Ibach and D.L. Mills, Electron Energy Loss Spectroscopy and Surface Vibrations, Academic Press, New York 1982, pp. 281-3.
2. M.J. Puska, R.M. Nieminen, M. Manninen, B. Chakraborty, S. Holloway and J.K. Norskov, Phys. Rev. Lett. 51 (1983) 1081; M.J. Puska and R.M. Nieminen, Surface Sci. 157 (1985) 413.
3. K. Christmann, R.J. Behm, G. Ertl, M.A. Van Hove, and W.H. Weinberg, J. Chem. Phys. 70 (1979) 4168.
4. H. Froitzheim, H. Ibach and S. Lehwald, Rev. Sci. Instrum. 46 (1975) 1325.
5. S. Semancik, G.L. Haller and J.T. Yates, Jr., Appl. Surf. Sci. 10 (1982) 546.
6. R.J. Koestner, M.A. Van Hove, and G.A. Somorjai, Surface Sci. 121 (1982) 321.
7. Ref. 1, Chapter 4.
8. M.W. Cole, D.R. Frankl, and D.L Goodstein, Rev. Mod. Physics 53 (1981) 199.
9. D. Tomanek, S.G. Louie and Che-Ting Chan, to be published.
10. J.W. Gadzuk and A.C. Luntz, Surface Sci. 14 (1984) 429.
11. S. Froyen, S. Holloway, J.K. Norskov and B. Chakraborty, J. Electron Spectrosc., 38 (1986) 313.
12. J.E. Demuth, D. Schmeisser and Ph. Avouris, Phys. Rev. Lett. 47 (1981) 1166; L.L. Kesmodel, Phys. Rev. Lett, 53 (1984) 1001; H. Conrad, M.E. Kordesch, R. Scala and W. Stenzel, J. Electron Spectrosc., 38 (1986) 289.

13. R. Difoggio and R. Gomer, Phys. Rev. B25, (1982) 3490; S.C. Wang and R. Gomer, J. Chem. Phys. 83 (1985) 4193.

14. K.B. Wahley, A. Nitzan, and R.B. Gerber, J. Chem. Phys. 84 (1986) 5181.

15. W. Ho, N.J. DiNarko, and E.W. Plummer, J. Vac. Sci. Technol. 17 (1980) 134.

16. H. Conrad, R. Scala, W. Stenzel, and R. Unwin, J. Chem. Phys. 81 (1984) 6371.

17. H.M. Baro, H. Ibach, and H.D. Bruchmann, Surface Sci. 88 (1979) 384.

FIGURE CAPTIONS

Fig. 7.1. a) Electron energy loss spectra for hydrogen and deuterium adsorbed on Rh(111). The instrumental resolution is 65 cm^{-1}. b) Angular dependence of the 450 cm^{-1} loss intensity for $\gamma_H = 0.4$. For comparison, the angular dependence of the dipole active Rh-C mode for CO adsorbed on Rh(111) is also shown. c) Angular dependence of the 750 and 1100 cm^{-1} loss intensities for $\theta_H = 1.0$.

Fig. 7.2. a) Elastic peak intensity, b) loss peak intensities, and c) band widths observed in the $\theta_H = 1.0$ HREEL spectra. Band widths are given after deconvoluting out the instrumental resolution of 55 cm^{-1}.

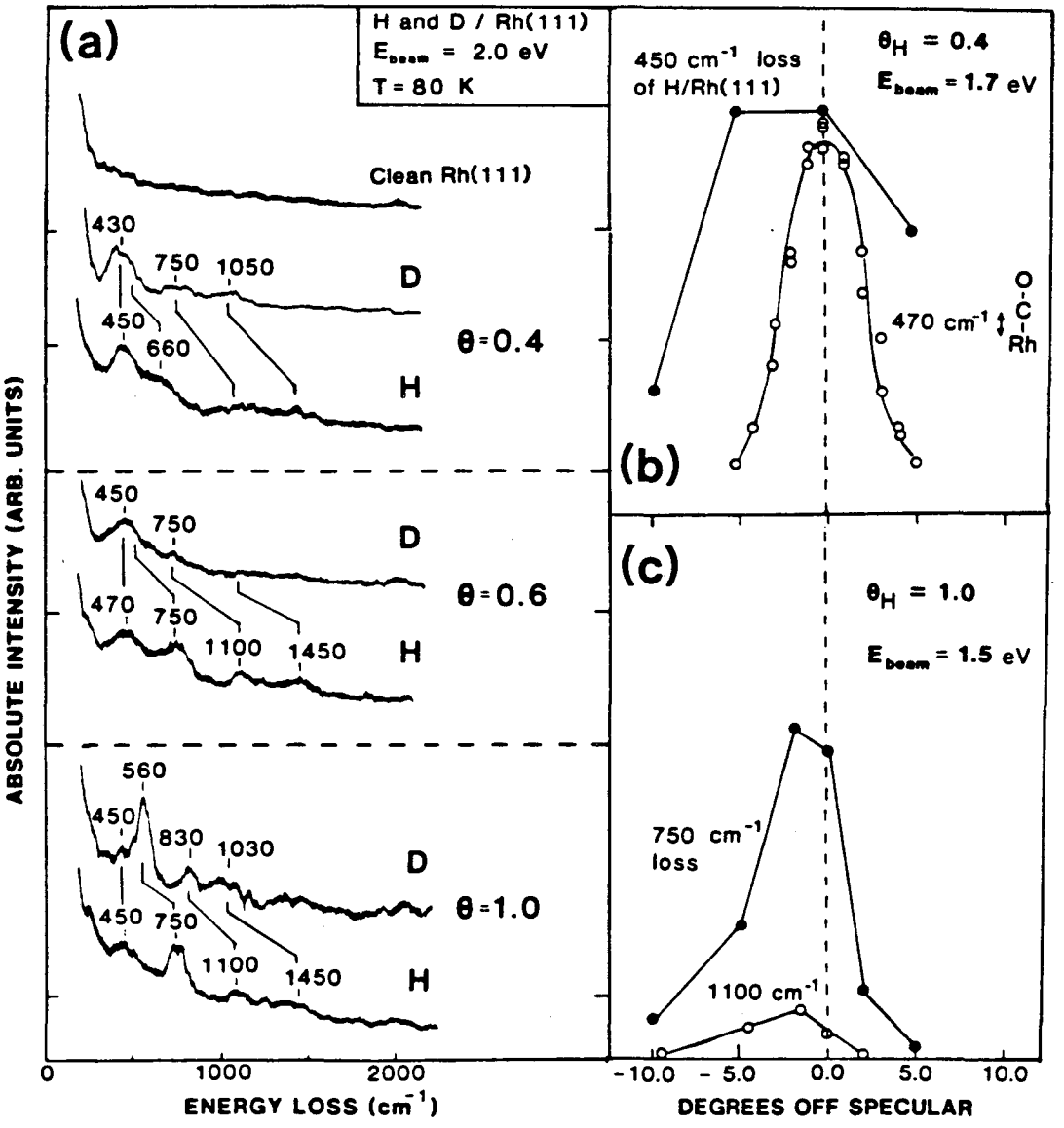

XBL 867-2649

Figure 7.1

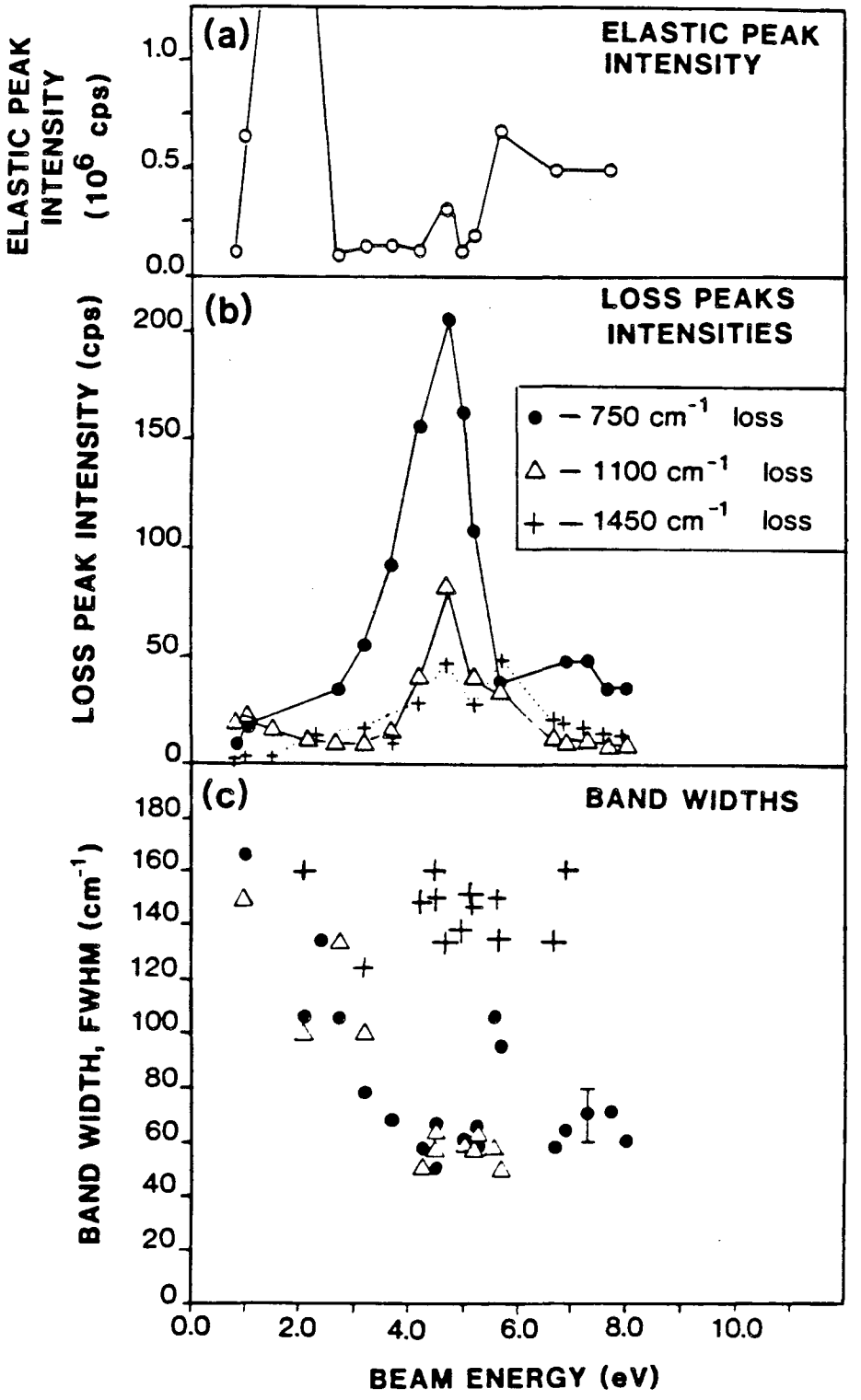

XBL 867-2650

Figure 7.2

CHAPTER 8

FRICTION EXPERIMENTS ON Rh(111)

Contents Page

8.1 Background

In many practical situations, an oil film separates two surfaces moving relative to each other with the coefficient of friction depending on the hydrodynamic properties of the oil. As the load is increased and the relative speed is decreased, the separation distance between the two surfaces becomes smaller, and increasing contact occurs between the two surfaces; as the surfaces come into contact, the coefficient of friction increases dramatically. This phenomenon can be described by what is known as the Stribeck curve [1], which is illustrated in Fig. 8.1; the abscissa quantity, (viscosity) (speed)/(load), is known as the generalized Sommerfeld number [3].

When the surfaces are in actual contact, the type of lubrication, is then called boundary lubrication. In this region the mechanism of lubrication should be suitable for study by surface science techniques.

Most surfaces, even smooth appearing ones, are actually very rough and irregular on the atomic scale. Consequently, when two surfaces come into contact, only the asperities actually touch, resulting in the real area of contact being much smaller than the apparent area. At these initial points of contact, the pressure is extremely large and the material around the contact points flows plastically until the local pressure falls to the yield pressure, P_m, of the softer material. Therefore, the actual area of contact is proportional to the load and is given by

$$A = \frac{W}{P_m}$$

where W is the load. For most metals, P_m is in the range of 10 to

100 Kg/mm^2, so in a friction experiment with a load of 100 gm, the true area of contact would be in the range of 10^{-4} to 10^{-5} cm^2.

When the two surfaces are moved relative to each other, there is a frictional force, F, opposing this motion. This force can, in general, be expressed as the sum of two terms [4]:

$$F = F_s + F_p$$

One term is the shearing force, F_s, required to shear the junctions at the points of actual contact. This is given by

$$F_s = As_m$$

where s_m is the shear strength per unit area. The second term is called the plowing force since it is the force required to displace the softer material from the front of the harder one; however, if both materials are hard, the friction is due mostly to the shearing term. Then

$$F = F_s = As_m = \frac{W s_m}{P_m}$$

or

$$\mu = \frac{F}{W} = \frac{s_m}{P_m} .$$

This result is just Amontons' law, which states that the coefficient of friction μ is independent of the apparent area of contact. For most metals, s_m/P_m is close to 1/3 [4].

In many cases, the surfaces are covered with a strongly bound film of lubricant, such as an oxide film or a fatty acid film, through which the asperities have to break in order to make contact with the other surface. Consequently, the load is supported over two areas:

A_1, the area of film-film contacts and A_2, the area of metal-metal contacts. The total frictional force then is

$$F = F_s = A_1 s_f + A_2 s_m$$

where s_f is the shear strength per unit area of the film-film contacts. Therefore, a good lubrication film should have a low s_f and should also be hard for the asperities to break through in order that A_2 remains as small as possible.

In these descriptive terms, the mechanism of metallic friction is fairly well understood; however, a good quantitative understanding is still lacking. Next, we briefly review some of the relevent experiments on metallic friction under the well characterized conditions necessary to obtain such an understanding.

There is ample evidence that clean metals if pressed together can adhere very strongly [5]. The force required to "pull off" one metal from the other clearly depends on the strength of the interfacial bond. Buckley and his group have shown that with similar metals the pull off force and the friction fall off very rapidly as the amount of d-bonding in the bulk is increased [6]. These results for friction are shown in Fig. 8.2 and have been interpreted in terms of reduced bond strengths. The adhesion and friction between two surfaces have also been found to be correlated with other bulk properties such as ductility [7], tensile strength and shear strength [8]. Another general result for when two clean metals are brought into contact is that transfer of the cohesively weaker metal to the cohesively stronger metal is always observed [5].

Practically all published work agrees that small amounts of contaminants on surfaces can greatly reduce the adhesion between metals [4,5]. For example, Fig. 8.3 shows the effect of H_2S adsorption on the Fe(011) surface. Even for a low coverage c(2x4) structure, the adhesion force is dramatically less that of the clean surface. Another dramatic example, shown in Fig. 8.4, is the reduction of the coefficient of friction between two W(001) surfaces after oxygen adsorption. Here the coefficient of friction drops by a factor of two even for small oxygen coverages ($\theta < 0.5$).

However, an atomic scale understanding of how these contaminants dramatically reduce adhesion and friction is still lacking. In particular, several questions remain unresolved: Do the contaminants change the way the metals deform or workharden in the surface region? How does the break-down of the lubrication film occur? Does shear sliding or tearing occur at the film-film contacts?

8.2 Objectives and Results

In our studies of friction and lubrication, our principal objective is to determine how the structure of a chemisorbed overlayer influences the coefficient of friction. An apparatus (discussed in section 2.2.7) has been built and tested that is capable of measuring the coefficient of friction between two well characterized surfaces under ultra-high vacuum conditions. The plan is to study the effect on friction of a wide variety of adsorbate surface structures under conditions where the only variable changed is the bonding of the

adsorbate to the surface. By concentrating on those adsorbates, such as ones described in this thesis, whose surface structures have been well characterized by other surface science techniques, it is hoped that a deduction of the underlying mechanisms for lubrication by chemisorbed monolayers will be possible.

In Fig. 8.5 we show the preliminary results of experiments done with a rhodium pin sliding over a Rh(111) single crystal sample under several conditions. In these experiments, the pin slides back and forth several times over the same track, which accounts for the oscillatory behavior of the coefficient of friction. Figure 8.5a shows the coefficient of friction as a function of time for the pin sliding over the sample in air with a 50 gm load and a sliding speed of 0.005 cm/s. The "noise" in the coefficient of friction is most likely from the pin sticking briefly then slipping across the surface. In Fig. 8.5a, the average value of the coefficient of friction for sliding in air is 0.24.

Figure 8.5b shows the coefficient of friction as a function of time for the pin sliding across a Rh(111) sample that was first cleaned in UHV then exposed to air. During this experiment the background pressure was 3×10^{-7} torr, the load is 50 gm, the sliding speed is 0.005 cm/s, and only a carbon Auger peak is visible in the Auger spectrum of the Rh(111) surface. From Fig. 8.5b, it is apparent that the nature of the slip-stick has changed and the average coefficient of friction has increased to 0.74 compared to the experiment done in air.

Figure 8.5C shows the coefficient of friction as a function of time for the pin sliding across the sample with an ambient pressure of 10^{-9} torr. Before the experiment, the Rh(111) sample was cleaned by cycles of Ar^+ sputtering, heating in O_2 and annealing in vacuum to the point where only small amounts of surface impurities (P, B, and C) were detectable by AES; a submonolayer of adsorbed CO may also be present on the surface during the experiment. The rhodium pin was cleaned by cycles of Ar^+ sputtering; AES indicated the presence of about one monolayer of carbon as well as a substantial amount of oxygen on the pin surface. Again, the load was 50 gm and the sliding speed was 0.005 cm/s. The average coefficient of friction is 0.9.

From the results in Fig. 8.5, one can see that the cleaner the rhodium surfaces become, the higher the coefficient of friction between them, in agreement with experiments with other metal surfaces. To achieve the high coefficients observed for atomically clean metal surfaces in contact (see Figs. 8.2 and 8.4) further cleaning of the two rhodium surfaces, particularly the rhodium pin, is needed. Modifications that make it possible to heat the pin should enable us to achieve better cleaning of the pin surface.

Experiments are currently in progress by Peter McAnally of our group using the "friction apparatus" described in this thesis to study the effect that adsorbates on Rh(111) have on the coefficient of friction. These experiments will concentrate on those adsorbates studied in this thesis in order to make use of the body of knowledge already gained; consequently, these experiments should be regarded as a continuation of this thesis.

REFERENCES

1. R. Stribeck, Zeit, V.D., 46 (1902) 1341.

2. A.W. Adamson, Physical Chemistry of Surfaces, 4th Ed., Wiley, New York, 1982.

3. D.F. Moore, Principles and Applications of Tribology, Pergamon, New York.

4. F.P. Bowden and D. Tabor, The Friction and Lubrication of Solids, Part I (1950) and Part II (1964), the Clarendon Press, Oxford.

5. D.H. Buckley; Surface Effects in Adhesion, Fiction, Wear, and Lubrication; Elsevier, Amsterdam, 1981.

6. D.H. Buckley, J. Colloid Interface Sci., 58 (1977) 36.

7. N. Gane, P.F. Pfaelzer, and D. Tabor, Proc. Roy. Soc. London, A340 (1974) 495.

8. K. Miyoshi and D.H. Buckley, ASLE Trans. 27, pp. 15-23.

FIGURE CAPTIONS

Fig. 8.1 Regions of hydrodynamic and boundary lubrications. (From Ref. 2.)

Fig. 8.2 Coefficient of friction of the indicated metals against a gold (111) surface at 25°C. (From Ref. 6.)

Fig. 8.3 Influence of hydrogen sulfide on adhesion of between two Fe(011) surfaces. (From Ref. 5.)

Fig. 8.4 Oxygen adsorption and friction for tungsten sliding on tungsten, both (100) planes. Load, 50 gm; speed, 0.001 cm/s; temperature, 20°C; pressure, 10^{-10} torr. (From Ref. 5.)

Fig. 8.5 The coefficient of friction as a function of time for a rhodium pin sliding on a Rh(111) crystal surface. The sliding speed is 0.005 cm/s and the temperature is 310 K. (a) Sliding in air; (b) sliding in 3×10^{-7} torr; and (c) sliding in 10^{-9} torr after some cleaning of the pin and sample surfaces. Note the scale for the coefficient of friction is different for each plot. The oscillatory behavior is from the pin sliding back and forth over the same track.

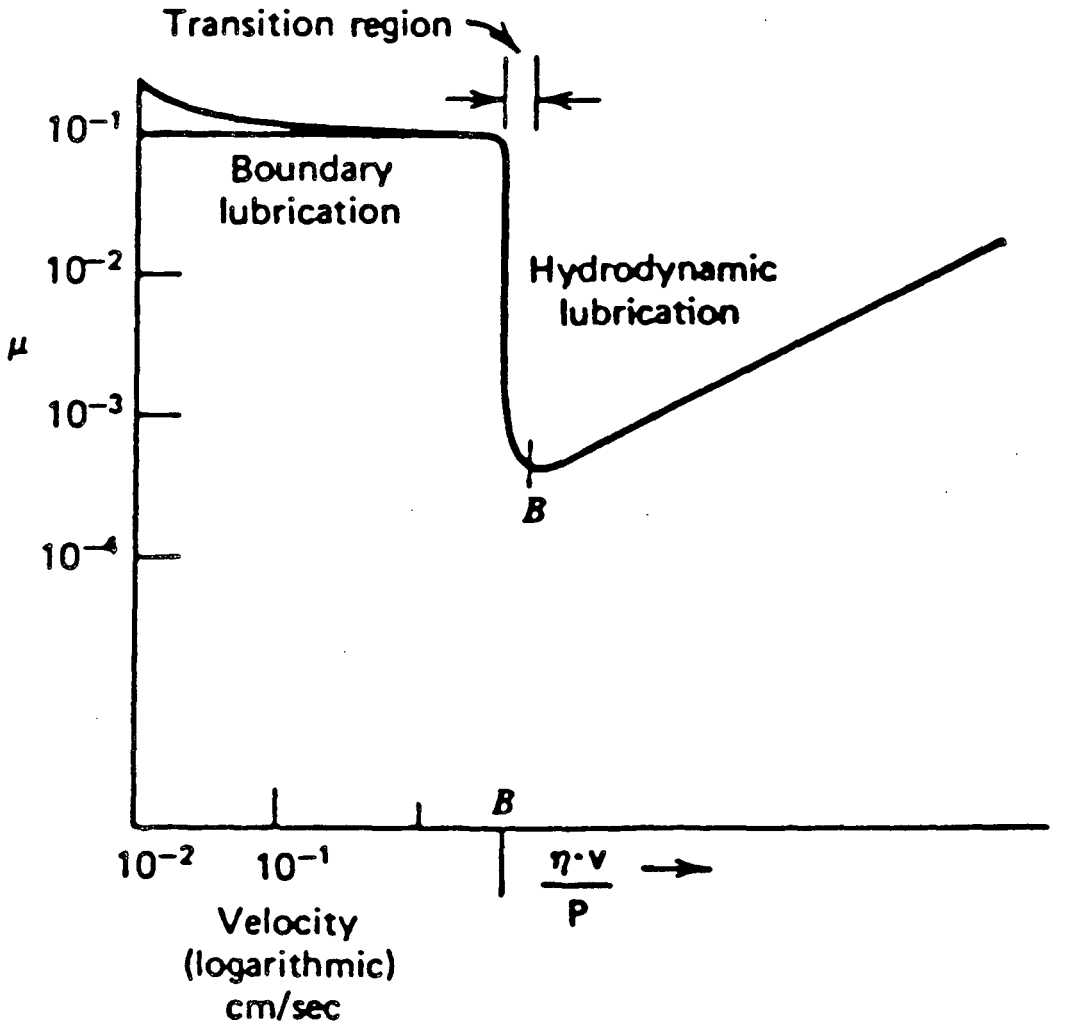

XBL 869-3431

Figure 8.1

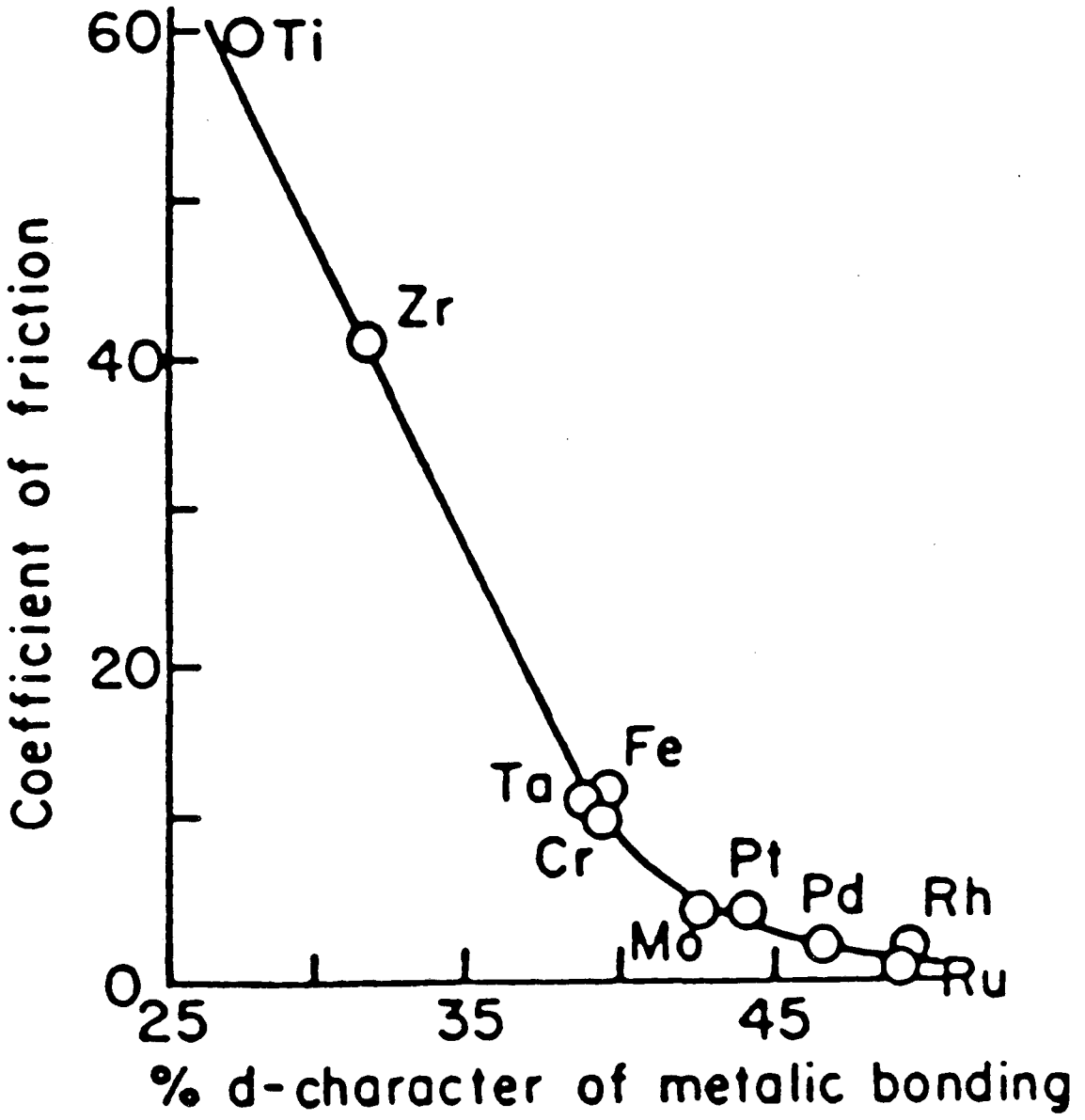

XBL 869-3428

Figure 8.2

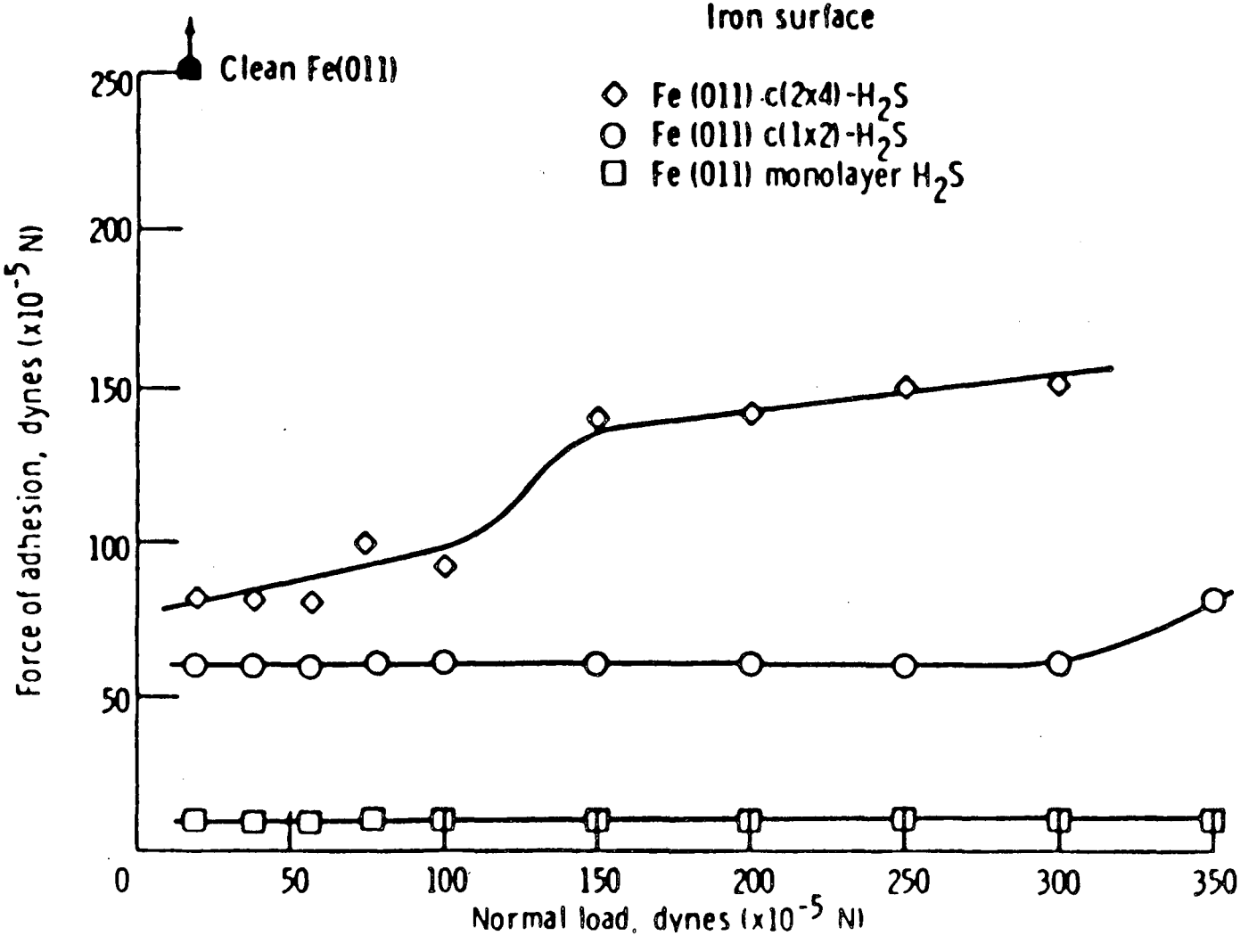

XBL 869-3430

Figure 8.3

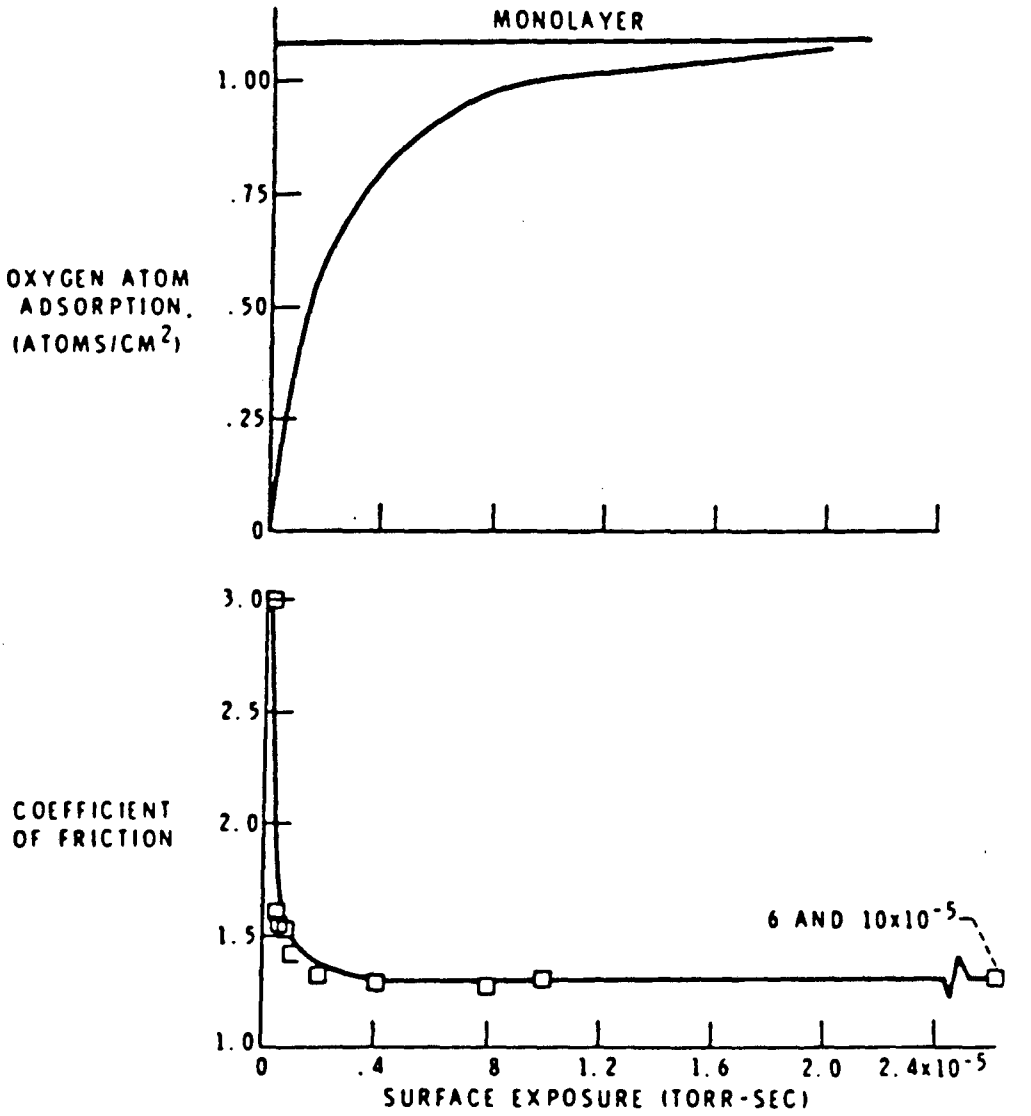

XBL 869-3427

Figure 8.4

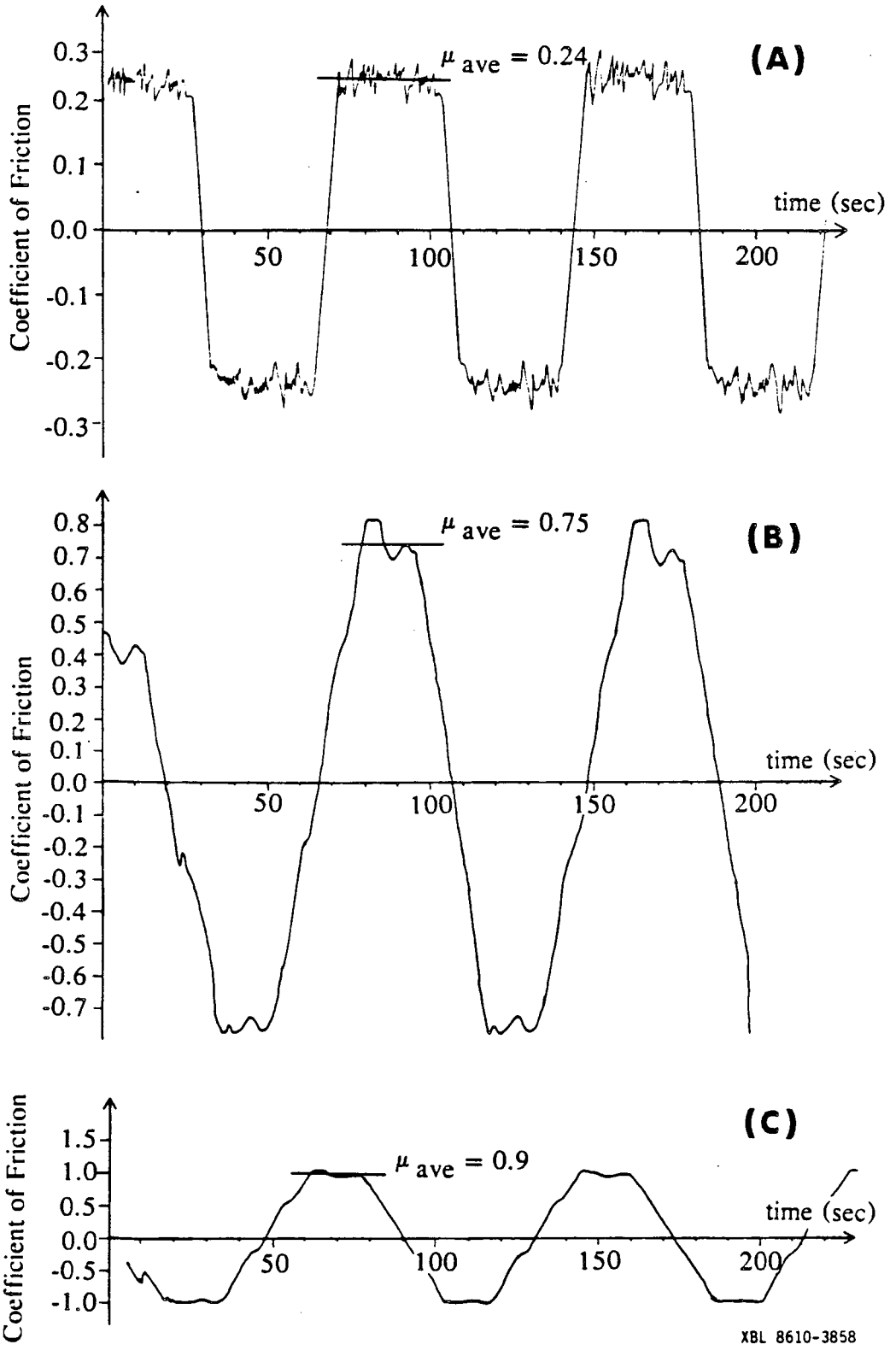
(A)
μ ave = 0.24
Coefficient of Friction
0.3
0.2
0.1
0.0
-0.1
-0.2
-0.3
time (sec)
50
100
150
200
(B)
μ ave = 0.75
Coefficient of Friction
0.8
0.7
0.6
0.5
0.4
0.3
0.2
0.1
0.0
-0.1
-0.2
-0.3
-0.4
-0.5
-0.6
-0.7
time (sec)
50
100
150
200
(C)
μ ave = 0.9
Coefficient of Friction
1.5
1.0
0.5
0.0
-0.5
-1.0
time (sec)
50
100
150
200
XBL 8610-3858

Figure 8.5

LAWRENCE BERKELEY LABORATORY
TECHNICAL INFORMATION DEPARTMENT
UNIVERSITY OF CALIFORNIA
BERKELEY, CALIFORNIA 94720